3D jet writing – controlled deposition of multicomponent electrospun fibers in three dimensional space

by

Jacob Herbert Jordahl

A dissertation submitted in partial fulfillment
of the requirements for the degree of
Doctor of Philosophy
(Chemical Engineering)
in the University of Michigan
2016

Doctoral Committee:

Professor Joerg Lahann, Chair
Professor Paul H. Krebsbach, University of California Los Angeles
Professor Ronald G. Larson
Associate Professor Gary D. Luker
Professor Michael J. Solomon

To my loving family.

Follow your dreams and anything is possible.

Acknowledgements

To those not familiar with the process of attaining a Ph.D., you may think it is a process which involves secluding yourself in a dark, dingy lab for the course of five years, and at the end you walk out smarter with a degree in hand. However, this is most definitely not the case. Now that I have reached the end of my tenure here at the University of Michigan, I can most definitely say that I could not have gotten where I am now without the help and support of a lot of people. First and foremost, my advisor Prof. Joerg Lahann has not only accepted me into his lab and provided me lab space to perform experiments, but he also helped me grow as a scientist and taught me how to look at experiments with a critical eye. Even when I did not have a source of funding, or when I became frustrated at the process of publishing research articles, his persistent support for me and the work that I do has helped me grow both personally and professionally. His leadership and mentoring style has created a lab environment where collaborations are fostered, which is a critical skill that I will be using for the remainder of my scientific career.

Again, my successes as a graduate student cannot be solely attributed to the work that I performed by myself, but many thanks have to be given to all the collaborators I had during my time here at the University of Michigan. I must thank all of my collaborators Prof. Paul Krebsbach, and his lab members Dr. Hongli Sun, Dr. Luis Villa-Diaz, and Tuğba Topal, each provided me with technical expertise in animal surgery and pluripotent stem cell culture that were critical to numerous portions of this disseration. Many thanks also need to be extended to

Prof. Gary Luker, his wife Dr. Kathryn Luker and undergraduate student Henry Haley, for the vast amount of intellectual contributions and animal surgeries towards my work in creating metastatic cancer microenvironments. Prof. Jinsang Kim, including Dr. Min Sang Kwan and Dr. David Bilby, must also be thanked for providing me with the opportunity to work on new organic sensing platforms and solar cell technologies which were not included in this dissertation. I would also like to thank Prof. Kotov, and his lab members Dr. Yunlong Zhou and Douglas Montjoy, for the projects that we attempted to start together. Projects which did not get off the ground still provided me with the opportunity to interface with many great researchers. Since the development of my project, and the introduction of new members to the Lahann Lab, my scaffolding technology has now distributed to numerous other researchers at the University of Michigan, and across the world, but there is not enough space (even in this thesis) to name all the collaborators who are helping to proliferate my contributions to science.

I would like to extend my gratitude to others who have contributed to my success here at the University of Michigan. Prof. Michael Solomon, Prof. Paul Krebsbach, Prof. Ronald Larson, and Prof. Joerg Lahann have provided me with valuable insight and suggestions throughout my journey through the Ph.D. program, as they have graciously agreed to serve as committee members for my preliminary exam, data meeting, and my final oral thesis defense. A special thanks needs to be extended towards Prof. Gary Luker for agreeing last minute to serve as a cognate member for my final thesis defense.

While there were many contributors to my work, the members of the Lahann Lab, past and present, have not only helped me develop my research, but they were also my friends that made the lab my home away from home. Dr. Kyung Jin Lee was my mentor during my first months of research. He provided me with an initial research project, and taught me a lot of what I know

about electrospinning polymer fibers. His patience, creativity, and expertise contributed greatly to my early success in the lab. Dr. Thomas Eyster helped to lay the foundation of culturing cells on scaffolds. Stacy Ramcharan was the first student taken to join in the project I had developed. I would like to thank her for all that she has done to progress the fiber scaffolding technology, the countless hours of discussion, and all of her help. Over the last four years she has become one of my dearest friends, and I am blessed to have her in my life. Dr. Luis Solorio joined the lab in the middle of my time here, and with his help we were able to revolutionize the use of fiber scaffolds as a cell culture platform. His expertise in with cells, hard work, and outgoing personality, made anything possible on scaffolds. In this time, I also worked with many undergraduate and high school students who helped immensely with the fabrication of scaffolds. Rachel Menchak, Charles (Chuckie) Daniels, Joshen Patel, Clarissa Baumgarten, Rachel Wilson, Ryan Carse, Brandon Lucas, James Kim, Kristen Enoch, Jeffery Noble, Christopher Dunlay, Kelsey Jordahl, and Steven Frey. Of the undergrads that worked on helping me develop the fiber scaffolding technology, Clark Teeple was indispensable. His skill as scaffold fabrication, and motivation to learn LabView programming, helped to fundamentally transform how scaffolds were made.

My research also benefitted from other members of the Lahann Lab which were not directly involved in scaffold related projects. I would like to thank current post-docs Kathleen McEnnis and Stephie Christau for insightful discussions over lunch. Thanks to current graduate student Kenneth Cheng, who joined the lab with me five years ago. He has been with me for the entire journey, and has become a good friend along the way. As the younger generations of graduate students join the lab, my role began to shift from mentee to mentor. I would like to thank Ramya Kumar, Jason Gregory, Nahal Habibi, and Dylan Neale for their tremendous help and friendship along the way. I would also like to thank Lahann Lab at KIT. I appreciate the input you have

provided me, and putting up with broken microphones and bad connections. Things have come a long way since I first joined the lab. We have left behind the days of camera-less Skype calls where I couldn't understand anything coming over the speakers, to now have high resolution video conferences every week. Nobody there probably remembers these days, but be grateful for Polycom. As the longest lived Lahannian currently in the lab, great changes have taken place since my time here began. I would like to thank those that have left the lab during my time here, as they helped create lasting memories of my days as a graduate student.

Visiting scholars from around the world provided an opportunity to make new friends. I am especially grateful for meeting Dr. Domenic Kratzer, who became a great friend in the short amount of time he had here. I am also thankful for getting to know Christoph Hussal, Dr. Amit Sitt, Gokcen Unsker, Yu Liang, Fan Xie, Prof. Jana Soukupova, and who could forget Hiro. All of your time here was too short. Former members of the Lahann Lab, Dr. Sangyeul Hwang, Dr. Taehong Park, Dr. Xiaopei Deng, Dr. Hakan Durmaz, and Dr. Afrin Ross, Kai Liu, Hyesun Jun, Gowthamy Venkidasubramonian, and Seyed Reza Roghani Esfahani all helped make my time in the Lahann Lab a great experience, and they laid the foundation of success for the students who followed in their path. This creates the environment for great collaborative research to continue in the lab. Three former members of the Lahann Lab who deserve special recognition are Dr. Jaewon Yoon, Dr. Asish Misra, and Dr. Sahar Rahmani. These three put up with a lot of questions from me in my first years here, and I cannot thank them enough for their patience and guidance through these years. What makes them stand out from other former lab members is that they helped make the lab feel like a family, which made me look forward to every day I went to work. I can only hope that my presence in the lab contributed to a similar environment for other students.

The technical staff at the core facilities also deserve many thanks. Chris Strayhorn at the University of Michigan School of Dentistry Histology Core performed much of the histological preparation of the various tissue samples generated from the *in vivo* studies included in this dissertation. Michelle Lynch from the MicroCT Core at the Dental School scanned and quantified all microCT data obtained. The staff at the Microscopy and Image Analysis Lab (MIL) also deserve many thanks for all their help over the years. Chris Edwards was always there if I needed any trouble with the instruments. Bruce Donohoe and Linda Barthel helped me learn how to use the confocal microscopes, Linda Barthel also trained me on numerous other instruments and her expertise in microscopy helped me greatly in my studies. Jeff Harrison trained me on scanning electron microscopy, and Sasha Meshinchi assisted me with my image analysis in Imaris.

Finally, I have to say that I could not be in the position I am today without my family. I would like to thank my parents, Kim and Vanessa Jordahl, for their continuous support and the encouragement they provided me for my entire life. My mom, the master of Christmas, the mommiest mom who makes such grand breakfasts, has a drive for perfection like no one else I know. Your self-sacrificing nature in pursuit of ensuring success in all that you do is an inspiration to me. My dad helped me to gain skills that most people do not have, from home construction to properly seasoning food. I also got a bit of your sense of humor. You also helped me to find my first jobs in high school, and while I am no longer making smoothies or building homes, they helped me to develop the necessary skills for success. Both of my parents have instilled within me the work ethic required to accomplish my goals, and your guidance has led me to acquire the skills that I need to succeed not only in an academic setting, but in all aspects

of life. Now, these things you have done for me have helped through my degree to get me my first job out of graduate school, and I cannot thank you enough.

Over the course of these five years in graduate school I have gained the perspective of what is it like being away from my family. Despite the distance, it was always abundantly clear that no matter what is happening in my life, or how far away I am, my family will always be there for me. After every trip back home, I was always looking forward to the next time I got to spend time with my mom, dad, sisters, and extended family. Any time there was a holiday weekend, I wanted to be with my family; traditions we formed growing up have cemented our bond together. I know that having such a close knit family is something unique that many people have never had, and it makes me appreciate how lucky I am to be a part of it. My sisters Amanda, Ashley, and Kelsey have significantly impacted who I am today. From my younger years where their idea of fun was teaching me math, to being my organic chemistry lab partner in college, to working with me here at Michigan, my sisters have always played a role in my education. Beyond that, they also fulfilled the customary sisterly role of teasing their brother, which only in hindsight can it be appreciated for helping to develop my personality. More recent additions to the family, Scott Keplin and Gregory Strand, have only enhanced the bonds we have formed as siblings, and I look forward to our family expanding more in the future. Last but not least is Arthur Keplin, my nephew and godson. Every day I would look up from my work and see your smiling picture on a stack of books. This would keep me motivated during times of struggle and stress, knowing I have such a wonderful family back at home. You are a little ball of energy and your curiosity about the world is inspirational. I hope that someday you can use these traits to pursue your greatest passions in life, always follow your dreams and know that you will achieve success. To any teachers or kids that tell you otherwise, don’t listen to them and keep your eyes

forward to the future. I will always be there for you, and I look forward to being there for you as you grow older, to help teach you the wonders of the world, to guide you in times of confusion, and to help you walk in the light of the Lord.

Table of Contents

Chapter 2: Needle-less EHD Co-Jetting

Chapter 3: 3D Jet Writing

Chapter 4: In Vitro Culture on Scaffolds

Chapter 5: In Vivo Applications

Chapter 6: Summary and Future Work

List of Figures

Figure 3.28. Curvilinear structures fabricated via 3D jet writing.
A) A MATLAB routine was utilized to produce a code to control the collection electrode. The route taken by the stage is outlined by the plot depicted. **B)** The resultant polar rose structure produced by the code in (A) when the jet speed was approximately equal to the collection electrode speed. **C)** The resultant polar rose structure produced when the jet speed was significantly slower than the collection electrode speed. **D)** A depiction of the path taken by the grounded collection electrode to create a nine petal polar rose. The path was generated via a MATLAB routine. **E)** The resultant nine petal polar rose structure produced by the code in (D) when the jet speed was approximately equal to the collection electrode speed. **F)** The resultant polar rose structure produced when the jet speed was significantly slower than the collection electrode speed. **G)** Scanning electron micrograph of a six petal polar rose structure fabricated with a collection electrode speed significantly greater than the fiber deposition speed. **H)** Scanning electron micrograph of the same six petal polar rose structure when the collection electrode speed was approximately equal to the depositing fiber jet speed. Scale bars indicate 1 mm.

Figure 3.29. Circular ring structures fabricated via 3D jet writing.
A) Scanning electron micrographs of a ring structure made via 3D jet writing containing ten fiber stacks. These rings formed flat annular ring shapes as opposed to circular vertical walls. **B)** When 40 fiber stacks are implemented, the stacking gets more difficult due to the accumulation of charged fibers. This results in buckles in the fiber deposition, which seem to occur at regular intervals around the fiber ring structure. Scale bars indicate 1 mm.

Figure 3.30. Other curvilinear fiber structures.
A) A Pacman structure showing a Pacman chasing a ghost highlights the difficulties in creating precise sharp corners, and repeating movements over curves. Slight changes in jet speeds results in poor stacking in the curved and cornered regions. **B)** Letters created from line segments were created in MATLAB to write a name out of electrospun fibers. Similar deviations in curved line segments are observed. Scale bars indicate 1 mm (A), and 5 mm (B)

Figure 3.31. Electric field streamlines around fiber stacks to explain fiber stacking behavior.
A) The overall setup of the COMSOL simulation, which includes a needle, a secondary ring electrode, grounded collection electrode, and five fiber stacks. **B)** Altering the fiber spacings from 150 µm, 300 µm, 500 µm, and 750 µm from left to right. The streamlines are bent towards the fibers, illustrating why smaller pore structures are difficult to fabricate. **C)** If the top fiber of the fiber stacks are discharged completely, the electric field streamlines are bent in towards the fiber stacks making stacking the preferred mode of fiber deposition. **D)** When the top fiber is charged (1000 V), a repulsive electric field is present making non-stacking the preferred means of deposition. Scale bars indicate 500 µm.

Figure 3.32. Pseudo-woven fiber structures fabricated with and without an insulating layer over the grounded electrode.
A) A schematic illustration of the programmed stage movements to create a pseudo-woven structure. i) The first layer is written, ii) the second layer is shifted by half a square in both directions, iii) repeating the first layer, iv) repeating the second layer. **B)** The top fiber is able to

List of Tables

List of Appendices

Abstract

Electrospinning is a fiber fabrication technique which has potential use in applications ranging from filters and sensors to regenerative medicine. Generation of multi-component fibers and particles is possible through the use of a technique called electrohydrodynamic co-jetting. Despite the many applications, the process suffers from two main limiting factors. First, the reliance on a bicompartmental fluid interface inherently limits the scalability of the system. Secondly, the random fiber placement resulting from a process instability leads to limited pore sizes and uncontrollable 3D architectures. Herein, both of these factors are addressed independently. Scalability was addressed by creating a device which creates an extended fluid interface composed of two polymer solutions. This method was shown to produce bicompartmental fibers and particles at throughputs in excess of 30 times greater than traditional methods while retaining consistent fiber size distributions. Next, a method of completely eliminating the whipping instabilities associated with the electrospinning process, called 3D jet writing, was shown to be capable of perfectly stacking of fibers on top of one another. This process utilizes radially directed electric fields to dampen the formation of whipping instabilities, and a moving collection electrode to produce 3D fiber geometries. Deposition of fiber lines within approximately 15 μm is achieved using this system, making direct writing of fiber stacks within 0.3° of perfectly parallel, and 1.1° of perpendicular, and fabrication of three-dimensional scaffolds with regular tessellated prismatic pore architectures possible with this technique. The

precision afforded by this technique was used to create 3D high-density stem cell culture environments which contain up to 1.4 million cells/mm^3 polymer material, with 96% of the scaffold volume consisting of open area for 3D cell growth. These scaffolds allow for 3D cell culture to be tessellated across large areas, addressing common limitations associated with other 3D culture techniques. When differentiated osteogenically, stem cell microtissues can promote healing of calvarial defects in mice, producing on average over three times the new bone volume compared to the control groups. Similar tessellated differentiated stem cell microtissues were also able to simulate a diseased tissue by promoting metastasis in anomalous anatomic sites in 5/5 cases.

Chapter 1

Electrohydrodynamic Co-Jetting

1.1 Electrohydrodynamic Phenomena

1.1.1 Introduction

The application of an electric field to a fluid can give rise to a wealth of novel electrohydrodynamic phenomena. Taylor cones and the jet that they emit are two such phenomena. Taylor cones are generated by placing a potential difference across a capillary and a grounded plate electrode.[1] An electrically semiconductive fluid being driven through an electrified capillary in an insulating medium is able to form a Taylor cone once a critical charge is attained.[2] To conserve charge and mass, a thin jet of charged fluid is emitted from the apex of the cone.[3] This jet eventually breaks up into a very fine spray, known as an electrospraying, or solidifies into a fiber, i.e. electrospinning.[4] Despite its stationary appearance, there are quite complex flows occurring within the Taylor cone.[5]

While these phenomena are not always evident during electrospinning experiments, having a basic understanding of the fluid dynamics present in the system allows one to speculate why a certain fluid jet behavior is observed. An example of such a phenomenon in electrospinning is the shape of the Taylor cone. The shape and behavior of the Taylor cone is one of the most critical aspects of electrospinning, as it provides a visual cue which can be used to determine jet stability, and to predict the quality of the material being fabricated. Cone shape and behavior can

then the used to modify the solvents used, polymer concentrations, and applied voltages among other parameters. Understanding of these mechanisms are not necessary to perform electrospinning experiments, but having a background in the electrohydrodynamic processes involved can prove to be invaluable in the troubleshooting process.

1.1.2 Taylor Cone Shape

One of the most prominent features in electrospinning and electrospraying is the formation of a Taylor cone. The origins of the deformation of a normally spherical droplet to a conical shape has been described extensively in literature, however they were first modeled as a cone by Taylor in 1964.[6] While previous methods of approximation were performed by Zeleny, in 1917, who approximated the cone as an ellipsoid,[7] Taylor showed that this evaluation did not provide a sufficiently accurate prediction of the electric field necessary to produce the cone shape. Taylor instead determined the final shape by balancing the electric shear stress with the surface tension present in the fluid. This approximation relied on the simplification that the fluid was infinitely conducting, therefore having an equipotential surface. By examining how curvature affects the surface tension of the cone, he deduced how the electric field must change throughout the cone to balance out the surface tension forces. He proposed the following equation for the electric potential that would produce an electric field that satisfies the balance between the surface tension forces and the electric field forces:[6]

$$V = V_0 + AR^{\frac{1}{2}}P_{\frac{1}{2}}(\mathrm{Cos}(\theta)) \qquad (1.1)$$

Where V is the electric potential applied, V_0 is the electric potential of the fluid, R is the radial coordinate, $P_{1/2}$ (Cos(θ)) is a half order Legendre polynomial, θ is the angle of the cone, and A is a coefficient to be experimentally determined. Based on Taylor's assumption of the surface being approximately equipotential, the Legendre polynomial portion of Equation 1.1 must equal zero[1].

$$P_{\frac{1}{2}}\big(Cos(\theta)\big) = 0 \tag{1.2}$$

$$\therefore$$

$$V = V_0 \tag{1.3}$$

The half order Legendre polynomial in Equation 1.2 equals zero at an angle of approximately 131.7°. Taylor called this value θ_0, which represented the only zero solution of Equation 1.2 within the physically meaningful range of θ (from 0 – 180°). Therefore, Taylor was able to predict the angle of the cone, α, of an infinitely conductive fluid was equal to 49.3°[6]

$$\alpha = 180° - \theta_0 = 180° - 131.7° = 49.3° \tag{1.4}$$

The results showed that this approximation was fairly accurate in predicting the cone angle that a fluid surface would make. While this result was a vast improvement to the previous work, it still was not perfect. The assumptions which led to the imprecision of Taylor's method were that the tip of the cone does not usually come to a point, the loss of charges due to electrospray emission was not accounted for, and no capillary needle was present feeding material into the cone.[8, 9]

Later investigations found that the shape of Taylor cones was due to a combination of balancing the liquid pressure, liquid-air surface tension, gravity, electrical stresses on the cone surface, liquid inertia, and the liquid velocity.[10] These experiments demonstrate that the Taylor cone angles are quite often smaller than the 49.3° originally predicted. Taylor's steady cone approximation, with no flow entering or leaving the cone, led to much of this error.

These studies have resulted in cone shape predictions for more complicated systems, but they are still highly idealized. Taylor cone shapes have been predicted with sharp cone tips, axisymmetric cones, and a needle feeding fluid into a cone with large applied electric fields.[11] These predictions were since shown to approximate values for the shape of the Taylor cones.[9, 12] It was also found that for a given applied voltage, there seemed to be a minimum and maximum sustainable flow rate. The minimum flow rate corresponds to microjet electrohydrodynamic stability limitations,[13] while the maximum flow rate corresponds to the stability of the meniscus.[9] Near the maximum flow rate, the meniscus was described as developing a progressively increasing jittering motion near the cone tip, while maintaining a stable jet.[9] Near the minimum flow rate, it was seen that the meniscus was not vibrating, but there was a "catastrophic disappearance" of the jet.[9] Each of these changes resulted in a change in the cone angle, and clearly demonstrated that the idealized value predicted by Taylor was not accurate for all cases of Taylor cone formation. Understanding how Taylor cone shape and behavior are related to flow rates among other parameters, and that minimum and maximum flow rates exist, aids in establishing a stable cone during an electrospinning experiment.

1.1.3 Flow Within Taylor Cones

In addition to their unique shape, Taylor cones also have unique flow characteristics inside of them. These flows arise from two factors. The first factor is the fluid flow from the capillary to the jet produced at the tip of the cone. The second driving force is the addition of a tangential shear stress component from the electric field on the surface of the fluid.[14] This shear stress is described by the following equation:

$$\tau_{\theta r} = \varepsilon_0 (E_\theta^o - \varepsilon E_\theta^i) E_r \tag{1.5}$$

where $\tau_{\theta r}$ is the tangential shear stress, ε_0 and $\varepsilon_0\varepsilon$ represent the permittivity of the outer insulating layer (typically air, dielectric fluid, or vacuum) and the permittivity of the fluid (typically a conducting liquid) respectively. E_θ and E_r are the normal and tangential component of the electric field respectively, and the terms o and i represent the outer and inner fluid phase respectively.

According to Barrero *et al.*, the liquid bulk can be approximated as quasineutral, so the electrical charge can be thought of as located only on a thin layer at the cone surface with thickness approximately equal to the Debye length.[2] This allows the electric field term of the inner fluid to be neglected, resulting in the following simplification of the electrically induced shear stress at the surface:

$$\tau_{\theta r} \approx \varepsilon_0 E_\theta^o E_r \tag{1.6}$$

This additional shear stress is not seen in highly conductive fluids since the surface of the cone would be approximately equipotential, meaning the term E_r would be about equal to zero. In this case the electrically induced shear stress is negligible, producing fluid motion comparable

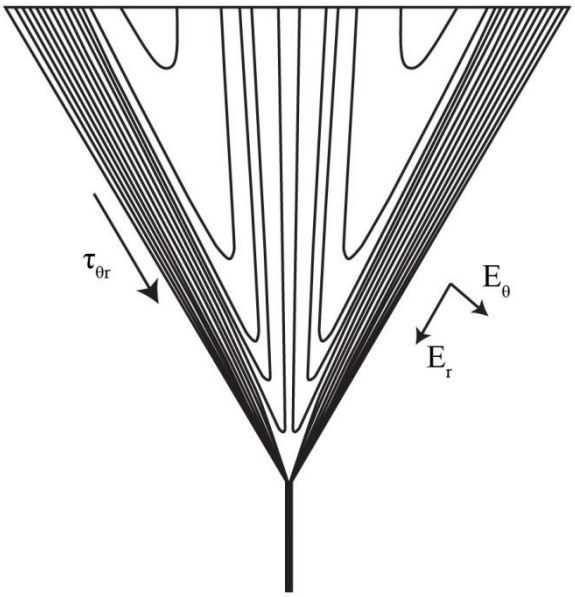

Figure 1.1. Meridonial flow profile within Taylor cones. This illustration depicts the fluid on the edges of the cone being pulled into the fiber, while near the middle of the cone has the meridional flow.

to a sink flow.[14] Therefore, as the electrical conductivity of the inner fluid decreases, the shear stress at the interface increases, leading to an increased interfacial velocity. A 'meridional' type flow arises if this induced velocity is greater than the velocity produced by the sink flow condition mentioned previously.[15] Exploration of the conditions necessary to form a stable jet, while simultaneously observing the flow within the Taylor cone, provided experimental verification of this mechanism for meridional flow.[16] When a stable jet of semiconducting (not high, but not low conductivity) fluid was formed, the fluid flow within the cone traveled along the surface of the cone and back up the central axis.[16] However, when the 'semiconducting' fluid was replaced with water, the flow stopped. The high conductivity of water led to the formation of an equipotential surface which suppressed the meridional flow within the Taylor cone, reducing the tangential component of electric shear stress to a negligibly small value. Interestingly, the meridional flow was found to be reversible if the gas outside the Taylor cone is switched from air to either He or Ne, which have lower breakdown potentials. If the breakdown potential of the gas is low enough, the formation of a jet is not allowable because the gas becomes conducting before the jet instability can arise.[16] This results in a coronal discharge from the capillary to the plate electrode below the droplet. Discharge at the capillary leads to a greater potential at the droplet apex than at the capillary, which causes the meridional flow to be reversed with no fluid

jet procuded.[16] These studies illustrate the importance of fluid conductivity, as well as atmospheric composition, in the formation of stable Taylor cones. Understanding how changes in fluid properties and atmospheric composition affect the fluid jet and cone formation is critical when troubleshooting new electrospinning techniques.

An alternative source of this meridional flow within a Taylor cone is the Electric Marangoni Effect. This effect arises in fluids when there is a variation in the surface tension of the fluid caused by a non-uniform electric field. Similar to a surfactant or temperature changes, an electric field can modify the surface tension. Therefore, if the cone is exposed to a non-uniform electric field, surface tension gradients would form creating the meridional motion seen.[5] The properties of the fluid and controllable variables can be used to approximate the flow within the Taylor cone by calculation of the Reynolds number. At low Reynolds number ($Re<<1$) the flow was considered to have purely meridional behavior. After a critical Reynolds number, the flow will contain a large swirling motion superimposed on the meridional motion seen at low Reynolds number.[2]

The swirling motion is another prominent flow characteristic of Taylor cones. The swirl arises spontaneously in liquids with low electrical conductivity and low viscosity (high Reynolds number), which leads to a helical motion of fluid. Formation of the swirling flow in conical geometries has been studied using conical similarity solutions to the Navier-Stokes equation.[5, 17] It was found that for the swirl formation to occur, distinct regions of positive and negative angular momentum need to be created to preserve angular momentum.[18] However, the polymer solutions typically electrospun in this work do not undergo this type of swirling motion within the Taylor cone. Further analysis of this phenomenon is examined extensively by Shtern *et al.*

1.1.4 Jet Properties and Scaling

Besides the flow within the Taylor cones, another property of this structure is the fluid jet emitted from the apex of the cone. This is the source of the particle and fiber formation. The first step in exploring the process of jetting is to determine the different flow regimes obtainable prior to the 'stable jet mode'.

The first mode of forming an electrospray or jet is obtained by flowing liquid through a capillary tube at a low flow rate. This alone, without the addition of an electric field produces liquid drops of a certain volume, which vary based on the surface tension of the fluid. The addition of a small electric field to the droplet reduces the critical volume of the drop, causing an increased rate of dripping (a larger quantity of smaller drops are formed, mass is still conserved). This is known as 'dripping mode'. The increased rate of dripping arises from two sources: First, the charged droplet is attracted to the grounded plate electrode due to electrostatic forces.[8] Secondly, the electrical shear stresses reduce the effective surface tension of the drop, causing it to break off earlier.

As the electric field becomes more significant, the liquid meniscus at the end of the capillary will suddenly deform and discharge either a small droplet or a long thin stream of fluid, then returning to its original shape.[15] This cycle continues indefinitely, and is called 'pulsating mode'.[19] Increasing the applied electric field even further results in an increased rate of pulsation until the meniscus deforms into a cone and a stable jet is emitted from the apex of the cone.[15] This is called 'stable jet mode' or ‘cone-jet mode’.[19] If the electric field is increased even further, multiple jets are possible, and at a high enough electric field the cone retracts up to the rim of the capillary, producing cloud of droplets.[15]

The formation of a fluid jet due to an instability of a droplet was first studied by Lord Rayleigh.[8] He also noticed that a minimum charge was necessary in order for this instability to occur. After Rayleigh, it was found that the critical voltage necessary to form this instability in a liquid drop scaled as $\gamma^{1/2}$, based on a basic balance of electrostatic pressure and capillary pressure. G.I. Taylor determined the minimum voltage necessary to produce a Taylor cone, given by the following scaling[2]

$$V \sim \left(\frac{\gamma d}{\varepsilon_0}\right)^{\frac{1}{2}} \tag{1.7}$$

where V is the minimum voltage, d is the diameter of the capillary tube, with the other parameters previously defined. This started laying the groundwork for the field of electrospraying to be explored.

The formation mechanism of a stable electrohydrodynamic jet produced by a Taylor cone derived from the studies involving the meridional flow pattern. This flow produced inside the Taylor cone causes fluid to travel from the capillary, along the surface of the cone, and back up the axis of symmetry. Therefore, it was postulated that the fluid contained in the emitted fluid jet was not drawn from the bulk of the cone, but instead derived from the outside of the cone.[16] With charge being carried on the surface of the cone, and the fluid jet forming from the fluid traveling along the cone surface, the fluid jet which emits from the apex of the cone has a significant electrical current associated with it. This provides the driving force for the jet and electrospun products to collect on a grounded surface.

The most significant feature of a fluid jet formed from a Taylor cone is its very thin diameter, typically orders of magnitude smaller than the capillary from which the fluid was dispensed.[20] A fluid jet is formed at the apex of the Taylor cone such that a minimum stable

surface energy is achieved while conserving charge and mass. Stable jet formation requires that the electric field penetrates into the liquid, which causes a tangential electric field along the surface of the Taylor cone. This creates the driving force which accelerates the fluid downward into a jet which is ejected from the vertex of the cone.[8] This fluid stream can have a diameter ranging from nanometers to microns.[21] The size of the jet is typically controllable by changing the conductivity of the cone or the flow rate imposed from the capillary into the cone. At a certain distance away from the apex of the cone, the jet breaks into an electrospray with charged droplets of diameter comparable to the jet diameter from which they originate. Due to the potential creation of nearly monodisperse charged particles, research into potential uses for electrosprays has been increasing. With this increased use of electrosprays, scaling relationships based on fluid properties and jetting conditions were developed. Despite the development of these relationships, a universal scaling has not yet been established. Many of the scaling relationships vary slightly from one another, and are applicable for only certain ranges of variables. While there are many other scaling laws that have been formulated, these relationships seemed to give reasonable approximations for polar liquids with a dielectric constant $\epsilon \geq 10$, and electrical conductivities, $K \geq 10^{-5}$ S m^{-1}.[5, 20, 22]

$$d = g(\epsilon)\left(\frac{\epsilon\varepsilon_0 Q}{K}\right)^{\frac{1}{3}} \tag{1.8}$$

Where Q is the volumetric flow rate from the capillary through the meniscus emitted through the jet and d is the size of the jet produced. The quantity $g(\epsilon)$ is a function that is determined experimentally, and has been found to take the approximate form[5, 22]

$$g(\epsilon) = -10.9\epsilon^{-\frac{6}{5}} + 4.08\epsilon^{-\frac{1}{3}} \quad (1.17)$$

or

$$g(\epsilon) = 1.66\epsilon^{-\frac{1}{6}} \quad (1.18)$$

Using the given equations, one can approximate droplet size given certain fluid properties and operating conditions.

The minimum flow rate possible to produce a stable jet for a given liquid solution has also been found to scale with certain parameters. This relationship is given below

$$Q_{min} \propto \frac{\tau\gamma}{\rho} = \frac{\epsilon\gamma\varepsilon_0}{\rho K} \quad (1.11)$$

where Q_{min} is the minimum flow rate to produce a stable jet, γ, ρ, ϵ, ε_0, and K are the surface tension, denisty, liquid dielectric constant, permittivity of a vacuum, and electrical conductivity respectively, and τ is the electrical relaxation time.

These equations were developed with electrospraying systems which are different than those which are used experimentally within this dissertation. However, the exact form of these equations is not as important as the general tendencies others have observed. In this manner, these equations provide a basis for determining how the fluid jet will change with alterations to specific fluid parameters. From equation 1.8, it can be seen that liquids of high conductivity will typically produce very thin fluid jets and by equation 1.11 only a small flow rate is necessary to obtain a stable jet. However, instabilities tend to form faster in these highly conductive fluids, so only thin jets at low flow rates are attainable.[8] Conversely, if a liquid of low conductivity is being jetted, only relatively large jets are produced, and they require higher flow rates.[8]

1.2 Electrohydrodynamic Co-Jetting

Electrohydrodynamic (EHD) co-jetting is a process which co-locates multiple compartments within a single fiber by electrospinning or electrospraying multiple miscible liquids in a parallel configuration under laminar flow.[23-25] This process is similar to standard electrospinning; however it utilizes parallel capillaries to produce a fiber with distinct spatial domains along the radial axis of the fiber, which can be used as compartments.[26, 27] Combination of multiple droplets at the end of the parallel capillaries creates a meniscus containing multiple fluidic domains which remain distinct from one another. Upon application of an electric field the fluid domains still do not mix, allowing the production of anisotropic particles and fibers from a single meniscus. Even upon breakup and whipping of the fluid jet, the two polymer phases remain in distinct compartments from one another, and are inseparable once solidified. Previous studies have shown that different components such as polymers, drugs, and surface functionalities can be placed independently into each compartment.[28-30] Other geometries, such as multifunctional microcylinders, can also be synthesized by collecting fibers on a rotating grounded electrode and subsequently cryosectioning the fibers into desired lengths.[31] Such particles and fibers have been demonstrated in applications such as drug delivery,[30, 32] tissue engineering,[26] actuators,[31, 33, 34] and catalysts.[35, 36]

1.3 Scope of this Work

The research undertaken in this dissertation was driven towards the development of new technologies which improve the potential utility of electrohydrodynamic co-jetting, and electrospinning in general. This will be accomplished by first, addressing the low throughput of EHD co-jetting. Second, the electrospinning technologies will be extended to form three

dimensional structures that provide a platform for creating smart 3D structures with anisotropic properties. Finally, these 3D microfiber structures will serve as novel cell culture environments which can be used as diseased tissue models and for tissue regeneration.

1.3.1 Aim 1: Increasing Throughput of EHD Co-Jetting Technology

One of the major drawbacks of the EHD co-jetting technology is its limited throughput. Other electrospinning and electrospraying technologies can utilize needle-less devices and high electric fields to generate large quantities of fibers and particles. The complex fluid interface required by EHD co-jetting is not compatible with these systems. Development of a new device consisting of an extended bicomponent fluid interface will allow for the spontaneous formation of multiple fluid jets, greatly increasing the production rate of both bicompartmental particles and fibers.

1.3.2 Aim 2: Precise 3D Patterning of EHD Co-Jetted Fibers

Electrospinning inherently produces fibers which are randomly deposited on a grounded collection electrode. Methods for patterning fiber deposition exist, however, none are capable of precise placement of aligned fibers into 3D structures. To accomplish this, suppression of the whipping instability in the EHD co-jetting system using a combination of techniques would allow for the 3D spatial patterning of anisotropic fibers.

1.3.3 Aim 3: Develop a 3D Cell Culture Platform

Current 3D cell culture is performed on both scaffold-based and scaffold-free platforms. Scaffold-based platforms tend to have poor cell infiltration and they lack 3D cellular interactions

typically present in physiological tissues. Scaffold-free platforms focus on maintaining 3D cellular interactions, but they cannot be scaled to sufficient size to be useful in many biological applications. Implementation of spatially patterned microfiber scaffolds provides a means to create arrays of tessellated microtissues which can be scaled across large areas. These have the advantages of both the scaffold-based and scaffold-free systems, without many of their drawbacks.

1.3.4 Aim 4: In Vivo Implementation

Tissue engineering technologies are typically developed with very specific goals in mind. Technologies which aim to regenerate or repair a tissue may be very effective at this task, however, they may not be as useful at creating a diseased tissue analog. Introduction of growth factors or poor growth conditions for different cells are a few reasons for these discrepancies. One of the advantages of using the spatially patterned microfiber scaffolds to create microtissue constructs is that it can be easily implemented in a wide variety of applications. Implantation of scaffolds laden with cells into two completely different model systems, tissue regeneration and a diseased tissue model, are all performed in mice to demonstrate the potential utility of such a scaffold based system.

Chapter 2

Needle-less EHD Co-Jetting

The material from this chapter has been adapted with permission from the following source:

> J.H. Jordahl, S. Ramcharan, J.V. Gregory, J. Lahann. "Needle-less electrohydrodynamic co-jetting of bicompartmental particles and fibers" *Macromolecular Rapid Communications*. (2016) In Press.

2.1. Background

Electrospinning and electrospraying have recently become popular means of creating particles and fibers on small length scales, e.g., dimensions ranging from microns to nanometers in size.[37-39] These techniques typically involve the transport of polymer solutions through a metal capillary. Upon application of a critical voltage, the droplet at end of the metal capillary is distorted into a Taylor cone, and a fluid jet is emitted from the cone apex.[38] While the fluid jet traverses towards a grounded electrode it can either break up into droplets, i.e., electrospraying,[8, 40] or is stretched into a fiber, i.e., electrospinning.[41] This technology has been implemented in a variety of applications ranging from chemical sensors,[42, 43] filtration membranes,[18, 44] and tissue

engineering [18, 45-47] using electrospinning, to drug delivery vehicles [40, 48] and microencapsulation.[49]

More recently, the development of electrohydrodynamic (EHD) co-jetting,[23] which imparts multiple chemical functionalities within distinct compartmental domains of both particles and fibers, has shown great promise in creating more complex drug delivery platforms[30, 50, 51] as well as patterned targeting domains.[28, 32] Additionally, multicomponental fibers have shown promise in creating next-generation tissue engineering constructs [26, 27, 33] and stimuli-responsive micro- and nanoactuators.[29, 52, 53] Scaling this technology to gram scale production has been difficult due to the limitation of one fluid jet per co-jetting setup, potentially limiting the commercial viability and widespread adaptation of this technique.

In the case of conventional electrospinning, the limited scalability has been addressed through the development of needle-less jetting processes which can produce fibers at rates orders of magnitude greater than what is possible with a single capillary.[54-58] In principal, needle-less electrospinning is based on the spontaneous ejection of multiple jets from a fluid reservoir in response to the application of sufficiently high electrical potentials. While this approach has been very successful for conventional electrospinning, it is not directly translatable to electrohydrodynamic co-jetting, because the latter requires controlled co-flow of two fluids prior to jet formation. Herein, we describe a needle-less electrospinning and electrospraying technology which allows for the fabrication of bicompartmental fibers and particles.

2.2 Materials and Methods

2.2.1 Materials

Poly(D,L-lactic-co-glycolic acid) (PLGA, MW 50-75 kg mol-1), poly(vinyl acetate) (PVAc, MW 113 kg/mol), poly[(m-phenylenevinylene)-alt-(2,5-dihexyloxy-p-phenylenevinylene)] (PMPDHPV), tetrahydrofuran (THF), chloroform, and N,N-dimethylformamide (DMF) were purchased from Sigma Aldrich. Methoxy-polyethylene glycol (PEG)-rhodamine (MW 5 kg/mol) used as a fluorescent red dye was purchased from Creative PEG Works.

2.2.2 Needle-less Co-Jetting Device Fabrication

The microchannel EHD co-jetting device was fabricated from 316 stainless steel to be 76.4 x 25.5 mm in overall size (length x width). A 0.35 mm microchannel was created on each side of a 0.7 mm thick plate by placing a raised edge on both sides of the device. The top of the device contained a 2 mm tall and 3.25 mm wide ridge, designed for glass slides to mount flush to the device. Fluid inlets were placed on both sides of the metal plate and were centered lengthwise on the ridge of the device. The plate edge at the outlet of the microchannels was sharpened to a point, and grooves were placed approximately every 1 mm along the edge to aid in fluid flow. Glass slides were cut to size and were mounted onto the device.

2.2.3 Particle and Fiber Fabrication

Bicompartmental particles were fabricated using two 6.5 wt% solutions of PLGA dissolved in a 97:3 ratio of chloroform:DMF. One of the solutions contained 30 µg/ml of PMPDHPV, while the second solution contained 30 µg/ml of mPEG-Rhodamine. Each solution

was each pumped at flow rates ranging from 1.0 to 13.2 ml/hr (for a total flow rate of 2.0 to 26.4 ml/hr) into the microchannel device, and a 60 kV electric potential was applied once solution was seen coming out of the microchannels. Flow rates reported represent flow of each individual component. The total flow rate through the device is twice what is reported unless otherwise specified.

Bicompartmental fibers were fabricated using two 35 wt% solutions of PLGA dissolved in a 1:1 ratio of chloroform:DMF containing similar dye concentrations as the particles. Each solution was pumped into the microchannels at a flow rate of 13.2 ml hr^{-1} at an applied electric potential of 75 kV. Bicomponent fibers were created by flowing PLGA and PVAc polymer solutions on either side of the microchannel EHD co-jetting device. A 35 wt% PLGA solution in a 1:1 THF to DMF solvent system was co-spun with a 35 wt% PVAc solution in a 6:4 chloroform to DMF solvent system. Total flow rates of 2 to 26.4 ml/hr were utilized at a tip to ground distance of 40 cm and an applied electric potential of 75 kV.

Scanning electron microscopy of the particles was performed using an FEI Helios SEM/FIB, while fibers were imaged using an AMRAY 1910 Field Emission Scanning Electron Microscope (FEG-SEM). Fiber diameter histograms were determined in ImageJ using the DiameterJ plugin, a process validated in previous literature.[59] In this process, grayscale images were segmented using an automated thresholding technique. Threshold setting M7 was used for all subsequent analysis. Fluorescence imaging was conducted with a Nikon A-1 inverted confocal laser scanning microscope (CLSM) using a 60x oil immersion objective with violet corrected lens, and were processed on Imaris (Version 7.5) software. Particle size distributions were determined by measuring all the particles across 140 x 240 μm quadrants in nine separate fields of view. Particle anisotropy was determined by counting all the particles containing either

one or two compartments within nine 3D fields of view within a confocal z-stack. Particles viewed from this perspective could be easily distinguished from one another. Relative compartmental ratios were computed by generating surfaces which encapsulated the volume of each compartment in Imaris. The volume of each surface on the particle was measured, providing a relative volume ratio for each component.

2.3 Results and Discussion

2.3.1 Device Design

Currently, electrohydrodynamic (EHD) co-jetting requires the use of two capillaries in parallel to create fibers or particles with two or more compartments (Figure 2.1).[23] To scale this technology, complex experimental setups involving multiple dual capillary orifices are required. Here, an alternative strategy is explored that relies on the ejection of multiple jets from the edge of an appropriately designed metal plate. Two fluids flow on opposite sides of the plate and combine at the edge to form a stable fluid interface. It was hypothesized that this elongated fluid interface would act similarly to the droplet interface which is formed by the dual capillaries typically used in EHD co-jetting; and that upon application of high voltage spontaneous formation of multiple fluid jets along the extended fluid interface will be feasible.

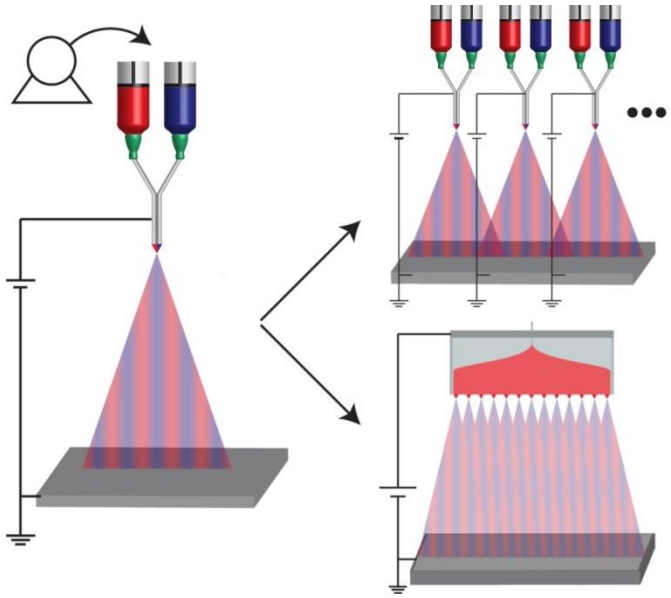

Figure 2.1. Needle-less co-jetting compared to standard co-jetting techniques. A standard EHD co-jetting experimental setup includes a single syringe pump which dispenses two fluids simultaneously through two parallel capillaries. A high voltage is applied to the dual-capillaries, resulting in either electrospinning or electrospraying of bicompartmental fibers or particles respectively. Scaling up this process would require many capillaries in parallel, which is fundamentally impractical. A needle-less co-jetting technique would allow for an increased cone density with high flow rates using a relatively simple design.

Schematic representations of the top (inlet) and bottom (outlet) of the device show the location of the two microchannels relative to one another, as well as the location of the fluid inlet ports (Figure 2.2 A). Pumping the fluids into the fluid inlet ports of the assembled device allows

for the polymer solutions to move on opposite sides of the metal plane. Once the device is filled, a fluid interface is formed at the lower edge. Upon formation of the fluid interface, a high electric potential is applied to the device, forming multiple Taylor cones along the device outlet (Figure 2.2 B). The fluid jets formed from the device are then accelerated towards a grounded electrode, where the final particles or fibers are collected and subsequently analyzed (Figure 2.2 C).

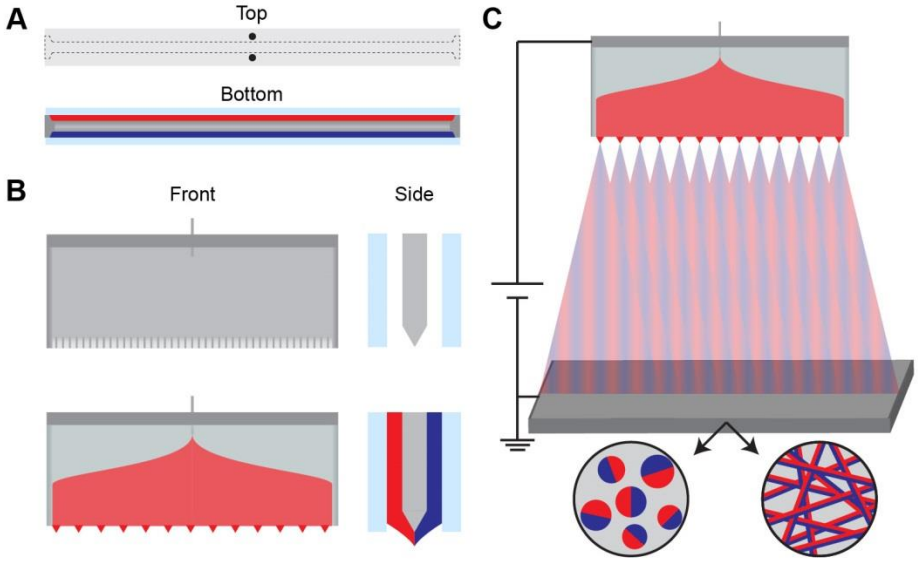

Figure 2.2. Experimental setup and fabrication of the needle-less EHD co-jetting device. A) A top and bottom view of the device showing glass slides spaced away from a center plate via raised edges on either side. Two holes in the top of the device allow for two different fluids to flow into either side of the center plate. The top ridge is wide enough to encompass the glass slides. **B)** The device itself consists of a center plate which is sharpened to a point and has grooves carved into the edge to aid in fluid flow. The device is assembled by placing glass slides on both sides of the center plate which are held in place by small binder clips. Fluid is pumped into the device from the top entry holes. Once the device is filled, a high electric potential is applied. **C)** Upon application of a high electric potential to the device, multiple Taylor cones are formed, resulting in the deposition of particles or fibers with multiple compartmental domains.

2.3.2 Bicompartmental Particle Fabrication

For microparticle fabrication, the needle-less co-jetting device was infused with two 6.5 wt% PLGA solutions containing different dyes. Each PLGA solution was infused at flow rates ranging from 2.0 ml/hr to 26.4 ml/hr to determine the optimum flow rate for bicompartmental particle preparation. For each flow rate, an electric potential of 60 kV was applied to the device. The distance between tip and grounded collector was held constant at 40 cm. It was observed that as the flow rate increased, an increasing number of Taylor cones were required to maintain a steady state of particle production. The number of Taylor cones increased from three at a 2.0 ml/hr flow rate, to seven at a flow rate of 26.4 ml/hr along the 7 cm outlet.

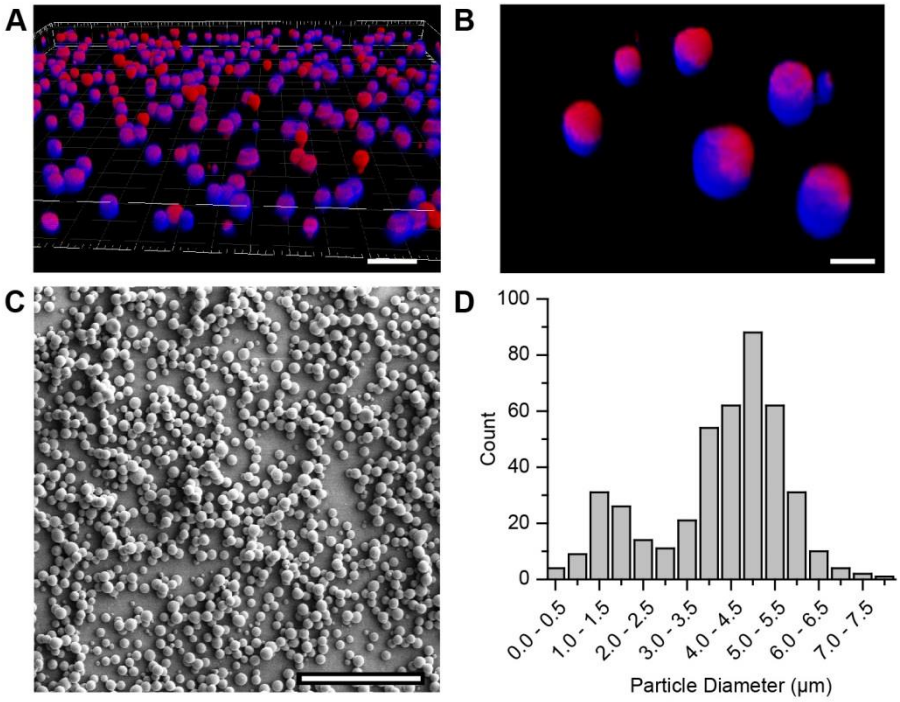

Figure 2.3. Bicompartmental particles fabricated via needle-less EHD co-jetting device. Bicompartmental particles composed of PLGA loaded with different fluorescent dyes fabricated via needle-less EHD co-jetting device. **A)** Confocal laser scanning microscopy was used to verify the bicompartmental nature of the particles. **B)** A zoomed in image of these particles highlights the bicompartmental nature of these particles. **C)** Scanning electron micrograph of particles fabricated using this device show particle morphology is consistent with previous EHD co-jetting capabilities. **D)** The particle size distribution as calculated from nine different fields of view via confocal microscopy validates these observations. Scale bars indicate 20 um (A), 5 um (B), 50 um (C).

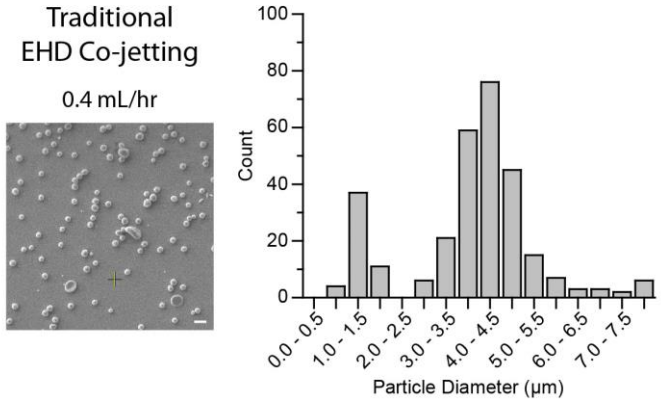

Figure 2.4. Microparticles fabricated using traditional EHD co-jetting technique. Parallel capillaries were utilized to obtain bicompartmental particles. A stable cone-jet is obtained at 0.4 mL/hr, and produces particles of a similar morphology and particle size distribution as particles fabricated using the needle-less high-throughput co-jetting device (Figure 2.3). Scale bar indicates 10 µm.

Visualization of the bicompartmental particles was performed using confocal laser scanning microscopy (CLSM). Z-stack imaging was utilized to reconstruct the 3D structure of the resultant particles (Figure 2.3 A-B). Analysis of the particles in the z-stack images revealed that at a flow rate of 2.0 ml/hr, 96.5% of the particles featured two clearly distinguishable compartments. Within these particles, it was determined that the relative ratio of each compartment was 50.8% ± 4.5% (n=150). This compares well with the yields described for needle-based co-jetting.[60, 61] Moreover, statistical analysis of the images obtained by confocal microscopy yielded particle size distributions for the particles prepared with a flow rate of 2.0 ml/hr (Figure 2.3 C). For comparison, electrohydrodynamic co-jetting of the same polymer solution using needles requires a total flow rate of 0.4 ml/hr (0.2 ml/hr for each component) to obtain a stable cone-jet. Under otherwise unaltered conditions, the resultant particles had size distributions and particle morphologies that matched the ones observed for needle-less jetting seen in Figure 2.3 C (see Figure 2.4 for comparison).

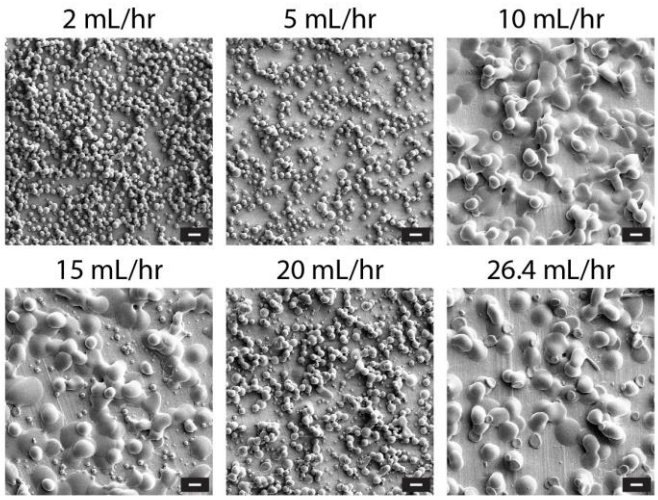

Figure 2.5. The effect of flow rate on resultant particle morphology. At flow rates of 2 to 5 mL/hr, particles with a spherical morphology were produced. At flow rates between 10 and 20 mL/hr a mixture of spherical particles and flattened disc morphologies were observed. The 26.4 mL/hr flow rate contained both discs and red blood cell shaped particles. Scale bars indicate 10 µm.

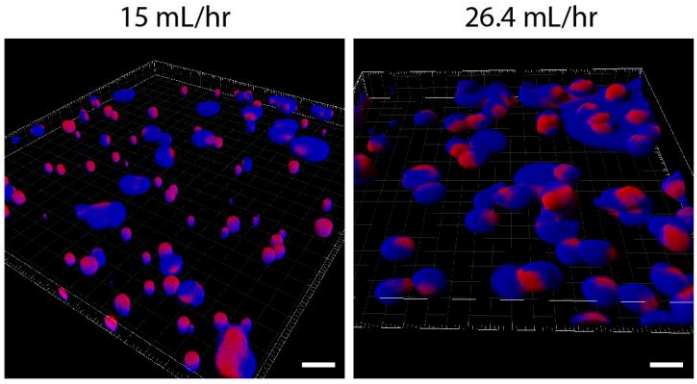

Figure 2.6. Bicompartmental particle architecture is maintained at higher flow rates despite different particle morphologies. At 15 mL/hr a combination of bicompartmental particles and discs were fabricated. Similarly, bicompartmental discs were observed at 26.4 mL/hr flow rates. Scale bars indicate 20 µm.

Not surprisingly, the flow rate had an important influence on particle morphologies: Bicompartmental particles prepared by needle-less co-jetting ranged from close-to-perfect spherical particles at lower flow rates to flattened discs at higher flow rates (Figure 2.5). A distribution of discs and particles were observed at flow rates as high as 20 ml/hr, and discs and red-blood cell shaped particles were predominantly observed for flow rates above 26.4 ml/hr. We note that disc-shaped particles are generally seen at higher flow rates during particle production at low polymer concentrations.[60, 62] The formation of discs can typically be avoided when the tip to grounded collector distance is increased. At even higher flow rates, the increased solvent concentration in the atmosphere around the depositing particles leads

to a slower evaporation rate which hinders the solidification of the particle, causing it to flatten into a disc shape.[62] These disc shaped particles prepared by needle-less co-jetting were found to still retain a bicompartmental character (Figure 2.6).

2.3.3 Bicompartmental Fiber Fabrication

Infusion of the microchannel device with two 35 wt% PLGA solutions, each loaded with a different colored fluorescent dye, resulted in the formation of micron to sub-micron sized fibers upon application of a 75 kV electric potential. Again, flow rates from 2.0 ml/hr to 26.4 ml/hr were examined to determine maximum production rate of bicompartmental fiber mats, and how flow rate affects the overall fiber morphology. For all fiber jetting experiments, the tip to grounded collector distance was maintained at 40 cm with a constant applied electric potential. Similar increases in Taylor cone numbers with increasing flow rates were observed during fiber electrospinning. However, these cones were more dynamic in nature, and the numbers varied with time. At flow rates of 2.0 ml/hr, one to three Taylor cones formed along the outlet of the device, and increasing the flow rate to 26.4 ml/hr produced four to eight Taylor cones.

For all flow rates examined, bicompartmental fibers were obtained. Even at the highest flow rate, the reconstruction of CLSM z-stacks confirmed that the fibers maintained a bicompartmental architecture (Figure 2.7 A, B). CLSM imaging of the cross-sectional view of the fibers further confirms the presence of two distinct compartments (Figure 2.7 B). SEM micrographs reveal fibers with a contiguous, bead-free morphology across all flow rates examined (Figure 2.7 C). Under the conditions used for needle-less co-jetting, fibers had an average diameter of 0.95 μm (Figure 2.7 E). Fibers formed at 2 ml /hr had a similar morphology

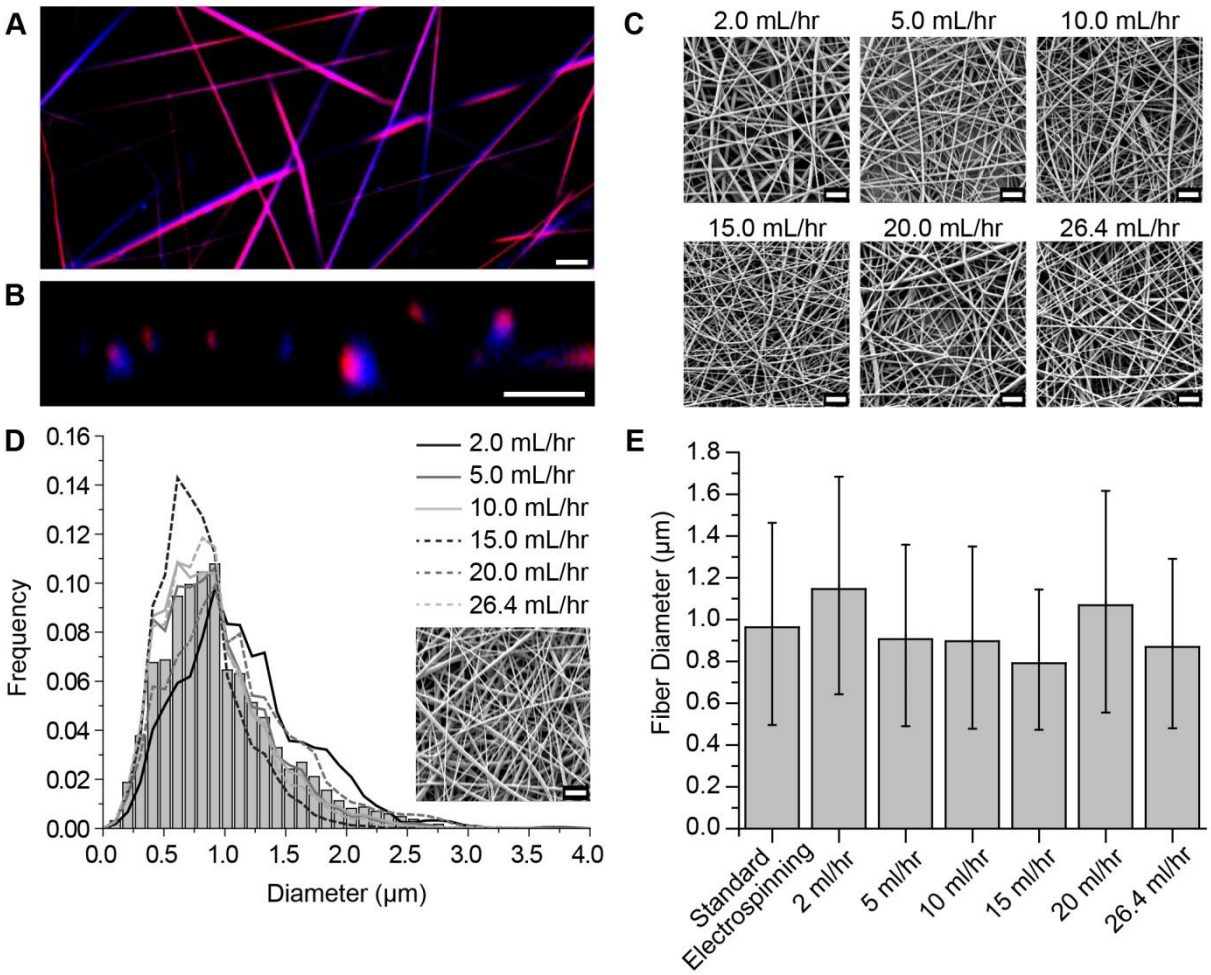

Figure 2.7. Bicompartmental fibers fabricated via needle-less EHD co-jetting device. Bicompartmental fibers composed of PLGA loaded with different dyes fabricated via needle-less EHD co-jetting device. **A)** Confocal laser scanning microscopy verifies the bicompartmental fiber architecture is maintained after being processed by the microchannel EHD co-jetting device, even at flow rates of 26.4 ml/hr. **B)** A representative cross sectional view of the fibers shown in (A) highlights the two compartments present within the fibers. **C)** Scanning electron microscopy of fibers produced from 2 to 26.4 ml/hr show a bead free morphology which is similar at each respective flow rate. **D)** A histogram of fiber diameters from fibers spun in a standard side-by-side capillary (SEM shown in inset) is compared to the fiber size distributions of the fibers produced using the microchannel EHD co-jetting device at different flow rates, as indicated by the respective lines. **E)** Average fiber diameter is shown for each of the samples, showing the fiber size is consistent for each condition. Error bars indicate standard deviations. Scale bars indicate 10 um (A-D).

and fiber size distribution as all other fibers, including the highest flow rates examined of 26.4 ml/hr. Comparison to fibers fabricated using standard needle-based co-jetting using identical PLGA solutions shows a similar fiber size distribution and morphology, demonstrating the stability of this method in fiber production (Figure 2.7 D). This was accomplished despite

increasing the overall fiber production rate by over a factor of 30, from a total flow rate of 0.8 ml hr-1 in the case of needle-based electrospinning to over 26.4 ml/hr using a needle-less device.

Similar results were found when electrospinning two dissimilar materials. Co-jetting the PLGA solution with poly(vinyl acetate) (PVAc) using the needle-less device produced fibers with a bicompartmental architecture, with 95.5 ± 3.4% of the fibers containing two compartments when electrospun at the highest flow rate of 26.4 ml/hr (Figure 2.8 A, B). The fibers had a consistent bead-free morphology, and a similar fiber size distribution relative to each other and to standard needle-based electrospinning techniques (Figure 2.8 C-E) indicating the system is self-regulating, adding more or less Taylor cones as the flow rate is modulated.

These results demonstrate that fiber production rates of over 9 g/hr (over a 30 fold increase in production rate), well over an order of magnitude higher than typical bicompartmental fiber electrospinning (approximately 0.2 g/hr), can be achieved using this novel needle-less co-jetting technology. This scaling is true for both fibers loaded with two differing dissolved factors as well as two distinctly different materials. Further increases in fiber production rate may be feasible, if higher flow rates can be achieved. Increasing the length of the extended edge used to stabilize the fluid interface would also provide a means of further increasing the rate of production of fibers.

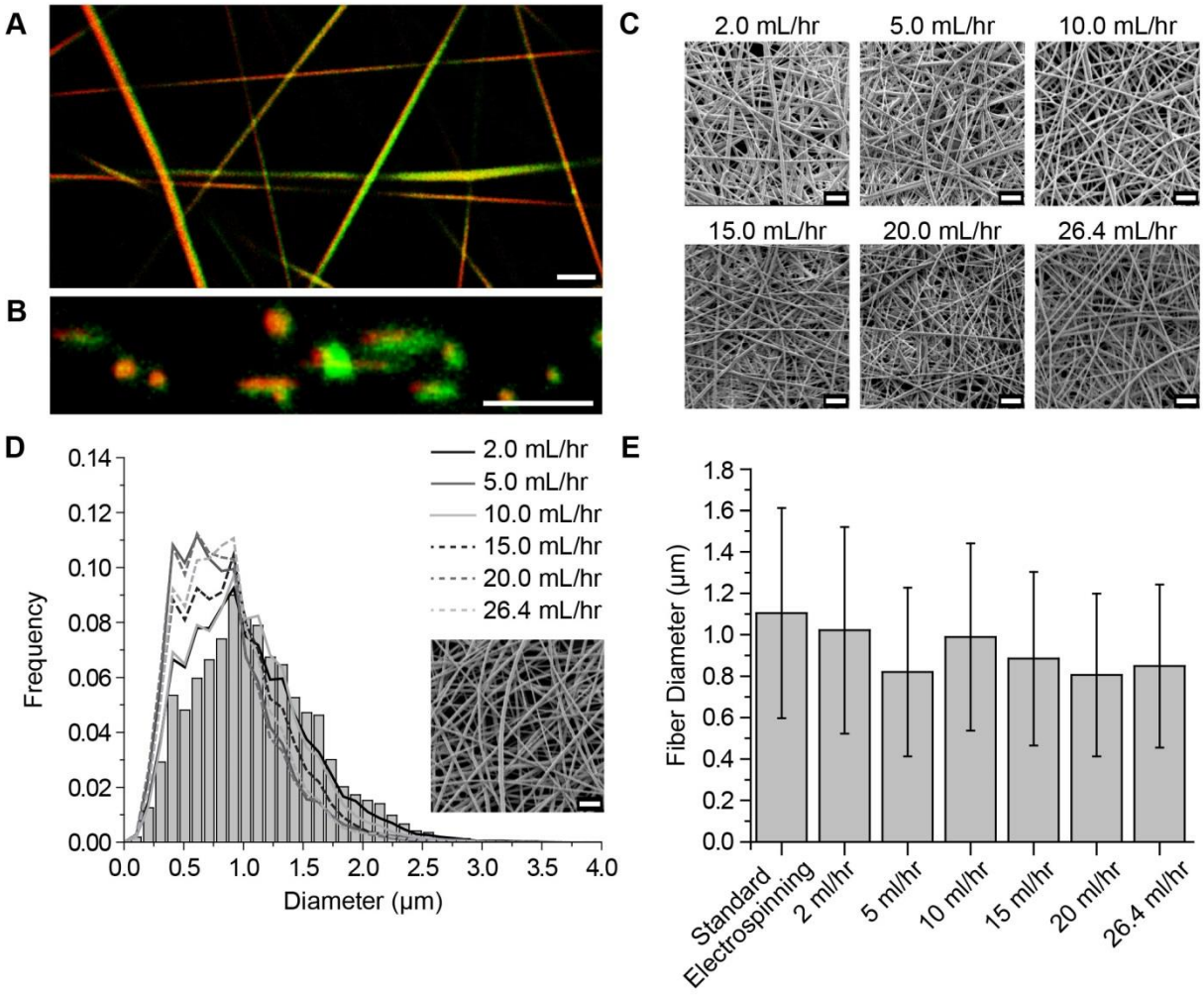

Figure 2.8. Bicomponent fibers fabricated via needle-less EHD co-jetting device. Bicomponent fibers with one compartment containing PLGA (red) and the second containing PVAc (green) were loaded with different dyes and fabricated via needle-less EHD co-jetting device. **A)** Confocal laser scanning microscopy verifies the bicompartmental fiber architecture is maintained after being processed by the microchannel EHD co-jetting device, even at flow rates of 26.4 ml/hr. **B)** A representative cross sectional view of the fibers shown in (A) highlights the two compartments present within the fibers. **C)** Scanning electron microscopy of fibers produced from 2 to 26.4 ml/hr show a bead free morphology which is similar at each respective flow rate. **D)** A histogram of fiber diameters from fibers spun in a standard side-by-side capillary (SEM shown in inset) is compared to the fiber size distributions of the fibers produced using the microchannel EHD co-jetting device at different flow rates, as indicated by the respective lines. **E)** Average fiber diameter is shown for each of the samples, showing the fiber size is consistent for each condition. Error bars indicate standard deviations. Scale bars indicate 10 μm (A-D).

2.4 Conclusions

Fabrication of bicompartmental particles and fibers, as well as bicomponent fibers containing distinctly different bulk polymer compositions, was accomplished using a newly developed needle-less EHD co-jetting technique. The device was designed to accommodate two independent fluid flows, which would combine to form a uniform fluid interface at the outlet of a microchannel. Application of a high electric field led to spontaneous formation of several distinct Taylor cones along the fluid interface, resulting in the deposition of bicompartmental fibers and particles. Production rates of fibers were calculated to be on the order of 9 g/hr, which is over 30 times higher than standard electrospinning approaches. Spherical particles also had increased production rates, around 5 times higher than needle-based EHD co-jetting. Other bicompartmental particle geometries are also accessible, including discs, which could be fabricated at a rate of nearly 2 g/hr. Scaling this technology using larger fluid interfaces and higher flow rates will be examined in future work. This technique provides a potential means for scaling up EHD co-jetted particles and fibers for commercial applications.

Chapter 3

3D Jet Writing

Some material from this chapter has been adapted with permission from the following manuscript in preparation:

> J.H. Jordahl, L. Solorio, H. Sun, S. Ramcharan, C.B. Teeple, H.R. Haley, K.J. Lee, T.W. Eyster, G.D. Luker, P.H. Krebsbach, J. Lahann. "3D Jet Writing: A novel route towards functional microtissues within tessellated 3D architectures" *In Preparation*.

3.1 Background

3.1.1 Introduction

As discussed in the previous chapter, the electrohydrodynamic (EHD) co-jetting technique unlocks a unique set of capabilities not available to other fiber or particle fabrication techniques.[23-25, 28-30, 32, 33, 63, 64] Despite the ability of this system to create fibers and particles with distinct functional domains, which can have varied bulk or surface characteristics, the technique has not yet been utilized to spatially pattern fibers in three-dimensional space. Controlling both the coordinate placement and alignment of the fibers would allow for unprecedented control in the functional anisotropy of 3D fiber scaffolds. These types of scaffolds would have use in a

variety of settings ranging from tissue engineering, to chemical sensors and optical waveguides. However, to achieve this goal a method of patterning the electrospun fibers first needs to be achieved.

3.1.2 Patterning Electrospun Fibers

The most prevalent methods for controlling the deposition of electrospun fibers involve electric field modification. Electric field modification is a powerful tool in controlling a depositing electrospun fiber since an electrospinning fluid jet generally travels along electric field streamlines[65] and the initiation and acceleration of such a jet is dependent on high electric fields.[66] Throughout the years of research, a variety of strategies have emerged as means of achieving some degree of fiber patterning capabilities, each implementing a different means of electric field modification.

Methods such as ring electrodes[67-70] (also known as electrostatic lenses) have been employed to generate non-woven mats of fibers that are randomly deposited in confined or discrete areas of the collection electrode. These methods modify the electric field by applying an electric potential to a conducting ring electrode located in or near the path of the electrospinning fiber to control fiber deposition. The downfall of these methods is that the fiber deposition is still random, and it is difficult to achieve predictable patterned structures without further modification. Utilizing a series of secondary ring electrodes to alter the electric field along the jet path results in an electric field that acts to maintain the center alignment of the jet at each concentric ring interval.[69] Use of secondary ring electrodes to modify the electric field was seen to minimize, or even eliminate, the whipping instability while the jet was inside the rings, an effect which was directly correlated to the electric potential applied to the ring electrode.[69] These

results indicated that utilization of a secondary ring electrode could prove to be useful in creating a precise fiber writing system, as they were shown to be effective in reducing the area of the randomly deposited fiber mats.[67, 70] However, these electrostatic ring electrodes they have not yet been used to control the placement of individual fibers. Instead, implementation of secondary ring electrodes simply result in disordered mats. Adding a third electrode of opposite polarity beneath an insulating collection plate created a system capable of writing detailed structures composed of non-woven mats.[68] However, this method only allowed for fabrication of crude topological control of the fiber spacing and mat thicknesses.

A second widely used method of controlling fiber alignment is collecting fibers on a rapidly rotating collection drum,[71-76] or any number of derivatives of this method including the edge of rotating discs.[77-79] The rotating motion of the drum aligns the depositing jet once the linear velocity matches the speed as the whipping fiber [18] (up to speeds of over ~4 m/s [76, 80]). This mechanically orients an otherwise randomly deposited mat. Implementation of a tapered edge, which is utilized in rotating disc technologies,[79] provides an altered electric field which is focused at the tip, further enhancing the fiber alignment. As in previous methods, the fibers are randomly deposited, but in a controlled orientation.[18] However, limitations of this method are the frequent fiber breakage at the high collection speeds [18] and the difficulty in achieving more complicated patterns, such as patterns in multiple directions or specific micropatterns.

Combining the use of auxiliary electrodes with rotating drums has also been implemented to achieve focused deposition of aligned polymer fibers.[81-83] Auxiliary electrodes in the form of a counter electrode of opposite polarity situated beneath a high speed rotating drum collector has also been shown to minimize the bending instability of the jet, resulting in highly aligned arrays of fibers.[72, 82] While these methods yield aligned arrays of nanoscale fibers, the lack of precision

placement limits their usefulness in creating complex three-dimensional constructs beyond pseudo-woven mats.

Patterning has also been obtained by using a conducting ground electrode with a patterned surface.[84-91] In these examples, electrospinning on collection electrodes which have patterned conductive elements leads to a certain degree of control over the fiber alignment and placement across an area. One of the most prominent examples of this type of collector is the collection of fibers across parallel plates,[87, 91] which technique results in an array of aligned fibers across an insulating void separating the grounded collection electrodes. Other examples result in more complex 3D fiber architectures which utilize more complex grounded collection electrodes. Utilizing a wire mesh collection electrode, for example, resulted in a patterned mat of fibers that oriented along the axis of the metal wires within the mesh, with some fibers spanning the gap between the wire mesh similar to the fibers seen with parallel plate collectors.[85] While these methods differ significantly from the secondary electrodes mentioned earlier, the mechanism driving the fiber alignment and placement is the same, altering the electric field along the depositing fiber path. These patterned collectors were able to achieve not only alignment of the fibers, but some control over the placement of the fibers across the three-dimensional object though the passive alteration of the electric field (i.e. no other electric potential source was introduced). However, the deposition of the fiber remained out of the control of the user, and the deposition of the fibers remained non-uniform as the fibers tended to prefer to be deposit on raised regions and did not deposit as densely in the non-conductive gaps in the mesh. While this provides a means of producing patterns of electrospun fibers, the mechanism behind the deposition still relies on the random motion of a whipping jet.

Other methods of patterning are the direct writing approaches. These incorporate different strategies to eliminate the whipping instability entirely, as opposed to dampening its effect through electric field modification or application of mechanical force. One such method, termed near-field electrospinning, implements a standard electrospinning setup with needle to collector distances on the order of hundreds of microns to a millimeter.[92-95] Removal of the whipping instability from an EHD jet in these cases is accomplished by decreasing the distance between the capillary and the grounded collection electrode to the point where there is not enough distance for a bending instability to develop. Incorporation of a moving platform beneath the stable jet allows for writing patterns of arbitrary complexity with nanoscale fibers. Due to the short working distance of 500 μm to 1 mm between the capillary and the collection electrode, specialized equipment and cameras are necessary to maintain the needle to collector distance. At such close proximity, small perturbations in electric field due to fluctuations in applied voltage or working distance affect the size distribution of the deposited fiber.[93] Despite these capabilities, this method can only produce fibers with nanometer diameters,[93] due to limited solvent evaporation which can take place at such small distances, and therefore has not been capable of forming three dimensional constructs.[92, 93] However, 3D structures have been reported in rare instances if the polymer concentration is increased to the point where micron scale fibers do not deform after being extruded from the needle.[96] These considerations significantly reduce the scale and potential applications of near-field electrospun structures or scaffolds.

Melt electrospinning is a second direct-writing technology which was recently developed to pattern electrified fluid jets.[97] Melt electrospinning is very similar to typical electrospinning, except it uses polymer melts as opposed to polymer solutions when creating fibers. It was found that PCL is a unique polymer that has the necessary viscosity, surface charge, and melting point

(among other characteristics) that make it feasible to create a polymer jet very stable at distances of about 3 cm, giving the fiber enough distance to solidify before being deposited.[97] With this, direct writing of large, complex, three-dimensional structures is possible however, it has only been demonstrated with a single polymer.[97] While the concept of a solvent free microfiber fabrication is alluring, it has an inherent downfall in that the fiber properties cannot be finely tuned. In melt electrospinning, the polymer must contain the proper viscosity and ability to carry charge for a stable jet to form. Typically, in solution electrospinning, the solvents which dissolve the polymers are used to tune the properties necessary to achieve a stable jet. To accomplish the same thing with homopolymer melts would require custom synthesis of the molecules until the desired melting point, viscosity, conductivity, etc. are achieved. Additionally, the high processing temperatures required, typically in the range of 80 – 300°C,[98] are incompatible with most biodegradable polymers [99-101] and virtually all biologics, such as proteins or small molecule drugs.[102] This could be an issue when trying to create a structure with uniform fiber diameters, a property which is directly related to molecular weight. These issues coupled with the specialized heating chambers necessary and the relatively few polymers which have been successfully melt electrospun[39] greatly limits the number of potential uses for this process.

Solution electrospinning opens up the possibility of using a wider variety of polymers, including biopolymers, incorporation of fragile small molecules and proteins, and creation of fibers with multiple distinct compartments, all of which is not possible with melt electrospinning methods.

3.1.3 Potential Applications of Patterned Electrospun Fibers

One of the most common applications of patterned polymer fibers fabricated via electrospinning is in the field of tissue engineering. Here, electrospun fibers have been used to create scaffolds simply due to the resulting fibers' resemblance to extracellular matrix (ECM), the biological support for cell growth. Techniques which alter the fiber surface modification, alignment, and mechanical strength were later developed to tailor the microenvironment created by these polymer fibers to more closely mimic the native ECM. Due to the flexibility of the electrospinning technique, it is also possible to implement biological polymers (e.g. alginate and chitosan) and ECM molecules (e.g. collagen) in the creation of electrospun scaffolds for tissue engineering. Patterning of these types of fibers have been demonstrated to be critically important to help mimic specific ECM fibers of certain tissue types, such as tendon, which are well aligned; while other types of tissues are more mesh like, such as skin. Alignment of fibers has also been shown to increase the structural strength of electrospun scaffolds.[103] However, since the fibers examined were only aligned in one direction the strength in the other direction was compromised. Therefore, alignment in two or more directions may improve mechanical properties even further.

Solution electrospinning not only opens the possibility of using biological polymers, but it also allows for incorporation of surface functionality and signaling molecules to be incorporated into the resulting fiber. Previous work has demonstrated the ability to spatially control cell adhesion to certain compartments of a Janus fiber created by electrohydrodynamic (EHD) co-jetting. Extending this technology into three-dimensional space could allow for the creation of unique patterns of co-cultured cells or directed differentiation of stem cells, bringing the field closer to the creation of functional tissue which is one of the great challenges in this field.

Other possible applications of patterned electrospun fibers is in the field of 4D printing, a 3D printed object which can react to a stimulus or change with time.[104] Materials which undergo distinct transitions from an environmental stimulus are quite prevalent in nature,[29, 105-107] and allow for such phenomena as movement in plants.[107] Many of these plant movements are caused by variations in moisture found within the cell walls of the plant, which cause bending due to non-uniform swelling.[105-107] Implementation of simple swelling and shrinking of compartments in plants has led to a vast array of complex motions and processes ranging from the opening of a pine cone[105, 107] to the catapulting mechanism used for fern spore dispersion.[106, 107]

This type of concept was recently utilized to make actuating microcylinders using EHD co-jetting.[29] These particles were created by creating anisotropic fibers, and subsequently cryo-sectioning them into cylinders. Cylinders which exhibited anisotropic swelling were used to create actuators. Creation of a hydrogel/PLGA bicompartmental fiber led to a cylinder which would toggle from straight to bent upon exposure to water.[29] A three way toggle was created when the two compartments were organogel/hydrogel, where the curvature could be changed from one direction, straightened, to the other direction by transferring it from organic solvent, dry, to a water solution.[29] The next step for this technology is to extend it into three dimensions to even more closely mimic the mechanical motions seen in nature.

Smart actuating materials such as PNIPam[108] and azobenzene[109] can be easily manipulated through temperature transitions and polarized light respectively. Incorporation of these smart materials into a co-jetted fiber could lead to even greater applications for the shape changing cylinders previously discussed. Intelligent fabrication of hydrogel bilayers have also been utilized to create origami particles that are able to transform from a simple 2D shape to a 3D encapsulating particle.[110] More complex shapes could potentially be fabricated through

patterning of co-jetted fibers with areas of low crosslinking density to act as creases to facilitate easy and controlled folding. Creation of such materials through electrospinning would drastically reduce the size scale of other 4D printed objects in the current literature.[104]

Patterning electrospun fibers could also have applications in other technologies such as pressure sensors,[111] mechanical energy scavenging devices,[112] fabrication of 3D microfluidic channels,[113] and optical waveguides.[114] Assembling electrospun core-shell fibers with a core composition of a carbon nanotube suspension with an elastomeric shell into a grid pattern could be used to create flexible pressure sensing devices similar to those fabricated by Lipomi et al.[111] Mechanical energy scavenging and pressure sensing technologies have also been created by patterning piezoelectric polymers, such as poly(vinylidene fluoride) (PVDF), using near-field electrospinning.[112] Electrospinning is a simple, scalable technique which inherently stretches and orients the dipoles of PDVF, which imparts piezoelectric properties to the polymer. Single PDVF fibers have demonstrated electrical signal in response to mechanical strain, and multiple aligned fibers deposited using near-field electrospinning have been shown to further increase the observed electrical signals.[112] Creation of pseudo-woven fiber structures created using EHD co-jetting could be used to incorporate these energy harvesting devices and/or other sensors such as pressure sensors and chemical sensors into fabrics or other soft flexible materials. While this is feasible using near-field technologies, larger scale production is not directly amenable using this technique.

Herein, we now report a highly scalable and versatile microfabrication technology, 3D jet writing, that produces regular tessellated geometric structures with microscale resolution from electrohydrodynamically driven polymer solutions under standard electrospinning conditions. Extraordinary jet stability is achieved through implementation of a secondary electrode in the

electrospinning setup that, in conjunction with a 2D motion platform, allows for controlled focusing and stacking of continuously deposited microfibers. This results in ordered honeycomb structures that address many, if not all, of the shortcomings of current fiber spinning approaches.

3.2 Materials and Methods

3.2.1 Materials

The following materials were purchased from Sigma-Aldrich: Poly(D,L-lactic-co-glycolic acid) (MW 50-75 kg/mol) for scaffold fabrication, poly[(m-phenylenevinylene)-alt-(2,5-dihexyloxy-p-phenylenevinylene)] (PMPDHPV) a fluorescent blue dye, poly[tris-2,5-bis(hexyloxy)-1,4-phenylenevinylene)-alt-(1,3-phenylenevinylene)] (PTDPV) a fluorescent green dye, and the co-jetting solvents chloroform, and N,N-dimethylformamide. Methoxy-polyethylene glycol (PEG)-rhodamine (MW 5 kg/mol) used as a fluorescent red dye was purchased from Creative PEG Works. Azide-PEG-FITC was purchased from Nanocs. Poly(lactic acid) with alkyne functionality was synthesized following previously published procedures.[28]

3.2.2 3D Jet Writing

Jetting solution for creating microfibers consisted of 30 w/v% PLGA dissolved in 93:7 v/v% chloroform:N,N-dimethylformamide. Each compartment contained a different fluorescent probe at a concentration <0.01 w/v%. Jetting solutions were loaded into syringes and pumped through side-by-side capillaries via a syringe pump (Fischer Scientific). A copper secondary electrode (5 cm in diameter, 2.5 cm in height, and 1.5 mm thick) was secured beneath the capillaries. Capillaries were placed nominally 5 cm above the collector, with the ring electrode positioned 0.5 cm below the capillary tip. A positive potential was applied using DC power supplies (Gamma High-Voltage Research ES30P-20W). A nominal potential of 16 kV and 9kV was applied to both the capillaries and the secondary ring electrode, respectively. Fibers were deposited onto a grounded electrode consisting of a stainless steel plate, aluminum foil, or silicon wafer. Two linear motion stages were implemented, one stage for x and y motion respectively

(ILS-300LM, Newport Corporation). A 4 axis universal controller (XPS-Q4, Newport Corporation) coupled with LabView software synchronized the stage movements.

3.2.3 Scaffold Characterization

Fluorescent images were taken on a Nikon A-1 inverted confocal laser scanning microscope (CLSM), and were processed on Imaris (Version 7.5) software. Scanning electron micrographs were obtained from an AMRAY 1910 Field Emission Scanning Electron Microscope (FEG-SEM). Photographs of resulting structures were taken with a Canon EOS 20D Digital Single-Lens Reflex (DSLR) camera.

Values for parallelism, perpendicularity, and geometric consistency were determined by using ImageJ software. Parallelism was determined by manually measuring the angle at which the fiber stacks were deposited. The average root mean square error (RMSE) of the measured angle to the average was reported as the 'parallelism' of the fibers. Perpendicularity was determined by a similar method in ImageJ. Angles of the fibers at each intersection were measured. The RMSE of difference between the angles and 90° was reported as the 'perpendicularity'. Geometric consistency was the third value determined using ImageJ analysis. The distance between parallel rows and columns of fiber stacks was measured across three entire scaffolds to determine the consistency between the fiber stack spacing. The RMSE was calculated from the difference between the measured fiber stack spacing and the average spacing across all the fiber stacks. The average RMSE was divided by the average fiber stack spacing to yield the percentage reported as the geometric consistency. All measurements were taken across three entire scaffolds consisting of 500 μm square pores.

3.2.4 Fiber Straightness Analysis

A series of linear stage movements in the x-direction were performed to create a horizontal array of electrospun fibers. The speed increased by 3 mm/s for each fiber row. As the speed increased, the liquid-coil effect was decreased until at a critical speed it was eliminated entirely. To examine how straight the depositing fiber was, the second fiber after elimination of the liquid-coil effect was chosen for analysis both with and without an electrostatic lens using the same polymer solution. Photographs of the horizontal array of fibers were taken on a Canon EOS 20D DSLR camera, and the fiber in question was examined using MATLAB. The top and bottom edge of the fiber were found using a custom MATLAB code. The middle of the fiber was determined by taking the value midway between the top and bottom edge. This was done across the entire image to obtain a scatterplot representing the fiber in the photograph. A five point running average was used to smooth the data. Linear regression of the scatterplot data provided a perfectly straight line, and the root mean square error was calculated for a total of seven samples for the samples with and without the secondary ring electrode. The root mean square error provided an estimate for how far the fiber deviated from a perfectly straight line on average.

3.2.5 Simulations

COMSOL simulations were used to visualize the electric potential and electric fields in the 3D jet writing system. All components were pre-defined in the COMSOL materials library, and were drawn to scale. Electric potentials were calculated using finite-element analysis. Boundary conditions used are given in the description of 3D jet writing.

3.3 Results

3.3.1 Secondary Electrode Simulations

Fundamentally, creating 3D microfiber structures via electrospinning requires the stabilization of the whipping instability during jet propagation and precise control over fiber deposition. During electrospinning, the application of a high electric potential deforms a fluid droplet resting at the orifice of the needle into a conical droplet, or Taylor cone. At a critical voltage, a fluid jet emits from the tip of the Taylor cone, and accelerates towards a grounded collection electrode. The jet stretches while traversing towards the grounded electrode, causing a large increase in surface area and rapid evaporation of the solvent, leaving a continuous solid fiber deposited on the grounded electrode.

Upon examination of the electric potential in a typical electrospinning setup using finite

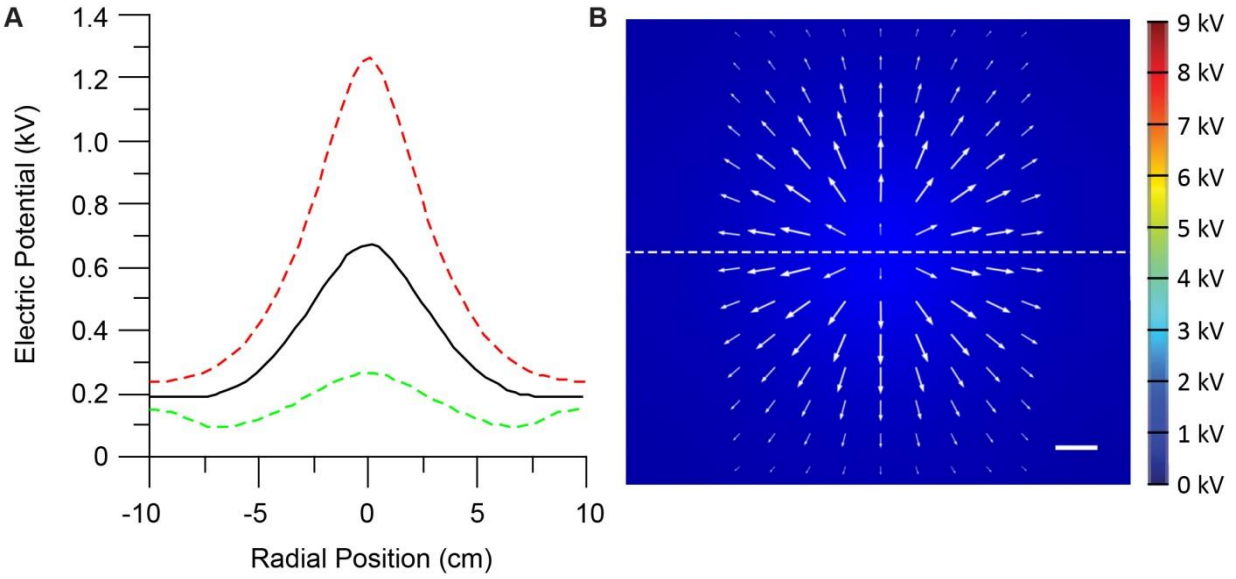

Figure 3.1. Finite element simulations of the electrostatic potential for standard electrospinning experiments. A) A typical electrospinning experiment results in an electric potential energy 'hill', and it is shown at a distance 2 cm, 3 cm, and 4 cm below the charged capillary tip (red, black and green respectively). **B)** A heat map of the electric potential 3 cm below the capillary tip shows the electric field which points radially outward (white arrows). Electric potential in (A) taken along the dashed line.

element analysis, a local electric potential hill is encountered, where the potential energy maximum is located exactly below the capillary tip. This configuration leads to an electric field pointing radially outward, which drives the fiber towards the periphery. This is illustrated in Figure 3.1. The outwards directed movement of the jet is further amplified by the repulsion of charges within the jet, resulting in randomly deposited mats of polymer fibers.

In principle, this outward movement of the jet, and thus the randomization of the fiber orientation during deposition, can be focused by a secondary electrode which modifies the local electric field, but the details are not yet fully understood. Secondary electrodes have been demonstrated to be capable of focusing the deposition of electrospun polymer fibers. A ring shaped secondary electrode leads to a modified electric field, where inside the ring the radial component of the electric field always points inwards. The radial component of the electric field inside of a charged conducting ring on a is found to be:

$$\vec{E}_r = \frac{k\lambda}{R}\int_0^{2\pi} \frac{cos(\theta)-\frac{r}{R}}{\left(1+\left(\frac{r}{R}\right)^2-\frac{2r}{R}cos(\theta)\right)^{\frac{3}{2}}}d\theta \tag{3.1}$$

where r is the distance from the center of the ring, R is the radius of the ring, λ is the charge density, k is Coulomb's constant, θ is the angle around the ring, and $\vec{E}_r$ is the radial component of the electric field. Plotting this equation demonstrates that inside a charged conducting ring with uniform charge density, an inward pointing electric field is produced.

The analytical expression from Equation 3.1 plotted in Figure 3.2 shows how the electric field changes as you move radially outward from the center point of a charged ring electrode. This is an idealized case, in which only the ring electrode contributes to the overall electric field of the system. A more complete view of the stabilizing forces produced when ring electrodes are

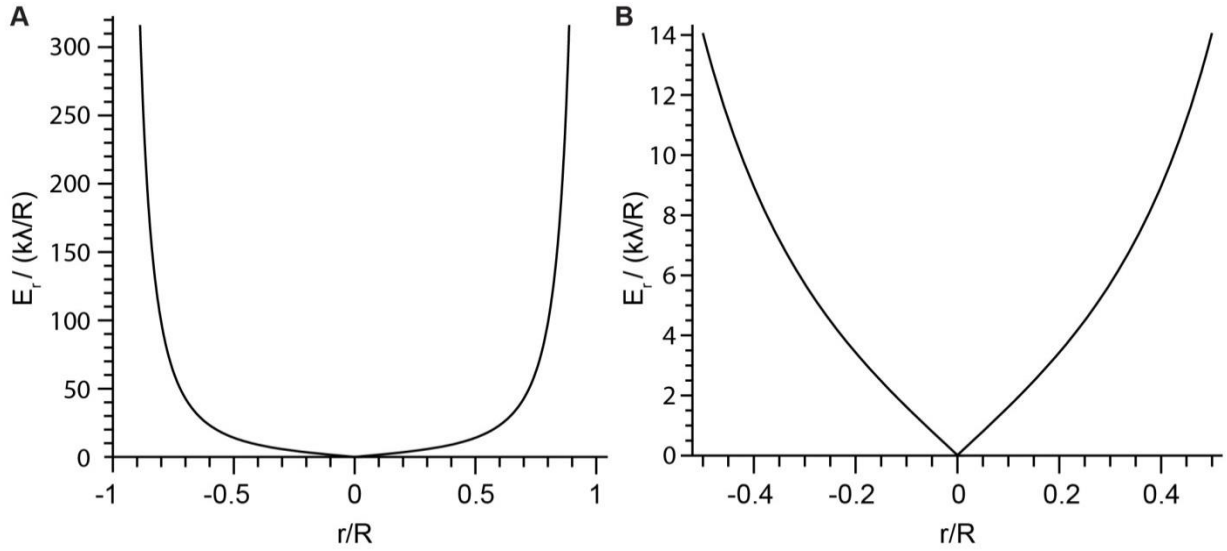

Figure 3.2. Analytical approximation of radial electric field inside a uniformly charged ring electrode. A) Plotting the non-dimensional radial component of the electric field with increasing distance from the center of the ring shows immense electric fields near the edges of the ring. **B)** Looking more closely between r/R values of -0.5 and 0.5 illustrates the focusing forces provided by the radial component of the electric field which would be applied at on a depositing fiber jet. Both plots demonstrate that as the fiber deviates further from the center of the ring, larger forces are applied to center the fiber.

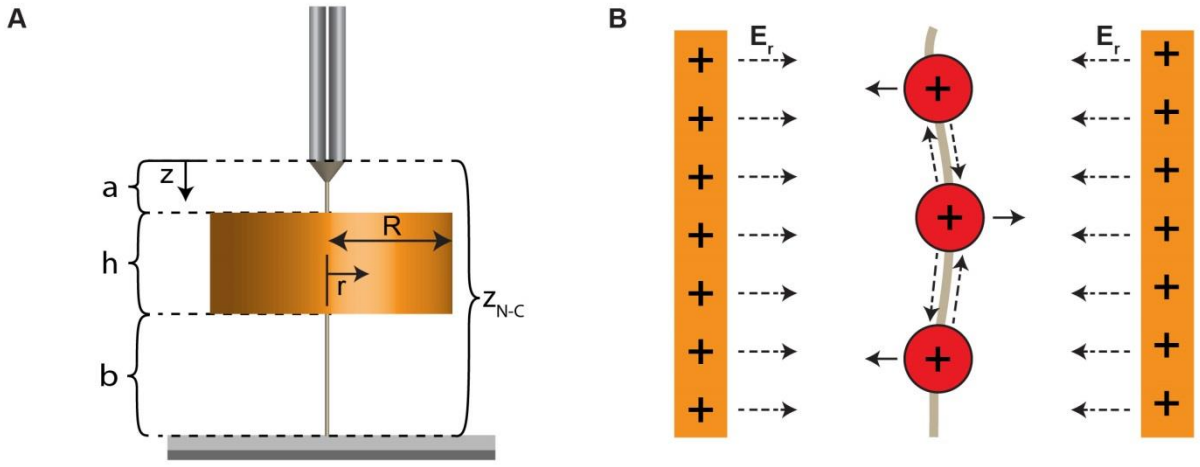

Figure 3.3. Schematic diagram of the electrode positioning in the 3D jet writing apparatus. A) This diagram outlines variables used in examining the optimal ring electrode position and size. The ring height (h) and ring radius (R) were both examined in COMSOL simulations. Electric potentials and electric fields are computed for various z distances below the capillary tip and r distances away from the center of the ring electrode. **B)** The radial component of the electric field is capable of providing stabilizing forces on depositing charged polymer fiber jets. Instabilities often arise from charge self-repulsion within the polymer fiber jet.

imparted into an electrospinning system between the capillary and grounded collection substrate (Figure 3.3) is accomplished using finite element analysis. Here, a charged copper ring (h=2.5 cm, R=1.5 inches, a=0.5 cm, b=2 cm from Figure 3.3), is inserted into a model containing a standard electrospinning setup. Modeling of the electric potential at different distances from the capillary tip revealed that a circular secondary electrode modifies the electric potential profile by creating an electric potential well, with an electric field pointing towards the center of the circular electrode (Figure 3.4). In this model, 16 kV were applied to the needles, 9kV applied to the secondary ring electrode, and the collection plate was grounded. This centering force is an important component in effectively dampening the initiation of whipping instabilities.

Examination of multiple permutations of ring shaped secondary electrodes was performed to determine the optimal aspect ratio and positioning. First, maintaining a constant ring height (h

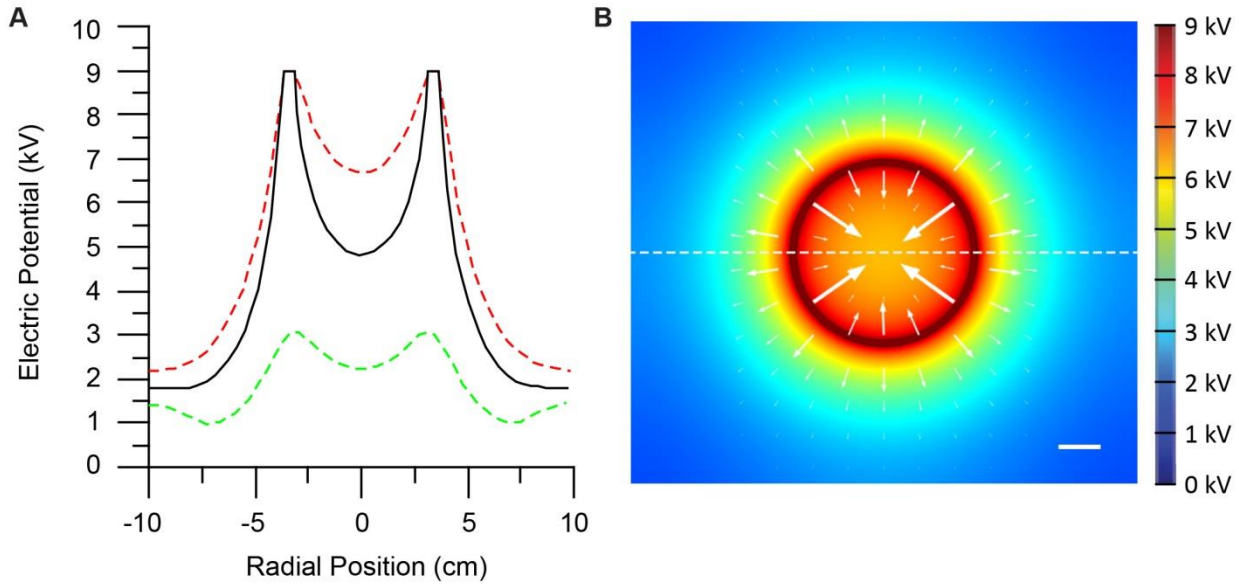

Figure 3.4. Finite element simulations of the electrostatic potential for 3D jet writing experiments. A) The electric potential of 3D jet writing experimental setup, which includes a ring shaped secondary electrode, is shown at a distance 2 cm, 3 cm, and 4 cm below the charged capillary tip (red, black and green respectively). **B)** A heat map of the electric potential 3 cm below the capillary tip shows the electric field which points radially inward (white arrows). Electric potential in (A) taken along the dashed line. Scale bar indicates 1 cm.

constant, see Figure 3.3A) the effect of a changing ring diameter (R) was investigated. It was seen that ring electrodes with smaller diameters yielded a stronger focusing capability, despite the fact that the larger diameter ring electrodes produced deeper electric potential energy wells. The focusing capability was characterized by the slope of the electric potential (ie. electric field), and as shown in Figure 3.5, the smaller rings have a larger electric field. This can also be inferred from Equation 3.1, where a decrease in the value of r/R (an increasing ring electrode radius) leads to a smaller radial component of the electric field (see Figure 3.2). All of the different secondary ring electrode diameters provided superior focusing to the standard electrospinning setup, which has a negative effect on fiber focusing.

If focusing capability were the only characteristic taken into consideration, the smaller

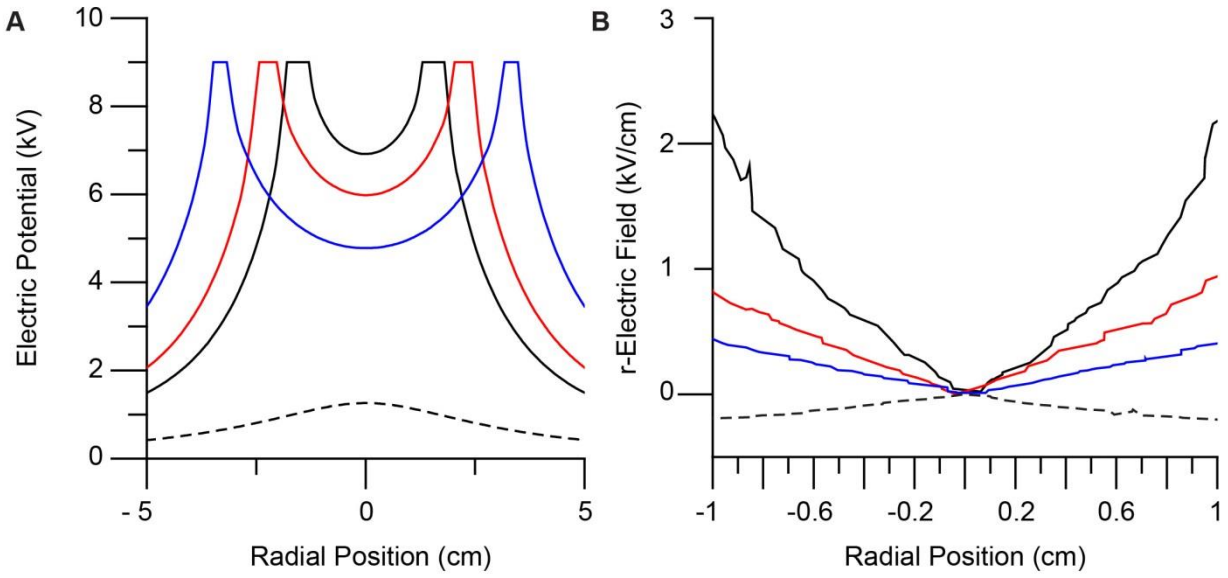

Figure 3.5. Finite element simulations of the electrostatic potential for various diameter ring electrodes in 3D jet writing experiments. A) The electric potential of 3D jet writing experimental setup, which includes a ring shaped secondary electrode. Simulations for rings of 1inch, 1.5 inch, and 2.5 inches in diameter are shown at a distance 3 cm below the charged capillary tip (black, red, and blue respectively). The dashed black line indicates the electric potential without a ring electrode. **B)** The slope of the electric potential plots from (A) are plotted to demonstrate the focusing capability of each ring type. The 1 inch ring has higher electric fields (i.e. more focusing) compared to the other rings, and all rings are opposite in sign from the configuration without a ring electrode.

secondary ring electrode are superior. However, the driving force which accelerates the polymer fiber to the grounded electrode is also a characteristic of importance. In practice, it can be observed that the polymer fibers do not evenly deposit onto the grounded collection electrode. Instead, the fibers get stuck inside the ring electrode until enough tension from the moving collection platform is applied, or enough polymer mass is accumulated for gravity to force the jet to be pulled down to the collection plate. It is hypothesized that this occurs when there is not enough of a driving force to pull the fiber down to the collection electrode. Modeling the electric potential along the z axis (with x,y=0) for secondary ring electrodes of varying diameter allows us visualize the driving force on the depositing polymer fiber. This will be utilized to predict which ring configuration will minimize this uneven fiber deposition. Figure 3.6 shows that smaller diameter rings have locations near the middle of the ring where the driving force nearly goes to zero. However, as the ring diameter increases, the driving force gets larger. Therefore, there is a tradeoff between having enhanced focusing provided by the ring, and the ability of the ring to provide even fiber deposition.

These criteria get further complicated when rings of constant diameter and varying height are examined. Changing the height (h) of the ring secondary electrode while keeping the needle to ring distance constant (parameter a in Figure 3.3A), and examining the electric potential energy and electric field at the bottom of the ring where the focusing effect is maximized, provided a platform for optimizing this parameter. It was observed that the larger height, the deeper the electric potential well. However, as before, the deeper wells did not always correlate to enhanced focusing. As the ring height increases from 1 cm to 3 cm there is a dramatic increase in focusing capabilities, but further increasing the height to 3.5 cm leads to a subsequent loss of the radial electric field. These results are summarized by Figure 3.7.

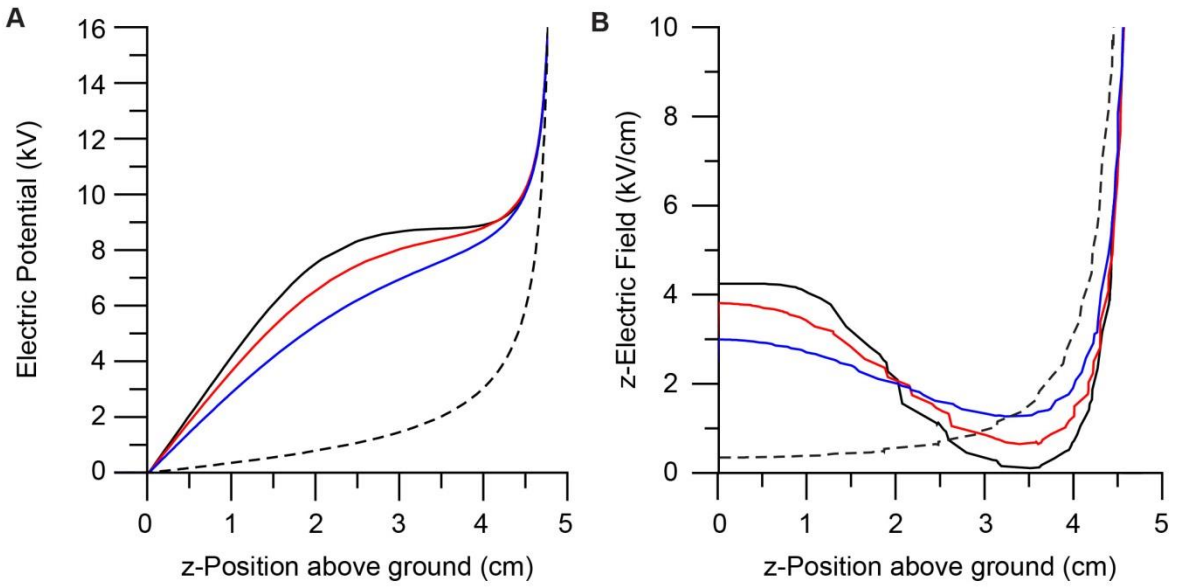

Figure 3.6. Finite element simulations which represent how the driving force changes with changing ring electrode diameter. A) The electric potential along the z-axis of 3D jet writing experimental setup, which includes a ring shaped secondary electrode. Simulations for rings of 1inch, 1.5 inch, and 2.5 inches in diameter are shown at the bottom of the ring electrode (black, red, and blue respectively). The dashed black line indicates the electric potential without a ring electrode. **B)** The gradient of the plots in (A) show the 'driving force' which is the z-component of the electric field. This field is responsible for accelerating the jet towards the grounded collection electrode. Lower values of electric field represent a loss in driving force.

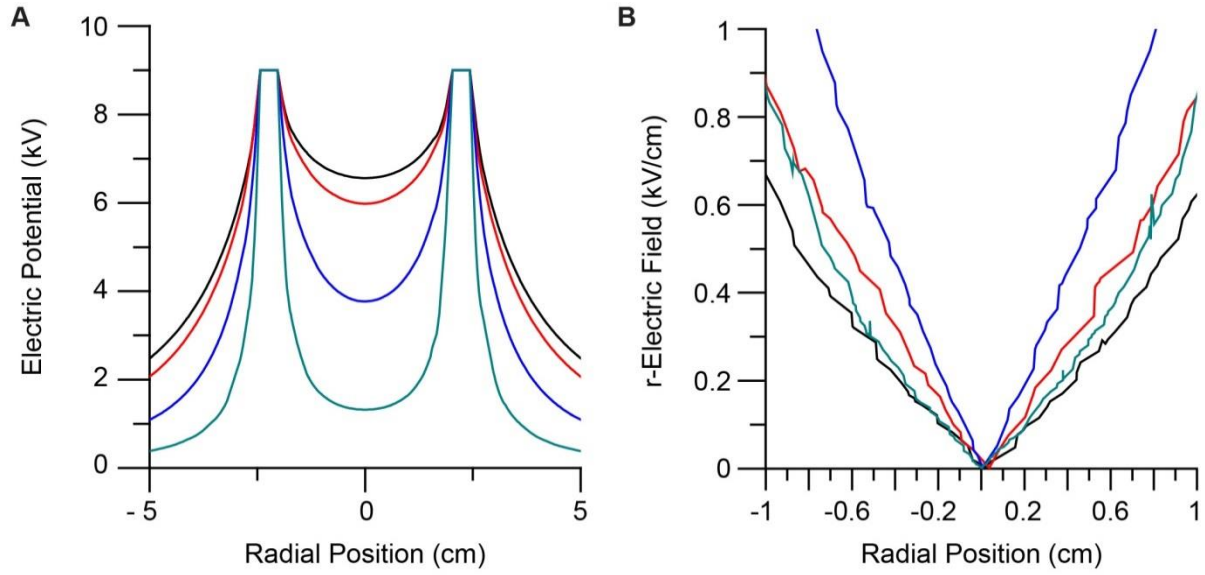

Figure 3.7. Finite element simulations of the electrostatic potential for various ring electrodes heights in 3D jet writing experiments. A) The electric potential of 3D jet writing experimental setup, which includes a ring shaped secondary electrode. Simulations are taken at the bottom of rings 1 cm, 2 cm, 3 cm, and 3.5 cm in height each 1 cm below the tip of the charged capillary (black, red, blue, and green respectively). **B)** The slope of the electric potential plots from (A) are plotted to visualize the radial component of the electric field, representing the focusing capability of each ring type.

Driving forces provided by the z-component of the electric field at r=0 in this system show trends similar to what was seen previously, where better focusing secondary ring electrodes often have less driving force accelerating the depositing jet to the grounded substrate (Figure 3.8). Interestingly, the 3.5 cm ring height had a driving force comparable to the 3 cm ring despite the fact that the 3.5 cm ring had significantly worse focusing ability. This can be attributed to the close proximity of the secondary ring electrode to the collection substrate surface and the long distance in which the depositing fiber has to travel through the ring electrode. This again leads to the concept of needing a trade-off between obtaining enhanced focusing and maintaining a sufficient driving force to achieve consistent fiber deposition.

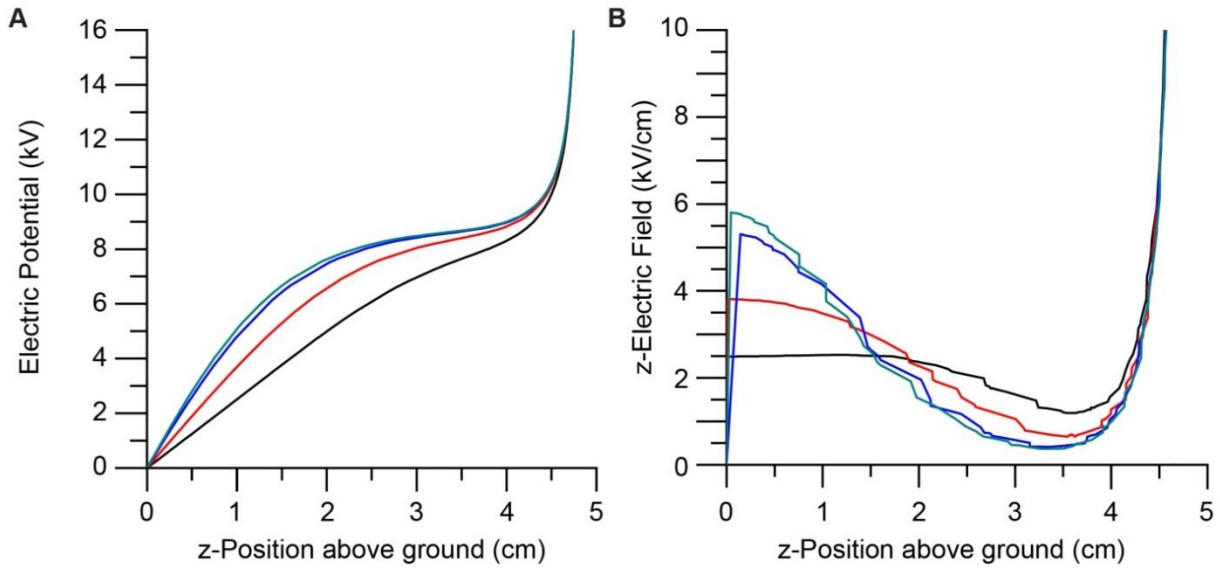

Figure 3.8. Finite element simulations which represent how the driving force changes with changing ring electrode height. A) The electric potential along the z-axis of 3D jet writing experimental setup. Simulations are taken at the bottom of rings 1 cm, 2 cm, 3 cm, and 3.5 cm in height each 1 cm below the tip of the charged capillary (black, red, blue, and green respectively). **B)** The gradient of the plots in (A) show the 'driving force' which is the z-component of the electric field. Lower values of electric field represent a loss in driving force.

Increasing the distance of the ring from the capillary tip can also have an effect on both the focusing ability and driving force of secondary ring electrodes. Simulations of a secondary ring

electrode with a 2 cm height and 1.5 inches in diameter were examined. Starting with the ring electrode such that the top of the ring is even with the tip of the charged capillary, and lowering the ring by 1 cm, 2 cm, and 2.5 cm. Lowering of the ring towards the grounded substrate leads to an enhanced focusing, similar to the beneficial focusing seen with the increased ring height (Figure 3.9). This indicates that the focusing increases due to the increased ring height are simply due to the bottom of the ring getting closer in proximity to the grounded electrode (Figure 3.11). Differences are seen however when looking into the driving force. Lowering the ring towards the grounded electrode leads to decreases in driving force, to the point where there are regions at which the z-component of the electric field goes to zero (Figure 3.10). These decreases are greater than the decreased driving force observed by increasing the overall ring height. The ideal secondary ring electrode z-position is therefore a compromise, as with the other parameters that have been examined.

With the collective data contained within the plots in Figures 3.7 through 3.11 it was determined that the overall focusing capability of the secondary ring electrode was dictated by the positioning of the bottom of the ring from the grounded collection electrode. While increases in focusing capability was seen by increasing the ring height, similar increases in focusing were found by simply lowering a ring of lesser height such that it was a similar distance from the grounded electrode. However, differences were observed in the driving force on the depositing fiber jet in the two cases. The ring with greater height had an increased driving force than the shorter ring electrode, indicating that maximizing ring height was a superior method of increasing focusing compared to moving a smaller ring closer to the grounded electrode.

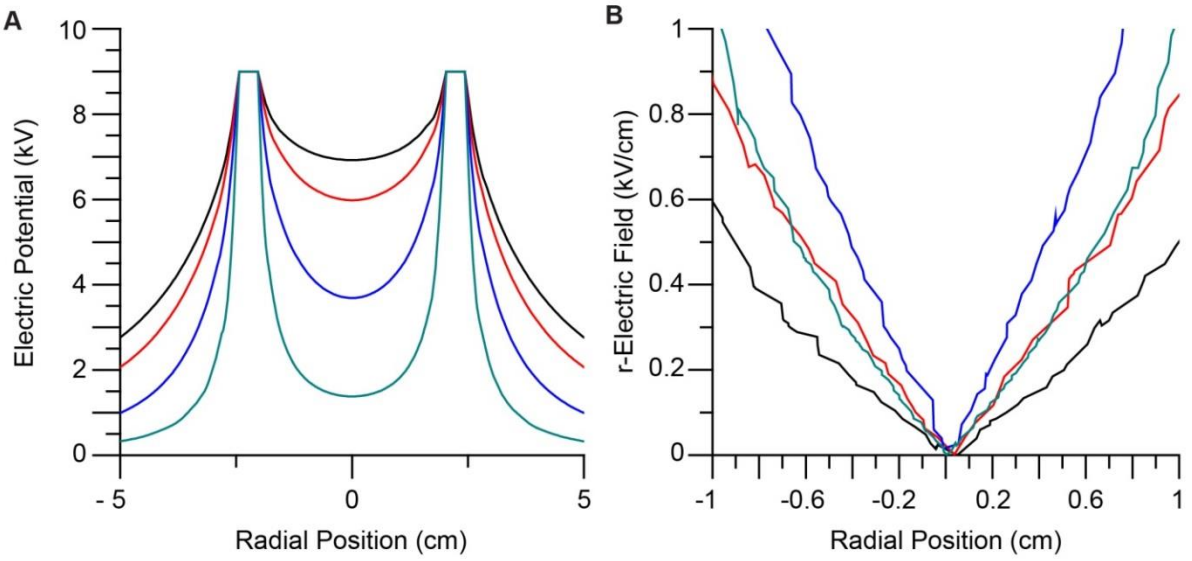

Figure 3.9. Finite element simulations of the electrostatic potential for various ring electrode positions in 3D jet writing experiments. A) The electric potential of 3D jet writing experimental setup, which includes a ring shaped secondary electrode. Simulations are taken at the bottom of rings positioned 0 cm, 1 cm, 2 cm, and 2.5 cm below the tip of the charged capillary (black, red, blue, and green respectively). **B)** The slope of the electric potential plots from (A) are plotted to visualize the radial component of the electric field, representing the focusing capability of each ring type.

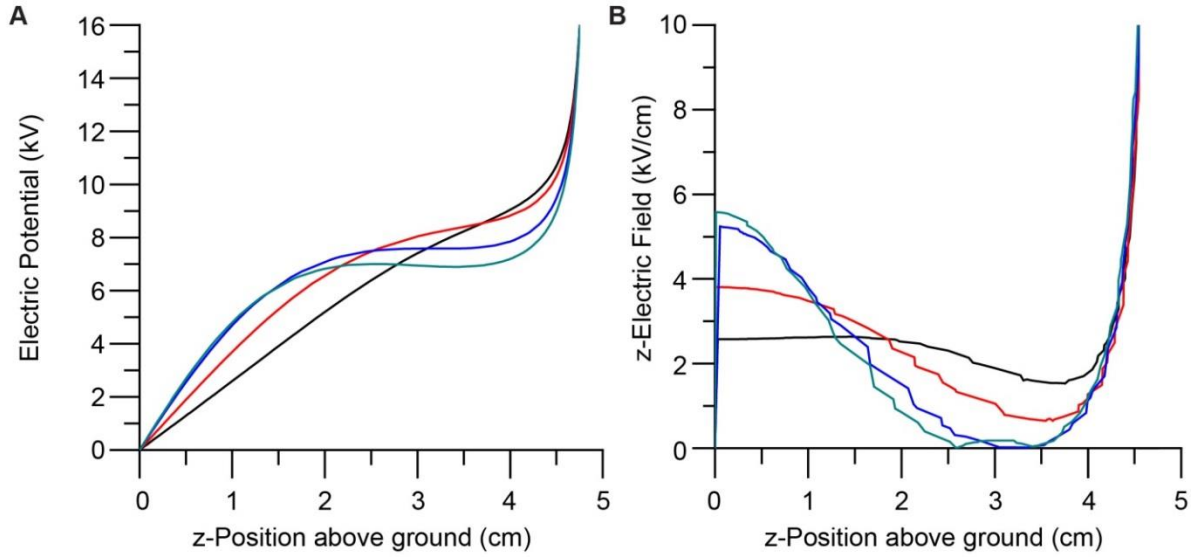

Figure 3.10. Finite element simulations which represent how the driving force changes with changing ring electrode z position. A) The electric potential along the z-axis of 3D jet writing experimental setup. Simulations are taken at the bottom of rings positioned 0 cm, 1 cm, 2 cm, and 2.5 cm below the tip of the charged capillary (black, red, blue, and green respectively). **B)** The gradient of the plots in (A) show the 'driving force' which is the z-component of the electric field. Lower values of electric field represent a loss in driving force.

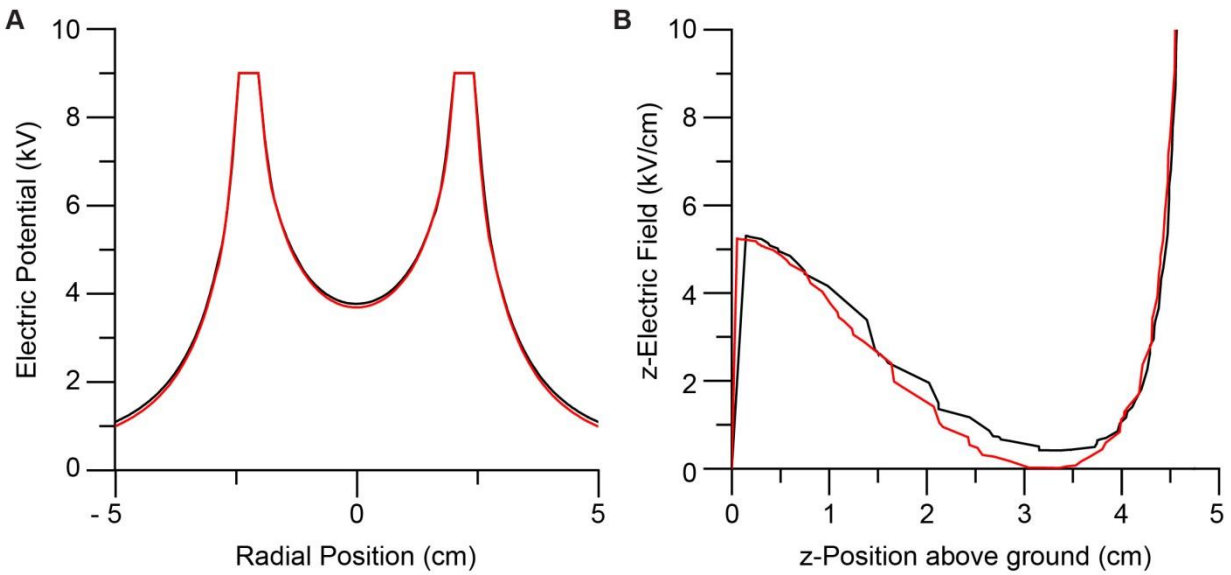

Figure 3.11. Comparing effect of changing the ring height and moving the ring electrode. **A)** Overlay of the electric potential wells produced by two different secondary ring electrodes. The red line indicates a ring electrode 2 cm in height 2 cm below the capillary tip. The black line represents a 3 cm ring electrode 1 cm below the capillary tip, placing the bottom of the ring in the same location in each case. Similar focusing capability is observed for each electrode configuration. **B)** Looking at the driving force produced by the z-component of the electric field shows that the 3 cm ring electrode has more driving force than the shorter ring electrode.

These findings led to the question of how the ring geometry and placement affects the driving force acting on the jet. If focusing is dependent mostly on the proximity of the bottom of the ring to the grounded collection electrode, what controls the minimum driving force? Simulation results of experimental setups containing secondary ring electrodes at various heights were again examined to answer this question. This time, however, instead of maintaining a constant needle to ring distance (distance a in Figure 3.3), the center of the ring was held in the same position. In these simulations, it was observed that the focusing provided by the secondary ring electrode improved with greater ring height (Figure 3.12 A-B), but this time the driving force remained constant for all cases (Figure 3.12 C-D). Therefore, it was determined for a given ring diameter, the focusing capability provided is determined by the distance above the grounded collection electrode, and the driving force is determined by the location of the center of mass of

the ring. This leads to the conclusion that the ideal secondary ring electrode configuration should aim to maximize the ring height while maintaining its centerline. The optimization process outlined in these simulations led to the final design of the ring electrode.

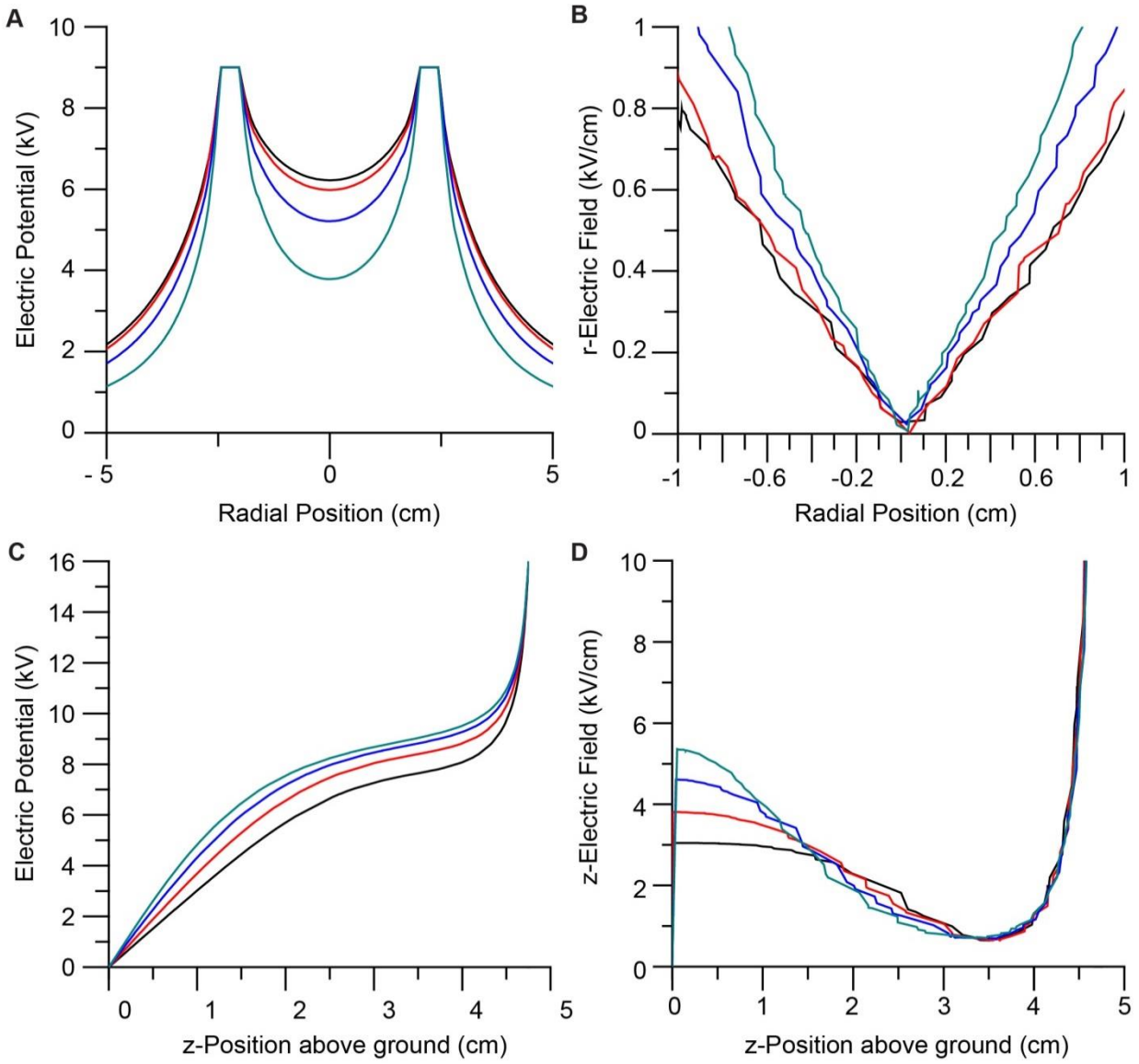

Figure 3.12. Effect of changing the ring height while maintaining the center of mass. A) The effect of four secondary ring electrode configurations were examined. Electric potential wells of 1 cm, 2 cm, 3 cm, and 4 cm (black, red, blue, and green respectively) in height show similar changes in the depth of the wells and **B)** focusing seen from simply moving the ring closer to the collection electrode. **C)** Plotting how the electric potential along the z-axis changes with ring height and maintained center of mass, shows a similar profile for each case. **D)** The slope of the plots from (C) show the z-component of the electric field which contributes to the driving force. This shows each ring has the same minimum driving force.

A secondary ring electrode, composed of commercially available copper tubing, 1.5 inches in diameter was chosen as a compromise between the competing effects of focusing and driving force seen in the simulation results in Figure 3.5 and 3.6. With the capillary to ground distance fixed at just under 5 cm, a final ring height of 2.5 – 3 cm was chosen to maximize the total height of the ring, while maintaining the top of the ring 0.5 cm below the tip of the capillary. Rings of greater height were not considered to minimize the risk of arcing between the bottom of the ring and the grounded collection electrode. This produced an electrostatic focusing element which was capable of stabilizing the depositing PLGA fiber jet.

Using the secondary ring electrode, which was designed and positioned according the described electrostatic simulation results, the effect of the applied electric potential on both the charged capillary and ring electrode was examined.

Changing the applied electric potential on the charged capillary yielded a couple interesting findings. First, it was seen that this does not have any significant effect on the focusing provided by the secondary ring electrode (Figure 3.13 A-B). The plots of the electric potential energy wells and the radial component of the electric field all overlap with one another, indicating that there is no distinguishing difference in the focusing capability within the range of applied electric potentials examined (from 14 kV to 20 kV). However, what did change with increasing applied potential was the driving force. As the applied potential was increased, the driving force acting on the depositing fiber jet also increased. This caused the minimum driving force to transition from negative at 14 kV, around zero at 16 kV, to positive values for higher applied potentials. This method of altering the 3D jet writing environment provides a means for controlling the deposition speed of the fiber jet without affecting the focusing ability of the secondary ring electrode. A larger driving force acting on the depositing fiber jet will result in more

acceleration, and higher jet velocities upon deposition on the grounded collection electrode. If the applied electric potential to the secondary ring electrode were altered, changes in both the focusing and driving forces are seen to change (Figure 3.14). As would be expected, increases in the applied electric potential leads to an increased focusing force produced by the electrode. This can be explained by the increased charge density on the copper ring electrode in Equation 3.1 which results in an increased radial component of the electric field. This is seen in Figure 3.14 A-B.

Changes in the applied potential to the secondary ring electrode also result in alterations to the driving force acting on the depositing fiber jet. As the applied electric potential increases, the driving force decreases, and at sufficiently high applied potentials can even become negative. Physically, this can be used to determine how the ring affects the depositing fiber jet for a given fixed secondary ring electrode geometry. Increasing the applied potential to the ring electrode results in increased focusing, but can also be used to decrease the driving force applied to the jet. This is important as it is a means of adjusting the driving force acting on the depositing fiber jet without altering the amount of charge being input into the polymer solution being electrospun. Using the combination of both changing the capillary and secondary ring electrode applied potentials can be used independently to tune the depositing jet speed and the focusing capabilities of the system.

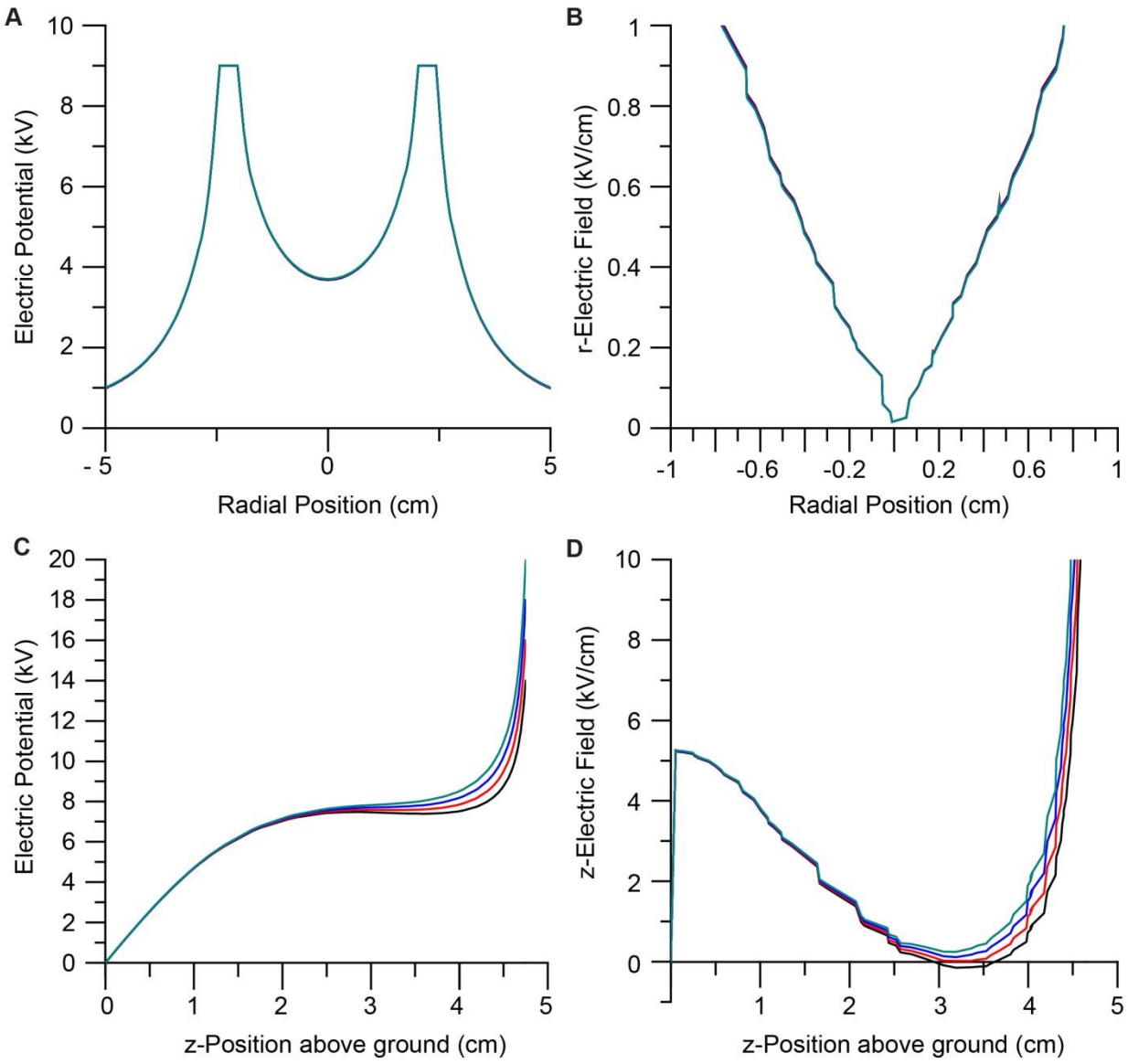

Figure 3.13. Determination of how changing the electric potential applied to charged capillary affects focusing and driving forces in 3D jet writing. A-B) Radial components of the electric potential (A) and electric field (B) were examined for varying applied DC electric potential to a charged capillary with a constant applied potential to the secondary ring electrode of 9 kV. Simulations of applied voltages of 14 kV, 16 kV, 18 kV, and 20 kV (black, red, blue, and green respectively) to the capillary tip demonstrate minimal effects on focusing. All lines overlap with each other, giving the perspective that there is only one plot in these examples. **C-D)** Z-components of the electric potential (C) and electric field (D) demonstrate that the applied electric potential does play a role in affecting the driving force acting on the depositing fiber jet. At lower applied potentials (14 kV), negative driving force can be seen, with continual increases with increasing applied potential.

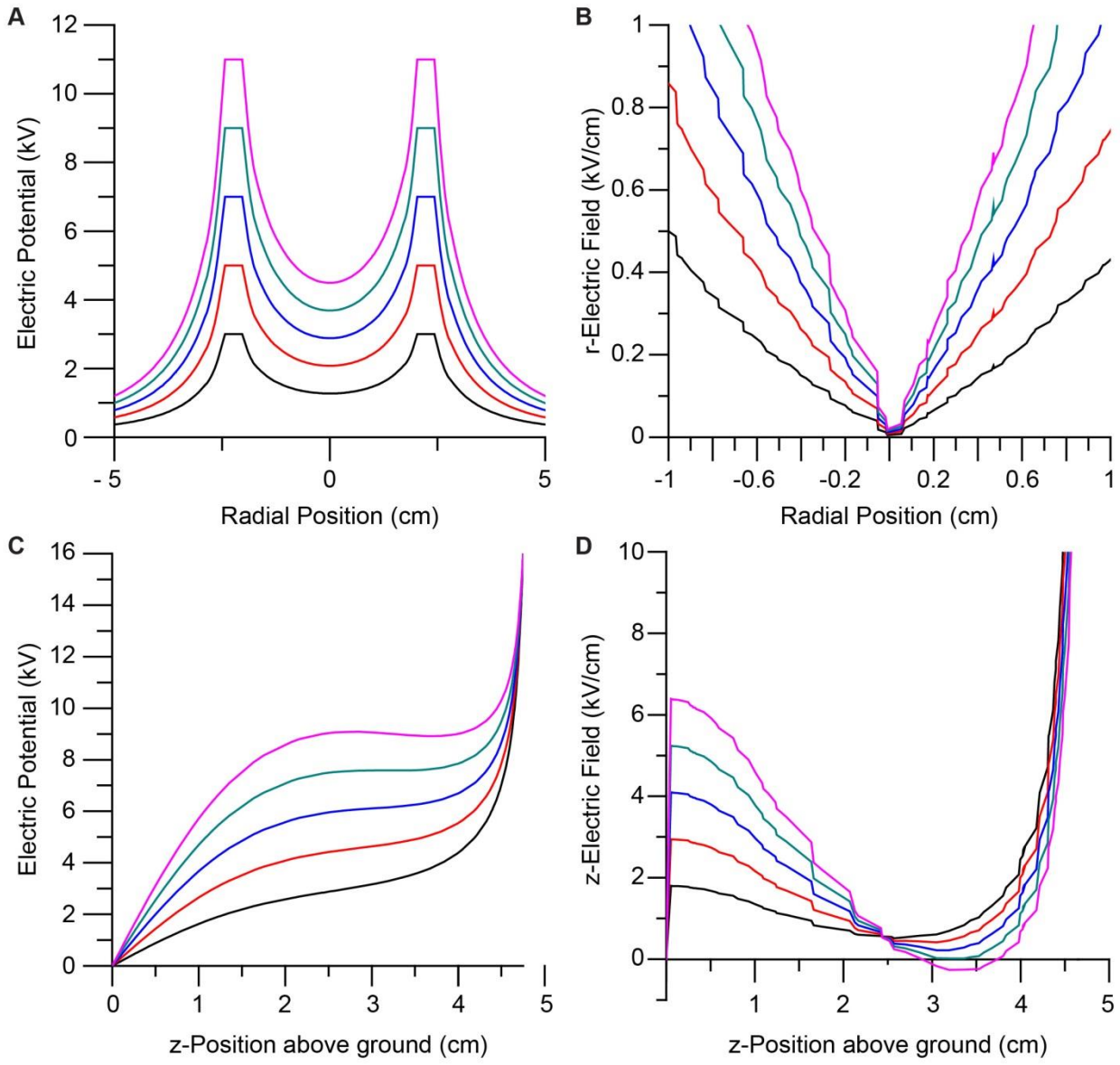

Figure 3.14. Determination of how changing the electric potential applied to secondary ring electrode affects focusing and driving forces in 3D jet writing. A-B) Radial components of the electric potential (A) and electric field (B) were examined for varying applied DC electric potential to the secondary ring electrode with a constant applied potential to the charged metal capilary of 16 kV. Simulations of applied voltages of 3 kV, 5 kV, 7 kV, 9kV, and 11 kV (black, red, blue, green, and pink respectively) to the capillary tip demonstrate consistent increases in focusing with increasing ring potential. **C-D)** Z-components of the electric potential (C) and electric field (D) demonstrate that the applied electric potential does play a role in affecting the driving force acting on the depositing fiber jet. As expected, increasing applied potential decreases the driving force on the depositing fiber jet. This emphasizes the importance of how the ring potential can be used to control the speed and focusing in the 3D jet writing system.

3.3.2 Precision of Fiber Deposition

While the electric potential well formed by the ring electrode described in Section 3.3.1 is on the order of cm in scale, a strong inward pointing radial component of the electric field (on the order of hundreds to thousands of V/m) is still present on the micron scale near the center of the ring. Numerical simulations of the electric fields present at these length scales is shown in Figure 3.15. These electrical forces effectively dampen the formation of the whipping instability through radial electric fields. This allows the fiber to be deposited along the path of least resistance due to the inertia associated with the depositing fiber. Moving the collection platform below the depositing fiber allows for straight lines of polymer fiber to be collected directly below the tip of the charged needle electrode. Other adjustments to the electric fields can be used to adjust the fiber deposition speed, and thus fiber diameter, and is discussed further in Section 3.3.4. Furthermore, how the deposition of polymer fibers affects the electric field, and the influence they have on the ability of the fibers to stack on top of one another, and even can limit the height of the fiber structures, are described in Sections 3.3.4 and 3.3.6. These descriptions illustrate the major role the electric field plays on fiber deposition in the 3D jet writing process.

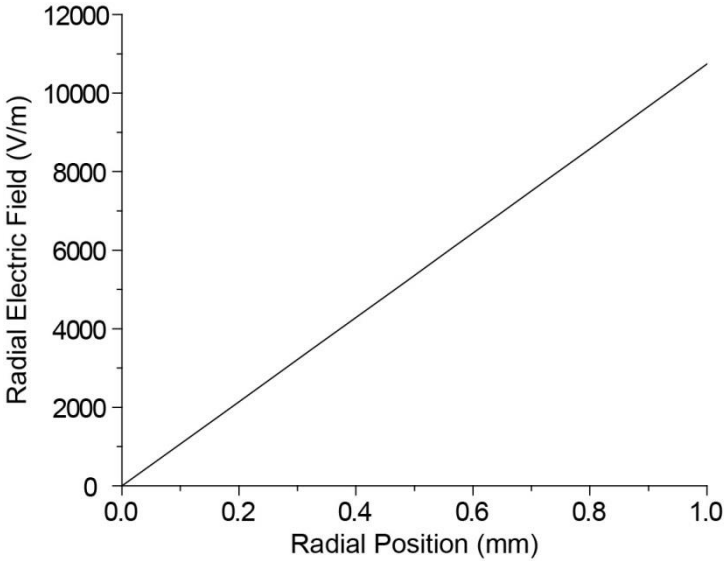

Figure 3.15. Radial component of the electric field on the sub-millimeter scale. Electric fields less than 100 μm away from the center of a ring electrode are on the order of hundreds to a thousand V/m, producing a force which acts on the depositing fiber.

After defining the desired electric fields in the electrospinning setup, the

effect of the secondary ring electrode was tested by depositing electrospun PLGA fibers on grounded collection electrode which was mounted to a dual axis motion control unit. This provided the means for depositing the fibers in controlled patterns by programming the x-y stage movements. Initial testing was performed by simply testing one dimensional movement to determine what effect the ring electrode has on focusing the fiber deposition. The stage was programmed to create an array of horizontal lines spaced 3 mm apart. At the start of each new horizontal segment the stage speed was increased by a factor of 3 mm/s until the stage reached 48 mm/s. A representative resulting fiber deposition pattern is depicted in Figure 3.16 with both with (Top) and without (Bottom) a secondary ring electrode.

Visual comparison of the two cases clearly showed a difference between the presence of the ring electrode and its absence. In the case with the secondary ring electrode, there was an appearance of very ordered and structured lines. Even at the lower speeds, where the fiber deposition is faster than the movement of the collection platform, the fiber deposition seemed very even and uniform. These speeds lead to the development of a liquid-rope coiling effect, which causes the depositing fiber jet to buckle in on itself. With the ring electrode in place, this resulted in an ordered set of coiled rings interlocking with each other at 3 mm/s, and at slightly higher speeds a series of alternating loops of fibers would appear above and below the line of trajectory. At higher speeds yet these alternating loops transformed into oscillations with the appearance of sinusoidal waves, until finally a straight fibers segment was deposited.

In contrast to these results are the lines deposited without the ring electrode. Overall, the deposition of the lines was ordered, but lacked the uniformity that was observed with the ring electrode. This is most easily seen at the lower speeds, where the liquid-rope coiling effect is much less controlled than when a stabilizing ring electrode is in place. At these speeds, when the

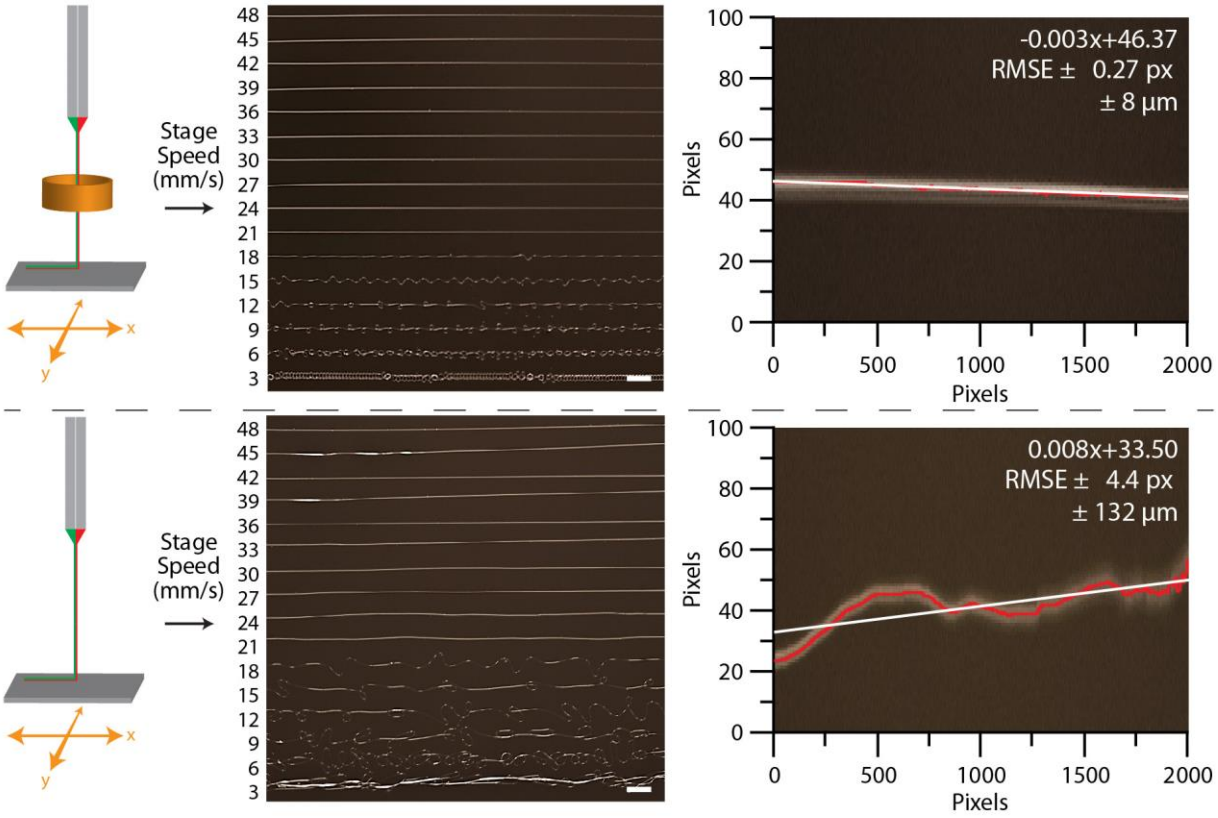

Figure 3.16. Testing effect of secondary electrostatic lens on depositing electrospun fiber jet. Horizontal lines of increasing speed were deposited on a collection plate. A line was selected two above the last line with periodic oscillations. This was performed with (Top) and without (Bottom) a secondary ring electrode. A line of best fit was generated for each case, and root mean square error from the fit line was reported as the deviation from straight. Scale bars indicate 3 mm

fiber jet buckles in on itself, it perturbs the entire length of the jet from the collector to the charged capillary. With no radial restoring force acting on the jet, only a horizontal force supplied by the moving collection plate, the depositional area of the fibers is much greater. Additionally, the regularity of the deposition at these low speeds is also lost, with little to no order observed until a jet speed of 21 mm/s is attained. At this speeds, the liquid-rope coiling effect is eliminated because the collection plate movement is greater than the speed of the depositing jet. Even at these higher speeds, the spacing between subsequently higher stage speeds lacks the consistency observed when a stabilizing ring electrode is introduced.

Beyond the qualitative improvements provided by the secondary ring electrode in the deposition of horizontal line segments, a quantitative benefit of the straightness of the line segments was also investigated. A line segment was chosen for each case, with and without a stabilizing ring electrode, and for consistency the line segment two speeds above the last line where oscillations were observed was chosen. In this case, both fiber segments were at the speed 24 mm/s, indicated by the arrows in Figure 3.16. These line segments were cropped out of the original image, such that they were the only segment within the image to be analyzed. They were then imported into a MATLAB file library, allowing the figure of the line segment to be converted into x-y coordinates which could then be statistically analyzed.

Seven separate trials were performed both with the secondary ring electrode and without. In each case the same process was utilized to select the fiber to be analyzed to prevent any unperceived bias. Each segment was translated into x-y coordinates, with each axis correlating to the x and y pixels of the image being analyzed, which plotted the fiber location. The obtained data points were smoothed using a 5 point running average to minimize noise seen, and extreme outliers caused by dust in the images were removed. The final data was then plotted and overlaid with the fiber image they represented to ensure the analysis performed produced a plot which correlated to the analyzed image. Once the accuracy of the technique was confirmed, a linear regression was applied to the x-y scatterplot data to generate a line of best fit. This line of best fit was interpreted as the intended trajectory of the fiber. Deviation from this line of best fit was therefore deemed to be a useful determinant of how straight the fiber segments were. Root mean squared error (RMSE) of the data from the line of best fit was calculated for each sample to give an average deviation from perfectly linear. In the seven samples which were prepared with a secondary ring electrode, an average RMSE of 0.57 pixels or 15 μm from perfectly straight was

determined using this analysis. The samples obtained without the ring electrode however were found to have an average RMSE of 2.29 pixels or 67 μm. Each image was independently taken by hand, leading to differences in the pixel to micron conversion for the two different conditions. Average fiber deviations from a perfectly straight line were over four times improved when a secondary ring electrode was in place.

Table 3.1. A summary of the precision at which the fibers can be deposited in a straight line is presented here. A 4x improvement was seen in straightness when a secondary ring electrode is present.

Measure	**With Ring (Pixels)**	**With Ring (μm)**	**Without Ring (Pixels)**	**Without Ring (μm)**
Average RMSE	0.57 ± 0.26	15 ± 6	2.29 ± 0.65	67 ± 23

3.3.3. Fiber Patterning: Conceptual Analysis

With the ability to control the deposition of straight fiber segments, organized arrays of fibers relative to one another are used to create complex 3D structures. Upon initial jet formation, a stabilization time is often necessary where the fiber speed changes, typically the jet will start depositing very slow and gradually speed up to normal deposition speeds near 30 mm/s. Deposition speed can be controlled during the jetting process through the alteration of the jetting parameters, namely the applied electric potential to the ring and the needles. Other parameters which affect the deposition of the fibers include the ring/needle height, ring electrode dimensions, solution flow rate, solution composition, and environmental conditions such as humidity and temperature. The fiber deposition speed is determined prior to any programmed stage movements simply by moving the collection electrode back and forth at increasing the speed until a lag in the depositing fiber jet is seen. Stabilization of the fiber jet is confirmed by continuing to move the collection electrode at this speed. If the lag in the fiber deposition is consistent, the jet is considered to be stabilized.

Two alternative conditions can also be observed (Figure 3.17). First, when the fiber deposition speed is greater than the speed of the moving collection electrode, the fiber undergoes what is known as a liquid-rope instability. This process arises from compressive forces acting on the fiber as the weight of the depositing jet is placed on the fiber which has already been deposited. Formation of a compressive heel causes the depositing fiber to buckle and twist, resulting in a coiled fiber deposition. Slowing the depositing fiber jet is accomplished through increasing the applied potential on the secondary ring electrode or decreasing the applied potential on the needle. Alternatively, simply increasing the collection electrode speed can eliminate this liquid-rope coiling effect. A second alternative is if the stage speed far exceeds the

fiber deposition speed. This typically arises when the fiber jet lacks the driving force necessary to exit the secondary ring electrode. This causes the fiber jet to either buckle and coil inside of the ring electrode, which only deposits once it reaches a critical mass, or else it will cause a stuttering (or interrupted) jet deposition, where an alternating depositing or not depositing occurs resulting in poor control over fiber alignment. This type of deposition is typically alleviated through altering the applied electric potentials or the height of the ring or needle electrodes.

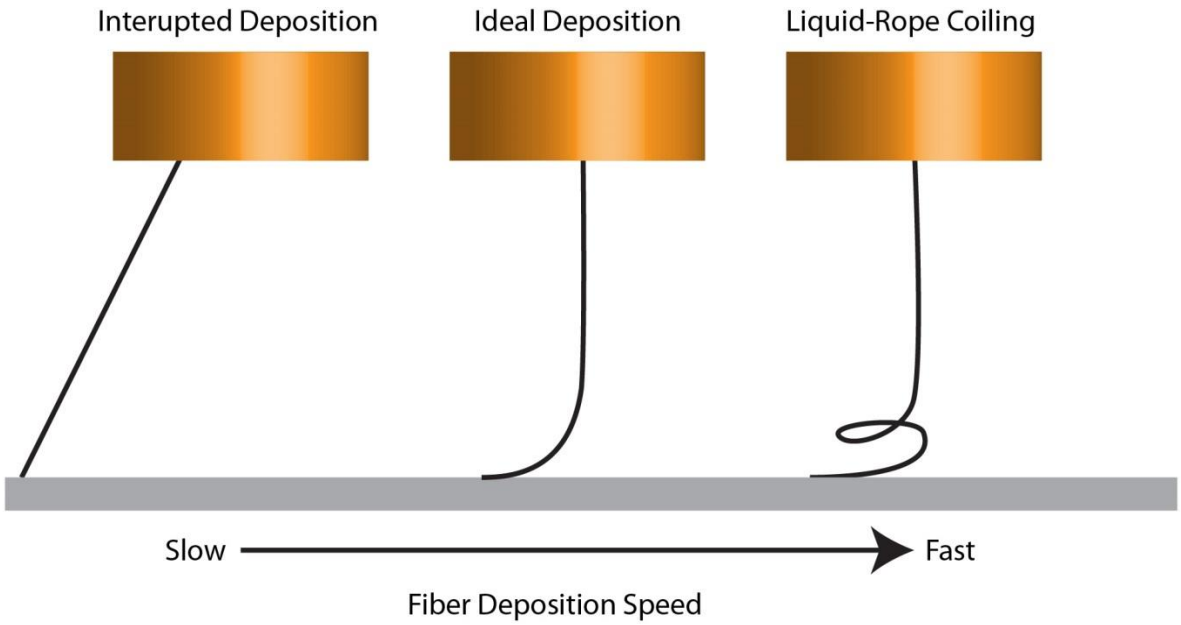

Figure 3.17. Fiber deposition regimes. The three major fiber deposition regimes exist. Ideal fiber deposition occurs when the fiber deposition speed is slightly slower than the collection electrode. This type of deposition is characterized by visible lag in the depositing jet. If the depositing fiber jet is faster than the speed of the collection electrode, a liquid-rope coiling effect arises. This type of deposition results in fibers deposited in rings or oscillatory structures. Finally, interrupted deposition occurs when the fiber deposition is either very slow or intermittent. This results in poor fiber organization and indicates a change in jetting conditions is necessary.

Fabrication of scaffolds is generally performed through the organization of straight lines to create a desired scaffold pattern. However, simply drawing arbitrary straight line segments often does not result in organized fiber structures. Due to the nature of the depositing fiber, the grounded collection substrate is moved at a speed slightly greater than the depositing fiber jet.

Because of this, there is always a lag to when the stage moves and when the fiber is deposited, and this can lead to curved corners if the stage makes sudden changes in direction. If this same trajectory is followed a second time, and the jet speed has changed slightly, the arc of the curved corner will be different, causing a defect in the fiber scaffold. Therefore, when creating fiber scaffolds, changes in direction are made outside of the desired scaffold area to ensure consistent fiber deposition. These changes in direction also include a zone in which the depositing fiber is allowed to catch up to the collection electrode. This is accomplished by incorporating a 'slow speed' segment in the programmed stage movement. When the fiber jet catches up to the stage movement, fiber coils are deposited until it reaches the next straight fiber segment, at which point the stage accelerates back to the 'fast speed'. These elements are critical for the design of organized fiber structures, and are illustrated in Figure 3.18.

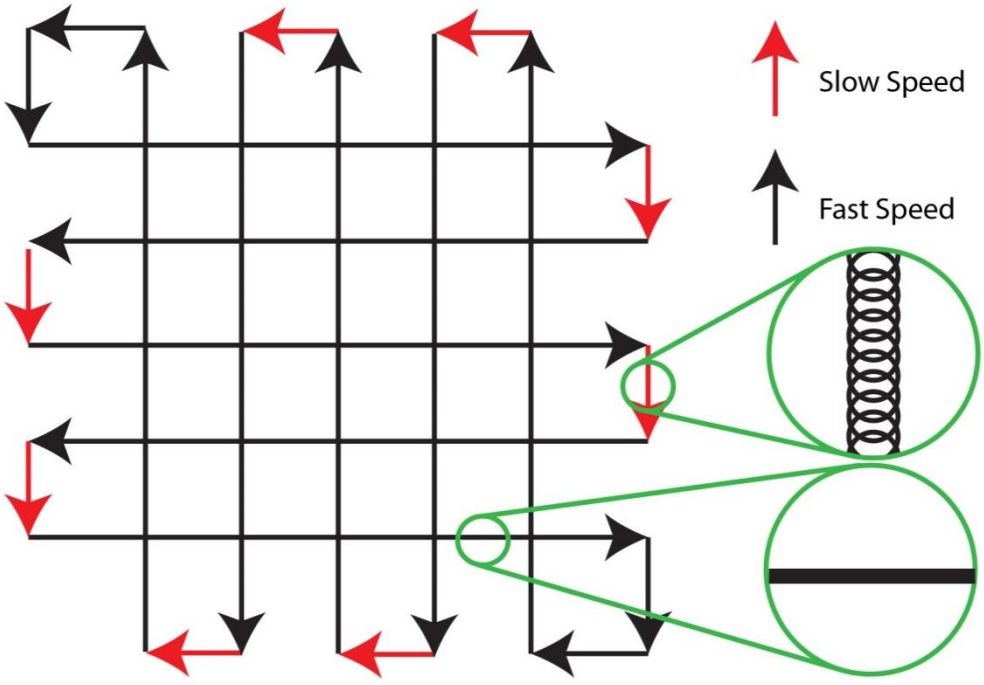

Figure 3.18. Design strategy for fabrication of fiber scaffold structures. A schematic diagram which illustrates the strategy used in designing fiber scaffolds. Straight line segments which compose the scaffold area are written using a 'fast speed'. When the collection electrode reaches a change in direction a 'slow speed' is used to allow the fiber jet to catch up with the stage movements, resulting in a coiled fiber segment. Combinations of fast and slow fiber segments lead to organized scaffolding structures.

In addition to the changes in collection electrode speeds, a 'lead in length'(indicated by L in Figure 3.19) is often desired. These are simply lengths of unused fibers which come before or after the desired scaffold architecture. The purpose of these lead in lengths is to: 1) allow the stage to accelerate to the proper deposition speed, 2) allow the fiber time to settle into the desired deposition location, and 3) ensure the fiber is deposited across the entire desired scaffold area prior to changing directions. This lead in length can be independently changed without altering the final scaffold architecture, and should be optimized to maximize deposition precision and minimize wasted material and fabrication time. Other parameters which are used in scaffold design include the pore size (p), the number of fiber stacks (s), and the number of pores (n) within a square scaffold structure. These values are illustrated in Figure 3.19.

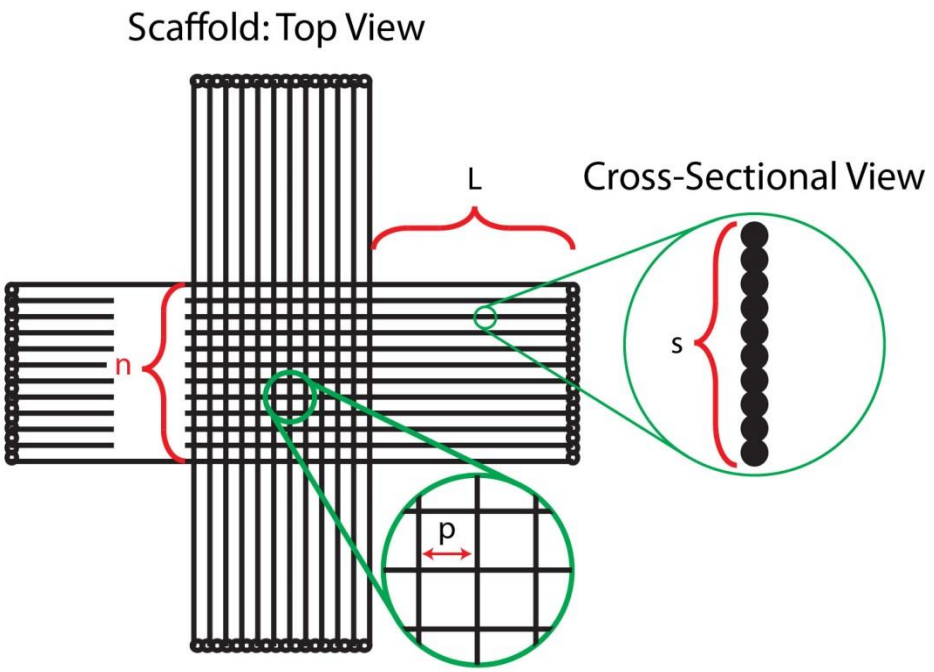

Figure 3.19. Design parameters for fabrication of fiber scaffold structures. A schematic diagram which illustrates the parameters used in designing fiber scaffolds with square pores. A square pore scaffold can have tunable pore size (p) which can be tessellated over the collection electrode to create n pores in either x or y dimension. A lead in length (L) is designed to enhance fiber deposition, and is optimized for the desired scaffold architecture. Repeating the scaffold pattern results in a honeycomb structured stacked fiber scaffold with s stacked fibers.

3.3.4 Fiber Patterning: Experimental Approach

3D scaffolds composed of polymer microfibers were created by: i) utilizing the secondary ring electrode described in section 3.3.1, ii) eliminating the liquid rope instability by increasing

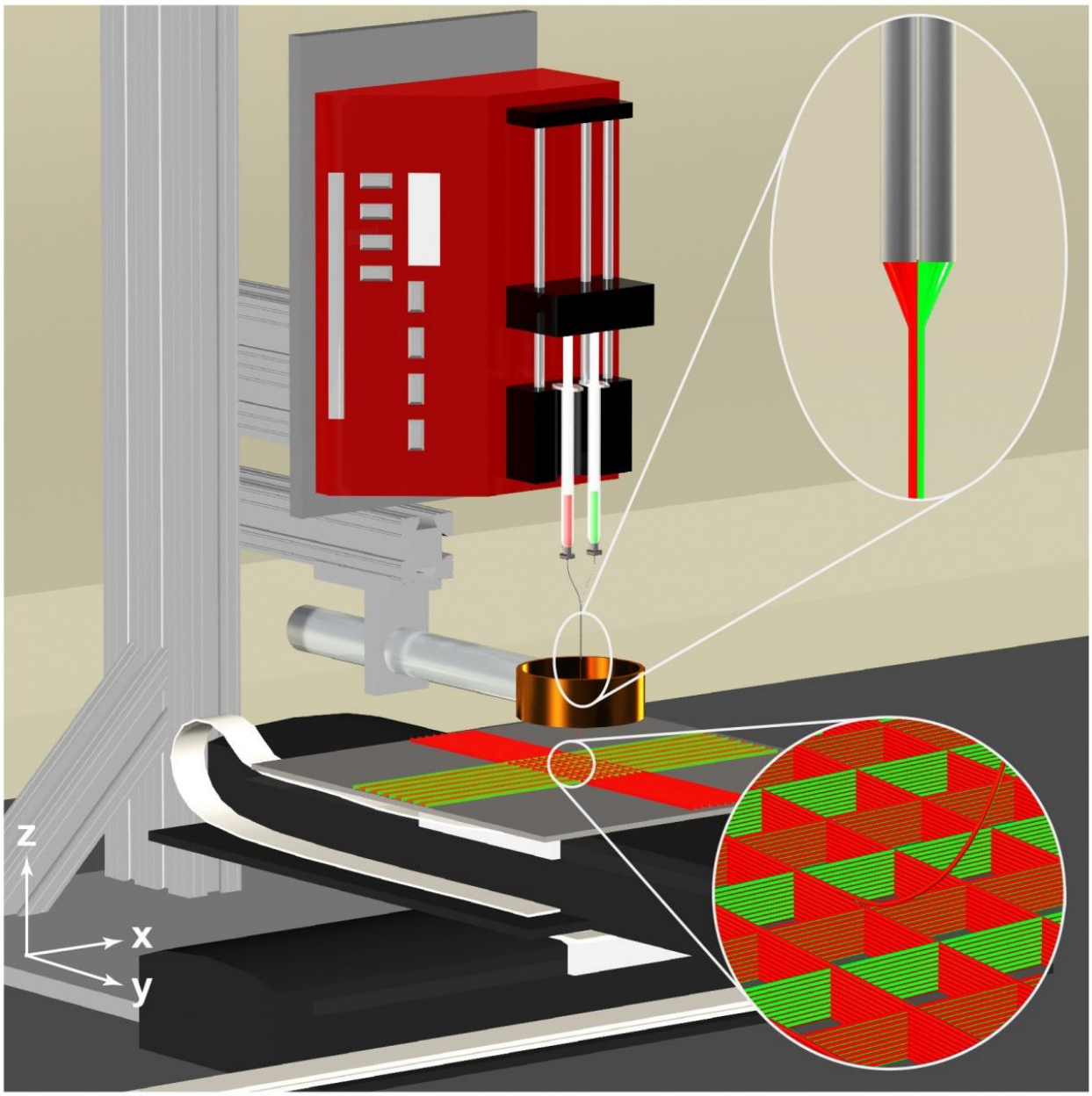

Figure 3.20. 3D jet writing experimental setup. Here, a schematic diagram which illustrates experimental setup of the 3D jet writing process is depicted. One or more syringes containing polymer solutions are mounted onto a syringe pump. A secondary ring electrode was placed between the tip of the needles and the grounded collection electrode to aid in jet stabilization. Programmed movement of the grounded collection plate was performed through an x-y motion platform. Separate high voltage power supplies were attached to the needles and the secondary ring electrode.

the collector speed as described in section 3.3.2, and iii) implementing the fiber patterning techniques described in section 3.3.3. Putting all of these elements together within an electrohydrodynamic (EHD) co-jetting experimental setup consisting of a syringe pump, one or more polymer solutions, and a grounded collection platform mounted to an x-y motion platform allowed for the fabrication of complex 3D scaffolds composed of polymer microfibers (Figure 3.20). This process was termed 3D jet writing.

The polymer solution used to create a majority of the fiber structures was composed of the polymer poly(lactic-*co*-glycolic) acid (PLGA) with a 85:15 ratio of L to G and molecular weight of 55k – 75k. Dissolution of PLGA in a dual-solvent system, composed of a 93:7 ratio of chloroform to N,N Dimethylformamide (DMF), created a 30 w/v% polymer solution which was used for fiber patterning. Pumping the solution at a flow rate of 40 – 50 µL/hr and applying a 16 kV electric potential to the needles, and a 9 kV electric potential to the ring electrode led to the development of a stable polymer fiber jet. Programming the grounded collection electrode to create a 14x14 square lattice, similar to that outlined in Figure 3.19, with a pore size of 500 µm, and lead in length of 12.5 mm, led to the structures depicted in Figure 3.21.

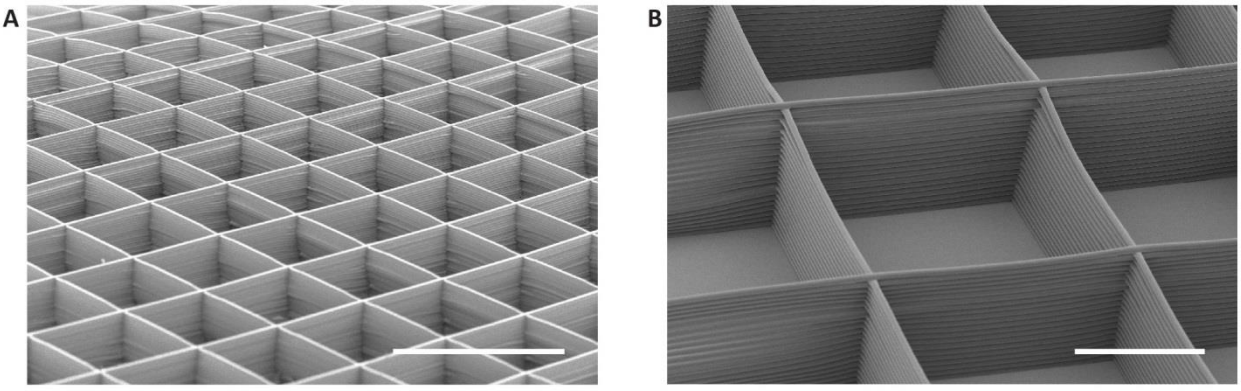

Figure 3.21. Square honeycomb structures composed of PLGA microfibers. Scanning electron microscopy (SEM) was used to characterize the resultant PLGA fiber structures. **A)** Square honeycomb structures, with 500 µm square pores, can be precisely fabricated across large areas, achieving heights in excess of 400 µm. **B)** The walls of each pore are composed of stacks of electrospun PLGA fibers interwoven with each other to create a macroscale fiber structure. Scale bars indicate 1 mm (A), and 400 µm (B).

These fiber structures are composed of interwoven polymer microfibers which are precisely stacked on top of one another to create a 3D porous scaffold. In programming the stage motions, it is important to start and stop the program at the same point, allowing for patterns to be repeated multiple times, with the number of repeats dictating the end height of the scaffold walls. The structures shown in Figure 3.21 consist of 25 (Figure 3.21 B) to 30 (Figure 3.21 A) fibers stacked on top of one another to create walls in excess of 400 µm in height. Higher stacks of polymer fibers are difficult to achieve due to buildup of charge which disrupts the electric field in the vicinity of the fiber stacks. In this example, repeating the square lattice pattern produced the square honeycomb shapes depicted in Figure 3.21, which was a 14x14 array of square prismatic pores. This fabrication process allows for the square pores to be tessellated across arbitrarily large planar surfaces, given that the motion platforms have the range of motion necessary. In Figure 3.22, the square lattice pattern was repeated to create a scaffold composed of 500 µm pores which were tessellated over a 5 x 5 cm area. These scaffolds retain a stiffness,

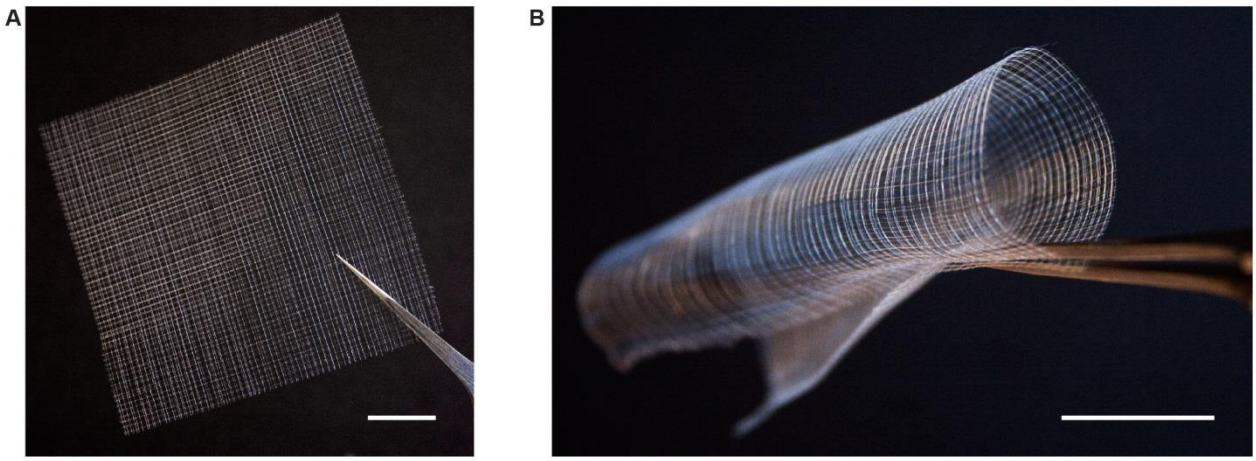

Figure 3.22. Scalable area coverage of tessellated cuboid pores. Digital photographs of the resultant PLGA fiber structures show the large area that the tessellated pore structures can be patterned over. **A)** A 5 x 5 cm scaffold composed of 500 µm square pores is large enough to be easily manipulated using tweezers, and can support its own weight. **B)** The large scaffold can be further manipulated into higher order structures, such as tubes, using tweezers. This demonstrates how robust the stacks of PLGA fibers are, as they remain intact even after such distortions. Scale bars indicate 1 cm.

which

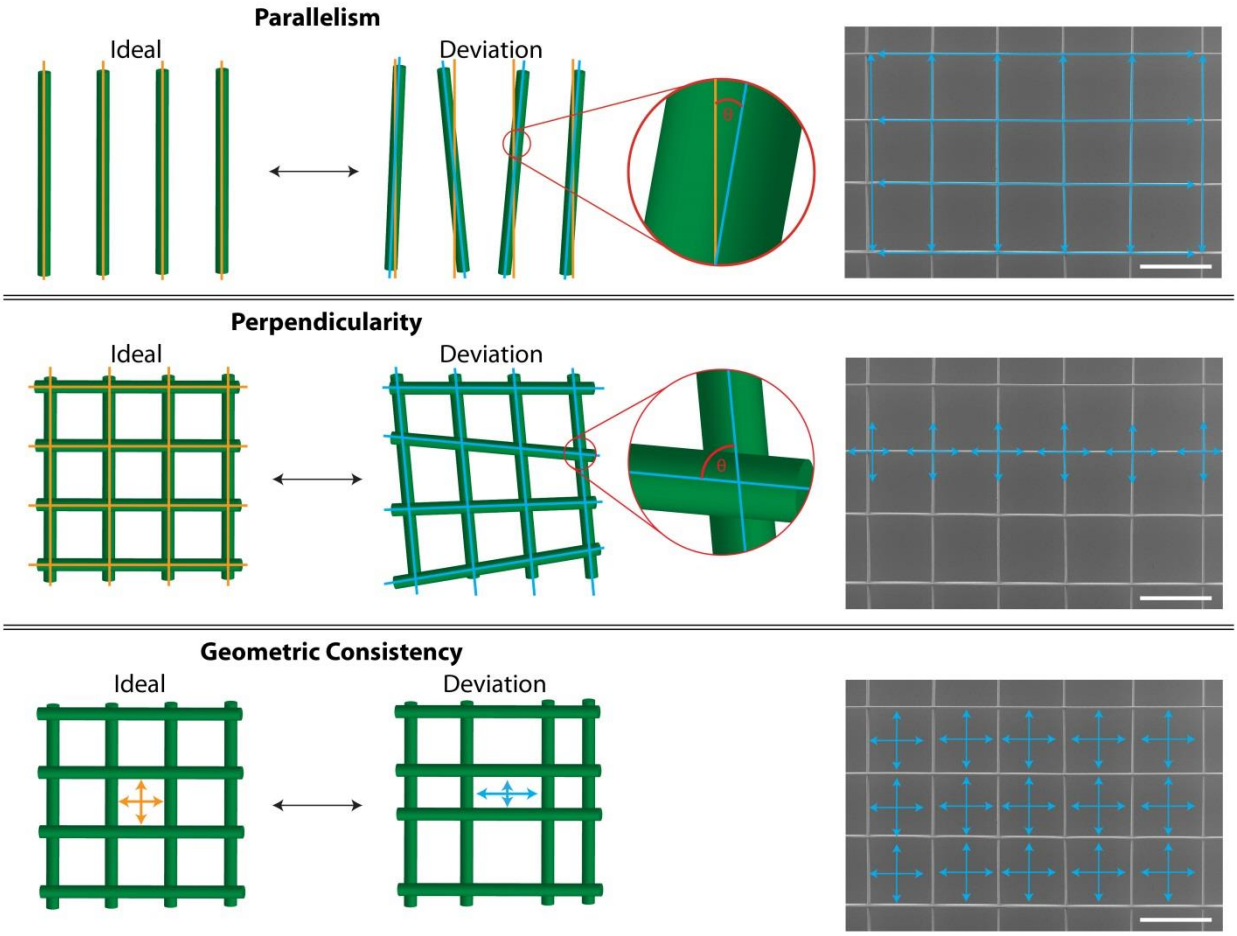

Figure 3.23. Example measurements used to determine fiber parallelism, perpendicularity, and geometric consistency. These three quantities were measured across three entire scaffolds using ImageJ analysis. Parallelism was used to describe how parallel fibers were relative to fibers running in the same direction. Perpendicularity describes how fibers running in opposite directions are oriented relative to one another. Geometric consistency is used as a measure of the regularity in the pore architectures achieved across the three scaffolds analyzed. On the SEM micrographs are examples of measurements taken in for each parameter. Scale bars indicate 500 μm.

allows them to support their own weight, while also having flexibility, allowing them to be deformed into higher order scaffold structures, such as tubes.

To fully characterize the precision at which the square honeycomb scaffolds were fabricated, three different parameters were measured: Parallelism, perpendicularity, and geometric consistency (Figure 3.23). Each of these parameters were measured across three entire

scaffold structures, composed of 500 µm square pores created by stacks of 10 fibers each, to give an idea to the precision capabilities that this fabrication process can achieve. The first parameter, parallelism, was determined by measuring the angle of each fiber section relative to the other fibers running in the same direction. Each fiber stack was measured in every scaffold, and was normalized relative to the average angle of deposition. The root mean squared error of the fiber stack angles from the average angle of deposition was determined to be the parallelism of the scaffold structures. In the case of the three fiber scaffolds measured (n=82 fiber stacks), the parallelism was 0.3 degrees, meaning that on average a fiber stack deviated from the average angle of deposition by 0.3 degrees.

Perpendicularity was the second parameter measured across the same three scaffolds. This differs from parallelism as this is a measure of how horizontal fiber segments are oriented relative to the vertical fiber segments. It is important to characterize this value as the fiber stacks could all be running parallel to one another in their respective directions, yet not be aligned perpendicular to each other (see Figure 3.23 perpendicularity deviation). For this reason, every intersection of two fiber stacks was measured to determine the angle at which they intersect with each other. Measuring every intersection across three scaffolds (n=560 intersections), a perpendicularity of 1.1 degrees was determined. The increased error in the perpendicularity compared to the parallelism can be attributed to minute alterations of the fiber angle when mounting the scaffold when preparing it for SEM analysis.

The final parameter which was characterized was termed the geometric consistency, or the deviation of the size of the pores. This value captures how precise the fiber stacks can be located within the x-y plane. While the fiber stacks could be perfectly parallel and perpendicular to each

other, the prismatic pore shapes could vary drastically across the honeycomb scaffold structure (Figure 3.23). Across each scaffold, the size of the rows and columns were measured and

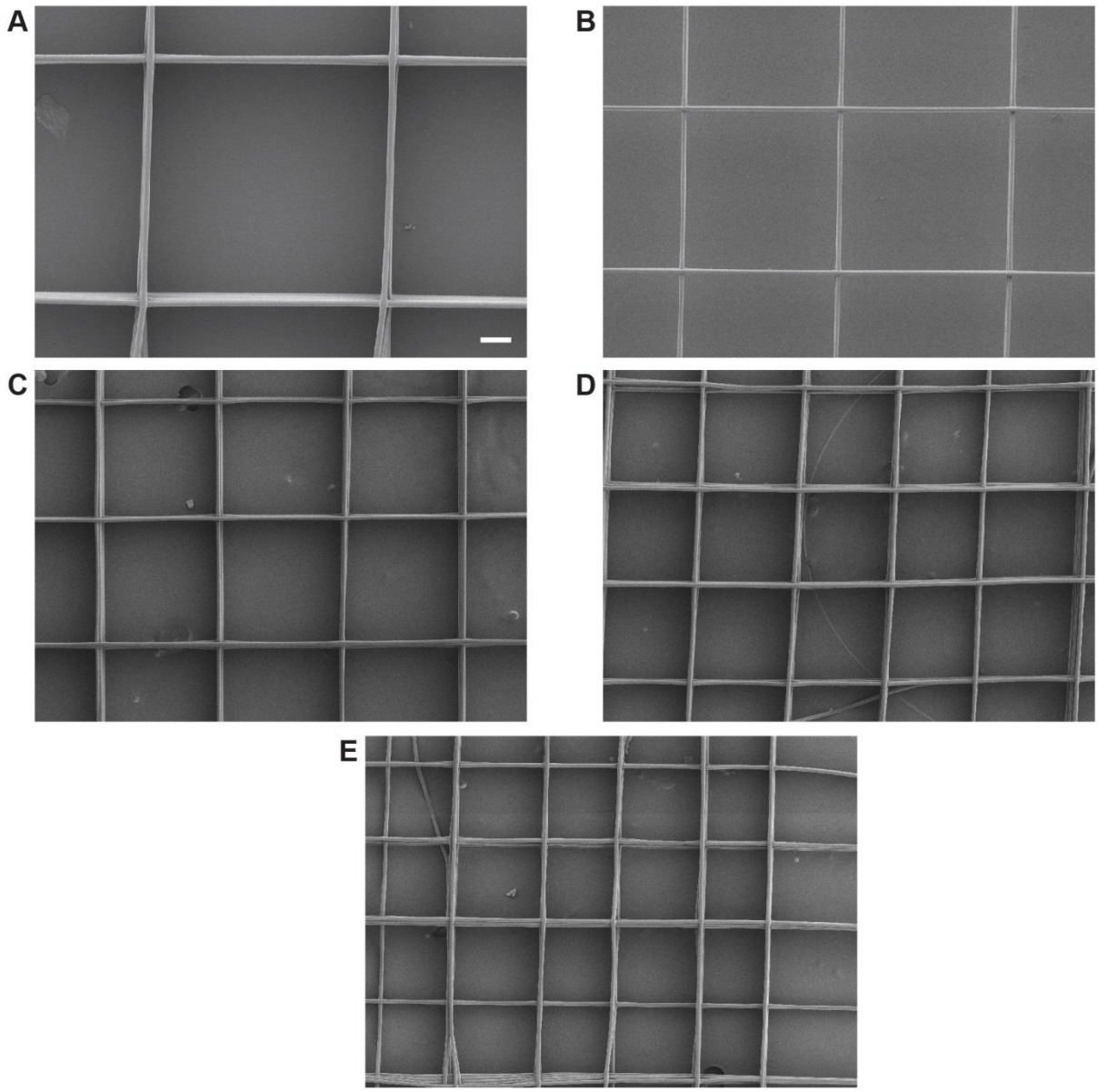

Figure 3.24. Controllable pore size scaffold from 3D jet writing. Scanning electron micrographs of scaffolds with the same pore shape, with differing pore size. These micrographs depict square honeycomb scaffold with pore sizes of 750 µm (A), 500 µm (B), 400 µm (C), 300 µm (D), and 250 µm (E). Each of the micrographs is at the same magnification, with the scale bar in (A) depicting 100 µm.

compared to one another (n=70 rows and columns). These measurements indicate that on average, a scaffold pore deviates from the intended pore dimension (in this case 500 µm) by

5.4%. With this level of precision, scaffolds can be fabricated with varying pore sizes, while maintaining the pore shape. Figure 3.24 depicts this concept, with a square honeycomb scaffold having square pores ranging from 750 µm down to 250 µm in size.

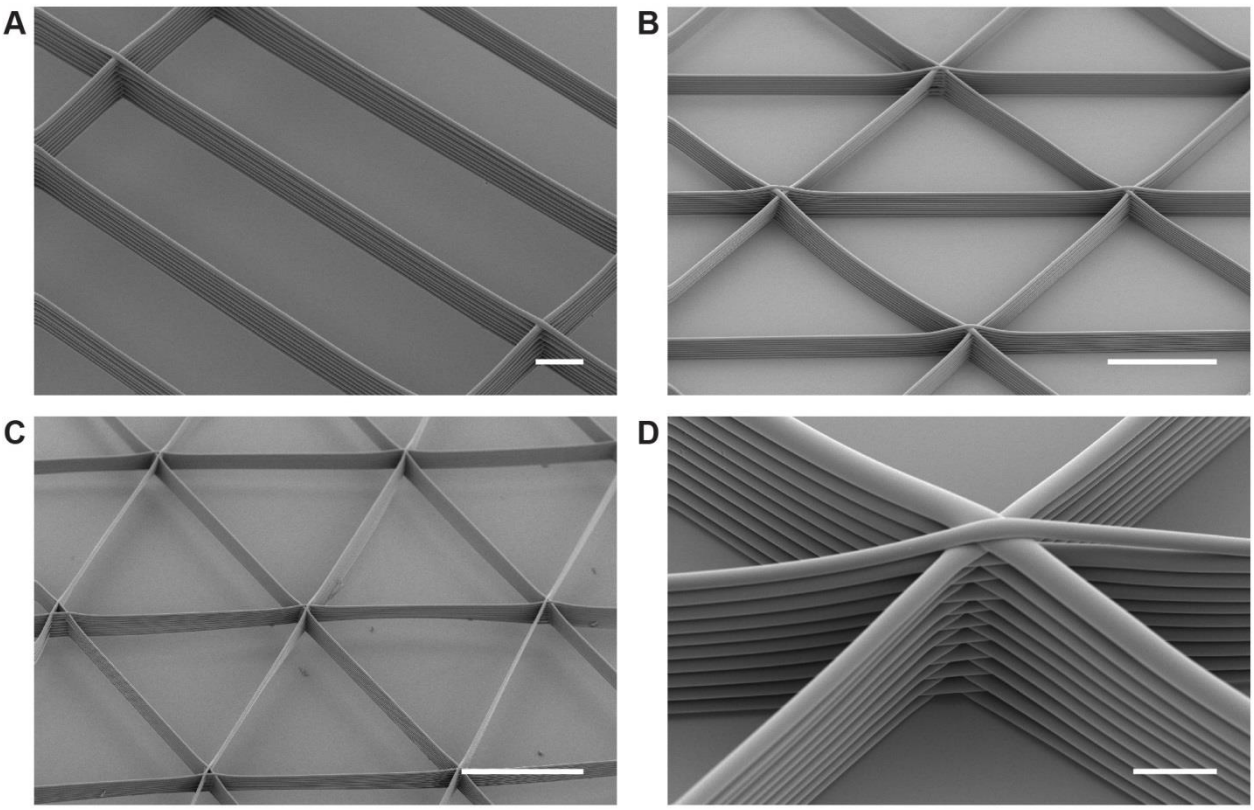

Figure 3.25. Tessellation of different pore geometries across a planar surface. A) Rectangular pores with an aspect ratio of 4:1 can be tessellated across the moving collection electrode in a similar manner as square pores. Rectangles of other aspect ratios are also feasible, but are not shown here. **B-C)** Regular arrays of isosceles (B) and equilateral (C) triangles can be used to illustrate the flexibility of the 3D jet writing system to create tessellated patterns with other types of geometries. Tessellations of triangular pores are also expected to have improved mechanical properties. **D)** A closer look at the intersection of three fiber stacks shows a perfect interweaving of the fibers with one another, further demonstrating the precision at which the fibers can be deposited. Scale bars indicate 100 µm (A), 350 µm (B), 500 µm (C), and 50 µm (D).

Besides square pores, other pore structures were also tessellated across large planar areas (Figure 3.25). Tessellation across a planar surface can be achieved with any repeating 4-sided geometries or 3 sided geometries, and also regular hexagons. Due to the method of fabricating

these structures with straight lines, different pore geometries consisting of three and four sided structures were fabricated using 3D jet writing. Changing the aspect ratio of the 1:1 square, rectangular pores, with a 4:1 aspect ratio were demonstrated; with the shortest segment being 300 μm. Alternatively, structures composed of tessellated triangular prism shaped pores can also be constructed, with both isosceles and equilateral triangles. It is presumed that these structures would all have different mechanical properties, as reported previously in literature on honeycomb structures.[115] Taking a closer look at the intersection of the fiber stacks in the tessellated triangular prism pores shows the precision at which the fiber stacks are placed relative to one another, with the fibers perfectly interweaving within one another at the intersection point.

With control over electric fields contributing to the deposition of straight lines of polymer fiber, similarly adjusting the fiber diameter can performed by adjusting the applied electric potential to both the needle and secondary ring electrode to change the fiber deposition speed. While holding the polymer solution flow rate constant, slowing down the speed of the depositing fiber jet results in fibers of increased fiber diameter. Conversely, if the deposition speed is increased, the resultant fiber diameter is decreased. These results can be seen in Figure 3.26 A-B, where fiber diameters ranging from 50 to 6 μm in diameter were achieved. This can be explained through a simple mass balance. At a constant volumetric flow rate, and varying deposition velocity, a theoretical fiber diameter can be calculated. The mass balance is given below:

$$V\varepsilon = \pi R^2 v \tag{3.2}$$

with V being the volumetric flow rate, ε being the ratio of polymer to solvent of the polymer solution, R being the solidified fiber radius, and v being the deposition velocity. Solving this equation for the value R and plotting it versus the velocity (keeping the volumetric flow rate constant) provides a predicted fiber radius for a given deposition velocity. The plot in Figure

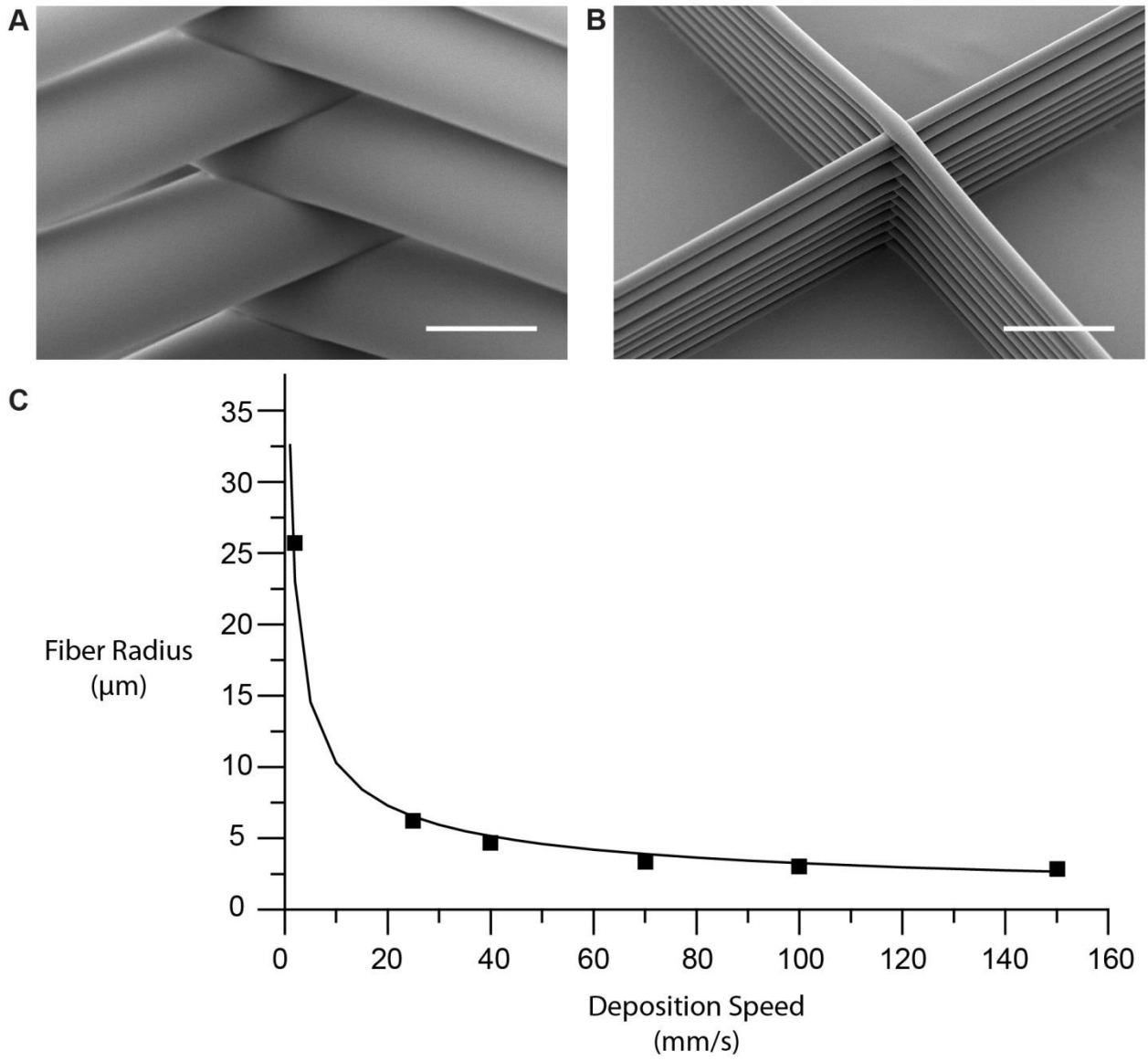

Figure 3.26. Controlling the fiber diameter through modulation of the deposition speed. A) PLGA fibers 50 μm in diameter were obtained by slowing down the depositing fiber jet to a speed of 2 mm/s. This was achieved through modulation of the electric field via the applied electric potential to the needle and secondary ring electrode. **B)** Using a similar technique, fibers with a diameter of 6 μm were achieved by increasing the fiber deposition speed to 100 mm/s. **C)** Comparing the theoretical fiber diameter calculated from the mass balance (line, Equation 3.2) to the fiber diameters measured experimentally (data points). The data points match closely to the predicted values, with error bars of measured fiber diameters being smaller than the data points on the plot. Scale bars indicate 50 μm.

3.26C shows the predicted value based on the mass balance (line) compared to the measured values obtained experimentally (data points). These data points show close agreement to the

theoretical values of fiber radius, indicating that controlling the deposition speed is a viable means of controlling the fiber diameter during the scaffold fabrication.

Beyond tessellation of regular tessellated prismatic pores, structures which contain non-repeating patterns can also be fabricated using 3D jet writing. Such structures can consist of similar pore structures which are similar to the honeycomb structures discussed previously. These structures can be composed of pores of various sizes and shapes, with combinations of shapes containing three or four sides. Within these non-regular structures, minimum pore resolutions approaching 100 µm can be attained (Figure 3.27).

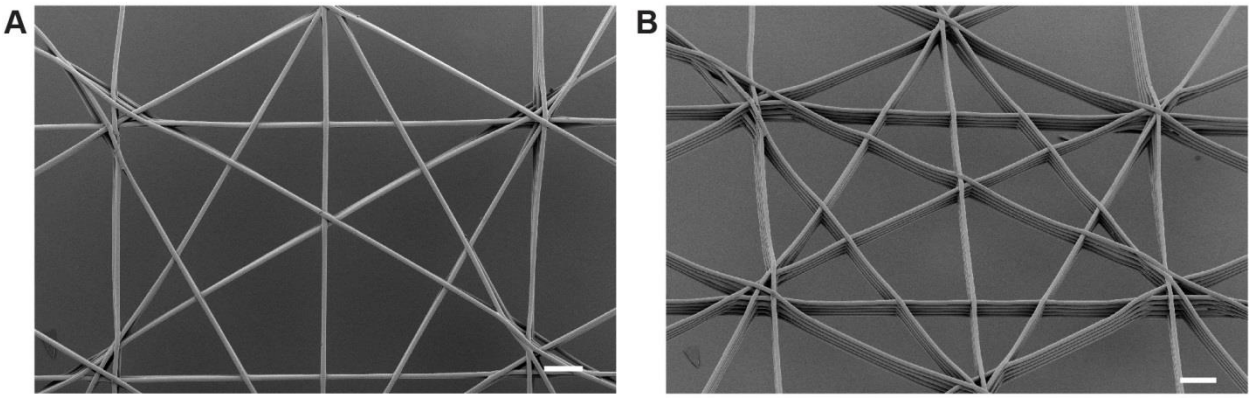

Figure 3.27. Non-regular pore structures created from straight fiber segments. A) A structure designed to be composed of three and four sided prismatic pores of varying size and shape was fabricated to demonstrate the range of capabilities of the 3D jet writing system. Pore architectures approaching 100 µm in size could be made using this technique. **B)** These structures are composed of stacked fibers, with this structure containing 5 fibers stacked on top of one another. Scale bars indicate 100 µm.

3.3.5 Curvilinear Fiber Structures

All of the previous structures described have been composed of an organized array of straight lines, but structures of arbitrary complexity can be fabricated using the 3D jet writing scaffold platform. However, it should be noted that objects composed of curved lines are inherently more difficult to fabricate. Difficulties arise as the speed of the fiber jet changes during processing, which causes the curved line segments to not line up exactly due to the lag in the fiber deposition. If the amount of lag time changes as the fiber structure is being made, the overall architecture will change. Lag time can also be altered by speeding up the collection electrode, which would have the same effect as slowing down the depositing fiber speed. Flower structures, which were modeled after the polar rose, were created from line segments using a MATLAB routine (Appendix D) and two synchronized COSMOS stages. Inputting different stage velocities into the MATLAB routine to get two codes to create flowers at two different speeds led to the structures in Figure 3.28. Here, a six petal polar rose was fabricated from the stage movements indicated in Figure 3.28 A. Despite there being pointed line segments in the stage movements, the resultant structures were composed entirely of curved fibers (Figure 3.28 B). This is due to the lag in fiber deposition described previously in this chapter. However, if the lag in the fiber jet is increased, by increasing the speed of the collection stage, a distinct difference in the flower structure is seen. There are much tighter twists in the flower petals, and a large open area in the middle of the flower appears. A similar phenomenon occurs when a nine-petal flower structure is made. The stage movements necessary to create a polar rose with nine petals required the use of more line segments. Still no sharp edges are seen in the resulting fiber structures. Increasing the stage speed produces flower petals with tighter turns and an open area in the middle opens up (Figure 3.28 D-F).

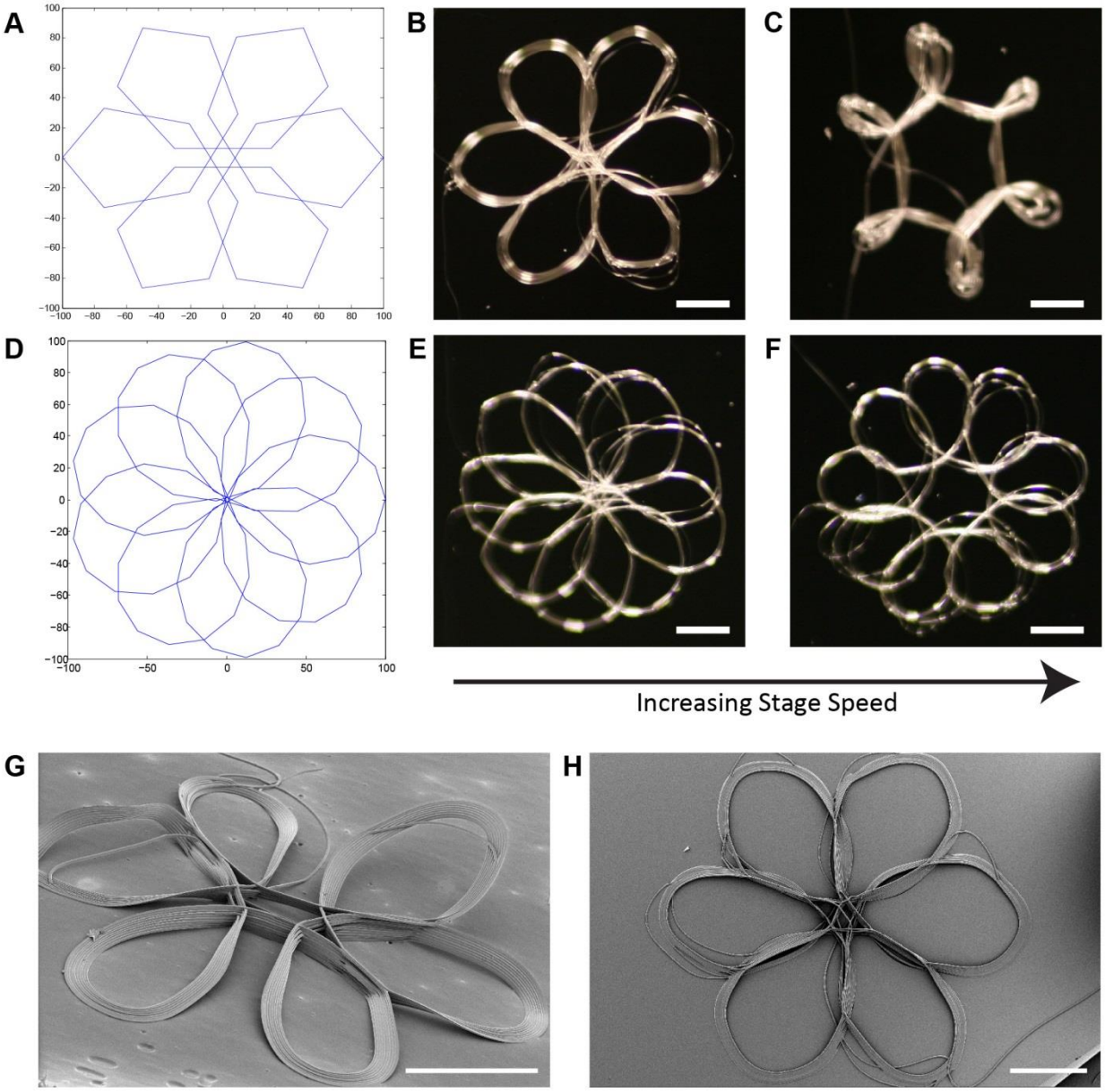

Figure 3.28. Curvilinear structures fabricated via 3D jet writing. A) A MATLAB routine was utilized to produce a code to control the collection electrode. The route taken by the stage is outlined by the plot depicted. **B)** The resultant polar rose structure produced by the code in (A) when the jet speed was approximately equal to the collection electrode speed. **C)** The resultant polar rose structure produced when the jet speed was significantly slower than the collection electrode speed. **D)** A depiction of the path taken by the grounded collection electrode to create a nine petal polar rose. The path was generated via a MATLAB routine. **E)** The resultant nine petal polar rose structure produced by the code in (D) when the jet speed was approximately equal to the collection electrode speed. **F)** The resultant polar rose structure produced when the jet speed was significantly slower than the collection electrode speed. **G)** Scanning electron micrograph of a six petal polar rose structure fabricated with a collection electrode speed significantly greater than the fiber deposition speed. **H)** Scanning electron micrograph of the same six petal polar rose structure when the collection electrode speed was approximately equal to the depositing fiber jet speed. Scale bars indicate 1 mm.

Taking a closer look at the six petal flowers using SEM, the detailed microstructure of the flowers can be revealed. While the digital micrographs depict a 3D flower shaped object in Figure 3.28 B, the SEM images show that the flower petals are flattened than they appeared. While the middle of the flower structure retains its 3D vertical walls, the fibers which compose the petals seem to stack on the inner surface of the curves. Because of this, the fibers were not stacked directly on top of one another, but instead at a diagonal angle, giving them a flattened structure. At a higher collector speed (Figure 3.28G), the tighter curvature of the petals results in a better 3D architecture. However, their overall appearance is similar to those made at the slower stage speeds.

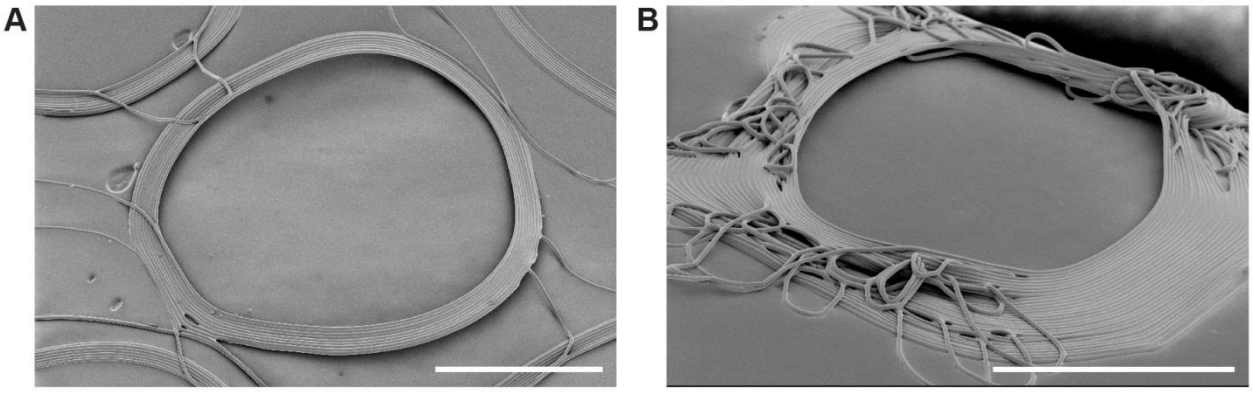

Figure 3.29. Circular ring structures fabricated via 3D jet writing. A) Scanning electron micrographs of a ring structure made via 3D jet writing containing ten fiber stacks. These rings formed flat annular ring shapes as opposed to circular vertical walls. **B)** When 40 fiber stacks are implemented, the stacking gets more difficult due to the accumulation of charged fibers. This results in buckles in the fiber deposition, which seem to occur at regular intervals around the fiber ring structure. Scale bars indicate 1 mm.

Other types of curvilinear structures created using 3D jet writing include annular rings. These rings were able to be arrayed across the collection plate, and similar to the polar rose structures the annular rings produced were flat. Rings fabricated with 10 fiber stacks could be created with few defects, and the fibers tend to spiral inward instead of depositing directly on top of the previous fiber (Figure 3.29 A). Increasing the number of fiber stacks to 40 results

enhanced local charge from the electrospun fibers, resulting in more fiber buckling (Figure 3.29 B).

Finally, structures representing more complex shapes were constructed through programming a series of line segments through MATLAB (Appendix D). These types of structures include everything from Pacman figures, to letters and words. However, similar to scaffolding and other curvilinear structures, difficulties in obtaining perfect fiber stacking can arise due to slight variations in the speed of the depositing fiber jet. As the jet speed deviates, the arc that the fiber takes changes, resulting in poor stacking. Nevertheless, these structures can be fabricated, and examples of which are depicted in Figure 3.30.

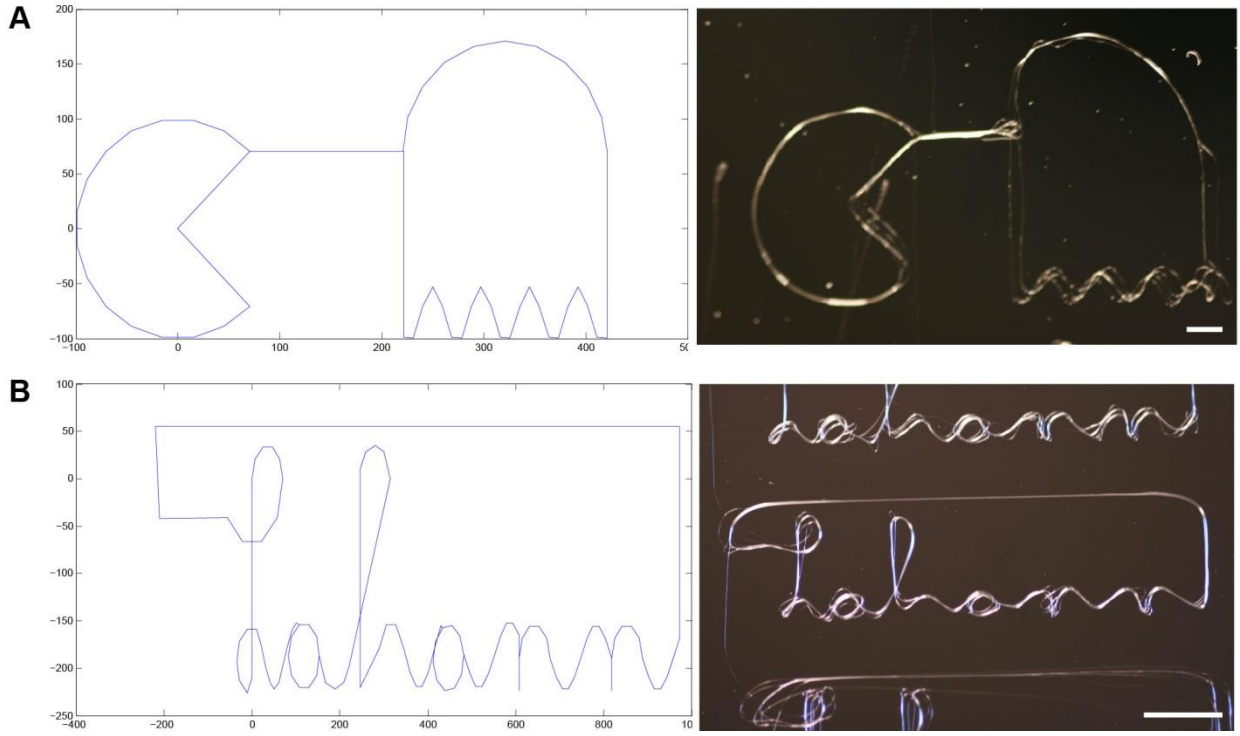

Figure 3.30. Other curvilinear fiber structures. A) A Pacman structure showing a Pacman chasing a ghost highlights the difficulties in creating precise sharp corners, and repeating movements over curves. Slight changes in jet speeds results in poor stacking in the curved and cornered regions. **B)** Letters created from line segments were created in MATLAB to write a name out of electrospun fibers. Similar deviations in curved line segments are observed. Scale bars indicate 1 mm (A), and 5 mm (B)

3.3.6 Non-stacked Fiber Structures

In previous sections, stacked fiber structures were fabricated by repeated movements of a collection electrode on a computer controlled stage. However, fabrication of non-stacked fiber structures proved to be difficult. Therefore, a closer examination of the fiber stacking mechanism was required to further elucidate the factors that dictate fiber stacking. Electrostatic simulations of the electric field around stacks of polymer fibers were performed for multiple cases (Figure 3.31). Placing stacks of fibers at varying distances away from each other demonstrated that at distances less than 300 µm the electric field lines exclusively bend in towards the stacks of

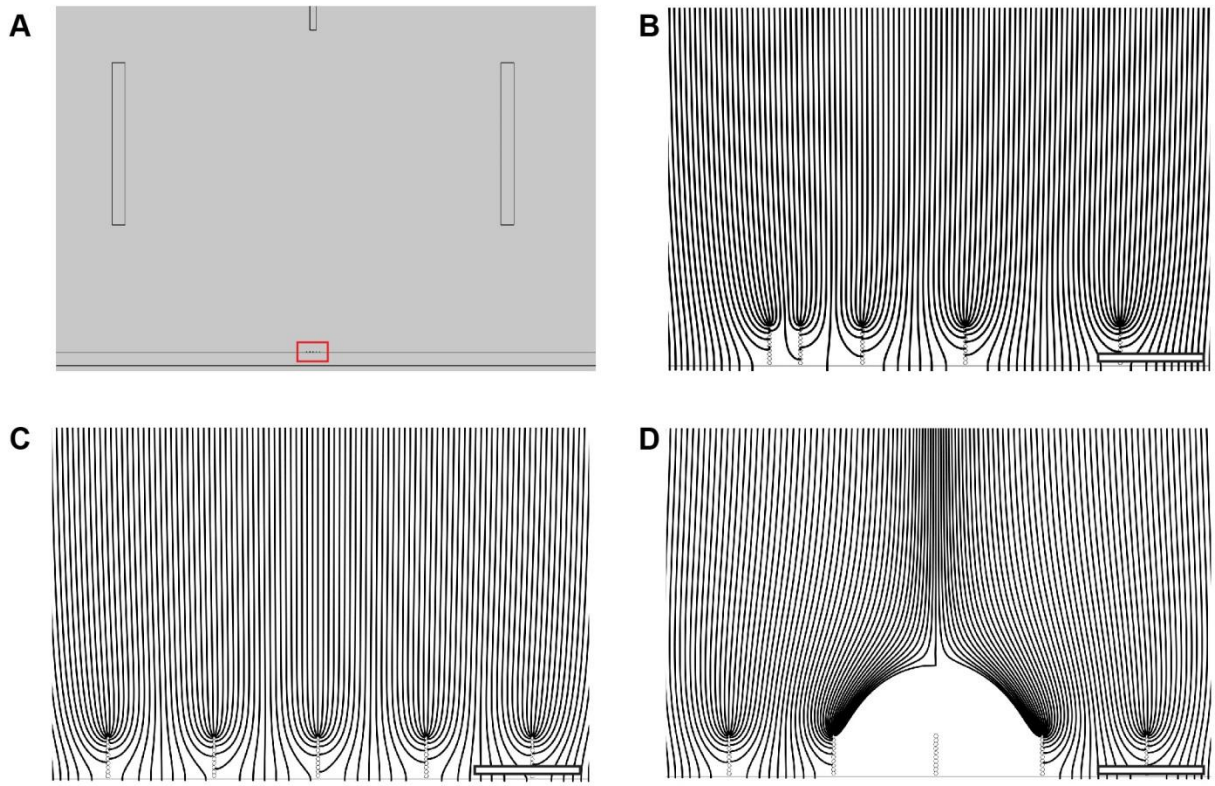

Figure 3.31. Electric field streamlines around fiber stacks to explain fiber stacking behavior. A) The overall setup of the COMSOL simulation, which includes a needle, a secondary ring electrode, grounded collection electrode, and five fiber stacks. **B)** Altering the fiber spacings from 150 µm, 300 µm, 500 µm, and 750 µm from left to right. The streamlines are bent towards the fibers, illustrating why smaller pore structures are difficult to fabricate. **C)** If the top fiber of the fiber stacks are discharged completely, the electric field streamlines are bent in towards the fiber stacks making stacking the preferred mode of fiber deposition. **D)** When the top fiber is charged (1000 V), a repulsive electric field is present making non-stacking the preferred means of deposition. Scale bars indicate 500 µm.

polymer fibers. As the distance between stacks increases, the bending in of the electric field streamlines still occurs, but the spaces between the fibers where the electric field remains relatively unaffected grows larger (Figure 3.31 B). Bending of the electric field towards the fiber stacks suggests that forces favoring fiber stacking are encountered if the depositing fiber is within approximately 150 μm of a discharged fiber stack.

Alteration of the electric field in this way occurs if the top fiber is able to discharge to the grounded electrode. This further explains why a maximum number of stacks exists before the stacking deviates from the desired deposition location. As the fiber stacks grow taller, the depositing fiber is further away from the grounded electrode, making it more difficult for the fiber to discharge to the grounded surface. Therefore, the charge on the deposited fiber persists for longer times, causing a repelling force which forces the fibers to deposit away from the centerline of the fiber structure (Figure 3.31 D).

To test this hypothesis, an insulating nylon membrane was placed over the grounded collection electrode to prevent the fibers from discharging. Patterned collector movements were designed to shift by half of a square pore spacing in both the x and y direction after each stack. This was intended to result in a pseudo-woven structure which consists of fibers which do not stack on top of each other (Figure 3.32 A). The same stage movements were performed with both a standard grounded collection electrode and containing an insulating nylon membrane. Scanning electron microscopy of these two trials indicated that with no insulating layer, the fibers are pulled towards the grounded collector and stack on top of one another (Figure 3.32 B-D). In the presence of an insulating layer, there was considerably less fiber stacking, and the fibers tended to remain suspended between the fiber stack (Figure 3.32 E-G). These results suggest that fiber discharging is an important phenomenon involved in the fabrication of fiber scaffolds.

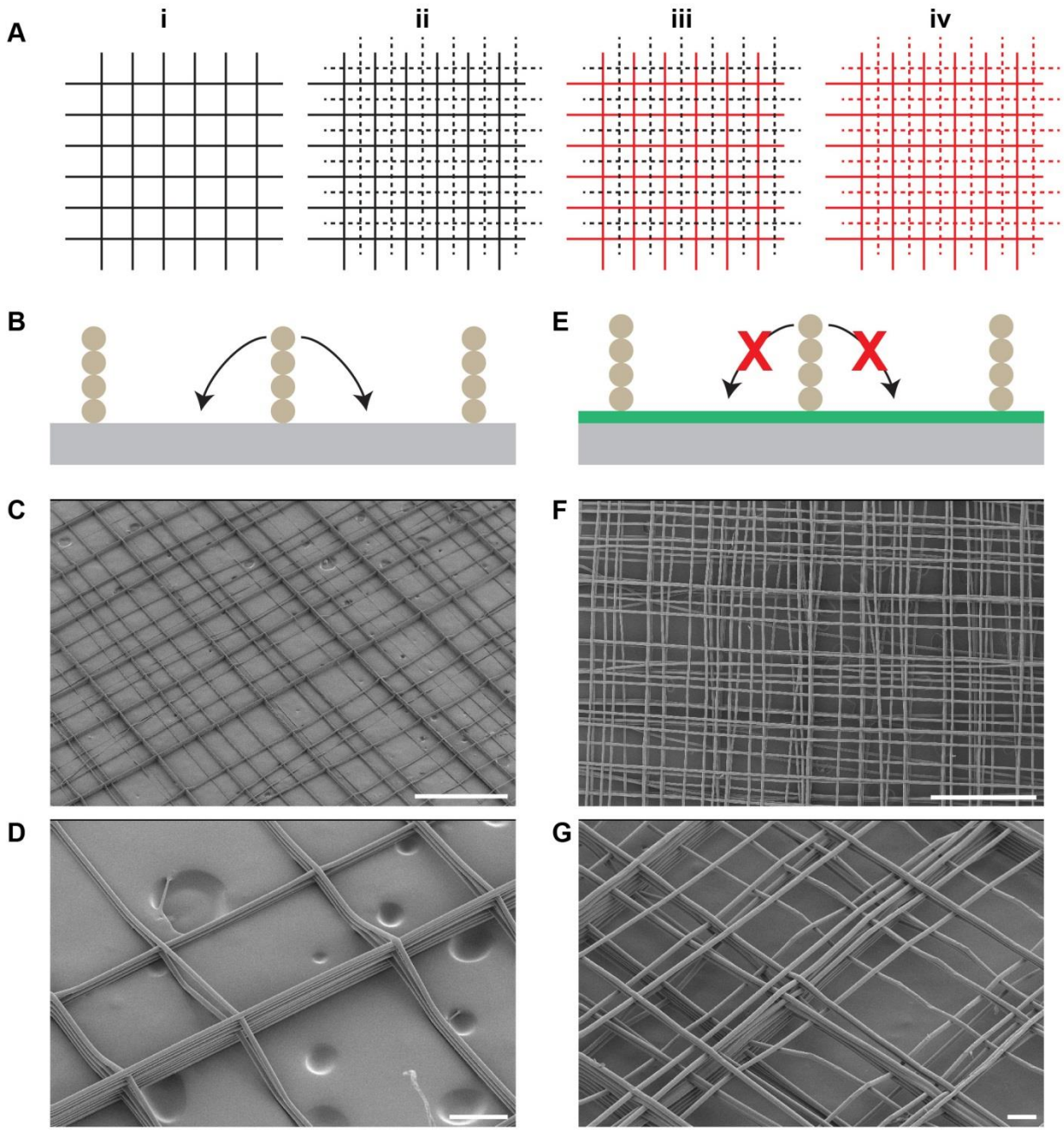

Figure 3.32. Pseudo-woven fiber structures fabricated with and without an insulating layer over the grounded electrode. A) A schematic illustration of the programmed stage movements to create a pseudo-woven structure. i) The first layer is written, ii) the second layer is shifted by half a square in both directions, iii) repeating the first layer, iv) repeating the second layer. **B)** The top fiber is able to discharge when there is no insulating layer is present. **C-D)** This results in a fiber structure where the fibers get pulled down towards to grounded electrode and form stacks of fibers. **E)** The top fiber is unable to discharge when there is an insulating layer over the grounded electrode. **F-G)** This results in a fiber structure with significantly less fiber stacking, and fibers suspended above the collection electrode. Scale bars indicate 1 mm (C,F), and 100 μm (D,G)

3.3.7 Three-Dimensional Multicompartmental Fiber Structures

Precise placement of the fibers provides a method for architectural control of the scaffold, but the physical and chemical properties are defined by the chemical composition of the fiber. In many applications, such as regenerative medicine, the architecture alone is not sufficient to guide cellular functions such as differentiation or spatially guided cell growth. In these cases, 3D spatiotemporal control over ligand presentation may provide the necessary effects for achieving these goals. Previous work using fibers made by EHD co-jetting demonstrates complex shape shifting and actuating, multi-modal drug delivery, and cell patterning in tissue engineering.[26, 29-34] Extension of these technologies into three-dimensional space using 3D jet writing brings the possibility of active scaffolding for sensors or cell culture, 3D patterning of cells, and precise location of surface chemistries which provide anisotropic signaling to cells. Characterization of the patterning of multicompartmental fiber domains within a 3D scaffold structure is necessary to determine the future applications of 3D jet writing scaffolds.

Fabrication of 3D jet writing scaffolds with two compartments initially allowed to for the observation of the fiber orientation within a scaffold structure. Introduction of a yellow or black optical dye into each compartment allowed for direct observation of the depositing fiber jet. It was seen that during the straight fiber segments of the scaffold the fiber remained a solid color. However, at the ends of each segment where the collection speed is slower, an alternating black to yellow was seen indicating the fiber was twisting (Figure 3.33 A). The twisting of the depositing fluid jet at the edges of the scaffold resulted in the deposition of a twisted fiber segment (Figure 3.33 B). It was hypothesized that depositing a straight fiber segment prior to the square scaffold would lead to a scaffold structure with aligned compartmental domains (Figure 3.33 C).

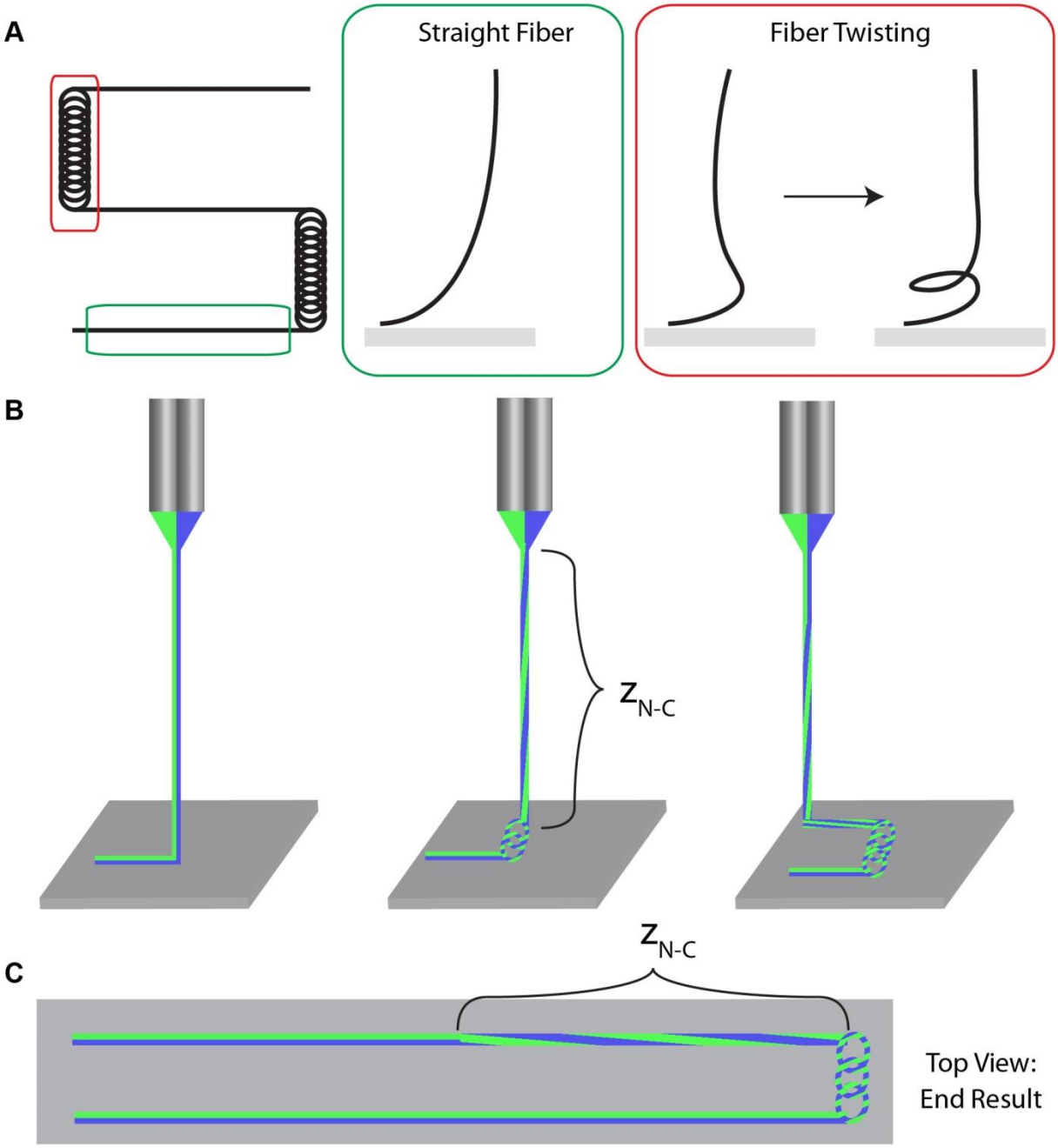

Figure 3.33. Schematic diagram of the origin of twisted fiber deposition. A) Straight fiber segments are deposited by moving the collection electrode at a speed greater than the fluid jet. At the ends of the scaffold segments, the slower speed leads to a buckling and twisting of the fiber jet up to the needle. **B)** A schematic depiction of the twisting up to the needle where the fiber is initially formed. **C)** Continuing along the next straight fiber segment halts the fiber twisting, and the twisted section of fiber, which is approximately the length from the needle to the collector, is deposited. After the twisted fiber segment, the fiber deposition regains the orientation determined by the needle configuration.

Testing this hypothesis was performed using fluorescent dyes and confocal laser scanning microscopy with two different lead in lengths (L from Figure 3.19) to the scaffold (Figure 3.34). If the lead in length of the scaffold is less than the needle to collector distance, a random fiber orientation was observed. This is due to the twisting of the fiber illustrated in Figure 3.33. When the fibers get twisted at the ends of the structure, the subsequent straight fiber is twisted for a set length before the aligned fiber segment gets deposited. When this process is repeatedly performed, creating multiple fiber stacks, the inconsistent rate of twisting yields fiber structures which contain compartments which are randomly oriented with respect to one another. If a lead in length which is longer than the needle to collector distance (Z_{N-C}), then the fiber section which gets twisted at the ends of the structure can be fully deposited prior to reaching the square pore

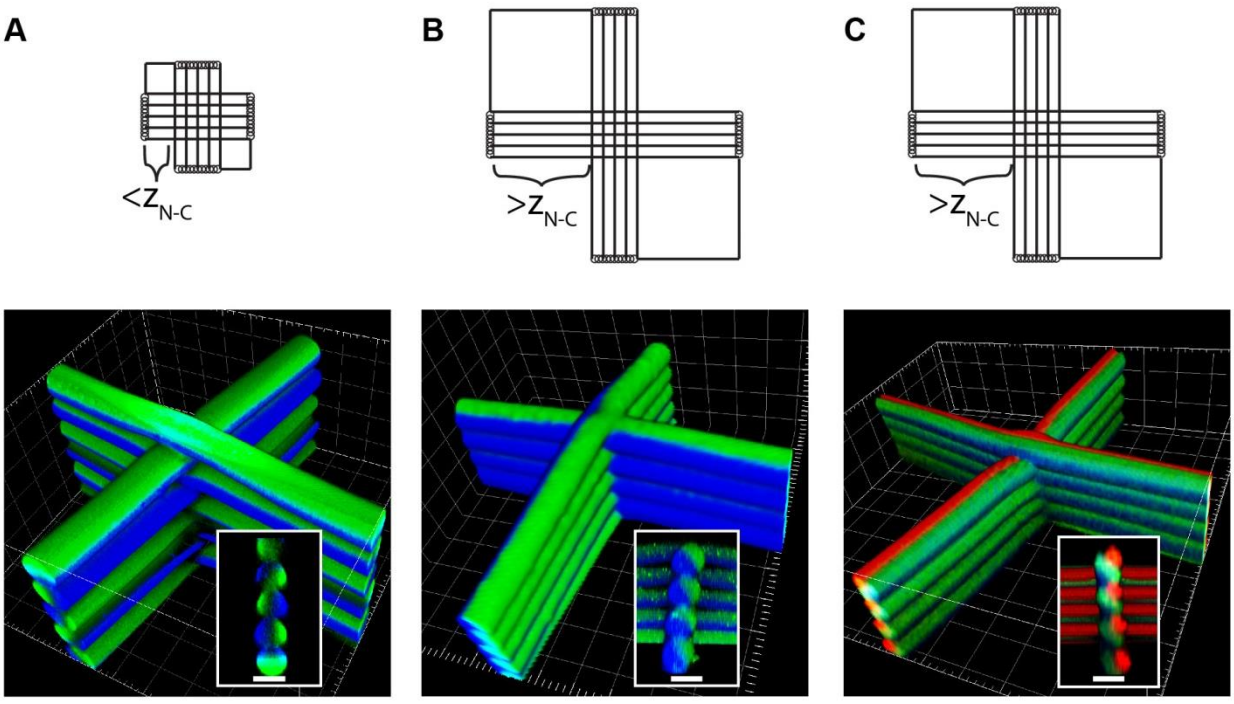

Figure 3.34. Resultant bicompartmental scaffold structures with different lead in length and compartments. A) A short lead in length in a scaffold with two compartments leads to a scaffold structure with randomly oriented fibers. **B)** A lead in length greater than the needle to collector distance produced scaffolds with uniformly aligned fiber compartments. **C)** Using the same lead in distance as in (B), also produces fiber scaffolds with three compartments aligned relative to one another. Square grids and scale bars represent 20 µm.

section of the scaffolding. Confocal imaging of these structures shows that the two compartments within the scaffold are well aligned relative to each other. Further expanding this to three compartments demonstrates this 3D jet writing not only controls where the fibers are place, but completely eliminates fiber twisting during the deposition of straight fiber segments.

These concepts are further illustrated through the incorporation of optical dyes in two different compartments. Creating an array of fiber stacks, with a yellow compartment on one side and black compartment on the other, leads to a structure which changes colors depending on the angle at which it is viewed (Figure 3.35). This color shifting effect is caused by the precision by which the fibers can be aligned relative to one another, and the compartment orientation is determined by the EHD co-jetting needle configuration. Zooming in on an individual fiber stack shows the degree to which the fibers within the stack are oriented relative to one another.

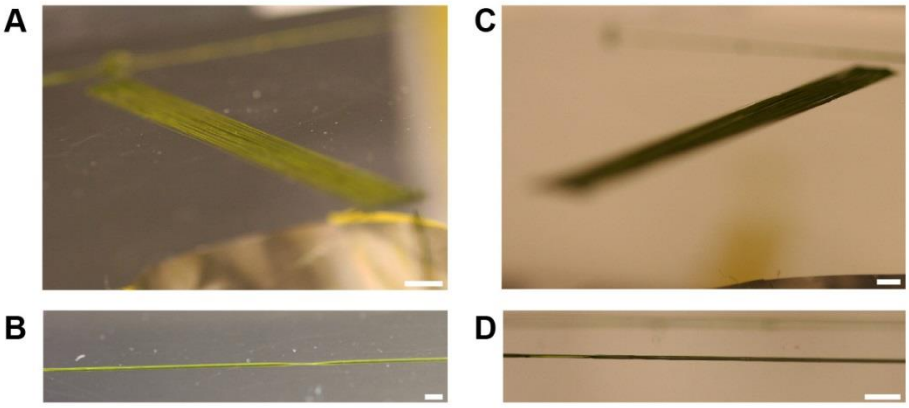

Figure 3.35. Color shifting structures fabricated using bicompartmental fibers with different optical dyes. **A)** An array of fiber stacks, each containing ten fibers, produces a yellow image when viewed from a specific angle. **B)** Looking at a single fiber stack, the compartmental alignment of the fibers within the stack is evident based on the yellow color observed. **C)** Viewing the fiber array from (A) at a different angle shows the fibers are now black. **D)** The fiber stacks in (B) when viewed from the opposite direction show the black color from the other compartment. Scale bars indicate 1 cm (A,C), and 2 mm (B,D)

Next, a specific surface chemistry was incorporated into one compartment of the polymer microfibers. Now, instead of the compartments simply having a different fluorescent signal, they will have a different specific functionality. Here, PEG immobilization was utilized, as previous literature has shown that PEG is non-fouling, and can prevent cell adhesion. Therefore,

patterning a PEG ligand onto the surface of an anisotropic fiber scaffold could be used to specifically pattern cells within the 3D scaffold construct. PEG immobilization was accomplished through the incorporation of an alkyne functional poly(lactic acid) (PLA-Alkyne). Incorporating 25 w/wPLGA% of the PLA-Alkyne into the 30 w/v% PLGA solution created a compartment within the scaffolding which had an alkyne functionality (Figure 3.36). Performing a Huisgen 1,3-Dipolar Cycloaddition to react a green fluorescent PEG-Azide to the alkyne functional surface provided a means of selectively modifying a single surface within the scaffold. Similar reactions have been utilized previously to selectively culture cells on the non-PEGylated domain of a polymer fiber to create biologically driven microactuators.[33]

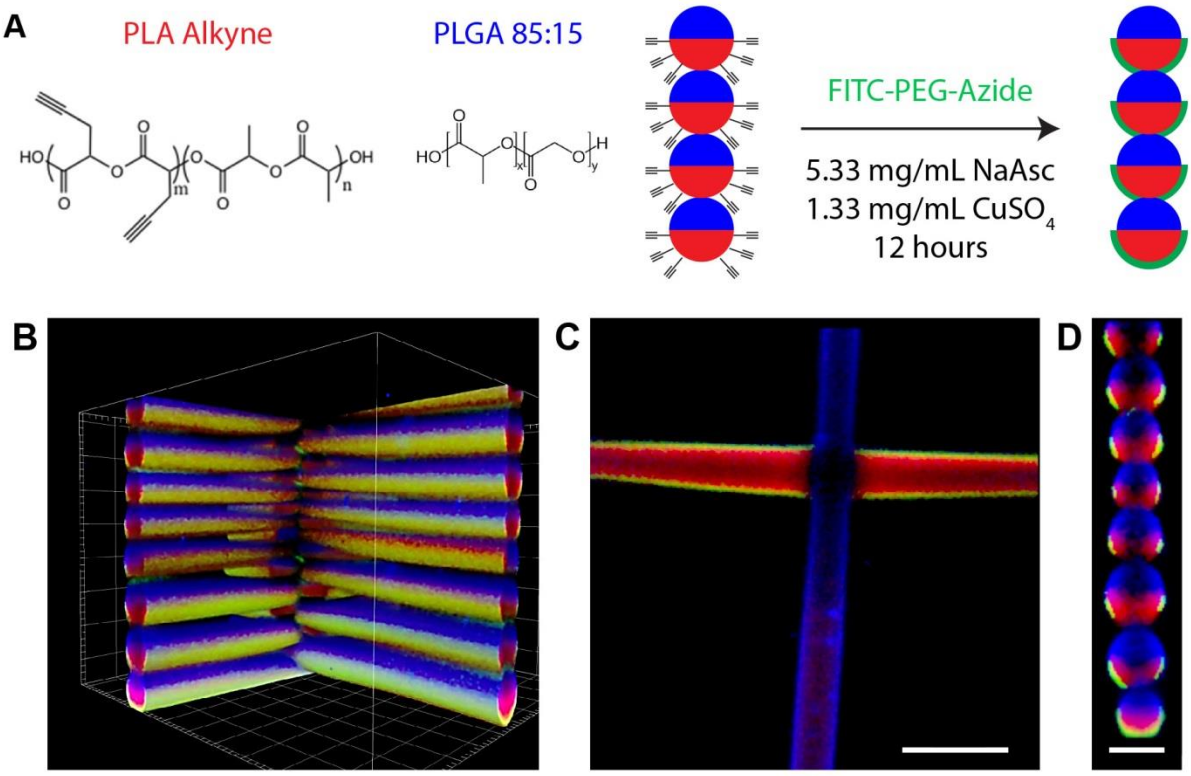

Figure 3.36. Spatioselective surface modification of 3D jet writing scaffolds. A) Incorporation of PLA-Alkyne into the red compartment of a 3D jet writing scaffold allows for specific immobilization of a green fluorescent PEG ligand to the red compartment of the fibers. **B-D)** CLSM imaging verified the green PEG was only located on the red surface of the fibers, with no green observed on the blue hemisphere of the fiber. 3D volumes (B), as well as x-y (C) and x-z (D) image planes depict the green PEG only on the red fiber domains. Grid spacings indicate 20 µm (B), scale bars indicate 50 µm (C), and 20 µm (D).

3.3.8 Post-Fabrication Modification

After initial fabrication of the polymer microfiber scaffolds, further modifications to the overall architecture can be made to create higher order structures. An example of such a modification is the creation of a tubular scaffold from what was initially a flat plane (Figure 3.37 A - C). Transforming the scaffold in this way can be accomplished generally by first deforming the scaffold into the desired geometry, then performing a heating and cooling cycle, followed by releasing the scaffold. Tubular scaffolds were fabricated by initially rolling a piece of aluminum foil tightly around a 26G needle. Unrolling the foil and placing an edge of the flat scaffold between the needle and pre-rolled foil holds the scaffold in place prior to performing the initial deformation. Securing the end of the foil after rolling the foil tightly around the needle holds the scaffold inside in a

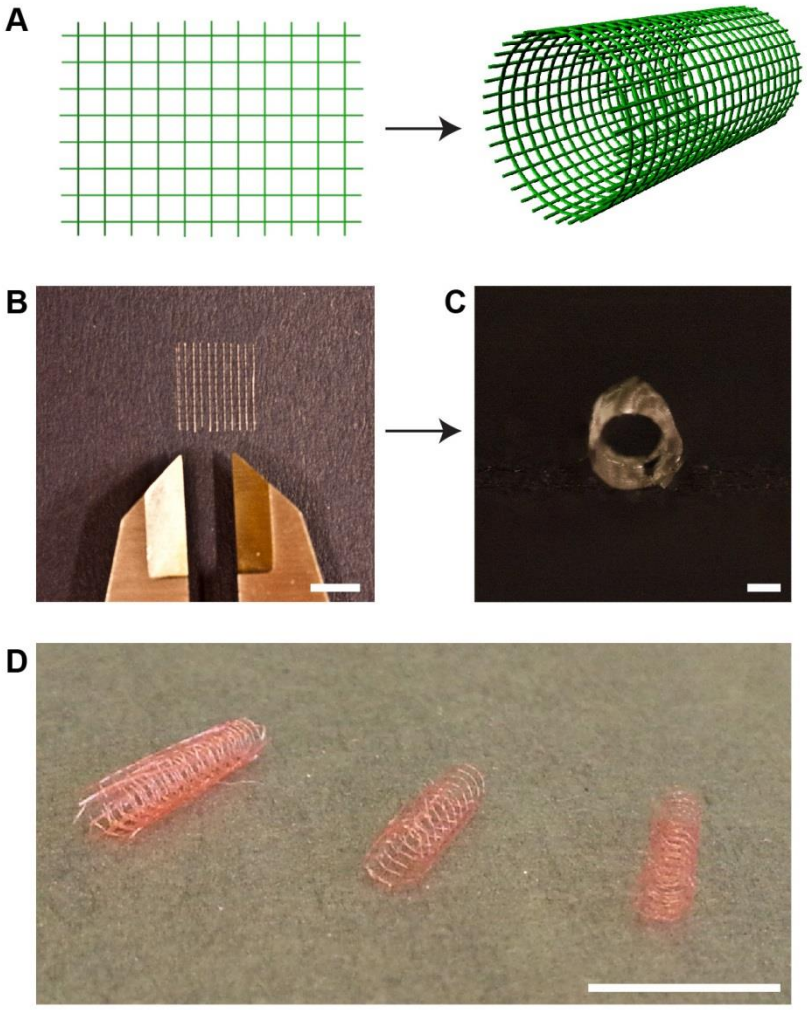

Figure 3.37. Fabrication of tubular shaped scaffolds. A) Modification of a flat scaffold into a tubular scaffold provides a higher order architecture to the scaffold structures. **B-C)** Heat cycling a flat scaffold (B),while it is deformed into a tubular geometry, creates a scaffold which maintains the deformed shape (C). **D)** Rolling long aspect ratio scaffold produces tubes with multiple layers. Scale bars indicate 5 mm (B), 1 mm (C), and 1 cm (D)

deformed state. Heating the roll in an 80 °C oven for 5 minutes softens the scaffold, and subsequently cooling in a liquid nitrogen bath locks it into its new configuration. Unrolling the foil reveals the newly formed tubular scaffold (Figure 3.37 C). Rolling longer scaffolds into tubes creates multi-layered tubes which give further strength and thickness to these tubes (Figure 3.37 D), which could be used as a vascular graft if pre-cultured with cells, or a biodegradable stent which can be loaded with drugs or other therapeutics.

A second post-fabrication modification of the 3D jet writing scaffolds involves the reduction of feature sizes using a heat treatment process. During the electrospinning process, the polymer coils in solution get rapidly stretched to form a slender fluid jet. As the diameter of the fluid jet reduces, the increased surface area allows for rapid evaporation of solvent, locking the polymer chains in an extended state. These fibers were patterned into 3D scaffold structures using 3D jet writing, so it was hypothesized that heating the structures would allow for the stretched polymer chains to relax causing the structures to shrink. A range of different methods were explored to effectively heat the scaffolds, as simply placing them on a hot surface caused them to stick. The first method was placing them on a Teflon surface in an 80 °C oven which led to the average feature size shrinking from 18% – 21%. While these results were promising, the scaffolds still seemed to be sticking to the Teflon surface, leading to the implementation of other methods which did not involve the scaffold sitting on a solid surface. Holding the corner of a scaffold with tweezers was found to have a

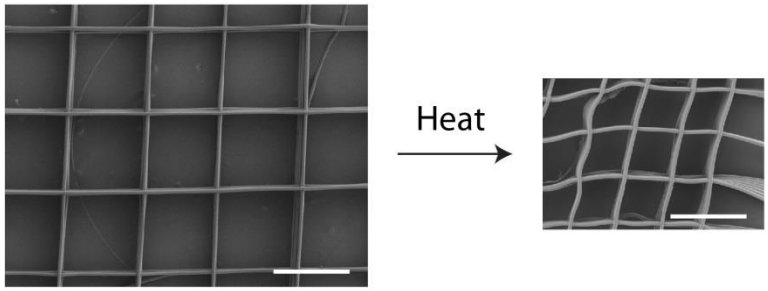

Figure 3.38. Shrinking scaffold features via heat treatment. Heating these scaffolds above their glass transition temperature in the right manner allows the extended polymer coils to relax, causing a reduction in feature sizes in excess of 40%. Scale bars indicate 300 µm.

reduction in size ranging from 40% to 42%, which was the most successful method (Figure 3.38). However, in doing this the scaffolds often deformed significantly, potentially limiting the applicability of this technique. To prevent the deformation of the scaffolds during shrinking, a method which involved placing scaffolds on the surface of 80 °C was examined. This led to scaffolds which retained their shape better than holding the scaffolds with tweezers, but the size reduction was not as great (around 33%). Using the water floating method on square scaffolds consisting of only two 500 μm square pores led to an average size reduction of 47% ± 4%. Size reduction was calculated two different ways, both yielding the same results. First, Photoshop was utilized to calculate the number of pixels within the two square section of the scaffold both before and after shrinking. The ratio of these areas was then used to approximate the shrinkage seen in each direction, assuming the shrinking was uniform in both directions. The second method was simply measuring the length and width of the two square scaffold before and after shrinking to determine both total area reduction and shrinkage in each dimension. Since both methods gave the same result, it shows that the shrinking of the scaffold is uniform in both directions, indicating both methods of measurement are sufficient to determine total shrinkage of the scaffolds.

3.4 Conclusions

Over the last century, electrospinning of polymer solutions has been utilized to create non-woven mats of polymer fibers. Recently, a push to control the deposition of these fibers has led to aligned arrays or patterned non-woven mats of fibers, with no method capable of producing ordered 3D geometries.[67-79, 81-91] While melt electrospinning and near-field technologies have demonstrated some capabilities in this field, their general utility is limited by the processes used to generate such structures.[96, 97] Herein, the development of a fully customizable 3D jet writing system was described. Modeling of the electric fields from various secondary ring electrodes demonstrated how altering the electric field can affect the depositing fluid jet. This theoretical framework was tested by gradually changing the speed of the collection stage until a straight fiber segment was deposited. Analysis of the straight fiber segments show that utilizing a secondary ring electrode significantly reduces the wobbling motion seen in the fiber when no stabilizing electric field is produced. Next, a discussion on the strategies involved in creating 3D fiber structures illustrated the complexities and variables which are critical to creating well-ordered fiber structures. Implementation of these techniques led to the generation of 3D microfiber scaffolds which were generated using this technique. Due to the computer controlled collection platform, tessellated geometric patterns of arbitrary complexity could be produced with feature sizes on the order of 100 μm in size and fiber diameters being controllable from 50 μm down to 6 μm. Subsequent experiments showed that these structures are not necessarily limited to linear fiber segments, but curved fiber structures are also feasible, with structures of flowers, letters, and complex shapes all being demonstrated in this work. It was noted that a force seemed to act on the fibers which caused a preferential disposition to stacking as opposed to not stacking. This was explained by the alteration of the electric field from the raised fiber

elements near the grounded electrode. Discharging of the fibers was shown to be an important mechanism for stacking to occur by placing an insulating nylon membrane on top of the grounded collection electrode. Depositing fibers on top of this membrane led to disrupted fiber stacking, which was utilized to create pseudo-woven fiber structures. Incorporation of multiple compartmental domains into the fibers provided a means of observing the twisting motion of the depositing fiber jet. Confocal microscopy confirmed that the twisting was occurring in structures which had a lead in length which was less than the needle to collector distance. Creating a longer lead in length led to a structure which had aligned compartmental domains; this was done with both two and three compartmental structures. This type of technology allowed for 3D spatial patterning of ligands, such as PEG, onto specific compartmental domains of the scaffold. Finally, post fabrication modification of the scaffolds allowed for both the shrinking of feature sizes in excess of 40% during heat treatment, and also to the fabrication of higher order structures such as tubes.

Overall, this work represents a leap forward in the field of electrospinning techlologies, providing capabilities far beyond any other solution electrospinning technology. 3D jet writing has opened up the possibility of

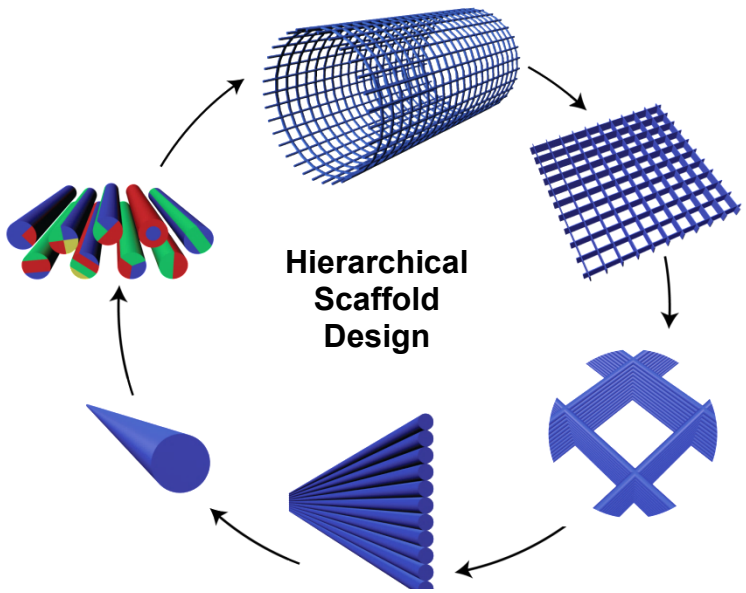

Figure 3.39. Hierarchical scaffold design. The 3D structures (tube) is composed of flat honeycomb structures which consist of tessellated pores. Each pore is fabricated by arranging polymer fiber walls which are made up of individual polymer fibers. Each polymer fiber can contain multiple distinct domains which then impart specific function to the overall scaffold.

creating fiber structures with six hierarchical levels (Figure 3.39): (1) the 3D structure of the scaffold, (2) the macroscale size and shape of the structure, (3) the arrangement of the fiber stacks to create pores of different size and shape (4) the fiber stacks and how the fiber compartments are oriented with respect to one another (5) the individual fibers within a stack and their diameter and (6) the compartments within the fiber which impart a specific function to independent fiber domains. Similar hierarchical levels are seen in natural systems ranging from plant stems[116] to bones[117, 118], which generally consist of: 1) assembly of the tissue structure, 2) tissue structure, 3) microstructure, 4) ultrastructure, and 5) biochemical composition. In subsequent chapters, these 3D jet writing scaffolds will be used as a 3D cell culture platform and in tissue engineering applications.

Chapter 4

In Vitro Culture on Scaffolds

Some material from this chapter has been adapted with permission from the following source:

J.H. Jordahl, L. Villa-Diaz, P.H. Krebsbach, J. Lahann. "Engineered Human Stem Cell Microenvironments*" Current Stem Cell Reports* **2**, 73-84 (2016).

J.H. Jordahl, L. Solorio, H. Sun, S. Ramcharan, C.B. Teeple, H.R. Haley, K.J. Lee, T.W. Eyster, G.D. Luker, P.H. Krebsbach, J. Lahann. "3D Jet Writing: A novel route towards functional microtissues within tessellated 3D architectures" *In Preparation.*

4.1 Background

4.1.1 Overview

Culturing cells outside of the human body is inherently unnatural. Biologists have thus dedicated decades of research to learning what conditions most are conducive to culturing cells in vitro. This included the development of substrates which cells can adhere and proliferate on for extended periods of time. When polystyrene petri dishes were first implemented for cell culture, they were unable to sustain cell growth due to insufficient cell spreading on the

surface.[119, 120] Surface modification techniques, such as chemical treatments with sulfuric acid[119] or glow discharge,[120] were utilized to allow enhanced cell adhesion through imparting a negative surface charge of the polystyrene.[121] These surface modification technologies enabled fundamental studies of how cells interact with their environment, and specifically how the substrate affects cell behavior.[122] These surface modified plastics were some of the first man-made microenvironments produced with the sole purpose of culturing cells, and they paved the way to the tissue-culture plastic which is still the gold standard in cell-culture labs around the world today.

Tissue engineering has aimed at recreating functional tissues by culturing one or more types of human cells in a supporting scaffold material. Research towards this goal has utilized a wide range of biodegradable support materials of natural[123-125] and synthetic origin.[47, 126-128] However, interactions between cells and the scaffold surfaces can alter cell phenotypes[129-133] and thus must be minimized, while cell-cell interactions should be maximized. Spheroid cultures and cell sheets have been proposed as potential solutions. However, cell sheets are fundamentally limited to 2D culture,[134, 135] and cell spheroids are restricted to diameters of about 400 μm in size because of the limited diffusion of oxygen and nutrients.[136] In addition, these systems often lack the mechanical stability or versatility required for effective use in many tissue regeneration applications.[137] Fundamentally, controlling the growth of cells within a defined 3D pore structure could overcome many of the problems with these systems. Precise tailoring of the open pore architecture of a scaffold to control tissue thickness, minimize contact area with synthetic surfaces, and maximize open area for nutrient transport, would provide a 3D space ideal for microtissue growth. Honeycomb pore structures would provide maximal open pore volume, while minimizing the surface area of material exposed to the cells and maintaining structural

support. [115, 138, 139] Tessellation of these pores across arbitrary length scales would therefore provide a means for producing macroscale arrangements of microtissues which could be utilized in regenerative medicine and as diseased tissue models.

4.1.2 Tissue Engineering Scaffolds

Tissue engineering is a rapidly developing field of study which aims to restore or regenerate functions to a tissue that is damaged or deficient.[140-142] Successful implementation of an engineered tissue would result in transplantations that have minimal chance of rejection, enhanced recovery times, and may provide treatments for otherwise untreatable conditions. Biological tissues are inherently complex, which makes it difficult to accurately mimic the structure, and in turn function, using an artificially engineered tissue.[108, 143] This is one of the major challenges which faces the field of tissue engineering today, to create artificial tissues with comparable complexity to natural biological tissues.[108, 144]

Many considerations need to be taken into account when developing a tissue engineering scaffold (Figure 4.1) including, but not limited to, degradability, biocompatibility, ability to incorporate biofactors, scaffold surface chemistry, pore architecture, easy manipulation, and mechanical properties.[128, 145] One particularly important aspect is enhancing cell-cell and cell-extracellular matrix interactions and minimizing cell-artificial substrate interactions which play a critical role in determining cell phenotype.[126, 129-132] Tissue engineering scaffolds are designed to support and guide cell adhesion, growth, and proliferation while also allowing for proper nutrient diffusion and eventual degradation once the tissue has been regenerated. Some of the most common methods of forming 3D tissue engineering constructs are phase separation techniques, solid freeform fabrication, and electrospinning.

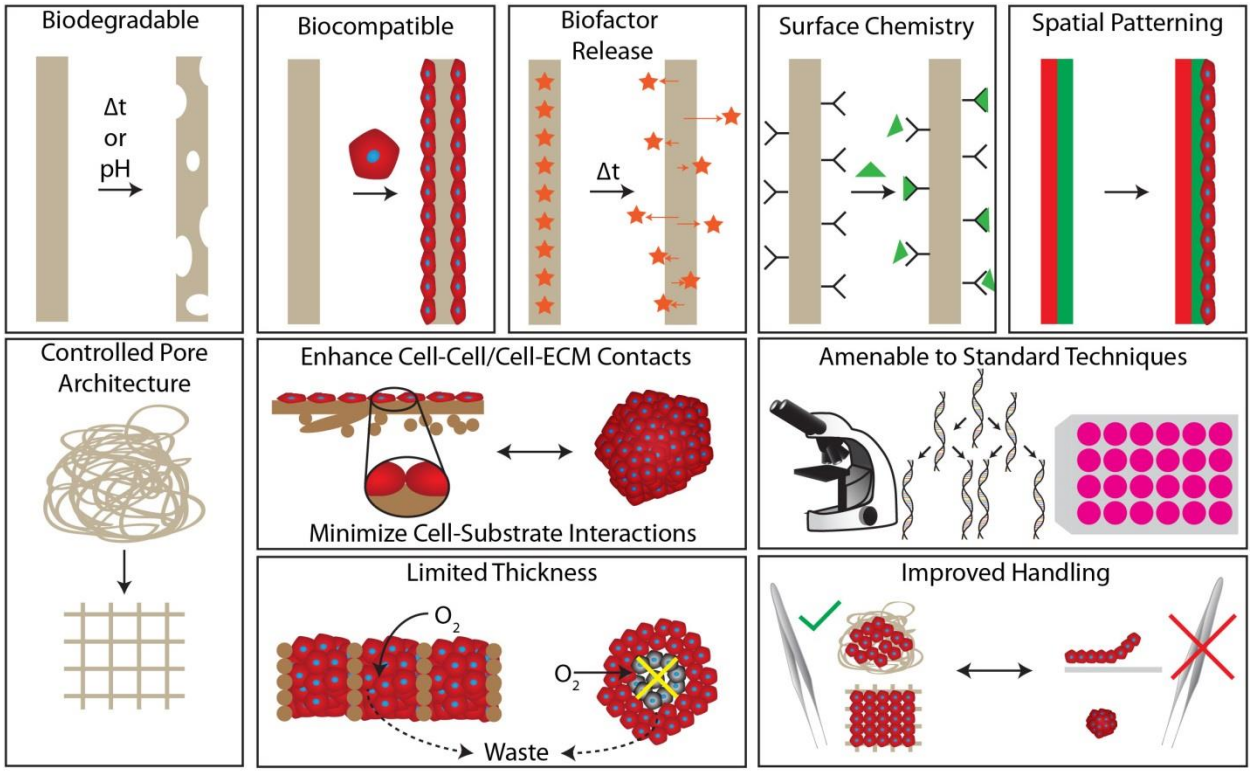

Figure 4.1 Considerations for design of ideal tissue engineering scaffolds. Here, a selection of different considerations which play a role in designing a tissue engineering scaffold are listed. Basic requirements such as biocompatibility, being easily handled, and amenable to standard characterization techniques are essential for widespread adoption of the technique. Other features listed provide means for generation of more complex tissue structures.

Phase separation scaffold fabrication includes methods such as gas foaming and emulsion freeze drying techniques.[146] The formed scaffolds consist of polymer foams created via trapping gas bubbles within a polymer matrix, leaving behind a polymer construct with a large number of pores.[146] The pores can be interconnected or isolated, depending on the overall porosity (porosity > ~70% is considered to have interconnected pores).[146] With this method, high porosities are achievable with common biodegradable materials, however, achieving such porosities is difficult and due to random pore formation there is no long range architecture, non-uniform mechanical strength, and lack of pore structure and distribution.

An alternative is the solid freeform fabrication techniques. These consist of methods which 3D scaffolds are written directly via stereolithography or through direct fiber deposition through

micronozzles.[147-149] Stereolithographic techniques, or laser-based scaffold fabrication approaches, can rapidly produce structures with controlled porosity with controlled and complex architecture. The limitation of this technique is that requires a photocrosslinkable polymer solution to create the structure, which limits the materials that can be used. It is also difficult to create large scale structures using this method.[147] Direct write techniques which extrude colloidal inks from micronozzles are also used in solid freeform fabrication.[147, 150] These methods can achieve highly ordered structures composed of large fibrils (on the order of hundreds of micron in diameter) with fairly small feature sizes. However, the scaffolds produced generally have low mechanical strength, the ink properties must be finely tuned, and capillary blockage/breakage is commonly encountered.

The third common way of producing tissue engineering scaffolds is electrospinning. Electrospinning of biodegradable and biocompatible polymers is a promising technique for tissue engineering applications.[151-154] Using the basic procedures previously described, fiber mats with ranges of properties can be produced. Mats with highly aligned or randomly deposited fibers have been used for scaffolding. Often, to control the pore structures of the mat, fiber thickness is altered. Pores of nanofibrous structures are extremely small making it difficult for cellular penetration and waste removal. Larger pores in non-woven mats are achieved with larger fiber diameters.[145, 155] However, as in the foam processing methods, the pore structure cannot be fine-tuned as the deposition is a random process. Highly aligned fibers can also be created using a rapidly rotating mandrel. Again, fiber spacing is not controlled and creating a homogenous or patterned non-homogenous structure is not feasible. Advantages of electrospinning are its large material library, essentially any material where polymer chains can entangle with one another can be electrospun. Electrohydrodynamic (EHD) co-jetting is a branch of electrospinning

technology which can produce fibers similar to normal electrospinning, except it can introduce multiple distinct compartments which can contain vastly dissimilar bulk, surface, and chemical properties.[31, 34, 156] These compartments have been implemented in the past for spatially selective cell adhesion,[156] and show much promise for patterning cell growth.

4.1.3 Scaffold-Free Tissue Engineering

The pursuit of creating accurate tissue mimics *in vitro* has been led by the development of scaffold-free tissue engineering constructs. These systems aim at simulating native tissue through maintaining a high degree of cell-cell and cell-matrix interactions for the purposes of high throughput drug screening,[133, 157, 158] tissue regeneration, and 3D cell culture models. In the case of high throughput drug screening, spheroids have been shown to have great potential due to the high degree of cell-cell and cell matrix interactions in addition to the introduction of diffusive gradients within these high cell density constructs.[136] While diffusive gradients aid in recapitulating *in vivo* tissues, these gradients inherently limit spheroid size, as they are restricted to radial growth. Oxygen and nutrient diffusion deficits occur when spheroids reach diameters around 400 μm leading to the development of a necrotic core.[136, 159] Small sample sizes results in difficult to characterize samples and limited use of spheroids in regenerative medicine. Limiting the cell growth by culturing cells in 2D thermal responsive culture dishes leads to the production of cellular sheets.[160, 161] While this technology has advanced the field of tissue regeneration,[135] the technique has limited applicability in performing *in vitro* studies due to the inherent use of 2D cell culture substrates. 2D cell culture has widely been accepted to produce cells with significantly altered morphology and gene expression and eliminates the possibility of formation of secondary 3D structures, such as ducts or capillaries, which are important structures

for the development of 3D cell culture models.[129] Other techniques such as cell aggregate systems utilize centrifugation or settling of cells into dense 3D pellets, which require millions of cells and randomly-dispersed, artificial filler to impart sufficient mechanical strength to be used *in vivo*.[162] Utilizing 3D jet writing scaffolds, with their tessellated honeycomb pore structure to support 3D cell culture across large areas would control the area and thickness of cell growth, reduce the number of cells needed to make a mechanically robust cell culture, and maintain cells in a controlled 3D environment consisting mainly of cell-cell and cell-matrix interactions. This type of cell-scaffold construct could be utilized in applications ranging from regenerative medicine to more accurate *in vitro* tissue models and high-throughput drug screening.

4.1.4 Three-Dimensional Pluripotent Stem Cell Culture

4.1.4.1 Perspective

The discovery of stem cells brought about a new challenge in cell culture substrates, as now instead of simply growing cells, specific cell properties, such as self-renewal and either pluripotency or multipotency, needed to be maintained or controlled. Maintaining these unique properties of stem cells during expansion is crucial to create sufficient populations of undifferentiated cells that can then be terminally differentiated into specific tissues.[163] While standard tissue culture plastic can be suitable for culturing both primary cells and cell lines, they are not well-suited for maintaining the stemness for prolonged periods of time. Recent trends in development of stem cell substrates have focused on recapitulating the stem cell niche *ex vivo* in a tissue culture environment. This has been accomplished using strategies, such as feeder cells, purified extracellular matrix proteins (ECM), peptide conjugated surfaces or hydrogels, and specialized synthetic polymers, to create an milieu that is conducive to stem cell expansion and maintenance of stem cell properties outside of the body.

Implementation of 3D cell culture strategies, similar to those outlined in previous sections of this chapter, of either embryonic (hESCs) or induced pluripotent stem cells (iPSCs) rapidly results in an uncontrolled differentiation process, forming what is known as an embryoid body.[164] An embryoid body is a mass of cells which have begun the differentiation process, and produce cells from the three different germ layers, the ectoderm, mesoderm, and endoderm.[165] While there are differentiation strategies in which these pluripotent cells go through an embryoid body stage, the efficiency of the differentiation is hindered by this process.[165] Additionally, studying how these populations of pluripotent cells differentiate in 3D is currently not feasible, leading to the need to develop substrates which can support hESC and iPSC culture in 3D. The development of 3D environments capable of preserving the pluripotency of embryonic and induced pluripotent stem cells is a major advancement towards defined stem cell microenvironments, and may serve as a blueprint for other stem cells with high levels of phenotypic plasticity, such as cancer stem cells or hematopoietic stem cells. In order to fully understand what the requirements are to maintain hESC and iPSC in 3D culture, and how they relate to other stem cell microenvironments, an examination of the development of 2D culture substrates is presented.

4.1.4.2 The Stem Cell Niche

Stem cells have the specific function of producing and replenishing specialized cells during the life of eukaryotic organisms. During early mammalian development, the fertilized egg divides into blastomeres with stem cell properties that gives rise to the first two cell lineages: the trophoectoderm cells from the outer blastomeres of the embryo which will form the placenta; the

inner blastomeres will become the inner cell mass (ICM), a population of cells with pluripotent properties [166]. The ICM eventually differentiates into specialized cell types of the three germ layers, namely the ectoderm, mesoderm, and endoderm [166]. *In vitro*, this pluripotent stage can be maintained over long periods of time by isolating and expanding the cells comprising the ICM, which are called embryonic stem cells.

Throughout life, fetal and adult stem cells, called somatic stem cells (SSC), are developed and maintained in specialized microenvironments named stem cell niches. These niches serve as protective environments that provide supportive conditions to maintain stem cell self-renewal and differentiation properties. The niche is comprised of soluble signaling from cytokines and growth factors, direct interactions with other cells, and the extracellular matrix (ECM). In combination with one another, these components activate signaling pathways involved in the maintenance of the undifferentiated and quiescence state of stem cells. While some signaling pathways and niche elements are commonly expressed among stem cells, there is not a defined pathway present in all of them [167-169]. However, the literature suggests that a common characteristic between stem cells and their niches can be found in the expression of an specific ECM protein in the niche and its receptor in the stem cells: laminin and integrin α6. The laminin and integrin α6 interaction has been documented as a critical niche component in corneal [170], colonic [171], epithelial [172], hepatic [173], spermatogonial [174], neuronal [175], glioblastoma [176], and embryonic stem cells [177]. Interestingly, laminin is one the first ECM proteins deposited during embryo development, and it is specifically expressed in the blastocyst stage, when the ICM is formed and, as explained above, a transient state of pluripotency exists. Human embryonic stem cells, the *in vitro* counterpart of the pluripotent inner cell mass (ICM) cells, express integrin α6 [178] and specific isoforms of laminin are able to support their self-renewal and proliferation [179].

Furthermore, although other ECM proteins such as vitronectin [180] and fibronectin [181] can support self-renewal of hESCs, it has recently been shown that hESCs cultured on those ECM-coated surfaces remodeled their microenvironment by depositing their own laminin [182]. Due to the similarities among pluripotent stem cells and several somatic stem cells and their corresponding niches, we propose that the knowledge of the *in vitro* culture of human pluripotent stem cells could be exploited to bioengineer stem cell niches for somatic stem cells.

4.1.4.3 Feeder Cells

The isolation and successful culture of hESCs opened an entirely new outlook on the future of cell and tissue culture. However, it came with its own set of challenges. While hESCs can adhere to normal tissue-culture plastic, the unique attribute of maintaining self-renewal is lost over time in these conditions. Thus, inactivated feeder cell layers, a technique derived from successful maintenance of pluripotency in mouse embryonic stem cells (mESCs) and mouse embryonal carcinoma cells (mECCs) [183-185], were used to support the culture of hESCs. A study using non-proliferative human oviductal epithelial cells as a feeder layer and human leukemia inhibitory factor (HLIF) to culture the ICM of a human blastocyst proved to be the first isolation and culture of human ICM cells, although the cells differentiated towards a fibroblast-like phenotype after two passages [186]. The first human embryonic stem cell (hESC) lines that could be sustained indefinitely *in vitro* were cultured on feeder layers composed of mouse embryonic fibroblasts (MEFs) in medium supplemented with FBS [163, 166, 187]. An alternative source of pluripotent stem cells is provided by human fibroblasts reprogrammed into pluripotent stem cells, termed induced pluripotent stem cells (iPSCs) [188]. The establishment of hESC and iPSC lineages provided the platform necessary to investigate i) what microenvironment is necessary to

sustain these cells in a pluripotent state, ii) how to eliminate components within the microenvironment which are undefined or derived from xenogeneic sources, and iii) how the physical properties of the microenvironment affect the differentiation and maintenance of these cells.

Similarly, feeder cells and co-cultures of stem cells with somatic cells are also used in the expansion and maintenance of human hematopoietic stem cells (HSCs). HSCs are a relatively rare cell type located primarily within the bone marrow, peripheral blood, or umbilical cord blood and are capable of differentiating into all mature blood cells of the human body. HSCs play a critical role in bone marrow transplants used in clinical treatments for hematological disorders such as leukemia, lymphoma, and sickle cell anemia [189]. *Ex vivo* expansion and maintenance of these rare cells could therefore provide an attractive platform for improving the treatment of several debilitating diseases. Engineering a culture substrate capable of expanding long-term repopulating hematopoietic stem cells began by examining the niche in which they reside. This led to co-culturing isolated human HSCs with stromal cells associated with the bone marrow microenvironment, and cells which secrete a specific set of cytokines and growth factors which have been attributed to maintaining HSCs [190-194]. Human feeder cells, such as osteoblasts [195] and mesenchymal stem cells [196-198], as well as porcine endothelial cells [199], mouse fetal liver [200], and mouse stromal cells [201] are some examples of the types of feeder cells associated with the expansion of human HSCs *in vitro*. While the interactions between these supporting cells and HSCs have not been fully characterized, the ability of feeder cells to promote HSC expansion *ex vivo* has shown some degree of success. The direct clinical relevance of HSCs to the treatment of blood disorders has led to the extensive use of human feeder cells to provide a microenvironment free from xenogeneic contamination, as opposed to MEFs used in early hESC

microenvironments. This has contributed to successful human trials which have demonstrated that *ex vivo* expansion of HSCs can provide an effective means of improving engraftment efficiency over standard cord blood transplants [202]. While *ex vivo* expansion over short periods of time have demonstrated successes, long term maintenance of HSCs has yet to be achieved, as it is possible for hESCs. Despite the successes provided by feeder cells to the culture of both hESCs and HSCs, the unknown interactions between the cells in co-culture systems contributed to a desire for feeder-free cell culture systems with fully-defined media components. Such a culture platform would be used to directly study how the composition of the microenvironment affects stemness.

4.1.4.4 Feeder Free Culture Using Purified Extracellular Matrix Proteins

While the expansion of stem cells on human [203, 204] and xenogenic feeder layers has shown success in maintaining pluripotent stem cells for prolonged culture times, and multiplying adult human HSCs for therapeutic use, these systems lack control over what signals are presented to the stem cells. Deconstruction of the stem cell niche has led to ECM-based microenvironments that provide an adhesive substrate that interacts directly with cells through integrin signaling, which is suspected to contribute to stem cell maintenance. However, the biological activity of ECM is more complex than a simple adhesive substrate, as it provides a reservoir for growth factors which can alter their release or presentation, contains cryptic signaling domains, modulates the mechanical stiffness of a substrate, and can be remodeled by cells based on environmental cues. A major advance in the development of more defined microenvironments using ECM coatings came with the first ‘feeder-free’ hESC culture system [177]. This study demonstrated that feeder layers could be eliminated through use of various matrix proteins, either

a product of Engelbreth-Holm-Swarm mouse sarcoma cells (Matrigel) or purified matrix proteins laminin, collagen IV, or fibronectin coated on tissue-culture plastic in conditioned medium supplemented by human basic fibroblast growth factor (hbFGF).

While the feeder-free systems were able to successfully eliminate the complexity and inconsistency associated with feeder cells, the reliance on MEF conditioned medium remained a source of xenogeneic contamination and unknown composition. Nevertheless, the concept of coating tissue-culture plastic with matrix proteins and utilizing conditioned medium both continue to be a popular technique for stem cell culture, including both pluripotent stem cells and adult stem cells.

Development and validation of the first defined hESC media, TeSR1, on a substrate coated with purified human matrix proteins marked a significant progression towards the ultimate goal of obtaining a fully defined microenvironment that preserves the pluripotency of hESCs and hiPSCs [205]. Initial work with TeSR1 demonstrated that hESCs could be grown on a matrix coating consisting of collagen IV, fibronectin, laminin, and vitronectin, an ECM combination that was determined through a screening process. Further studies demonstrated the ability to maintain pluripotent stem cells on substrates coated with purified fibronectin [206],laminin [207, 208], or vitronectin [209, 210]. Although these ECM-coated surfaces can maintain hESC and iPSC stem cells, not all surfaces coated with these purified ECM components are successful in maintaining the pluripotent stem cell phenotype [209, 211]. This could be explained in part by the conformational changes of the ECM proteins on the coated substrates, which have been demonstrated to depend significantly on the underlying substrate and been shown to impact integrin binding interactions [212-215]. Therefore, proteins adsorbed onto different surfaces could have differing ability to support pluripotent stem cell culture [210]. Specifically, in the case of pluripotent stem cells, different

conformations of Matrigel coated on glass, polystyrene, or tissue culture surfaces have been shown to drastically alter ESC proliferation and differentiation [216]. Similarly, conformational change in osteopontin (Osp) by thrombin-cleavage (tc) results in an inhibitory effect on proliferation and differentiation of human HSCs (CD34+CD38- cells) compared to native Osp coated surfaces, which induce apoptosis in these cells [217]. Interestingly, the effect of tc-Osp is lost in committed hematopoietic progenitor cells (CD34+CD38+).

The reason for the success of these substrates is not clearly understood. However, speculation over integrin binding with matrix molecules [209, 218], and several cell-signaling pathways are suggested to play a role in stem cells retaining their pluripotency. Nevertheless, limited success of culturing pluripotent stem cells on collagen substrates [219], which contain multiple integrin binding domains complementary to receptors found on the surfaces of hESCs, leads to questions as to what specific interactions are necessary to preserve the cell's ability to self-renew. One interaction of note that is found in hESCs and hiPSCs is integrin α6β1, which binds the different subtypes of the laminin family of ECM proteins [176], and recently has been associated with maintaining stemness of pluripotent stem cells and other stem cells. Recent reports show that a novel function of integrin α6 is blocking the activity of integrin β1 in hPSCs, which in turn prevents the phosphorylation and activation of focal adhesion kinase. This is important because after phosphorylation of this kinase, degradation of key pluripotent transcription factors was observed: Oct4, Sox2 and Nanog in hESCs.[220] Furthermore, it has recently been shown that integrin α6 can be used as a marker to identify long-term repopulating human hematopoietic stem cells from other multipotent progenitors within a cord blood sample [221]. Integrin α6 has also been implicated as an important regulator of glioblastoma cancer stem cell self-renewal, proliferation, and tumor formation capacity [176]. This has led to recent successes

of laminin coated culture substrates in maintaining the cancer stem cell (CSC) phenotype [222]. Primary brain tumor cells cultured on laminin coated tissue culture flasks led to the isolation of multiple glioma neural stem cell lines, a significant achievement in the field of cancer stem cells. Laminin has also been identified as an important ingredient in the expansion of CSCs from other tissue types as well, including breast cancer where laminin 511 has been linked to enhanced CSC adhesion and growth [223]. With the demonstrated similarities between the transcriptional factors and signaling pathways associated with hESCs and cancer stem cells [224], it is not surprising that similar culture methods for maintaining these stem cells has been achieved. These results indicate ECM coatings have some ability to mimic the stem cell niche, without the integration of stromal cells.

The importance of the elimination of the feeder cells, in terms of contributing to basic understanding of stem cell pluripotency, cannot be overstated simply due to the reduction of variables within the culture system. Despite the successful elimination of the unknowns contributed by the feeder cells, conditioned media, and xenogenic materials through the use of matrix coated substrates, the inherent complexity of these systems continues to mask the mechanism of how these systems work. This has led to the development of newer surfaces through peptide modified hydrogel substrates which can be utilized to examine specific details and interactions between cells and their microenvironment.

4.1.4.5 Peptide-Conjugated Polymer Substrates

It has been demonstrated that proteins bind to cells through specific oligopeptides, often consisting of only a few amino acid units. This concept was first demonstrated with the discovery that the peptide sequence RGD is responsible for cell attachment to the extracellular

matrix protein fibronectin.[225] Since then additional peptide sequences have been discovered within other ECM proteins, such as laminin and collagen, and include: KQAGDV, YGYGDALR, FYFDLR, KRLDGS and LDV [226]. These binding motifs have been found to associate with different integrins on the cell surface, making these peptide sequences a potentially powerful tool to study how integrin binding affects stem cells fundamental characteristics of self-renewal and differentiation. However, studies using peptide sequences for binding have found that the conformation can drastically alter how the peptides interact with their corresponding integrin [227]. These types of conformational changes that alter cell binding to peptides may also explain some of the discrepancies seen in the protein coatings on the substrates. This concept has been demonstrated in pluripotent stem cell culture through the attachment of a cyclic-RGD peptide to an amine modified tissue culture plate [228]. Coupling of an NHS-PEG-maleimide linker to the surface allowed for the immobilization of cyclic-RGD through a Michael addition reaction. As result, it was shown that the cyclic-RGD surfaces were capable of expanding pluripotent stem cells, while the non-cyclic form of the RGD was not.

Attaching adhesion peptide sequences to other types of substrates has also been explored. Modification of bioinert substrates, such as polyethylene glycol (PEG), with adhesion peptides to create tunable tissue engineering substrates has been accomplished [229]. Attachment of adhesion peptides to bulk hydrogels, or to self-assembled monolayers provided a new method for creating bio-inspired synthetic substrates for pluripotent stem cell expansion. The first example of these types of substrates were acrylate gels modified with peptide sequences from either fibronectin, vitronectin, bone sialoprotein (BSP), or laminin, and were studied in parallel to determine which surface was superior in pluripotent stem cell maintenance [230]. Interestingly, each of the peptide sequences contained an RGD sequence motif, however, only the BSP and vitronectin modified

acrylate gels were capable of sustaining stem cell self-renewal, providing further evidence for the importance of the adhering peptide conformation. This study led to the first commercialized biosynthetic substrate, Synthemax™, which promotes the sustained self-renewal and proliferation of human pluripotent stem cells. Other peptide conjugated substrates have also been reported, including those which do not include the well documented RGD sequence [231]. A notable example is the heparin-binding peptide GKKQRFRHRNRKG, which when bound to the surface using self-assembled monolayers (SAMs), was able to maintain the pluripotency of multiple different hES and iPS cell lines for 1-3 months. This peptide is thought to interact with the glycosaminoglycans on the surface of the cells, facilitating adhesion to the substrate and aiding in the maintenance of the stem cell phenotype. The peptide conjugated onto surface was found to have superior performance compared to surfaces with integrin binding RGD sequences by instead interacting with the glycosaminoglycans on the cell surface. Performance of these surfaces could be further enhanced through co-presentation of RGD containing peptides and the glycosaminoglycan binding regime, suggesting that both adhesion and integrin interactions contribute to the success of this type of surface modification. Therefore, while integrin interactions play an important role in pluripotent stem cell maintenance, there may be other signaling pathways involved. Peptide conjugated peptides in defined conditions allow for studying these alternative interactions, demonstrating the power of this technique.

Current trends in stem cell culture have expanded the use of biofunctional hydrogels into 3D culture matrices, with the goal of these systems being to mimic certain aspects of the extracellular matrix. A 3D polyethylene glycol diacrylate hydrogel conjugated with the heparin-binding peptide WQPPRARI, similar to the SAM surface that was able to expand pluripotent stem cells, was utilized for the proliferation of CD44+/CD24- breast cancer stem cells *in vitro*

[232]. Other peptides, such as an integrin binding peptide or CD44 binding peptide, conjugated to the PEGDA hydrogel led to decreased CD44 expression, indicating a reduction in the CSC population. Similar peptide conjugation strategies that utilize integrin-binding peptides, such as RGD, have also been implemented in 3D hydrogels for culturing HSCs [233]. However, these studies often demonstrate little efficacy in expanding stem cell populations. Current research in tuning the hydrogel mechanics without altering the ligand density [234], as well as creating enzymatically degradable hydrogels are leading the way towards fabricating synthetic ECM mimics which can study specific interactions of cells and their environment [130]. Peptide-conjugated hydrogels therefore provide the capability to probe whether specific cellular interactions are required or sufficient to promote stem cell self-renewal and expansion and therefore makes them a unique tool to study specific interactions in the stem cell microenvironment.

4.1.4.6 Fully Synthetic Polymer Substrates

While the bio-inspired culture platforms provided a means for examining how specific interactions affect stem cell culture, the surfaces are costly and have limited shelf-life. Therefore, the development of a fully synthetic surface for pluripotent stem cell culture could result in affordable culture surfaces for scaled up cell expansion of stem cells in an environment never exposed to undefined biological components [235, 236]. This could lead to widespread use and implementation resulting in consistent and comparable results, unlike the ECM coated surfaces that have shown conflicting reports, due to batch-to-batch inconsistency.

The first fully synthetic surface for pluripotent stem cell culture was a zwitterionic hydrogel with negatively charged sulfate groups and positively charged ammonium groups, called

PMEDSAH, short for poly[2-(methacryloyloxy)ethyl dimethyl-(3-sulfopropyl)ammonium hydroxide] [237]. This hydrogel is attached to culture surfaces using surface initiated atom transfer radical polymerization (ATRP), and has been shown to maintain multiple human iPS [238] and hESC lines [239], for extended number of passages in both chemically-defined medium or medium conditioned by human feeder cells. A recent report of iPS cell lines derived on PMEDSAH, and subsequent maintenance of their pluripotency for over 9 months of continuous culture, demonstrates that this platform is a cost effective and consistent alternative to recombinant protein coatings for the derivation and long-term culture of hiPSCs [240]. The mechanism for how these surfaces work is not yet fully understood. However, despite the non-fouling nature of the PMEDSAH surfaces, a possible protein interaction on the surface of the zwitterionic hydrogel has been proposed in which the sulfate groups of PMEDSAH act as a mimic of heparan sulfate [219]. The mechanism proposes that the surface would sequester of bFGF from the growth media, effectively concentrating it on the surface and protecting it from degradation, thereby enhancing the performance of the surface in maintaining stem cell pluripotency [219]. The role of PMEDSAH in supporting pluripotent stem cells is refined further in recent work investigating how PMEDSAH properties affect pluripotent stem cell growth and maintenance [241]. The conformational state of the PMEDSAH was demonstrated to play an important role in the growth of pluripotent stem cells. At intermediate hydrogel thicknesses, the hESCs studied show significantly higher growth rate of undifferentiated colonies when compared to thin or thick coatings of PMEDSAH. This arises from a combination of different properties including hydrophilicity, surface charge, and the inter-chain interactions of the hydrogel brush.[241]

Since the development of PMEDSAH there have been other synthetic hydrogel systems developed for culturing pluripotent stem cells. An aminopropylmethacrylamide (APMAAm)

surface has been used to maintain cell pluripotency in the defined medium, mTESR-1 [242]. Analysis of its surface dynamics suggests that adsorption of bovine serum albumin (BSA) from the culture media plays a role in the attachment of hESCs on the culture surface. Advancement of high throughput microarray screening platforms have led to the development of additional synthetic hydrogel substrates capable of supporting pluripotent stem cell self-renewal and pluripotency. Screening of polymer arrays for cell adhesion, proliferation, and differentiation potential capabilities determined that 16 polymers could sustain short-term maintenance of pluripotent stem cells. However, only the poly(methyl vinyl ether-*alt*-maleic anhydride) (PMVE-*alt*-MA) polymer was capable of supporting pluripotent stem cell growth over five passages.[243]

Despite the successes of synthetic culture surfaces in maintaining pluripotent stem cells, reports of culturing other difficult to culture stem cells, such as cancer stem cells or hematopoietic stem cells, on these types of surfaces are scarce in the current literature. A recent study documenting the importance of laminin and integrin interactions demonstrated that the ability of these surfaces is at least partially due to their ability to support cell secreted laminin [182]. With laminin and integrin α6 being crucial components in different types of stem cells, fully synthetic hydrogel surfaces could potentially provide a culture platform for expanding and maintaining stem cells beyond just pluripotent stem cells.

The ability to preserve the phenotype of stem cells *in vitro* has been a major challenge over the last few decades. This is true for pluripotent stem cells, including embryonic stem cells and more recently induced pluripotent stem cells, as well as some difficult to culture adult stem cells, such as cancer stem cells and hematopoietic stem cells. Expansion and preservation of these rare stem cells is critical for tissue engineering or regeneration, *in vitro* drug testing, and treatment of many diseases. While each of these stem cells reside in unique microenvironments in the body,

their niche components each consist of extracellular matrix, stromal cells, and soluble signals. This has led to similar *in vitro* culture strategies for the maintenance of each of these stem cell types. Interestingly, techniques that have been successful in maintaining pluripotent stem cells have also been found useful in culturing other types of stem cells. These platforms typically utilize specific elements of the niche to recapitulate specific functions or signals thought to be important in maintaining stem cells. This includes implementation of feeder cells, laminin coated substrates, and peptide conjugated hydrogels to engineer microenvironments suitable to human stem cell preservation.

The development of pluripotent stem cell culture platforms has provided great insight into the necessary interactions to preserve the stem cell phenotype, and has been instrumental in developing techniques useful in culturing other types of stem cells. It has been revealed that there are many similarities between the preservation of pluripotent stem cells and other adult stem cells. One such commonality includes signaling through the laminin binding α6 integrin, which is expressed by stem cells ranging from hematopoietic stem cells, cancer stem cells, and pluripotent stem cells [176, 177, 221-223]. This expression has led to many successful culture techniques using laminin-coated surfaces. However, it should be emphasized that the success of these coating technologies relies on maintaining the conformational state of the protein, which has been demonstrated to affect pluripotent stem cells cultured on Matrigel coated surfaces [216]. Therefore, exploring how ECM conformation affects stem cell maintenance may reveal new strategies for their expansion and preservation. With this in mind, the creation of a 3D extracellular matrix microenvironments engineered into natural conformational states could provide a unique culture environment that could be used to study stem cell interactions with specific matrix components.

4.2 Materials and Methods

4.2.1 Fibronectin Preparation

Frozen aliquots of human fibronectin (Corning Inc., Corning, NY) at concentrations of 1 mg/mL were allowed to thaw at 4 °C and subsequently diluted to a concentration of 100 µg/ml in magnesium and calcium free cold Dulbecco's phosphate buffered saline (DPBS). The scaffolds were coated overnight at 30°C and stored at 4°C until use.

4.2.2 Cell Culture Media Preparation

Culture medium for hMSCs was composed of low glucose DMEM supplemented with 10% MSC qualified FBS, 1% Penicillin Streptomycin, and 10 ng/ml human recombinant basic fibroblast growth factor (Life Technologies, Carlsbad, CA) prior to use. Osteogenic medium was prepared using an hMSC osteogenic bullet kit (Lonza group, Basel Switzerland). hMSC differentiation basal medium was supplemented with dexamethasone, L-glutamine, ascorbate, penicillin streptomycin, mesenchymal cell growth serum, and β-glycerophosphate per the manufacturer's recommendation.

Culture medium for NIH3T3s was composed of DMEM supplemented with 10% certified FBS, 1 % Anti-Anti, and 1% non-essential amino acids prior to use.

4.2.3 Cell Culture

2D culture of hMSCs (Lonza, Basel Switzerland) and NIH3T3 were seeded at a density of 5,000 cells/cm^2 and cultured at 37ºC in 5% CO_2. The medium was replaced every 3-4 days and the cells were passaged when they were approximately 80% confluent. All hMSCs used in the

studies were passage 5 or less. Once seeded onto the scaffolds, medium was replaced every 3 days.

NIH3T3 fibroblast were cultured on scaffolds in Eppendorf tubes which were were sterilized overnight in UV. Prior to seeding with cells, these scaffolds were incubated with 100 µg/ml human fibronectin (FN) in pure H_2O on a rotator for 1 hour at room temperature. These were washed with sterile DPBS three times for five minutes each. NIH3T3 (p.6) were thawed from cryogenic storage, then incubated with the structures at a concentration of 200,000 cells/tube.

Single human embryonic stem cells (hESCs) were seeded onto fibronectin scaffolds by seeing 200,000 cells in 500 µl of human conditioned medium with 1 µl Rock inhibitor in an ultra-low-binding 24 well plate. After incubation on scaffolds for 4-5 hours, an additional 1.5 ml of human conditioned medium is added to the well. A complete change of media is performed the day following cell seeding to remove any non-adhered cells.

4.2.4 Cell Staining

Actin was stained using phalloidin labeled with an Alexa Fluor fluorescent probe. First, cells on scaffolds were fixed in 4% formaldehyde for 24 h and then permeabilized using 0.1% Triton X-100 for 5 min. Blocking was performed using 5% BSA for at least 30 minutes. A 0.33 µM solution of Alexa Fluor 488 phalloidin was added to the scaffold for 1 h, then the solution was washed with PBS. The cell nucleus was stained using a 2 µM solution of TO-PRO-3 Iodide, and then washed using PBS. Fibronectin was stained using an anti-Fibronectin made in rabbit primary antibody, and followed by counterstaining with an anti-rabbit IgG made in goat secondary antibody typically conjugated to an Alexa Fluor 647 fluorescent probe.

Von Kossa staining (American MasterTech, Lodi, CA) was performed on fixed scaffolds by first washing the scaffolds in DI water. The scaffolds were then placed in a 5% silver nitrate for 45 min under exposure with a UV light. The scaffolds were then rinsed using distilled water and placed in 5% sodium thiosulfate for 3 m and then rinsed using tap water. Finally the scaffolds were placed in nuclear fast red stain for 5 min and washed with tap water before imaging.

2% Alizarin Red staining solution was added to the a 24 well plate containing a fixed scaffold. The solution was rocked side to side, ensuring complete coverage of the scaffold. Stain was incubated on the scaffold for 15 minutes, followed by removal and rinsing three times for five minutes using DI water.

The OsteoImage bone mineralization assay (Lonza) provides a quantitative measure of bone mineralization for *in vitro* cell culture systems, and can be used to measure changes in mineralization over time. Fixed scaffolds containing cells were rinsed twice in PBS for five minutes. Concentrated wash buffer was diluted 1:10 in DI water, and was subsequently used to rinse the scaffolds twice in the 24 well plate, five minutes for each wash. Staining reagent was diluted 1:100 using the 'staining reagent dilution buffer', and was incubated in the 24 well plate for 1 hour in the dark. The diluted staining reagent was then removed, and the scaffolds were washed three more times for five minutes each wash. This assay was performed at different time points to monitor the mineralization seen during osteogenic differentiation.

4.2.5 RNA Isolation

RNA was isolated using an RNeasy mini kit (Qiagen, Venlo, Limburg). RNA was obtained immediately before the cells were seeded onto the scaffolds and weekly after expansion on the tissue engineered constructs. Briefly, cells were lysed directly on the scaffolds using cell lysis

buffer RLT. The cell lysate was then homogenized using a QIAshredder spin column, and the RNA was isolated using RNeasy spin columns. RNA concentration and quality was determined using a Nanodrop (Thermo Scientific, Waltham, MA). Samples with RNA concentrations less than 2 ng/µl, with an OD 260/280 less than 1.8, and OD 260/230 less than 2.0 were not analyzed and a replacement sample was used.

4.2.6 qPCR Analysis

Changes in ostegenic markers (Table 4.1) were evaluated using the TaqMan gene expression assay system (Life Technologies, Carlsbad, CA). The StepOne Real-Time PCR system (Applied Biosystems, Carlsbad, CA) with TaqMan Fast Advanced Master Mix (Life Technologies, Carlsbad, CA) were used to conduct real time PCR in triplicate for each sample. Primers used are listed in Supplementary Table 1. GAPDH was amplified as an internal standard and quantification was performed using the comparative C_T method.

Table 4.1. List of primers used for qPCR

Gene	UniGene	Amplicon Length
GAPDH	Hs.544577	93
RUNX2	Hs.535845	116
SP7	Hs.209402	104
IBSP	Hs.518726	95

4.3 Results

4.3.1 Initial In Vitro Studies

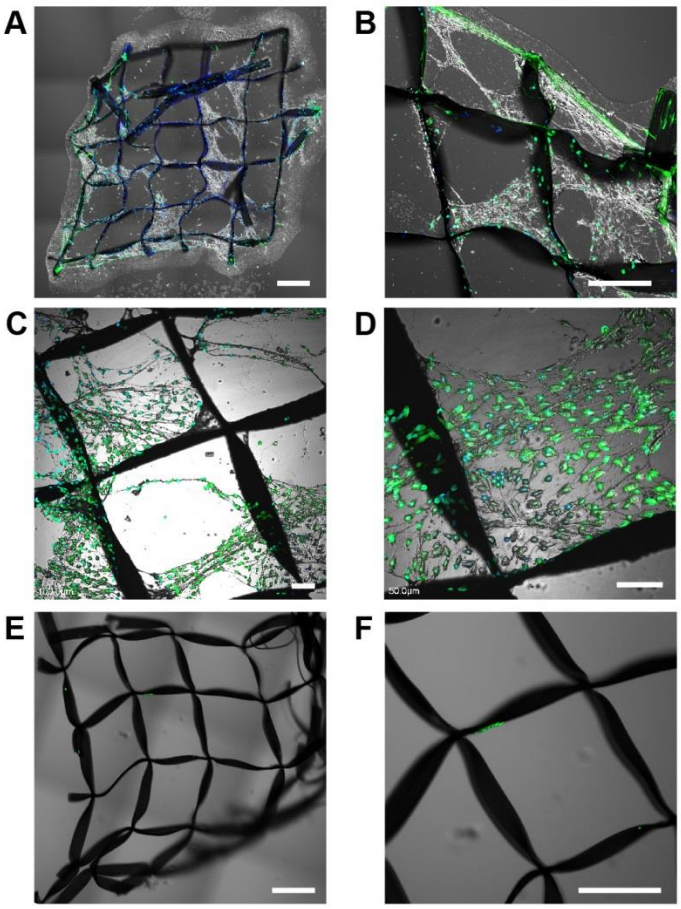

Figure 4.2 Cells require fibronectin coating to adhere and span across tessellated square pores. A-B) Human mesenchymal stem cells seeded at a density of 90k cells/ml and cultured for 18 hours were found to span 750 µm gaps of fibronectin coated scaffolds. **C-D)** NIH3T3 fibroblasts were also found to span similar gaps when seeded on fibronectin coated scaffolds at densities of 200k cells/ml. **E-F)** When no fibronectin coating was used, very few NIH3T3 fibroblasts adhered to the scaffold after 18 hours of culture at a seeding density of 200k cells/ml. This demonstrates the critical role that fibronectin plays in forming these cellular structures. In all cases the scaffolds were rotated in an Eppendorf microcentrifuge tube for the entire 18 hour time. Scale bars indicate 500 µm (A,B,E,F), and 100 µm (C,D).

Initial exploration of using 3D PLGA microfiber scaffolds was performed using NIH3T3 fibroblasts. Scaffolds which were coated with fibronectin were seeded with NIH3T3 fibroblasts to study cell attachment to the polymer microfiber construct. After roughly 15 hours, the fibroblasts were found to be well-adhered to the scaffolds, and some of the scaffolds contained regions where the cells seemed to span across the large open pores of the scaffolds (Figure 4.2 C-D). These cellular sheets appeared to be anchored to the scaffolds, and were only present in some of the pores of the scaffold, with none of the scaffolds fully covered with cells. Formation of these sheetlike structures were intriguing, and further study into how these features formed were subsequently performed.

Scaffolds coated with fibronectin,

and without a fibronectin coating, were incubated with fibroblasts and human mesenchymal stem cells (hMSCs) at different concentrations to further examine how the cells span across the PLGA microfiber scaffolds. In this study, it was found that when no fibronectin was coated onto the scaffolds, there was little to no attachment of cells to the polymer fiber constructs (Figure 4.2 E-F). However, precoating the scaffolds with fibronectin led to significanly enhanced cell attachment, and the cells, including the hMSCs, again demonstrated the ability to span large distances (750 µm) (Figure 4.2 A-B). This indicated that fibronectin coating played an important role in the formation of these structures. However, the extent to which this coating affects the formation of these features was yet to be discovered.

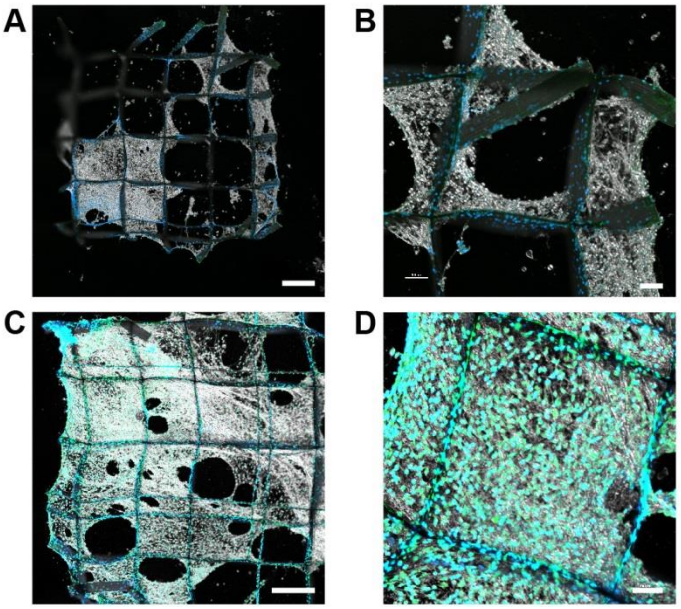

Figure 4.3 Cells spanning large gaps is dependent on cell seeding density. A-B) NIH3T3 fibroblasts seeded on fibronectin coated scaffolds cover about a quarter of scaffolds at seeding densities of 200k cells/ml. **C-D)** At higher seeding densities of 600k cells/ml, a much higher degree of cells spanning the scaffolding was observed. Scale bars indicate 500 µm (A,C), 100 µm (B,D).

Seeding NIH3T3 fibroblasts at higher cell densities of 200,000 cells/mL and 600,000 cells/mL demonstrated that the spanning of cells across these open pore speaces was greatly influenced by cell densities. Previous studies had seeded NIH3T3 fibroblasts at a density of 200,000 cells/mL, which led to only a couple areas where the pores were spanned by cells. However, in some cases up to a quarter of the scaffold was spanned completely by NIH3T3 fibroblasts. When 600,000 cells/mL were

seeded onto the scaffold, nearly the entire scaffold was spanned by cells and cellular material (Figure 4.3).

Besides simply examining how cell concentration affects the process of cells spanning the constructs, a timecourse study of the spanning process was initiated by examining what the cells and their secreted extracellular matrix (ECM) looked like after 6, 18, and 72 hours of culture in a rotating environment (Figure 4.4). After 6 hours of incubation, the cells had started forming initial colonies by attaching in small clumps at various locations across the scaffold. These clumps are characterized by very round cell morphologies, with fibronectin visible in small

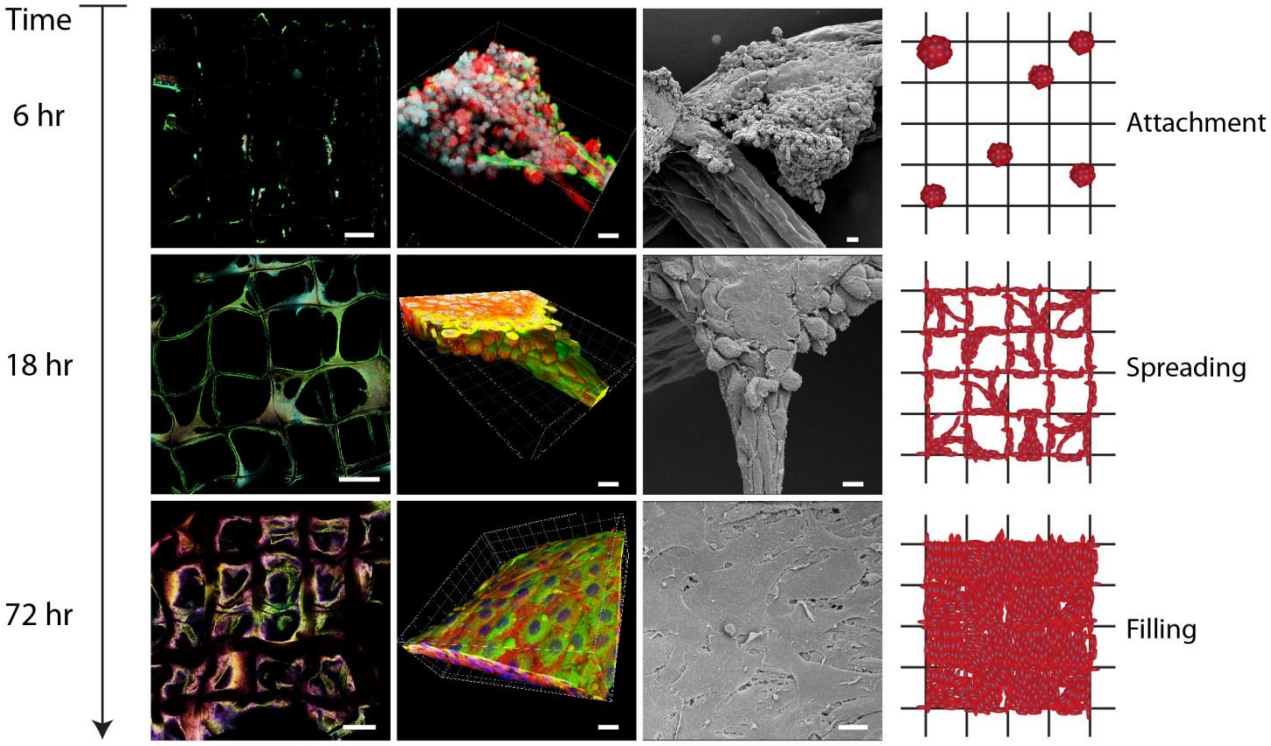

Figure 4.4. Time course dynamic culture of NIH3T3 fibroblasts. Culturing NIH3T3 mouse fibroblasts on square pore scaffolds with a grid spacing of 750 μm for 6, 18, and 72 hours was performed to observe how the tessellated microtissues form. Characterization of these constructs was performed using Confocal Laser Scanning Microscopy in parallel with Field-Emission Scanning Electron Microscopy on the same samples. Cells were stained for fibronectin (green, Alexa 488), actin (red, phalloidin), and nuclei (blue, TO-PRO3). The SEM images of the structure corresponds to the same area where the confocal micrographs were taken, which shows a more detailed image of the cellular morphology and interaction with the scaffold. The top row shows the initial binding of small cellular clumps to the scaffold. The middle row shows that after 18 hours the cells begin spreading out and spanning across the grid spacing. Finally, the bottom row shows that 72 hours of culture yields confluent sheets of cells, which are able to completely span the entire scaffold. Scale bars indicate 500 μm (Left), 25 μm (Middle), and 10 μm (Right).

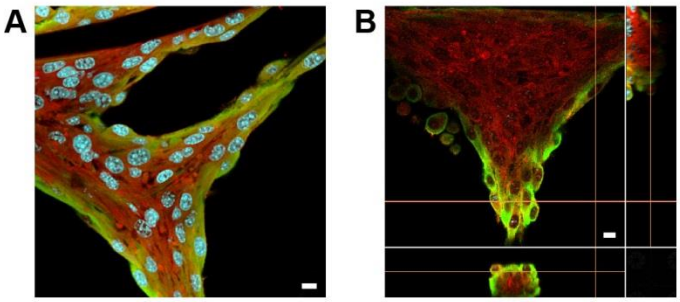

Figure 4.5 Fibronectin is distributed primarily around outside of cellular structures. A) A 2D slice of a confocal image of cellular structures which span the square pores of the scaffold shows localization of fibronectin (green) on the outside leading edge of the cell structure. **B)** A cross sectional view of 3D z-stack images of similar structures show the fibronectin envelops the entire cellular structure. Actin (red) and nucleus (blue) are also stained in this figure. Scale bars indicate 10 µm

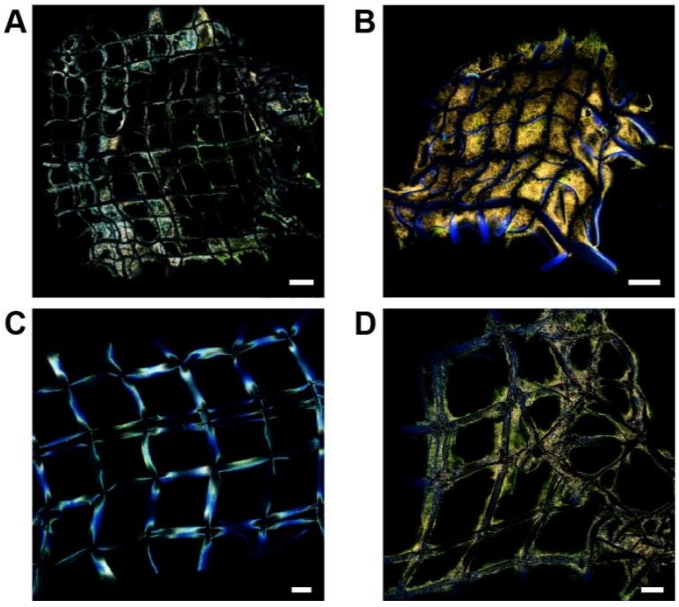

Figure 4.6 Scaffold pore size affects ability of cells to fill in void spaces. NIH3T3 fibroblasts at a density of 600k cells/ml were incubated on fibronectin coated scaffolds with pore spacings of 500 µm (A-B) and 1500 µm (C-D) for 18 hours (A,C) or 72 hours (B,D). **A)** Some of the cells were able to span across the 500 µm pores after 18 hours of culture. **B)** After 72 hours the entire structure was able to fill in with NIH3T3 fibroblasts. **C)** No spanning of the 1500 µm pores was seen after 18 hours of culture. **D)** After 72 hours of rotary culture the only spanning cell structures occurred at points of deformation of the scaffold. Scale bars indicate 500 µm.

unorganized streaks. After 18 hours of culture, the cells began the process of stretching across the large 750 µm gaps of the scaffold, and began the initial filling in of the scaffold with cells.

This spanning seemed to be feasible by the cells enveloping themselves in a fibronectin web, which was potentially able to support themselves across such large distances where no synthetic material was present (Figure 4.5). At the 72 hour time point, the entire scaffold construct was completely filled in with confluent layers of cells, with fibronectin seen in a fibrilar state throughout the cellular sheet formations.

Control over sheet formation, beyond altering the culture time, was also investigated by altering the scaffold grid spacings (Figure 4.6). Scaffolds with grid spacings of 500 µm and 1500 µm were created to compare with results from the 750 µm scaffolds. This experiment had

two objectives: to observe whether smaller grid spacings produced sheets in less time and whether sheet formation could be prevented by using grids with larger spacing. Cultures of 18 and 72 hours were performed on each of the two different scaffolds, and the results were compared to the findings from the previous study (Figure 4.4). It was seen that the scaffold with 500 μm between fiber stacks did not form sheets appreciably quicker than the 750 μm grid structure. In both cases a small degree of sheet formation after 18 hours of culture and produce sheets at the 72 hour time point. Since the 500 μm scaffolds were more difficult to fabricate, further studies were continued on scaffolds with grid spacings of 750 μm. The 1500 μm scaffold had no sheet formation after 18 hours of culture, and had very little sheet formation at 72 hours. Sheets that were formed at the 72 hour time point were mostly where the scaffold had been deformed, and therefore the spacing was not entirely consistent. With this data, it is evident that cell sheet formation can be controlled by varying the grid spacing of the fabricated scaffold.

These preliminary studies indicate that fibronectin coating of scaffolds is necessary to facilitate cell adhesion, and it plays a role in mechanically supporting the cells as they span large distances across the PLGA microfiber scaffold. The process is time dependent, and also depends on the cell seeding density, with higher seeding densities able to more readily span the large distances. Additionally, changing the pore size of the scaffold also influences the spanning behavior of the cells, with larger pores proving to be incapable of having cells span across them. These pieces of evidence led to the theory that the tumbling motion involved during the culture applied a mechanical force to the cells which stretched them and the ECM they secreted across the large gaps. SEM micrographs depict the initial spanning of cells across these large gaps, with cells often showing substantial elongation across the pore, especially along the leading edge of the spanning structures (Figure 4.7). Small fibrils, which appear to have an extracellular origin,

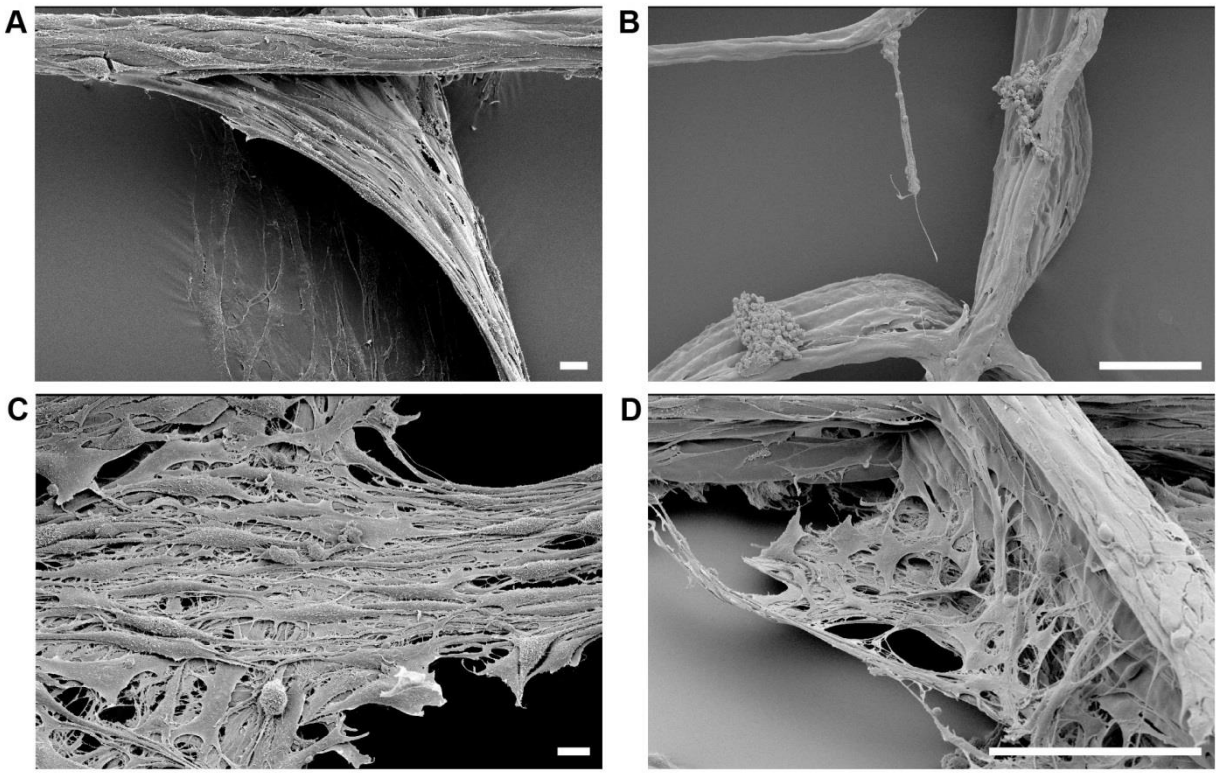

Figure 4.7 SEM analysis of cells spanning across large gaps. A) A characteristic feature of cells which span across the open pores of the scaffolds are attaching across a wide area of fibers, and narrowing down into a rope-like structure. This structure is mechanically stable enough to bridge the entire open gap. **B)** At early time points extreme stretching of cells across large areas can be seen. This behavior is attributed to the mechanical stimulation and stretching provided by the fluid motion of the rotary cell culture. **C)** Polarization of large groups of cells can be seen as the populations narrow towards narrow bridges which span distances much larger than the cells. These constructs seem to be held together in part by fibrilar material outside of the cell. **D)** A micrograph depicting the initial formation of cells as they bridge across the pores of the scaffolds. Multiple layers of cells anchor themselves to the PLGA fiber walls to support the larger cell structure. Again, fibrilar material is seen forming a matix between the cells. Scale bars indicate 10 μm (A,C), and 100 μm (B,D).

within these spanning cellular structures seem to be holding the cells together, indicating the presence of extracellular matrix. These observations tend to support the hypothesis that the cells are being mechanically stretched across these large gaps, and this stretching process is assisted by the deposition of extracellular matrix.

While this method of culturing cells provided an initial understanding of how these large scale free-standing cellular structures are formed, there remained multiple flaws in this

technology which needed to be worked out. First, the tumbling motion for long periods of time at physiological conditions mechanically damaged the scaffolds inside of the microcentrifuge tube (Figure 4.8). The tumbling motion which is thought to have played an important role in forming these cellular bridges across such large distances was also deforming the scaffolds. This motion combined with the traction forces of the large number of cells pulling on the softened PLGA microfiber stacks in some instances caused the entire scaffold to be pulled into a tight ball.

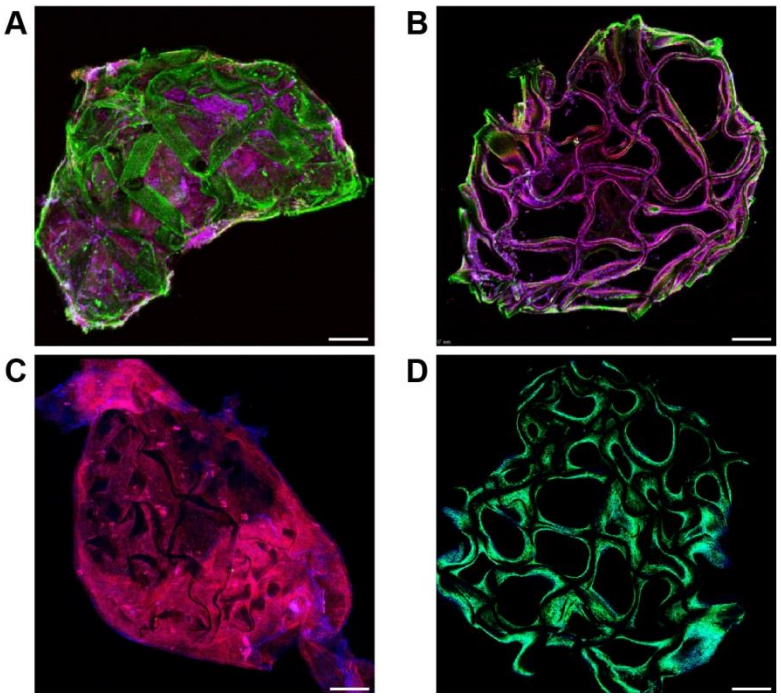

Figure 4.8 Deformation of scaffolds during rotary cell culture experiments. A-D) Selected images depicting how scaffolds can become distorted during rotary cell culture are depicted. This distortion arises from both the tumbling of the scaffold, and the traction forces provided by the cells. Scale bars indicate 500 µm.

A second issue associated with this method of culturing cells was the hypoxic environment which was developed over time. Since this culturing method required sealing the scaffolds inside of a microcentrifuge tube, oxygen was rapidly depleted from the system. While hypoxia is beneficial for the expansion of fibroblasts, it may cause other unwanted signaling events inside of the cells which are unknown. Therefore, for this process to be applied to address fundamental biological questions it is critical for the culture environment to be as defined as possible. Attempts at creating microcentrifuge tubes with oxygen permeable PDMS membranes

showed some initial success, but the process was laborious and difficult to fabricate. Therefore, improvements to the culture platform were required to address these concerns.

4.3.2 Scaffold Frame Development

To address the issue of the scaffolds unexpectedly collapsing from the stresses applied to them during cell culture, a frame system to hold the scaffolds in place during culture was developed. The first generation of frames was hand cut from a stainless steel sheet. The scaffold was placed between two 'C' shaped frames, which were held together by neodymium rare-earth magnets (Figure 4.9 A). Preliminary tests showed that the frames significantly reduced deformation of scaffolds during cell culture, leading to the next generation of scaffold holding frames.

Rectangular frames were cut using a water jet such that they could fit inside of the microcentrifuge tubes used during cell culture (Figure 4.9 B left). The scaffolds were mounted and cultured with cells utilizing a similar technique as with the 'C' shaped hand cut frames. After culturing cells for more than three days in this setup, it was found that the cells did not look healthy, and many had died. Presence of the rare-earth magnets in the cell culture media was determined to be the issue, making a redesign of the scaffold frames necessary. The redesigned system utilized a frame which contained notches at the top and bottom which allowed for placement of orthodontic bands. Additionally, it was shortened such that it could be propped up inside the well of a 24 well plate, reducing the footprint necessary to culture cells using this system. This provided a means of holding the scaffold together with sufficient force to prevent scaffold deformation (Figure 4.9 B right). Preliminary experiments with the third generation scaffold frames proved to be successful; however there was a significant waste of space in this

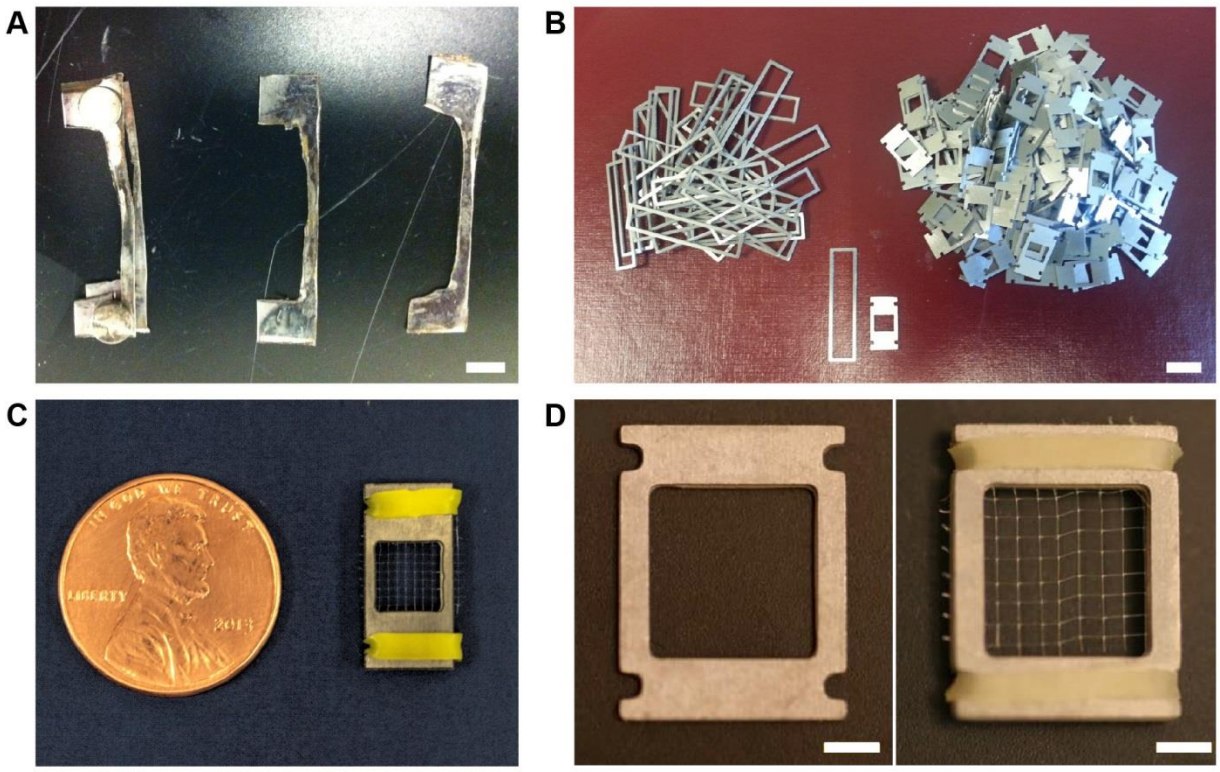

Figure 4.9 Evolution of scaffold frames. A) First generation scaffold frames were hand cut and held together by rare-earth magnets. They were designed to fit inside of microcentrifuge tubes. **B left)** Second generation scaffold frames function in much the same way as first generation, but are fabricated using water jet cutting. **B right)** Reducing the size of the scaffold frames and notches for orthodontic band fastening were introduced in the third generation of scaffold frames. **C)** Fourth generation scaffold frames contained enlarged area for cell culture. **D)** Fifth generation scaffold frames were fabricated using water jet cutting, and were designed to lay flat in the bottom of a 24 well plate. Frames were tumbled in silica after fabrication to smooth the edges to prevent them from cutting the scaffold. Scale bar indicates 5mm (A), 1 cm (B), 2 mm (D).

design, which led to the fourth generation scaffold frames, also created using water jet cutting. These frames functioned in the same way as the third generation design, but had significantly greater area for cell growth (Figure 4.9 C). This fourth generation of scaffold frame was placed at an angle inside of a 24 well plate during cell culture experiments, which was non-ideal. However, smaller frames could not be made using the water jet cutting technology. Therefore, a photoetching process was utilized to create a frame which could fit inside of a 24 well plate

(Figure 4.9 D). After photoetching, the frames were tumbled in silica to smoothen the edges, as the photoetching process created sharp corners which cut the scaffolds during mounting.

Beyond simply holding the scaffold in place, the frames served two other purposes. First, it allowed the handling of scaffolds laden with cells without disturbing the cellular formations. Transferring scaffolds to different wells is necessary after seeding scaffolds, as the cells which did not adhere sink to the bottom of the well and die, giving off unwanted chemical signals. With the frame, transferring the scaffold from well to well is as easy as picking up the frame and moving it to a new well. The second role of the frame is to suspend the scaffold off the bottom of the 24 well plate. The orthodontic bands which hold the frames together also act as a spacer between the face of the frame and the bottom of the well. This suspends the scaffold away from the surface, allowing for the cells to be cultured only on the scaffold, not on the plastic.

4.3.3 Improved 3D Cell Culture System

Development of the new scaffold frames led to a change in how cells were cultured on scaffolds. The general schematic is illustrated in Figure 4.10. A scaffold was mounted into the scaffold frame and dynamically coated with fibronectin. Improved fibronectin coatings were obtained when the scaffolds were held in place by the frames. These coated scaffolds were then seeded with cells in one of two ways. The first way was by placing 1 ml of a cell suspension containing 100k to 200k cells into a microcentrifuge tube with the fibronectin coated scaffold. Tumbling the tube overnight allows for the fluid motion to help the cells spread evenly across the entire structure. The second seeding method uses a 24 well plate, where the frames holding fibronectin coated scaffolds are placed in an ultra-low-binding surface. The orthodontic bands on the frames hold the sandwiched construct off from the surface of the plate, allowing transport on both sides of the scaffold. The cells were concentrated such that the 100k to 200k cells were suspended in 0.1 ml of medium. Placing a 100 µl droplet onto the scaffold, and letting it incubate for 4 hours prior allows the cells to attach to the fibronectin matrix deposited onto the scaffolds. After 4 hours, an additional 900 µl is added to the 24 well plate. The next day, the scaffolds are removed from the well they were seeded in, and placed in a new ultra low-binding well to minimize effects from cells which did not bind to the scaffold. If the cells were seeded using the tumbling method, after tumbling overnight (at least 4 hours) they were removed and placed in an ultra-low-binding 24 well plate and covered with 1 ml of media. From here, the cells on scaffolds were treated in the exact same manner as cells cultured in 2D on 24 well culture plates. The culture medium was changed every 2 – 3 days, or as needed, depending on the cell type. After three days of culturing, it was found that cells formed confluent 3D volumes, henceforth referred to as microtissues, across the entire scaffold structure.

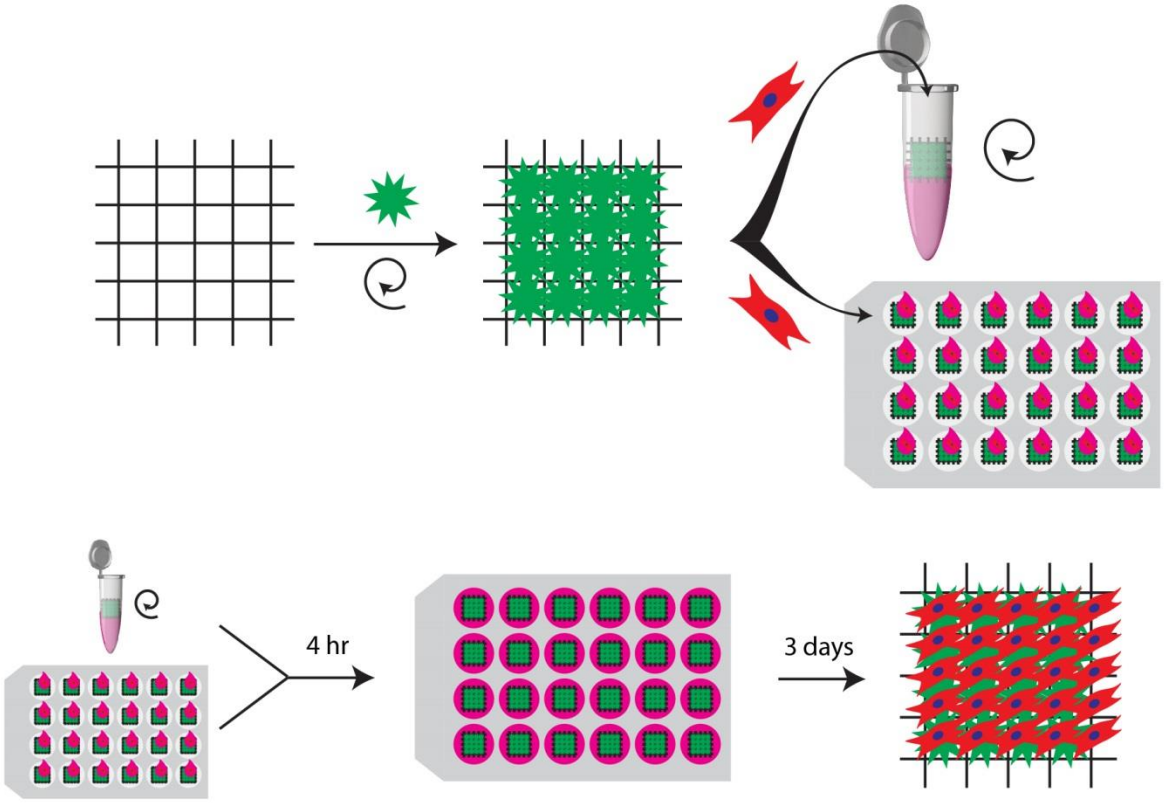

Figure 4.10 Schematic of improved 3D cell culture system. Scaffolds mounted in frames are dynamically coated with fibronectin. Cells are seeded in one of two ways: tumbling in a microcentrifuge tube, or in concentrated droplets in ultra-low-binding 24 well plates. After seeding for at least 4 hours, the scaffolds are placed in 1 mL of media in ultra-low-binding 24 well plates, and are henceforth treated like normal cells on tissue culture surfaces. Medium exchange is performed every 2 – 3 days as needed. After approximately three days of culture, cells reach confluence on the scaffolds.

4.3.4 Application of New 3D Cell Culture System

One of the major advantages of the new cell culture system is that the culture environment is no longer limited by the space confinements within a microcentrifuge tube. Placing a scaffold on any 2D surface allows for cells to be cultured in a 3D environment, which provides a direct means for potential wide adaptation in the field, and no longer suffering oxygen depletion concerns. This is also useful because now larger scaffolds can be fabricated for larger scale applications. Many tissue engineering applications potentially require hundreds of millions to trillions of cells in constructs at least on the centimeter scale. Such constructs may also have specific shape requirements associated with it to match the defect that needs to be regenerated.

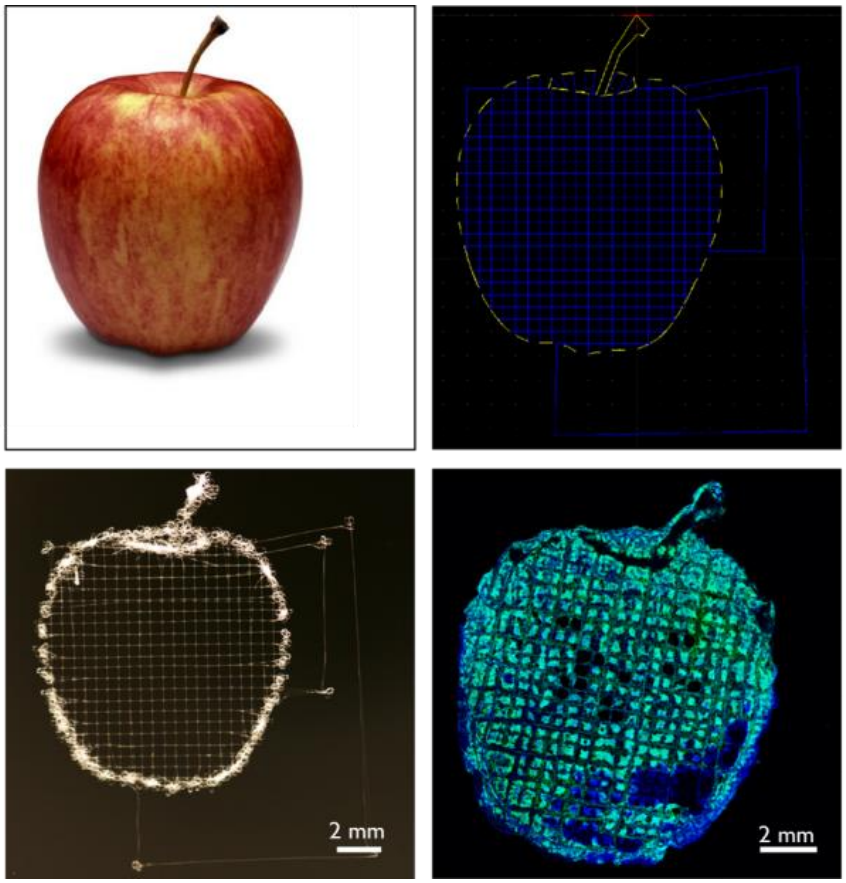

Figure 4.11 Cell culture within defined 3D structures. 3D jet writing stage movements were patterned across an apple figure using CAD software. Yellow lines indicate a slow speed and blue the speed of the depositing fiber. This patterned movement created the scaffold shown in the lower left. Coating the scaffold with fibronectin and culturing with cells demonstrates the scalability of the culture platform. Alexa Fluor 488 phalloidin was used to stain the cell actin green. Scale bars indicate 2 mm.

First steps towards this goal using 3D jet writing scaffolds were performed on apple shaped scaffolds which were approximately 1 cm in diameter. A 500 µm square pattern was tessellated across the picture of an apple, and slow and

fast regions of writing were applied (see Section 3.3.3) to create a curled fiber outline and straight fiber segments which form the 3D cell culture area (Figure 4.11). This type of strategy could be used in conjunction with medical imaging to create thin cross sections of tissue corresponding to specific defects. After scaffold fabrication, cells (NIH3T3) were seeded onto the fibronectin coated scaffold placed on a 25 mm petri dish, and cultured for seven days, allowing extra time to ensure the all the pores filled in with cells. Confocal imaging confirms that cells were found across all sections of the scaffold.

Further characterization of the microtissues which develop within the defined 3D pores of the 3D jet writing scaffold was performed using stem cells. Human mesenchymal stem cells (hMSCs) were seeded using the tumbling method on fibronectin coated scaffolds. After culturing the cells for three days on ultra-low-binding 24 well plates, the cells on the scaffold were found to be completely confluent across the entire 36 mm^2 scaffold area (approximately the area of a 96 well plate) (Figure 4.12 A-B). Closer examination of the structure revealed that the cells within the pores of the scaffolds formed complex three-dimensional structures which in some cases were in excess of 200 μm thick. This thickness corresponded to the approximate height of the PLGA fiber stacks which compose the 3D jet writing scaffolds. These 3D microtissues were self-supported within the square pores of the scaffold, and were tessellated across the entire scaffold area.

Comparison of the cell morphology on other tissue culture substrates demonstrate the dramatic difference in cellular environment provided by the 3D jet writing scaffolds (Figure 4.12 C-E). Culturing cells on fibronectin coated glass yields flat 2D cell morphologies, as would be expected from a 2D culture surface. However, comparing cellular behavior on a fibronectin coated non-woven PLGA fiber mat demonstrated that the cells tended to form a thin film across

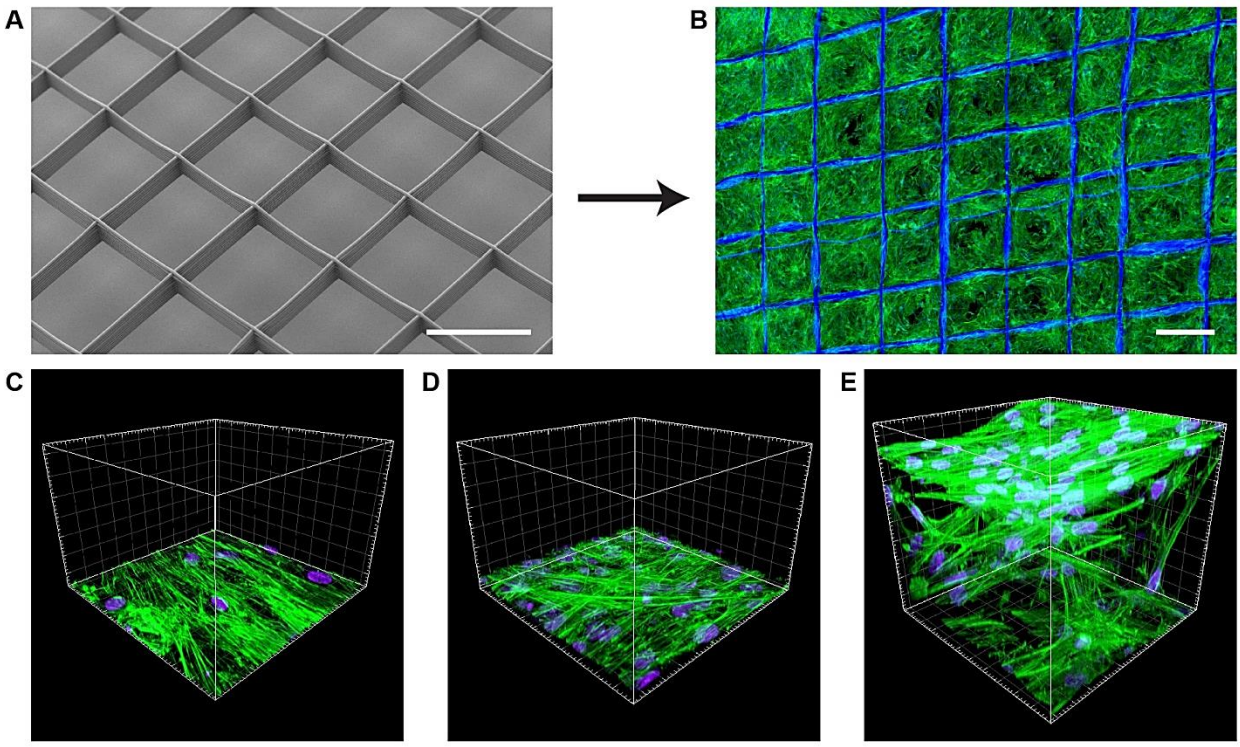

Figure 4.12 PLGA microfiber scaffolds made via 3D jet writing provide an unique 3D cell culture environment. Top) Culturing hMSCs on fibronectin coated 3D jet writing scaffolds for 3 days led to the formation of microtissues which were regularly tessellated across the scaffold structure. Bottom) Comparing the growth of cells on standard tissue culture platforms such as fibronectin coated glass (left) and non-woven PLGA fibers (middle) to 3D jet writing scaffolds showed dramatic differences. The 3D cell growth seen in 3D jet writing scaffolds was unlike any of the other surfaces examined. Scale bars indicate 500 μm (Top), grid spacing represents 20 μm.

the entire surface, with little infiltration into the mat itself. This non-woven substrate was cultured in the exact same manner as the 3D jet writing scaffolds, and similar structures are often used in tissue engineering applications. This direct comparison of scaffolds demonstrates the significantly different environment which the 3D jet writing scaffolds provide to the cells. Culturing cells in this type of environment provides a means for the cells to interact in a 3D environment, forming interactions with other cells and ECM. The tessellated geometry design of the 3D jet writing scaffolds maximizes the amount of open space available for cells to form these 3D interactions, and minimizes the interactions of cells with artificial substrates. In these cases, approximately 96% of the scaffold is open volume, while the PLGA fibers only take up about

4% of the total volume of the scaffold. This leads extremely high ratios of cells to material, with hMSC densities on the scaffolds in excess of 1,400,000 cells/mm^3. Imaging of the entire pore of the scaffolds illustrates the high densities of cells obtained in the 3D jet writing scaffolds (Figure 4.13), and the morphology of the tessellated microtissues formed.

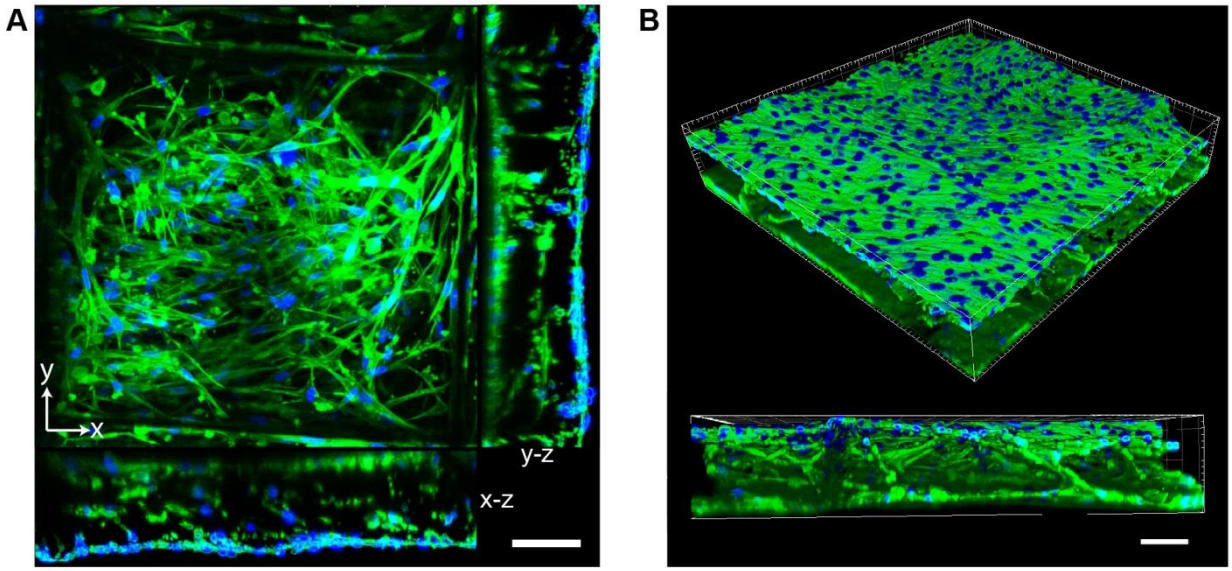

Figure 4.13. Characterization of cells across entire 500 µm pore highlight the microtissue structure. A) Cross sectional views of the entire pore section reveal the consistent thickness of the formed microtissue. Sections in the x-y plane illustrate the complete closure of the entire pore structure. Sections in the y-z and x-z planes both show the depth of the microtissue that is formed. **B)** 3D reconstruction of the entire pore section further shows the density of cells within the pores, and the 3D interactions they are able to formacross the large areas provided to them by the 3D jet writing scaffolds. Scale bars indicate 80 µm (A), and 100 µm (B).

Another benefit of the open scaffold design is that it is readily applicable to many different characterization techniques. Since the cells grow in open 3D constructs, standard assays which utilize automated plate readers can be readily used on this cell culture system. Similarly, confocal microscopy through the entire pore of the scaffolds is feasible. While this seems trivial, the non-woven polymer fiber mats, which are abundant in the field of tissue engineering, interfere with light penetration making imaging through them very difficult to impossible. The large open pores of the scaffolding also make it easy to remove the cells from the scaffold for further analysis using techniques such as flow cytometry, qPCR, and Western blot analysis. In

other 3D cell culture platforms, such as hydrogels, removal of cells from the support is very difficult. Culturing cells in polymer foams or non-woven fiber mats also makes it difficult to extract all of the cells, as the cells which did penetrate into the structure are inherently difficult to remove for further characterization.

With all of these considerations in mind, 3D jet writing scaffolds provide a 3D cell culture environment which can be used in a similar manner as standard 2D cell culture platforms. Seeding of cells can be performed in 24 well plates, requiring only simple media changes, fixing cells follows the same protocols, and final analysis can be performed with any type of analysis which can be performed with 2D cell culture platforms. One advantage that the 3D jet writing scaffolds have that 2D substrates do not is the possibility of serial passaging of cells without the use of digestive enzymes or mechanical separation. Placing an empty scaffold under a cell laden scaffold causes cells to migrate into the new open environment. Subsequent removal of the old scaffold allows the cells to proliferate and fill in the new scaffold. This type of serial passaging could be useful for culturing sensitive cells such as patient derived cells or stem cells.

4.3.5 Human Mesenchymal Stem Cell Differentiation

While hMSCs were shown to form 3D cellular networks within the 3D jet writing scaffolds, the ability of these stem cells to differentiate needed to be ascertained. One of the primary uses for these stem cells is for their therapeutic benefit which derives from their ability to differentiate into a variety of different cell types.[244] Examination of the differentiation ability of these cells was determined through a series of experiments which were meant to drive osteogenic differentiation of the hMSCs while they are in the 3D cell culture environment (Figure 4.14). Fibronectin coated scaffolds in frames were to be cultured with hMSCs for approximately 3 days (or until confluence is reached). After confluence, one set of scaffolds would be maintained in growth medium for four weeks, while the other set was cultured in osteogenic differentiation medium. Evaluation of the cell populations after each week was to be done using qPCR, where gene expression of various bone makers including SP7, RUNX2, and bone sialoprotein (BSP) were evaluated. Additionally, matrix mineralization was monitored using the OsteoImage assay, a fluorescent assay which yields relative amounts of hydroxyapatite concentrations of the matrix. The quantitative nature of this test allows for direct comparison between the growth medium and

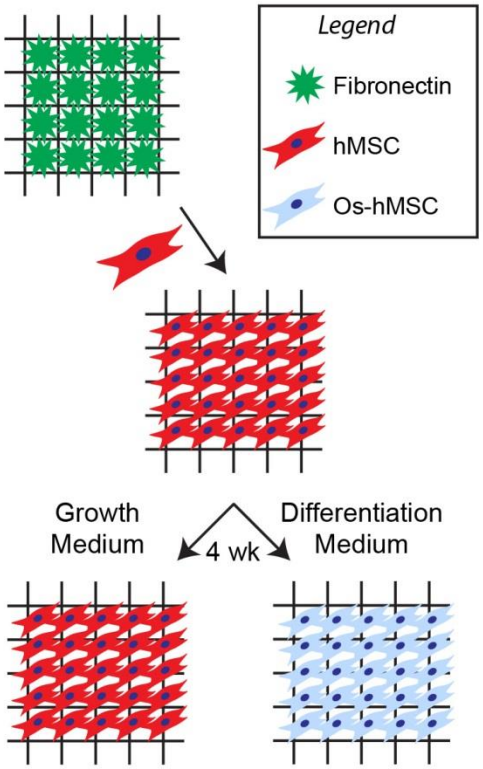

Figure 4.14 Osteogenic differentiation scheme. Fibronectin coated scaffolds in frames are seeded with hMSCs. Once the cells are confluent, half the scaffolds are maintained in growth medium while the other set is cultured in osteogenic differentiation media. The different groups were monitored weekly using a variety of characterization techniques for a total of four weeks.

osteogenic differentiation groups. Colorimetric staining of the two groups after four weeks further verifies the results from the qPCR analysis and hydroxyapatite assay.

Three genes were examined while performing qPCR of the two sets of cells. This analysis was used to indicate whether the hMSCs were differentiating towards an osteogenic lineage in the 3D culture environment. The first gene examined was runt-related transcription factor 2 (Runx2). This gene is often associated with osteogenic differentiation, and has been ascribed the role of 'central control gene' for hMSC differentiation towards an osteoblast phenotype.[245] It is also thought to be the first transcription factor to be turned on in the differentiation cascade. Sp7, the human homolog of osterix, is a second gene specifically associated with the osteoblast phenotype.[246, 247] It is suggested that this gene is activated after Runx2 to aid in the development of mature osteoblasts.[245] This gene, like Runx2, is involved in the regulation of many downstream pathways which affect the production of proteins necessary for osteogenic differentiation. One of these proteins that it regulates is bone sialoprotein (BSP).[247] BSP is a protein present within the matrix of bone, and it is associated with hydroxyapatite formation, and a key protein in the early mineralization of the osteogenic matrix.[245, 247] Analysis of all three genes in qPCR showed that there was little to no increase in any marker until the third week of study. By week 3, the expression of all three genes showed a significant increase ($p<0.05$) relative to the growth medium control (Figure 4.15 A-C). These results provide a good indication that the hMSCs are being driven towards an osteoblast type lineage, as the gene expression of the bone specific transcription factors and proteins is enhanced in the cells relative to the growth medium controls.

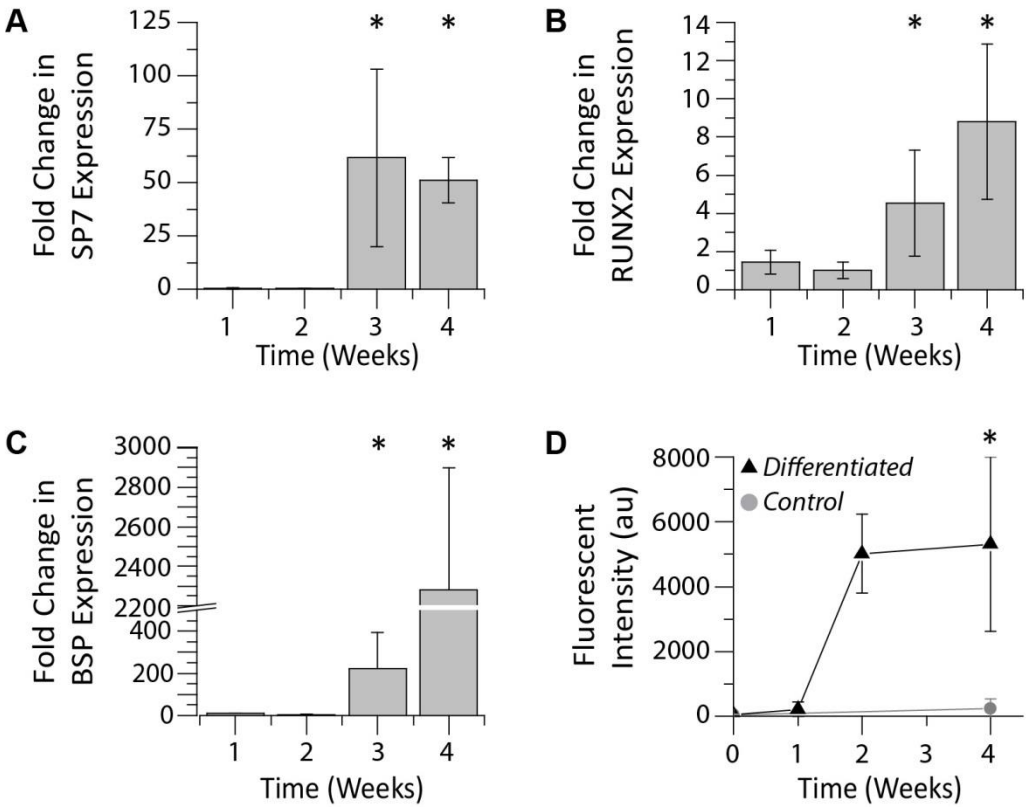

Figure 4.15 Validation of differentiation of hMSCs using qPCR and monitoring hydroxyapatite formation. A-C) Sp7 and Runx2, two genetic regulators corresponding to the osteoblast cell phenotype, demonstrated substantial increases in expression in scaffolds which were cultured in osteogenic differentiation medium compared to the same cells cultured in growth medium. Subsequent increases in bone sialoprotein, a bone specific protein associated with hydroxyapatite, was found to also increase after three weeks of culture in osteogenic medium. **D)** A fluorescence assay for hydroxyapatite was performed on both groups of cells. The growth medium control group was observed at time zero and after four weeks in culture, while the differentiation medium group was monitored after one, two, and four weeks. Large increases in hydroxyapatite were observed after two weeks in culture when cells were cultured in the differentiation medium, while no significant increases were seen in the growth medium controls.

Further verification of successful differentiation of hMSCs on the 3D jet writing scaffolds is given by the presence of hydroxyapatite. As a complement to the genetic markers used in qPCR, a fluorophore which binds to hydroxyapatite, an important mineral component in bone, was used in a fluorescent assay to determine the relative amount of mineralization present in two different groups.[248] Little to no hydroxyapatite was present in the cells maintained in growth medium over the course of four weeks, as no statistical difference was seen between the cells at initial seeding

and after four weeks. However, in the group where the hMSCs were cultured in osteogenic differentiation medium, large increases in hydroxyapatite were observed after two weeks of culture (Figure 4.15 D), consistent with commercial literature differentiation hMSCs on 2D substrates.[249] This corresponded to a visual color change of the cells on the scaffold which were initially transparent, to an opaque white color.

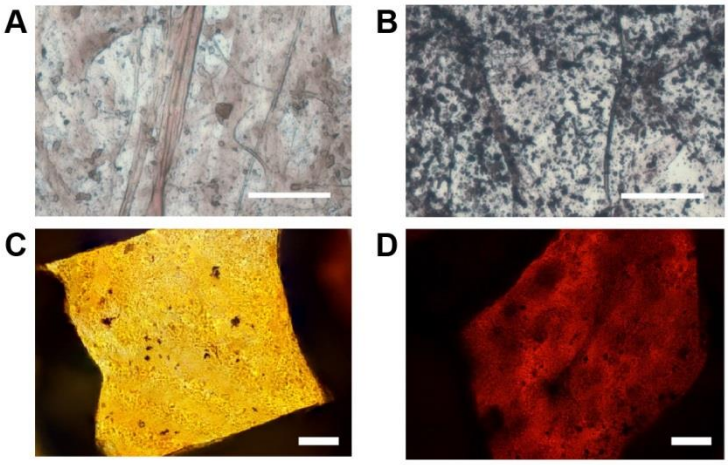

Figure 4.16 Validation of differentiation of hMSCs using von Kossa and Alizarin Red stains. A) hMSCs cultured on 3D jet writing scaffolds for four weeks show little matrix mineralization when cultured in growth medium, as indicated by the lack of black aggregates in von Kossa staining. **B)** When cultured in osteogenic differentiation medium, substantial amounts of black aggregates in von Kossa staining suggests the presence of mineralized matrix. **C)** Alizarin Red staining of hMSCs cultured in growth medium on 3D jet writing scaffolds results in a yellowish color, which in these thick cell constructs corresponded to a diffuse red color. **D)** When cultured in osteogenic differentiation medium, a deep red color is observed, indicating the presence of calcium in the 3D cell environment. Scale bars indicate 50 µm (A,B) and 100 µm (C,D).

In addition to the quantification of matrix mineralization using the OsteoImage assay, mineralization was also visualized using Von Kossa staining,[250, 251] and the presence of calcium was determined using an Alizarin Red staining protocol.[252] Von Kossa staining verified the results seen in the hydroxyapatite fluorescent staining, as a substantial increase in matrix mineralization was observed in samples cultured in osteogenic differentiation medium for four weeks, as indicated by the high density of black aggregates, indicating silver precipitation in the presence of phosphates which are often associated with matrix mineralization (Figure 4.16 B). In comparison to the control which shows little to no matrix mineralization (Figure 4.16 A), which was maintained in hMSC growth medium for four weeks, it is evident that matrix mineralization does

not occur spontaneously on the scaffolds. Similar results were observed in Alizarin Red staining, which is used to detect the presence of calcium. A deep red staining of the hMSCs cultured in differentiation medium after four weeks (Figure 4.16 D), as compared to the small amount diffuse red (seen as yellowish in color) in the growth medium control. This suggests a significant presence of calcium in the hMSCs cultured in differentiation medium, with a corresponding increase in matrix mineralization and hydroxyapatite formation. These staining results coupled with the qPRC, which indicates the genetic activation of osteoblast specific transcription factors and proteins, imply successful differentiation of the hMSCs towards an osteogenic lineage.

This pattern of evidence suggests that the stem cells are not spontaneously differentiating on the scaffolds after four weeks of culture. Instead, the differentiation observed is due to the chemical cues provided by the media. The combination of increased expression of the osteogenic markers and enhanced matrix mineralization validates that hMSCs were differentiated towards an osteogenic lineage [253, 254]. This outlined pattern of evidence indicates that the cells retain their ability to differentiate while in a 3D cell-dense culture environment.

4.3.6 Human Embryonic Stem Cell Culture

Culturing human embryonic stem cell cultures in 2D supports was reviewed extensively earlier in this chapter (see Section 4.1.3). This overview described over a decade of research, all with the same end goal in mind – maintaining the pluripotent nature of these stem cells. The ability of these cells to be differentiated into any type of cell within the human body is what gives them such great therapeutic potential. However, challenges still remain in the development of therapies and tissues from this source of cells. One major challenge is how to culture these cells in a 3D environment. Typically, 3D culture of pluripotent stem cells is performed in hanging drop plates or liquid suspensions.[255] When pluripotent stem cells are placed in these environments they spontaneously and uncontrollably differentiate into all three germ layers.[164] Upon this initial differentiation, various culture strategies have been used to produce the desired cell population. Isolation of the targeted cell type includes such techniques as mechanical dissociation of the cells and sorting for the phenotype of interest, or alternatively incubating them in the proper medium permits only the desired cell type to proliferate.[164] While there are few studies which suggest it is feasible to maintain stem cell pluripotency in specific hydrogel systems, they are limited to culturing small spheroids, with on the order of 30,000 cells.[255-258] Other 3D culture platforms are aimed at directing the differentiation of stem cells.[259] Culturing human pluripotent stem cells in large 3D synthetic constructs has not been achieved, and has great potential in developing treatments for and studying disease states,[260, 261] studying how pluripotent stem cells differentiate in 3D environments,[262, 263] and high throughput expansion of pluripotent stem cells.[264, 265]

Preliminary experiments involved in the culturing of human embryonic stem cells on fibronectin coated 3D jet writing scaffolds, the same scaffold system utilized in the previous section describing human mesenchymal stem cell culture. Characterization of the cells was

performed using immunohistochemical staining of three markers which indicate the self-renewal capacity of the stem cells and their pluripotent nature. The markers Nanog, Oct4, and Sox2 are associated with the self-renewal and pluripotency of human embryonic stem cells.[261] Specifically, the colocalization of all three of these markers in the nucleus of the cell provides initial insight into whether the cells retain the unique set of attributes associated with embryonic stem cells. Previously obtained data by a collaborator (Tugba Topal) illustrate the difference between an undifferentiated and differentiated single cell, when stained by these three markers. In the undifferentiated state, all three signals overlap with the DAPI signal, whereas when the cell has been differentiated, the maker either disappears or moves outside the nucleus (Figure 4.17). This same phenomenon is seen in colonies of cells on 2D culture substrates.

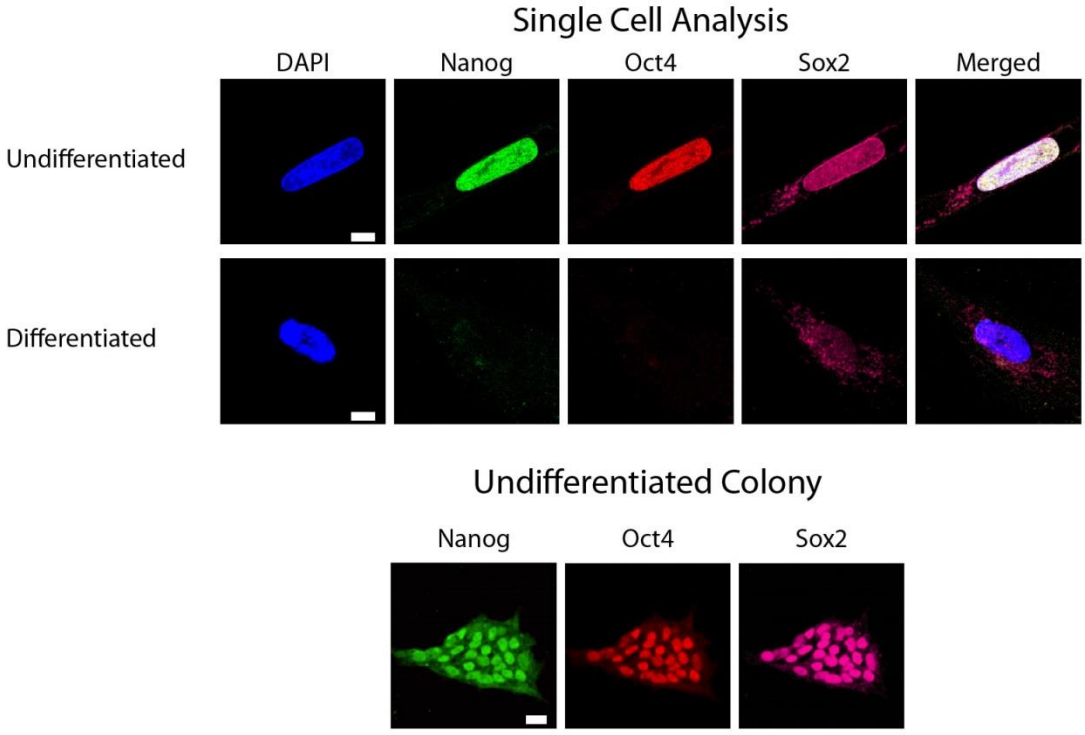

Figure 4.17 Example of immunohistochemical signal expected from differentiated and undifferentiated pluripotent stem cells. Top) Colocalization of Nanog, Oct4, and Sox2 with the nucleus (DAPI) are characteristic phenotypes associated with human embryonic stem cells which are undifferentiated. Middle) Loss of signal, or movement of signal outside of the nucleus, indicates the cell is no longer in an undifferentiated state. Bottom) Undifferentiated colonies have a similar appearance as the single cells. Scale bars indicate 10 μm (Top, Middle), 20 μm (Bottom).

hESCs were seeded onto fibronectin coated 3D jet writing scaffolds, and were cultured for a period of six days prior to fixing and staining with the three markers of interest. Confocal laser scanning microscopy was used to characterize the 3D cell constructs which had formed on the scaffolds after six days. Large image scans of the culture area showed that the hESCs were capable of forming three-dimensional assemblies across the entire 36 mm^2 culture area of the scaffold, similar to the human mesenchymal stem cells (Figure 4.18). Higher magnification z-stack imaging of the structures revealed that all three pluripotent markers (Nanog, Oct4, and Sox2) were collocated in the nucleus of the cells, indicating the cells retained their pluripotency during culture in the scaffold microenvironment. This phenotype was consistent in all areas which were imaged. Further characterization of the pluripotent stem cell populations on fibronectin coated 3D jet writing scaffolds needs to be performed to confirm these preliminary results, including western blot analysis, qPCR, and cell differentiation assays.

This preliminary data is the first demonstration of a 3D cell culture platform which can support large populations of over one million pluripotent cells in a single colony. Cells cultured on these scaffolds form 3D assemblies which are multiple cells thick, and can span over large areas. Implementing these constructs which allowing for expansion and controlled differentiation of pluripotent stem cells in a 3D microenvironment, could have major implications in the field of tissue engineering. With the large numbers of cells in a 3D environment, it also provides a means for studying how populations of stem cells differentiate, potentially leading to new discoveries in pluripotent cell culture and embryonic development.

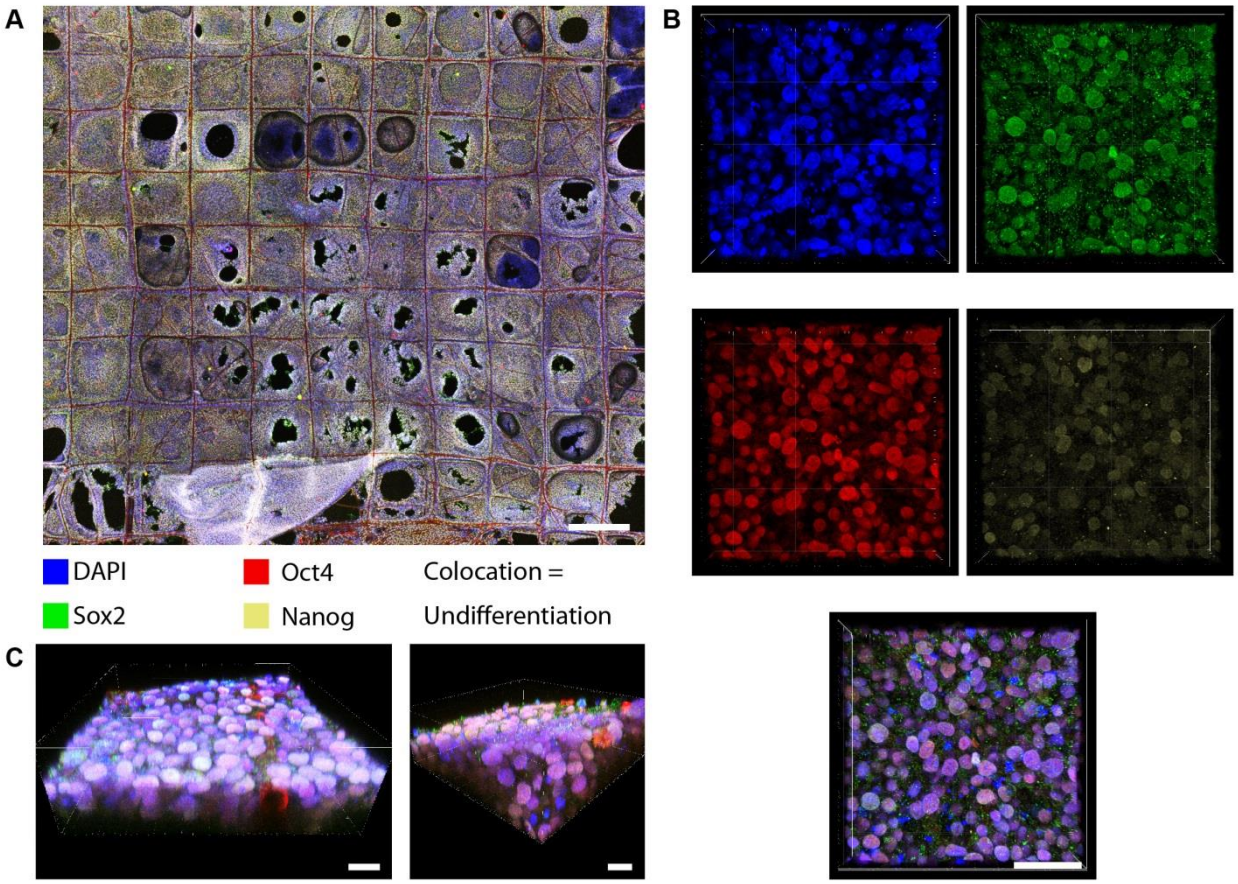

Figure 4.18 Immunohistochemical staining of hESCs cultured on fibronectin coated 3D jet writing scaffolds. A) Large image scans using confocal microscopy reveal the vast area covered by the 3D hESC assemblies. **B)** Blue, green, red, and far red channels all indicate the presence of the corresponding antibody shown in the legend. Colocalization of all three antibodies with the DAPI channel (nucleus) indicates the cells shown are retain their pluripotency. **C)** 3D views in multiple areas demonstrate the 3D nature of the cellular assemblies.Top views all have same scale. Scale bars indicates 500 µm (A), 30 µm (B,C).

4.4 Conclusions

Preliminary works in this area demonstrated that fibronectin coating of 3D jet writing scaffolds provided a platform where cells could adhere to the PLGA microfibers. The rotary motion of the cell culture environment coupled with the fibronectin deposition allowed for the cells to then span, and eventually fill in, entire regions of the designed open area of the scaffolds. This provided a means for culturing cells in an open 3D geometry, with little cellular interaction with artificial substrates. Issues with mechanical deformation of scaffolds during culture were resolved through the design of a scaffold frame, which eventually allowed scaffolds to be implemented using standard cell culture techniques.

In an effort to elucidate the role of scaffolds for the creation of microtissues, human mesenchymal stem cells were cultured on regular square honeycomb scaffolds with 5% relative density (0.25 mm^2 square pores). The large open pore design of the PLGA scaffold created a cell-scaffold biocomposite, where the regular tessellated pattern of cuboid pores minimizes the presence of the synthetic scaffold substrate. Over the course of three days, cells were capable of filling the free volume of the scaffold, creating large areas composed of tessellated microtissues within a polymer fiber scaffold. These biocomposites are more reminiscent of *in vivo* physiology than randomly deposited fiber scaffolds or 2D substrates which tend to promote monolayer cultures rather than 3D microtissues. The PLGA fiber framework acted as a structural skeleton that supported confluent 3D microtissues of stem cells to designed thicknesses of around 150 μm, the diffusion limit of oxygen, with minimal interactions with synthetic surfaces. This allows 3D microtissues, containing high cell densities, to be scaled over large areas due to the user-defined scaffold footprint, which defines both the growth area and microtissue thickness. In addition, the customizable open pore geometry eliminates the tortuosity associated with the pores

of many synthetic polymer constructs, allowing for increased nutrient transport and cell infiltration [126, 155, 266]. The mechanical reinforcement of the 3D microtissues by the fiber scaffold ensures easy handling, and the open honeycomb pore structure allows for compatibility with standard fluorescent assays, histology, confocal microscopy, and quantitative polymerase chain reaction (qPCR).

Osteogenic differentiation was performed on hMSCs microtissue arrays. To validate successful differentiation of the hMSCs towards an osteogenic lineage using a supplemented growth medium, the osteogenic markers runt-related transcription factor 2 (*RUNX2*), bone sialoprotein (*BSP*), and osterix (*SP7*),[253] were monitored over the course of four weeks by qPCR. By week 3, the expression of all three genes showed a significant increase ($p<0.05$) relative to the growth medium control. Additionally, matrix mineralization of the hMSCs on scaffolds was quantified using a fluorescent hydroxyapatite maker, and visualized using Von Kossa and Alizarin Red stains. Over the course of four weeks in osteogenic differentiation medium, a substantial increase in hydroxyapatite deposition was observed on the scaffolds after two weeks which was maintained for the remaining two weeks of the experiment. Von Kossa staining verified this result, as a substantial increase in matrix mineralization was observed in samples cultured in osteogenic differentiation medium for four weeks compared to the control which was maintained in hMSC growth medium. The presence of calcium in the differentiated stem cell groups, and not in the growth medium, further supports the claim that these cells are being differentiated towards an osteogenic lineage. Furthermore, this differentiation is not driven by the 3D culture environment provided by the 3D jet writing scaffolds, or the fibronectin coatings.

Finally, preliminary studies demonstrated the potential of culturing human embryonic stem cells on millimeter scale constructs in a 3D environment. Despite the vast body of literature on

hESC culture, few examples of successful 3D culture techniques have been shown to maintain the pluripotency of these delicate cells. Immunohistochemical staining, and confocal microscopy analysis show the colocalization of three important markers in the nucleus of the pluripotent stem cell phenotype (Oct4, Sox2, and Nanog). Additionally, these cells are shown to be in a 3D culture environment, suspended in the middle of the pores designed into the 3D jet writing scaffolds. This technique could prove to be a new way of implementing pluripotent stem cells in a wide range of applications.

Chapter 5

In Vivo Applications

Some material from this chapter has been adapted with permission from the following manuscript in preparation:

> J.H. Jordahl, L. Solorio, H. Sun, S. Ramcharan, C.B. Teeple, H.R. Haley, K.J. Lee, T.W. Eyster, G.D. Luker, P.H. Krebsbach, J. Lahann. "3D Jet Writing: A novel route towards functional microtissues within tessellated 3D architectures" *In Preparation*.

5.1 Background

5.1.1 Bone Regeneration Models

The ability of the engineered microtissue arrays to regenerate a critical bone defect *in vivo* was assessed in the experiments performed in this chapter. The purpose of these experiments is not to show that these tissue engineered constructs are the only means of healing this type of defect. Instead, the aim of this work was to show the versatility of the 3D cell culture platform, its ability to be utilized in a wide variety of applications, and how cell-dense structures can heal critically sized defects. Healing this type of defect has been accomplished using a wide variety of

different techniques, which often include a combination of three different components: A scaffold, cells, and growth factors.

Tissue engineering strategies aimed at healing a critical sized defect in bone typically relies on a growth factor loaded scaffold, either with or without cells. The most common growth factor used in this field is bone morphogenic protein-2 (BMP-2), and it is delivered to the defect site in a number of ways. First, it can be released from a growth factor delivery vehicle.[267] This can take the form of particles, hydrogels, or fiber based delivery systems.[267-269] Maintaining a constant release over long periods of time is of critical importance to achieve proper healing of the defect.[270] Genetic manipulation of cells which overexpress growth factors such as BMP-2 provide a means of circumventing this problem, as they consistently deliver the necessary growth factor to the desired site over longer periods of time (as long as the implanted cells remain within the defect). [271] The issue related to these methods is the supraphysiologic doses of growth factors needed to elicit the desired healing response, making it an expensive treatment method.[272] Half-lives of free growth factors are generally very short, as these molecules are powerful signaling agents within the body.[272] Therefore, prolonged exposure to such high levels of growth factors may have significant implications that are yet not fully understood. [272]

This has driven the field of cell based techniques which utilize a scaffolding platform to deliver cells to a defect site.[273-280] Incorporation of hydroxyapatite on the scaffold delivering cells to the defect site is a common means of regenerating bony tissue without the use of growth factors.[275, 277] While these systems have demonstrated that pre-culturing stem cells or differentiated stem cells can improve defect healing outcome, other sources have shown surfaces coated with hydroxyapatite cements are sufficient to heal substantial defects in humans.[281] Still other examples include polymer based scaffolds which elicit some healing response within the

defect. However, inclusion of cells with these scaffolds generally improves the regeneration capacity of the device.[273, 275-277, 279, 280] The most common type of cells used in regenerating bony defects are human mesenchymal stem cells (hMSCs).[273, 275-277, 279, 280] Bone marrow, fat tissue, and dental pulp are some of the more common site from which hMSCs are isolated from donors.[282, 283] These are multipotent cells which are found in various tissues of the body that retain the capacity to osteogenically differentiate.[244] Other common methods utilize co-cultures of hMSCs with endothelial cells, which are used to create more vascularized tissue engineered samples.[274, 280] This helps incorporate the implant with the host tissue, and also enhance transport within the device itself. Examples of utilizing scaffold-free tissue engineering constructs, such as spheroids or cell sheets, have not been shown effective in healing bony defects, although there has been some success in creation of ectopic bone implants.[284, 285]

While these cell based techniques have shown success in healing bony defects in a variety of different animals, they all consist of scaffolds seeded with fairly low ratios of cells to material volume. Generally, these constructs contain from 2000 to 200,000 cells/mm^3 of scaffold material.[273-280, 286, 287] In comparison, scaffolds generated using 3D jet writing contain cell densities in excess of 1,400,000 cells/mm^3 scaffold material. These implanted devices, with the high loading of cells, were used to demonstrate the potential of tessellated 3D microtissues to regenerate critical sized defects in mice.

5.1.2 Bone Metastatic Microenvironments

In the United States, one in eight women will be diagnosed with invasive breast cancer within their lifetime. This correlates to nearly 250,000 new cases in the year (as of 2016).[288] While these statistics can be humbling, the death rate from this disease has been dropping since 1989, which is often attributed to early detection and improved treatment regimens. However,

once a tumor has metastasized, overall prognosis is poor.[289] Among the most common metastatic sites is bone, a site detected in 65 – 80% of patients with metastatic breast or prostate cancer.[290] Consequently, bone metastases are found in approximately 350,000 cancer related deaths per year.[291] While seen within about three years of diagnosis, metastases can occur throughout the lifetime of the patient.[292] This makes the treatment of these malignant sites ever more important.

While the origin of metastatic cancer cells has yet to be clearly understood, numerous mechanisms behind metastatic breast cancer cell association to the bone microenvironment have been proposed. Initial homing of the cancer cells to their final metastatic site is thought to be a chemotaxis driven process, which also requires proper integrin interactions.[290, 293, 294] The fibronectin, vitronectin, and osteopontin are thought to be important extracellular matrix proteins found in the bone metastatic environment. Invasion of the bone, after the cells have homed to the metastatic site, relies on the remodeling of the bone to release factors which enhance the growth of tumor cells, producing a positive feedback loop leading to metastasis formation.[290] Presence of soluble calcium ions, bone sialoprotein, bone morphogenic protein, and other factors including hypoxia found in osteolytic lesions, formed by the metastasized cancer cells, all have been associated with tumor growth within the bone matrix.[295]

Current model systems include orthotopic tumors, xenograft models, humanized rodent models, and tissue engineered systems. However, each of these model systems have significant drawbacks associated with them. Orthotopic bone metastasis models involve direct injection of cancer cells into the long bones of mice, such as the femur. While this can produce tumors, they are more characteristic of late stages of the disease.[296] Intracardiac injection allows for human cancer cells to be distributed throughout the body of the model animal, and often leads to

metastasis.[297] However, the different signaling pathways present between the two species limits the utility of these models in studying metastasis to human bone.[298] Humanized rodent models aim at getting around this limitation through the implantation of human bone into an immune compromised mouse. This often leads to preferential invasion of human cancer cells to the human bone microenvironment.[297] The natural variation of donor bone, the loss of tissue viability, and the limited supply of donor tissue limits the widespread use of these systems. These studies often include radiographic analysis of the bone to look for metastases, however micrometastatic lesions are typically below detection thresholds.[299] Other methods which utilize PCR and histological analysis of bone metastases rely on analysis of small sample populations.[300] Therefore, there is an inherent need for model systems which can recapitulate the metastatic process into bones.

Tissue engineered bone constructs have also been used in a similar manner as the humanized rodent models.[301] The scaffolding used to create the tissue engineered bone can be customized to probe specific aspects of the metastatic microenvironment, and can be seeded with consistent populations of cells, eliminating much of the variability seen in the humanized rodent models.[301] Examples of such tissue engineered systems include polymer scaffolds seeded with human osteoblastic cells or differentiated mesenchymal stem cells. These systems often utilize scaffolds composed of dense mats of polymer fibers, which limits the ability of cells to evenly penetrate into the device.[155, 296] This leads to a layer of cells which encase the outer surfaces of the tissue engineering scaffold, with more disperse seeding of cells within the middle of the construct.[296] Coating the surfaces of the devices with extracellular matrix proteins enhances the adhesion of the cells to the surface of the fibers, and incorporation of growth factors is often used to induce bone formation.[296, 301] These models often require long implantation times, on the order

of 2 – 3 months, to engraft into the host and form the desired bone environment.[296] Additionally, tissue engineered bone implants for these studies are often large in comparison to the size of the mouse, making it difficult to monitor in real time. The long implantation times, large implant size, and utilization of growth factors all limits the data that can be obtained from these devices. Development of a bone-like microenvironment created in a tissue engineered construct to address these drawbacks could be used to accelerate the development of targeted therapies to reduce or eliminate metastasis into bone.

5.2 Materials and Methods

5.2.1 Calvarial Defect Model

Use and care of the animals used in this study followed the guidelines established by the University of Michigan Committee for the Use and Care of Animals. Severe combined immunodeficiency (SCID) mice were anesthetized by intraperitoneal injection of ketamine and xylazine before the surgery as an analgesic. The skin on the head of the mouse was disinfected with a 70% ethanol solution. Two 3 mm-defects were created in the left and right parietal bone of the skull with a trephine bur. Four treatment regimens were administered to the defect site: 1) No treatment, 2) PLGA microfiber scaffold, 3) PLGA microfiber scaffold with a cultured volume of human mesenchymal stem cells which had been differentiated using osteogenic media *in situ* for two weeks, 4) injection of non-differentiated human mesenchymal stem cells. Treatment options were administered directly to the defect site. Circular cutouts of PLGA microfiber scaffolds with and without cells were made using a 3mm tissue punch. Three circular cutouts were stacked on top of one another to achieve a comparable thickness to the defect. hMSC injections, containing the same number of cells as the PLGA microfiber scaffolds with differentiated hMSCs, were suspended in a volume of saline equal to the volume of three PLGA microfiber scaffold cutouts. After implantation, the overlying tissue was surgically stapled over the defect area and allowed to heal for 8 weeks. After 8 weeks the mice were euthanized for further analysis.

5.2.2 Metastatic Cancer Model

The University of Michigan IACUC approved all animal procedures performed in this study. We implanted 4 week osteogenically differentiated hMSC scaffolds or control scaffolds

coated with fibronectin into subcutaneous tissues of backs of 8-10 week-old female NSG mice (Jackson Laboratory) (n = 5 per experiment). Two weeks after implanting scaffolds, we injected 1 x 10^5 MDA-MB-231 human breast cancer cells (ATCC) directly into the left ventricle of mice to produce systemic metastases.[302] We used MDA-MB-231 cells stably transduced with a lentiviral vector for FLAG labeled click beetle green luciferase to enable bioluminescence imaging and histological analysis.[303] We imaged living mice with an IVIS Spectrum instrument (Perkin-Elmer) to detect metastases as described.[304] When mice had to be euthanized for tumor burden, we injected luciferin immediately before euthanizing each animal and then imaged metastatic foci ex vivo as we have reported previously.[302]

5.2.3 Tissue Preparation and Histology

Extracted samples of mouse calvaria were placed in Z-fix (Anatech Ltd.) for three days, and were subsequently stored in 70% ethanol until microCT imaging was completed. Prior to histological processing, samples were decalcified in a 10% EDTA solution in DI water (adjusted to pH7 with NaOH). Decalcified samples were embedded in paraffin and 10 μm sections were taken at the middle of the defect. Sections were stained using hemotoxylin and eosin for light microscopy observation.

Ectopic scaffold implants in cancer metastasis studies were dissected out of the mouse flank, were scanned with bioluminescent imaging where appropriate, and placed in a 4% formaldehyde solution for 2 days. The 4% formaldehyde was then exchanged for a 70% ethanol solution for storage prior to histological processing.

5.2.4 Immunohistochemical Staining of Metastatic Cancer Cells

Ten micron paraffin embedded tissue samples containing the explaned scaffolds, both the fibronectin coated control and osteogenically differentiated hMSCs, were deparaffinized by soaking the slides in two changes of xylene for five minutes each. Once cleared, an ethanol ladder was used to rehydrate the tissue sample, with three minute washes in 100%, 100%, 95%, 70%, 50% ethanol respectively. This was followed by a ten minute soak in a 3% hydrogen peroxide in methanol to block endogenous peroxidase activity. The slides were then rinsed two time, for five minutes each , in PBS. Antigen retrieval was accomplished via a 10 minute incubation in 95 - 100°C citrate buffer at pH 6.0. After cooling for 20 minutes, the slides were then washed two times for five minutes in PBS. The tissue sections were circled with wax, and blocked for 1 hr in blocking buffer (10% bovine serum albumin in DI water). Slides were then washed two times for two minutes in PBS, and then droplets of diluent (1% bovine serum albumin in DI water) were incubated on the sections for five minutes. The excess diluent was removed from the slide, and primary antibody (anti-FLAG produced in rabbit) diluted in the diluent to a concentration of 10 µg/ml. Droplets of the primary antibody were placed on the tissue sections for 60 minutes, and the slides were rinsed two times for five minutes in PBS. This was followed by incubation of the tissue sections in secondary antibody (Alexa Fluor 647 conjugated anti-rabbit IgG produced in goat) diluted in diluent at 10 µg/ml for 30 minutes. After secondary antibody incubation, slides were washed twice in PBS for five minutes, and subsequently counterstained using 4',6-diamidino-2-phenylindole (DAPI) at a 2 µg/ml concentration. Slides were then rinsed under running tap water for 15 minutes, and subsequent dehydration using an alcohol ladder consisting of 50%, 70%, 95%, 95%, 100%, 100% washes respectively, each for five minutes. Slides were then cleared by incubating in three xylene

washes for two minutes each. Once dried, ProlongGold was used to mount a cover slip to the slide, and allowed to cure for 24 hours prior to confocal imaging. Negative controls were performed without the use of a primary antibody to ensure non-specific binding of the secondary antibody to the tissue sections was not occurring.

5.2.5 MicroCT

Specimens were embedded in 1% agarose and placed in a 34 mm diameter tube and scanned over the entire length of the calvariae using a microCT system (µCT100 Scanco Medical, Bassersdorf, Switzerland). Scan settings were: voxel size 18 µm, 70 kVp, 114 µA, 0.5 mm AL filter, and integration time 500 ms. Analysis was performed using the manufacturer's evaluation software, and a fixed global threshold of 18% (280 on a grayscale of 0–1000) was used to segment bone from non-bone. A 3 mm diameter cylindrical ROI was centered over the defect in the calvariae to determine the amount of bone regeneration at the site.

5.2.6 Statistics

Statistical significance was determined by one way analysis of variance (ANOVA, $p<0.05$). A Tukey multi-comparison test was used to distinguish differences between groups. Minitab was used to perform all statistical analyses. All data is reported as mean ± standard deviation unless otherwise noted.

5.3 Results

5.3.1 Tissue Regeneration: Calvarial Defect

A mouse calvarial defect model [305] was used to investigate the *in vivo* integration of osteogenic microtissues into damaged tissue. The following treatments were administered to the defect sites: no treatment, a PLGA scaffold, a PLGA scaffold with osteogenically differentiated hMSCs (Os-hMSC), and an equivalent injection of undifferentiated hMSCs (Figure 5.1). After treatment, the defects were allowed to heal for eight weeks and were subsequently analyzed by microCT and histology. Os-hMSC samples were prepared by incubating hMSCs on fibronectin

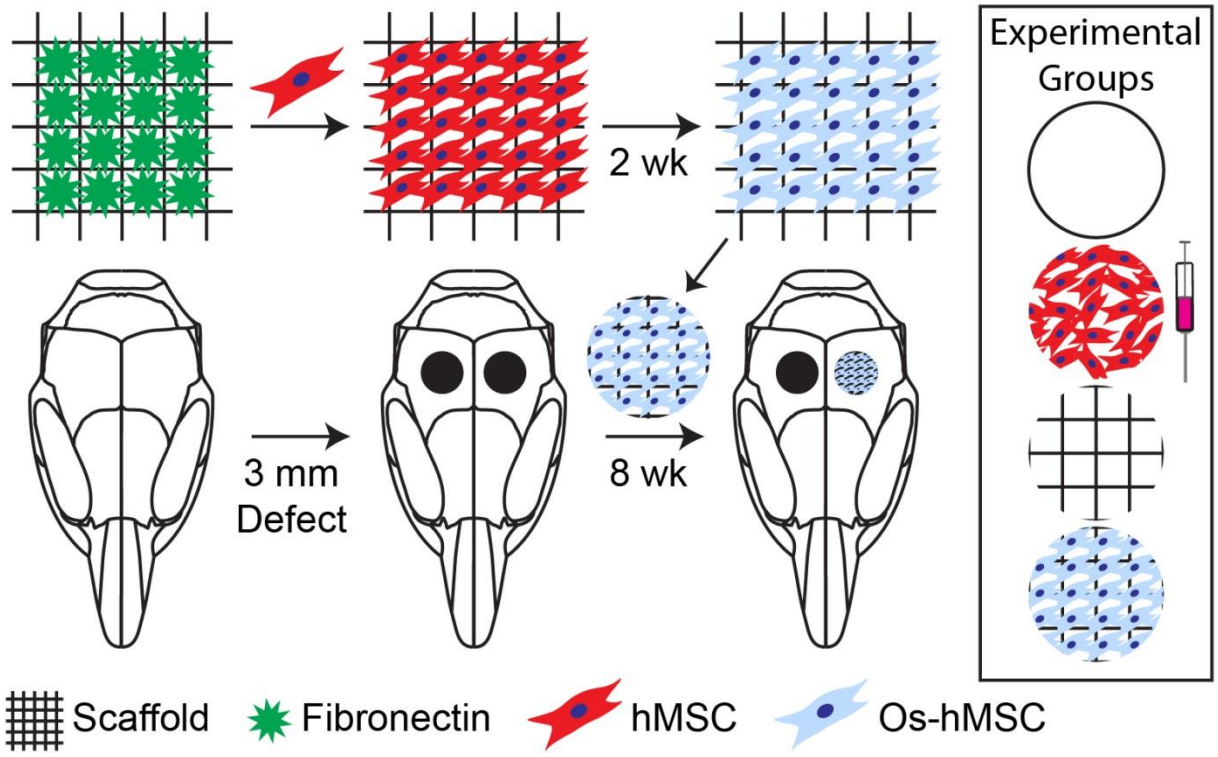

Figure 5.1 Schematic illustration of the calvarial defect model for tissue regeneration. Fibronectin coated scaffolds were incubated with hMSCs until confluence was reached. The stem cells were subsequently differentiated for two weeks using osteogenic differentiation medium. Two 3 mm defects were placed in the left and right parietal bone of the mouse, allowing for two groups to be tested in each mouse. Experimental groups included: No treatment, injection of hMSCs, scaffold implantation, and Os-hMSCs cultured on scaffolds. Circular cutouts of these scaffolds, equivalent injection of cells, or no treatment was administered directly to each defect site.

coated 3D jet writing scaffolds. The scaffolds were made using PLGA, and had a square honeycomb design with 500 µm pore spacings. Once the cells were confluent, the culture medium was changed to osteogenic differentiation medium where the cells were cultured for two weeks. The two week time point in previous experiments correlated to the time right before the cells began expressing high levels of osteogenic transcription factors. Three circular punchouts, 3 mm in diameter, of the Os-hMSC scaffolds were stacked on top of one another and implanted into a 3 mm calvarial defect. Defects were placed into the left and right parietal bone of the mouse, allowing for two groups to be placed into one mouse.

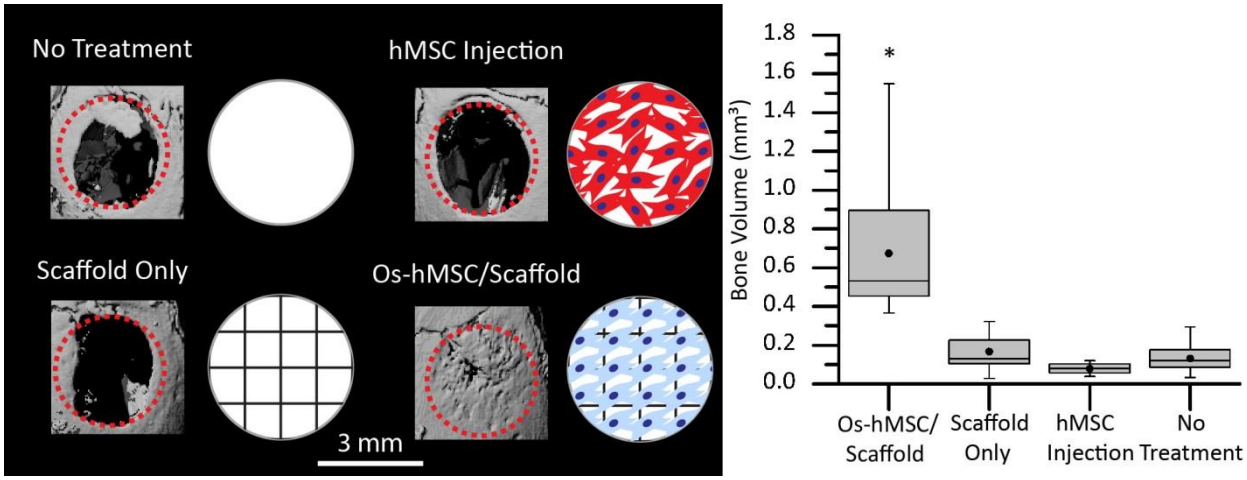

Figure 5.2 MicroCT analysis of calvarial defects after eight weeks. Explanted defect sites were analyzed using microCT. 3D reconstructions of the defect site were created from the scan data. This demonstrated that the Os-hMSC on scaffolds group was the only experimental group capable of filling in the defect site. Quanification of new bone volume was performed by selecting a 3 mm diameter region of interest corresponding to the defect site. This demonstrated the Os-hMSC groups produced significantly more bone in the defect than the other three groups.

MicroCT demonstrated that the osteogenically differentiated samples produced significantly more new bone than the other treatment methods (Figure 5.2). Visualization of the entire defect site revealed that only the Os-hMSC group was capable of completely closing the defect site, with other groups having minimal new bone growth restricted to the periphery of the defect. Quantifying the amount of new bone formed within the defect was performed by creating a 3

mm cylindrical region of interest where the defect was created. Further analysis of this selected volume allowed for a calculated new bone volume within the defect site.

Histological analyses affirmed this result, showing significant new bone volume present in the Os-hMSC group. Looking over the entire defect site (Figure 5.3), it was seen that very little new bone (Bright pink) was formed in most groups, with only small ingrowths of bone near the edges of the defect. The Os-hMSC group, however, was able to produce significant amounts of new bone, nearly closing the entire defect area. Closer examination of the middle of the defect areas show more histological detail (Figure 5.4), including the presence of what is thought to be PLGA fibers from the 3D jet writing scaffolds, embedded within the new bone. Again, the other three treatment methods provided little new bone formation.

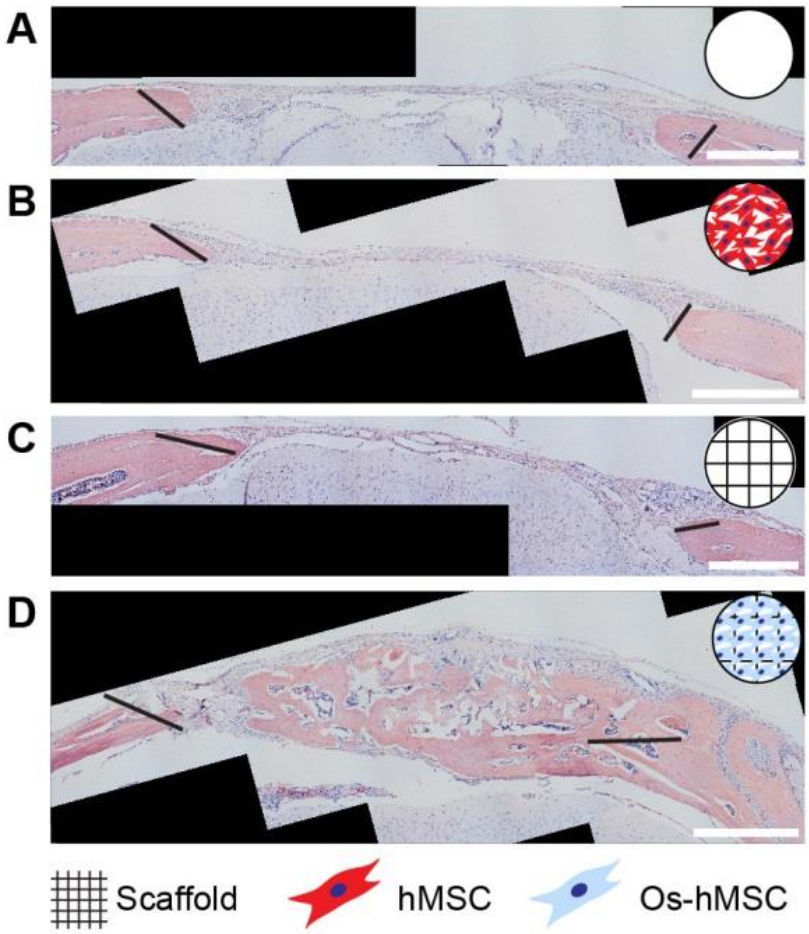

Figure 5.3 Histological analysis of entire calvarial defect site. Hemotoxalin and Eosin (H&E) staining of the histological tissue sections was used to discern the areas in which new bone had formed within the defect site. Groups of no treatment (A), hMSC injection (B), and scaffold alone (C) produced little to no new bone formation within the defect site. The Os-hMSC on scaffold group (D) was able to produce substantial new bone formation, nearly closing the entire defect site. Scale bars indicate 500 μm.

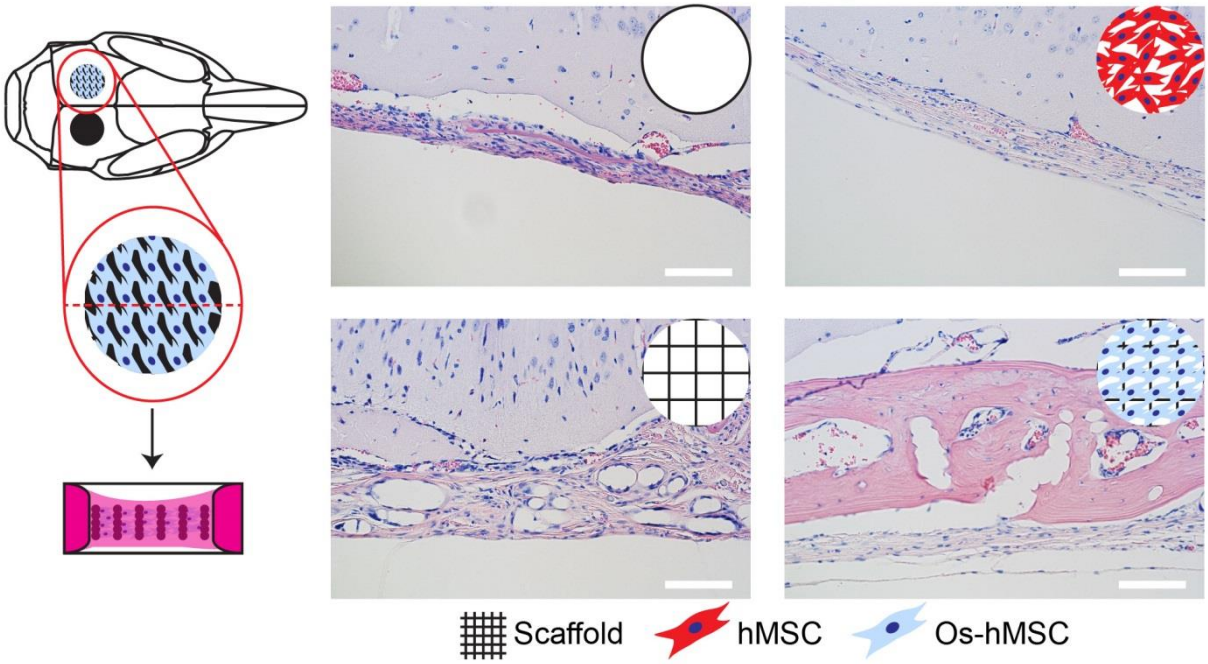

Figure 5.4 Detailed view of histological analysis of calvarial defect site. H&E staining of histological sections revealed significant new bone formation (bright pink areas) in the Os-hMSC on scaffold group, with PLGA microfibers embedded within the new bone. Other treatments led to little to no new bone formation within the defect site. Scale bars indicate 100 µm.

Overall these results demonstrate that neither cells nor scaffolds alone are sufficient to heal the defect. Instead, the delivery of hMSCs differentiated directly on 3D jet writing scaffolds proved most efficacious, as they produced the highest volume of new bone within the defect and even showed potential to close the defect site. It is hypothesized that improved healing of the defect can be attributed to preservation of cell-cell and cell-matrix contacts in a pre-established 3D environment during *in vitro* culture and throughout the implantation process. [135] One of the significant advantages of this process is the lack of growth factors used to heal the defect. While most devices which are used to heal calvarial defects utilize growth factor immobilization and release to aid in tissue regeneration, this method simply uses differentiated stem cells which are assembled into arrays of microtissues on biodegradable scaffolds.

5.3.2 Diseased Tissue Model: Metastatic Bone Microenvironments

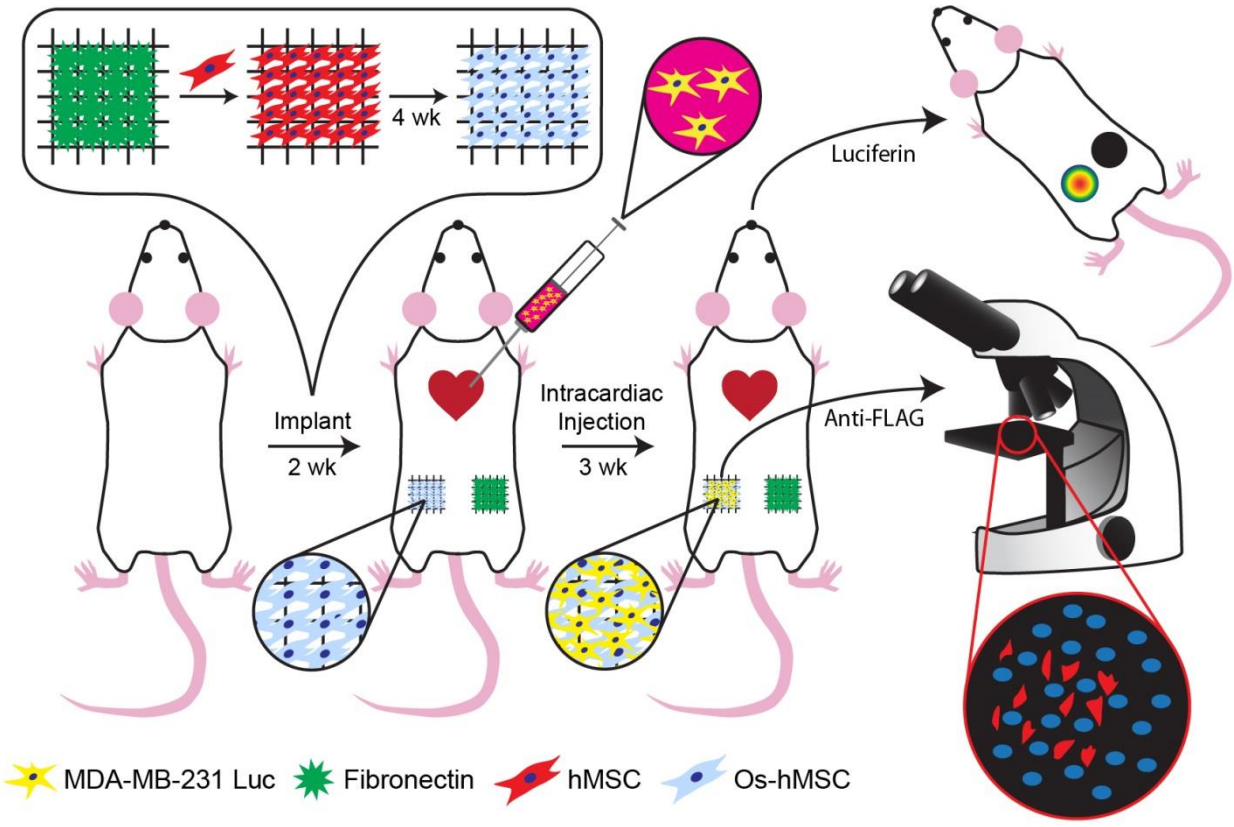

Figure 5.5 Schematic illustration of metastatic bone microenvironment experimental procedure. Fibronectin coated scaffolds were incubated with hMSCs until confluence was reached. The stem cells were subsequently differentiated for four weeks using osteogenic differentiation medium. Circular cutouts of these scaffolds were implanted subcutaneously in the flank of the mouse, with fibronectin coated scaffolds implanted in the contralateral flank as a control. After two weeks, luciferase expressing MDA-MB-231 cells were infused via intracardiac injection. Three weeks after injection, mice were analyzed using bioluminescence and sacrificed. Explanted scaffolds were stained for FLAG, indicating the presence of metastases.

The biological relevance of 3D tissue models have been utilized in applications beyond tissue regeneration, with recent implications as diseased tissues models for cancer and as drug testing platforms.[136, 296] Specifically, we evaluated the use of 3D microtissue arrays cultured in 3D jet writing scaffolds to create a metastatic bone environment at a non-metastatic site (Figure 5.5). Fibronectin coated square honeycomb scaffolds were seeded with hMSCs, and once confluence was reached they were osteogenically differentiated for 4 weeks. These scaffolds

were then subcutaneously inserted into the flank of 6-10 week old female NSG mice (N=5 mice per group). The flank was determined to be an ideal implantation site as metastases are typically not observed in this tissue, allowing for effective determination of implant efficacy and bioluminescent monitoring. Cell free scaffolds, coated with fibronectin and not containing any cells, were implanted in the contralateral flank to demonstrate that metastasis was a function of the implanted engineered tissue. Two weeks after implantation of the microtissues, luciferase expressing MDA-MB-231 breast cancer cells were administered via intracardiac injection, reducing first pass effects of the liver and lungs, thus ensuring that the cells were distributed systemically.[296] Bioluminescence and immunohistochemical analysis were used to verify the presence of cancer cells at the implantation site. Explanted scaffolds were examined via histological analysis. Nodule formations, seen in Figure 5.6, indicate that new bone is beginning to form near the implanted 3D jet writing scaffolds.

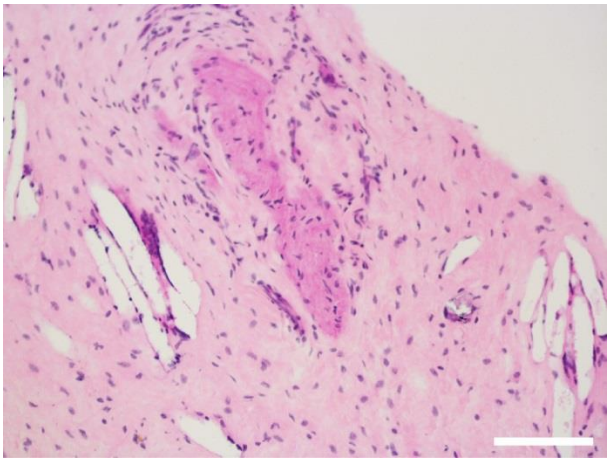

Figure 5.6. Initial ossicifacion indicated by nodule formation. Early indications of ectopic bone formation were seen via H&E staining of histological sections. This demonstrated the formation of nodules indicative of early bone formation. Scale bar indicates 100 µm.

Metastasis of MDA-MB-231 cells was observed in 5/5 osteogenically differentiated hMSC implants, with 2/5 fibronectin coated scaffolds containing metastases, as determined by immunohistochemical analysis (Figure 5.7). Bioluminescent images of explanted scaffolds from mice confirmed the presence of luciferase expressing cells in the mice which were successfully injected with luciferin. The premature death and injection into the bowels allowed only two of the mice to be imaged in

this way. Previous work where two scaffolds containing osteogenically differentiated hMSCs were implanted into both flanks of the mouse demonstrated selective metastasis into the humanized tissue engineered constructs. While these results are preliminary, it demonstrates 3D jet writing scaffolds with a regular square honeycomb scaffold provide a cell culture environment which translates into *in vivo* activity in both tissue regeneration and as a diseased tissue model.

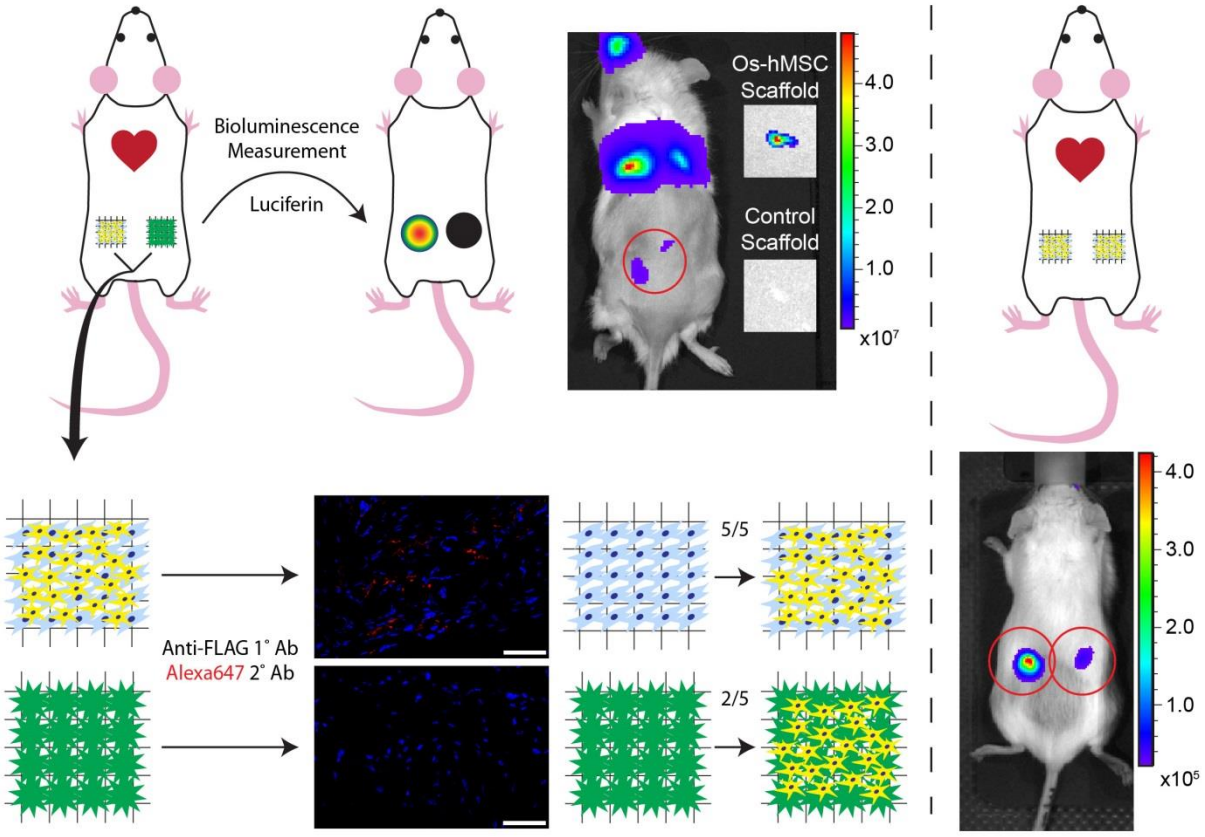

Figure 5.7 Analysis of metastatic bone microenvironments. Mice were examined under bioluminescence to detect the presence of luciferase expressing cells. Explanted scaffolds initially containing osteogenically differentiated hMSCs showed bioluminescent signal, while the fibronectin controls showed no bioluminescence. Immunohistochemical analysis of paraffin embedded tissue sections showed that 100% of scaffolds containing differentiated hMSCs were positive for the presence of FLAG labeled luciferase, while only 40% of fibronectin coated scaffolds stained positive for that marker. Implanting osteogenically differentiated hMSCs into both flanks showed the potential for luciferase expressing cells to selectively metastasize into the tissue engineered bone constructs. Scale bars indicate 50 μm.

5.4 Conclusions

The studies outlined in this chapter were designed to validate the versatile nature of the 3D jet writing scaffolds. First, osteogenic induction of hMSCs cultured as 3D microtissues on PLGA microfiber scaffolds were shown to be capable of closing a calvarial defect in mice. While there are numerous tissue engineered constructs which have demonstrated similar capabilities, they often include supraphysiologic doses of growth factors at the defect site.[267-269]

The long term implications of this type of treatment are unknown, and thought to potentially lead to development of cancer.[272] Other systems, which only utilize cells on scaffolds, often contain a low cell to scaffold material ratio less than 200,000 cells/mm^3.[273-280, 286] In the 3D jet writing system, the amount of scaffolds is minimized to the extent where it only takes up approximately 4% of the volume implanted into the defect site. The remaining volume consists mostly of cellular material which was pre-cultured, and differentiated, *in vitro*. Cell to material ratios around 1,400,000 cells/mm^3 scaffold material set this system apart from others used in calvarial defect models. Other cell only based systems, such as spheroids or cell sheets have not been demonstrated to heal bone defects, although they have been shown to create ectopic bone *in vivo*.

The second study highlights the potential of the a similar cellular system to be utilized as a diseased tissue model. Since bone is one of the most prevalent sites for metastasis for many cancers, including breast cancer, studying how cancer metastasizes into a human bone sample is of particular interest. The simulated human bone environment created by the 3D jet writing technique only required two weeks to integrate sufficiently into the surrounding tissue to enable cancer cell metastasis to the site. This model demonstrated that human breast cancer cells are able to home to the site of simulated bone environment, forming metastases in all samples three

weeks after injection of the cancer cells. Other tissue engineered bone metastasis models require months of integration time prior to intracardiac injection of cancer cells, and even at that point only 40% of the samples obtained a metastasis. 3D jet writing scaffolds are also optically transparent, potentially allowing for future use of imaging windows for intravital microscopy to study how cancer cells invade the simulated bone tissue. Other future studies need to be performed to improve integration of the osteogenically differentiated hMSCs with the host tissue.

Chapter 6

Summary and future work

6.1 Summary

This dissertation focused on creating improvements to the electrohydrodynamic co-jetting technology. In Chapter 1, a general theory of electrohydrodynamics was discussed, giving the reader an basic introduction into the fluid dynamics associated with electrified fluid droplets. This set up the work presented in Chapter 2 which focused on addressing one of the major downfalls of the EHD co-jetting technology by developing a high-throughput needle-less device to produce multicompartmental fibers and particles. Chapter 3 aimed at creating a new 3D fiber writing process by eliminating the whipping instabilities typically seen during electrospinning processing. Chapter 4 utilizes the scaffolds developed in Chapter 3 to create a new 3D cell culture platform. This platform was then implemented in two different *in vivo* studies in Chapter 5, demonstrating the potential use in both tissue regeneration applications and as a diseased tissue mimic. While significant progress has been made in each of these areas, further development of key technological areas should be explored to expand the potential applications of this technology.

6.2 Future Work in 3D Jet Writing

6.2.1 Manifolded Scaffolding

While the scaffolds produced using the 3D jet writing system are fabricated from anisotropic polymer microfibers, the fiber composition remains constant throughout the entire structure. Implementation of a microfluidic manifold would allow for the composition of the fiber to change axially as the 3D microfiber scaffolds are fabricated. This would allow for complete control over the 3D architecture of the fibers within the scaffold. Changes in the fiber composition could be to vary the ratio of one compartment to another using one continuous fiber, or completely changing the fiber composition to an entirely different material. Applying this technique to the current 3D jet writing system would allow for unprecedented control over scaffold anisotropy and patterning capabilities.

6.2.2 Incorporation of New Materials

The work demonstrated within this dissertation mainly focuses on the creation of PLGA microfiber structures. While PLGA is an extremely versatile biomaterial, as it is biodegradable and biocompatible, certain properties such as elasticity and modulus are difficult to control simply using this one material. Incorporation of elastomers, hydrogels, organogels, or environmental sensing polymers would greatly increase the number of applications these scaffolds could be used in.[31] Examples of the enhanced properties would be tunable elastic modulus, selective compartmental swelling of fiber structures in specific solvents, or 3D patterning of cells using different surface chemistries.[26, 31, 33] Performing this work would require numerous trials where solvent parameters and process variables are altered until a stable fiber jet is formed.

6.2.3 4D Printing

Implementation of a manifold type device with an enhanced materials library could allow for 4D printing.[104] This involves printing a 3D object which can change with time, typically due to environmental changes. Temperature sensitive polymers, and combinations of organogels or hydrogels, and selective cross-linking reactions using photomasks, could impart environmental sensing scaffolds which could change over time.[29] Manifolding the outlet polymer composition would allow for precise patterning of these polymers throughout the 3D structure. Patterning of temperature responsive materials could be used to create complex structures which changes shapes over time.

6.2.4 Controlled Scaffold Degradation

Previous work in the Lahann lab has incorporated specific polymeric materials which undergo controlled degradation. Implementation of these materials, which include a modified dextran and a UV degradable PEG, into scaffolding would produce structures with anisotropic release kinetics.[30, 51, 306] This could be used to deliver antibiotics to a wound site, release growth factors, or just simply speed up the rate at which the scaffold is degraded *in vivo*.

6.3 Future Work in Utilizing Scaffolds for 3D Cell Culture

6.3.1 Further Characterizing Microenvironment

The studies involving 3D cell culture on scaffolds included within this dissertation include the use of fibronectin. Fibronectin was used to enhance cell adhesion to the scaffolds, and seemed to be involved in the formation of free-standing 3D cellular constructs within the open geometry of the scaffolds. Further study of the exact role which fibronectin plays in the formation of these structures needs to be performed. Additionally, implementing other extracellular matrix proteins, such as laminin and collagen, should be investigated to determine if the fibronectin effect is unique. Furthermore, mixtures of proteins should be used to more closely mimic the extracellular matrix naturally found *in vivo*.[126] This type of platform could allow for investigation of how changes in the matrix composition of the microenvironment affect phenotypic changes in various cell lines.

6.3.2 Studying Cancer

With the capability of controlling the matrix environment on the 3D jet writing scaffold, it should be feasible to study how the matrix affects cancer cell populations and metastasis.[307] A hypothesis, termed the 'Soil-seed hypothesis', states that the right kind of cell (the seed) needs to encounter the proper matrix environment (the soil) for a metastatic lesion to form.[308] Much of literature in the field of cancer research has been focused on studying the role that cells play in the metastatic cascade, however, not as much attention has been paid to the matrix. This is mostly due to a lack of platforms which can effectively present purified extracellular matrix components. Utilizing scaffolds with varying matrix conditions with different cancer cell types could provide useful insight into the metastatic cascade.

6.3.3 Furthering the Study of hESCs

Initial studies indicated the culturing hESCs on fibronectin coated scaffold leads to 3D microtissues of undifferentiated pluripotent stem cells. Further verification of these results needs to be performed using western blot and PCR analysis of the cell populations. Additionally, the ability of these cells to differentiate in these 3D environments also needs to be explored. Differentiation into cell lineages in the three different germ layers, namely the endoderm, mesoderm, and ectoderm, needs to be performed. Other initial studies have indicated that these pluripotent stem cells may retain their pluripotency over the course of weeks. Therefore, a detailed examination of how long these cells can remain pluripotent should also be explored. Other experiments aimed at exploring alternative differentiation pathways of hESCs could be performed with these large scale 3D hESC cultures.

6.3.4 Expanding Difficult to Culture Cells

The 3D cell culture platform described in this dissertation has demonstrated the ability to culture many different kinds of cells, even cells which are normally quite difficult to culture. Expansion of patient derived cancer cells, or other primary cell lines, is typically quite difficult to achieve. The environment provided by the 3D jet writing scaffolds may prove to be suitable to expand these kinds of cells due to the enhanced cellular interactions and 3D matrix environment it provides.

6.4 Future Work in Implementing Scaffolds In Vivo

6.4.1 Cancer Metastases

Osteogenically differentiated hMSCs form a diseased tissue model for cancer metastasis into bone. Initial studies described in this dissertation show the successful metastasis of human cancer cells into the humanized bone model. Future work will aim at using intravital microscopy to image the cancer cells metastasizing into the implanted bone mimic. This will be used to study homing and invasion of cancer cells into a bone microenvironment. Furthermore, pathways thought to be critical for cancer cells could be studied by knocking down specific genes, and examining if metastases still occur. Other studies on examining drug efficacy against metastasized cancer cells could also be performed, as these cells are often distinctly different populations from the primary tumor they derived from.

6.4.2 Improving Xenograft Take Rates

Typically, xenografts of patient tumor cells are formed in mice to study the cancer biology and for specific drug testing.[309-311] Unfortunately, forming these xenografts by injecting cancer cells into mice is rather inefficient, and those that successfully form take months to make a palpable tumor.[312] However, utilizing 3D jet writing scaffolds could be used to expand the patient cells *in vitro* in a 3D microenvironment. Once the cells are expanded, and in a 3D culture environment, implanting the cell laden scaffolds into the mouse may result in improved xenograft formation efficiencies. Additionally, culturing the cells in the 3D environment *in vitro* may be an alternative method of mimicking a xenograft formed in a mouse.

Appendix A

MATLAB Code for Analysis of Fiber Lines

A.1 MATLAB Code for Analysis of Fiber Lines

A cropped image containing only a single deposited line of fiber was saved as a .png file for analysis using MATLAB. The image was cropped to a width of 2000 pixels. The code converts the file to black and white and finds the edges of the fiber from the top and bottom, and stores the top and bottom pixel value. The average between to top and bottom pixel was taken to be the centerline of the deposited fiber and was used for subsequent analysis. All points are output in the MATLAB command output window. Those points were copied into a spreadsheet and subsequently analyzed.

```
clear all
I=imread('Image File Name Here.png');
gray=rgb2gray(I);
BW=edge(gray,'prewitt');
s=size(gray);
y(1)=0;
x(1)=1;
for i=1:2000
    i;
    for j=1:s(1)
        if BW(j,i)==1
            y(i)=s(1)-j;
            x(i)=i;
            j=s(1);
        end
    end
end

for k=1:2000
    k;
    for l=1:s(1)
        if BW(s(1)-l+1,k)==1
```

```
y2(k)=l;
            x2(k)=k;
            j=s(1)
        end
    end
end

y3=(y2+y)/2;
plot(x,y3)
    formatSpec =('%1.1f\n');
    fprintf(formatSpec,y3);
```

Appendix B

Stage Navigation

B.1 COSMOS Stage Control

Controlling the COSMOS stage can be accomplished in multiple ways. First, the stage can be manually moved, one direction at a time, using the physical buttons on the controller. The plus button correlates to movement of the collection stage away from the motor, and minus correlates to movement of the collection stage towards the motor. However, once the controllers are connected to the computer, movement of the stage via these buttons is disabled. Therefore, control over the stage can be accomplished using the 'Quick Moves <Relative Move' tool. This tool allows control over displacement and velocity of up to four different stages. This allows the user to move the collection stage to the desired position prior to patterning the fibers.

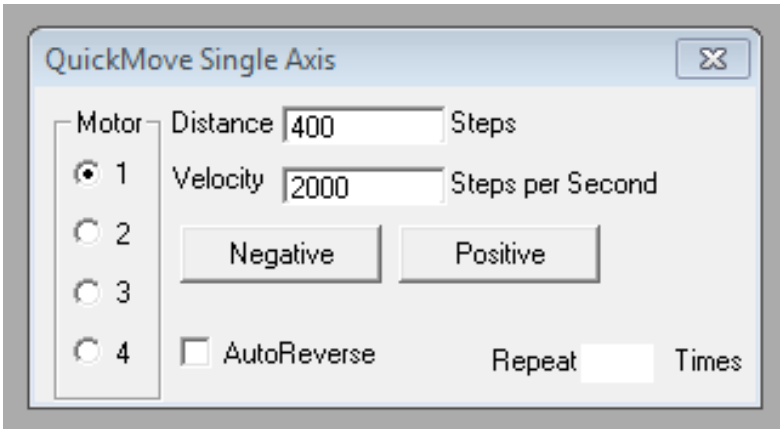

Figure B.1. COSMOS software QuickMove Relative Move tool. A screenshot of the QuickMove – Relative move tool. This allows you to move one of four different axes a set distance, given by 'steps', at a given velocity, given in 'steps per second'. An autoreverse function exists which executes the exact opposite move at the end of the first move. The movement desired can be repeated as many times as desired by typing in the number of repeats into the dialog box. Here each step equates to $1/1000^{th}$ of an inch.

B.2 Newport Stages MATLAB

Controlling stage movement on the Newport stages is inherently more difficult initially, however once the programs have been made it makes control by inexperienced users very easy. As opposed to the COSMOS stage, where the program needs to be rewritten when any changes to the program are made, the Newport stages allow for assigning variables with stored values. This makes it quick and simple to change the value of the stored variable, such as speed, across the entire program. These changed stored values can also be used across multiple programs, so if ideal conditions were found using one program, those same conditions can be used in programs which are subsequently executed. Here, the section of code below is for initializing stage communication with MATLAB, and introduces the variables 'speed' and 'inc', where 'speed' is the speed of the stage, and 'inc' is the increment of motion in millimeters used to manually move the stage into the desired position. This program loads the commands that are used to communicate with the stage, initializes the stage, and centers the stage at the (zero, zero) coordinate.

```
XPS_load_drivers;
IP='192.168.254.254';
Port=5001;
TimeOut=60.0;
socketID=TCP_ConnectToServer(IP,Port,TimeOut);
inc = 40;
if (socketID<0)
    disp 'Connection to XPS failed, check IP & Port';
    return;
end
group='RightXY';
positionerx='RightXY.X';
positionery='RightXY.Y';
[errorCode]=GroupInitialize(socketID,group);
if (errorCode ~=0)
    disp     (['Error'     num2str(errorCode)     'occurred     while     doing
GroupInitialize!']);
    return;
end

[errorCode]=GroupHomeSearch(socketID,group);
if (errorCode~=0)
```

```
    disp(['Error'      num2str(errorCode)      'occurred      while      doing
GroupHomeSearch']);
        return;
end
speed=25
inc=10
```

Once the stages are initialized, manual movement of the stage in set incremental motions was determined by the variable 'inc'. The speed of these movements was set by the variable 'speed', where the value of speed is in mm/s. Changing the values of these and other variables is accomplished by typing 'command=x' into the MATLAB control window, where 'variable' is the name of the variable you want to change, and 'x' is the value you want it to change to. These commands were set to .m files named w, a, s, and d which correspond to up, left, down, and right respectively. Typing the name of the file into the MATLAB command window and pressing enter results in the program to be executed. This allows for initial movement and positioning of the stage prior to execution of the complex, coordinated stage movements required to fabricate scaffolds. Here the command PositionerSGammaParametersSet is followed by the values for the socket the stage is connected to, which stage subsequent values are applied, the stage speed, the stage acceleration, the minimum stage jerk, and maximum stage jerk.

Program 'a'

```
PositionerSGammaParametersSet(socketID,positionerx,speed,50,.0004,0.0040);
GroupMoveRelative(socketID,positionerx,inc);
```

Program 'd'

```
PositionerSGammaParametersSet(socketID,positionerx,speed,1000,.004,0.04);
GroupMoveRelative(socketID,positionerx,-inc);
```

Program 'w'

```
PositionerSGammaParametersSet(socketID,positionery,speed,1000,.004,0.04);
GroupMoveRelative(socketID,positionery,inc);
```

Program ‘s’

```
PositionerSGammaParametersSet(socketID,positionery,speed,1000,.004,0.04);
GroupMoveRelative(socketID,positionery,-inc);
```

B.3 Newport Stages LabView

A LabView program was developed (Credit: Clark Teeple) which essentially executed the same MATLAB program from section B2, but accomplished this through a graphical user interface. Initial stage connection to the computer and homing to the (0,0) reference point is accomplished by simply pressing the ‘Initialize stage’ button. Disconnecting the stage from the computer is accomplished just as easily using the ‘Disable’ button and reconnecting stage control using the ‘Enable’ button. This allows the user to simply type the desired speed, displacement, and acceleration of the collection stage into a dialog box. From here, the keyboard buttons ‘Home’, ‘Delete’, ‘Page Down’, and ‘End’ can be used to displace the stage up, left, right, and down respectively at the specified velocity. This program can be utilized to position the collection stage prior to executing a pre-programmed scaffold fabrication routine, creating an easy to use and manipulate platform which require no programming on the user’s end. A screenshot of the user interface is depicted in Figure B2.

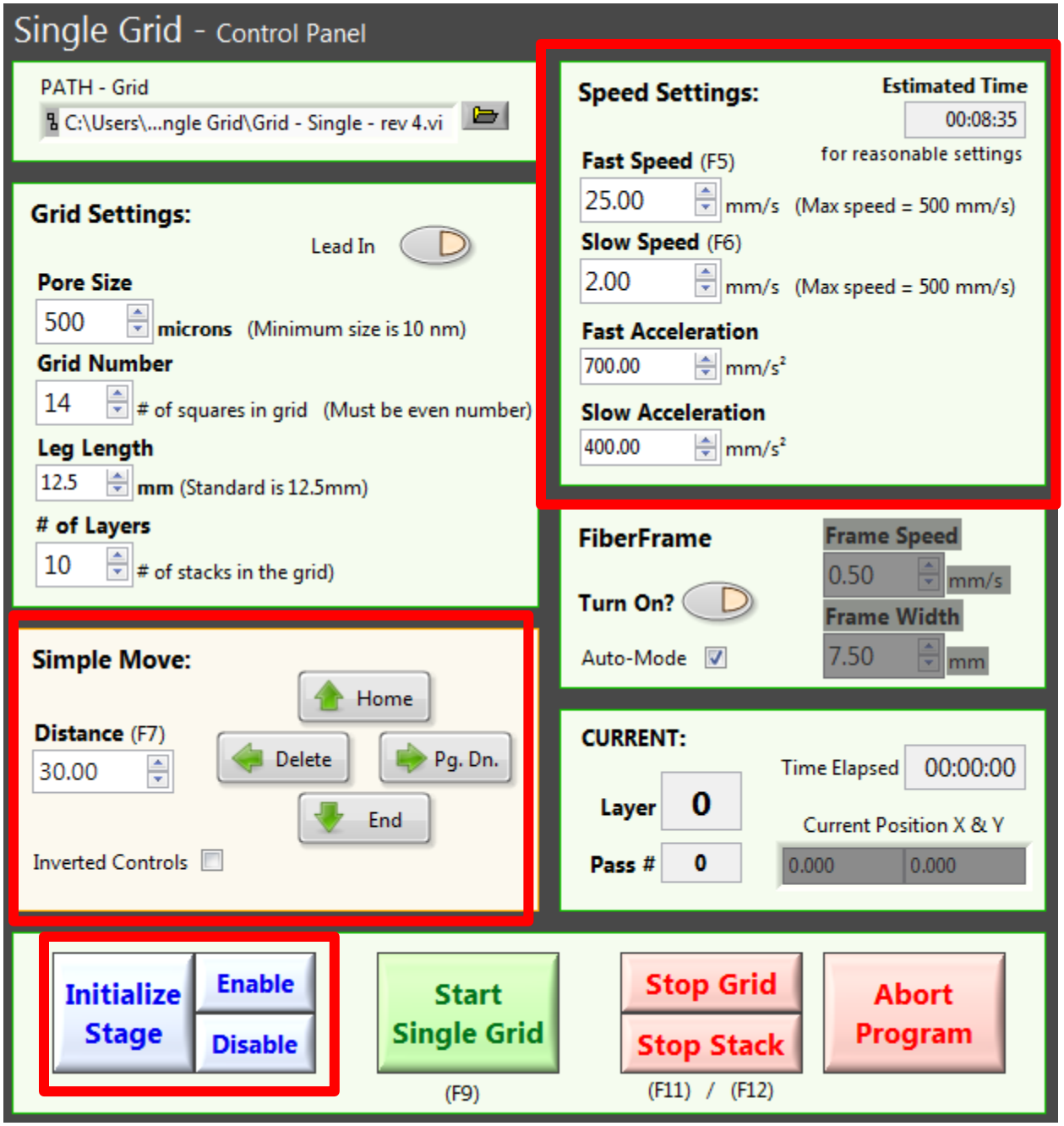

Figure B.2. LabView graphical user interface for stage control prior to scaffold fabrication. The portions of the graphical user interface enclosed in the red rectangles depict the stage controls which are used prior to scaffold fabrication. In the "Speed Settings" window, the 'Fast Speed' and 'Fast Acceleration' boxes dictate the speed and acceleration of the stage during the manual control mode. The "Simple Move" window has a 'Distance' option which allows the user to dictate how far the stage will move for each movement command, with the option of inverting the controls. The up, down, left, and right arrows can be either pressed on the screen via mouse click, or the corresponding keyboard hotkeys can be pressed to move the stage in the desired direction. Initializing the stage is required prior to any controlled movement of the stage, and connection can be disabled or enabled as needed.

Appendix C

Code for Making Square Honeycomb Structures

C.1 COSMOS Stage

Creating scaffolds using the COSMOS stage is accomplished using the following code. The code contains elements which control speed (SXMXXX), displacement (IXMXXX), pauses (PX), repeates (LX), and acceleration (AXMXXX). These variables can be altered for each motor, corresponding to x and y movement. All units are in 'steps' or 'steps per second', with a step corresponding to $1/1000^{th}$ of an inch. In the example below the structure of the code is organized such that the speed controls are all aligned to the left, easing the task of changing the speed of the scaffold program. This is the biggest downfall of using these stages in the scaffolding process, as it takes significant time to change any parameters of the program. In fact, the program needs to be rewritten each time any small changes are desired,, whether that is small changes in collection speed or different pore sizes are desired.

```
F,C,A1M20,A3M20,
S1M800,
S3M40,P2,LM0,I1M1200,I3M30,L-11,
S3M800,I3M450,I1M-450,
S1M40,P2,P10,LM0,I3M-1200,I1M-30,I3M1200,I1M-30,L5,I1M-30,I3M-1200,
S1M800,I1M-30,
I1M-420,I3M450,P10,
LM-0,
L10,R
```

C.2 Newport Stage MATLAB

Upgrading the stages to the IL series of stages from Newport, MATLAB code could now be written to program stage movements. A square honeycomb scaffold structure was programmed through a series of linear movements, similar to the technique used in the COSMOS program. However, MATLAB allows for the use of user defined variables in the code. Therefore, the speed, acceleration, pore size, number of layers, and number of pores can be predefined in the MATLAB code and stored as variables. These can then be input into the base code which creates the scaffold with the properties input into the variables. This significantly simplifies how the scaffold parameters are changed, as the program does not need to be rewritten each time, but the value of the variable simply needs to be altered. Execution of this program begins the scaffold fabrication. Parameters cannot be changed once the program has been executed.

```
speedf=30 %fast speed mm/s (Max speed = 500 mm/s)
speeds=2 %slow speed mm/s (Max speed = 500 mm/s)
accelf=200  %fast acceleration mm/s^2
accels=100   %slow acceleration mm/s^2
length=115    %length per pass in mm (Max displacement = 300 mm)(standard =
40)
grid=.75   %grid size in mm (Minimum size is 10 nm)
gridnumber=10     %number of squares in grid (Needs to be an even number,
standard=10)
layers=10  %number of stacks


%Begin program. Do NOT change anything below this line.

repeat=gridnumber/2;
adjust=(length-(grid*repeat*2))/2;
for j=1:layers
    j
for i=1:repeat
[errorCode]=PositionerSGammaParametersSet(socketID,positionerx,speedf,accelf,
.004,0.04);
if (errorCode~=0)
    disp(['Error'       num2str       '       occurred       while       doing
PositionerSGammaParametersSet']);
    return;
end

[errorCode]=GroupMoveRelative(socketID,positionerx,length);
if (errorCode~=0)
```

```
    disp(['Error' num2str ' occurred while doing GroupMoveRelative']);
    return;
end

[errorCode]=PositionerSGammaParametersSet(socketID,positionery,speeds,accels,
.004,0.04);
if (errorCode~=0)
    disp(['Error'       num2str       '       occurred       while       doing
PositionerSGammaParametersSet']);
    return;
end

[errorCode]=GroupMoveRelative(socketID,positionery,grid);
if (errorCode~=0)
    disp(['Error' num2str ' occurred while doing GroupMoveRelative']);
    return;
end

[errorCode]=GroupMoveRelative(socketID,positionerx,-length);
if (errorCode~=0)
    disp(['Error' num2str ' occurred while doing GroupMoveRelative']);
    return;
end

[errorCode]=GroupMoveRelative(socketID,positionery,grid);
if (errorCode~=0)
    disp(['Error' num2str ' occurred while doing GroupMoveRelative']);
    return;
end
end

[errorCode]=GroupMoveRelative(socketID,positionerx,length);
if (errorCode~=0)
    disp(['Error' num2str ' occurred while doing GroupMoveRelative']);
    return;
end

[errorCode]=PositionerSGammaParametersSet(socketID,positionery,speedf,accelf,
.004,0.04);
if (errorCode~=0)
    disp(['Error'       num2str       '       occurred       while       doing
PositionerSGammaParametersSet']);
    return;
end

[errorCode]=GroupMoveRelative(socketID,positionery,adjust);
if (errorCode~=0)
    disp(['Error' num2str ' occurred while doing GroupMoveRelative']);
    return;
end

[errorCode]=GroupMoveRelative(socketID,positionerx,-adjust);
if (errorCode~=0)
    disp(['Error' num2str ' occurred while doing GroupMoveRelative']);
    return;
```

```
end

[errorCode]=PositionerSGammaParametersSet(socketID,positionerx,speeds,accels,
.004,0.04);
if (errorCode~=0)
    disp(['Error'       num2str       '       occurred       while       doing
PositionerSGammaParametersSet']);
    return;
end

for k=1:repeat

[errorCode]=GroupMoveRelative(socketID,positionery,-length);
if (errorCode~=0)
    disp(['Error' num2str ' occurred while doing GroupMoveRelative']);
    return;
end

[errorCode]=GroupMoveRelative(socketID,positionerx,-grid);
if (errorCode~=0)
    disp(['Error' num2str ' occurred while doing GroupMoveRelative']);
    return;
end

[errorCode]=GroupMoveRelative(socketID,positionery,length);
if (errorCode~=0)
    disp(['Error' num2str ' occurred while doing GroupMoveRelative']);
    return;
end

[errorCode]=GroupMoveRelative(socketID,positionerx,-grid);
if (errorCode~=0)
    disp(['Error' num2str ' occurred while doing GroupMoveRelative']);
    return;
end
end

[errorCode]=GroupMoveRelative(socketID,positionery,-length);
if (errorCode~=0)
    disp(['Error' num2str ' occurred while doing GroupMoveRelative']);
    return;
end

[errorCode]=PositionerSGammaParametersSet(socketID,positionerx,speedf,accelf,
.004,0.04);
if (errorCode~=0)
    disp(['Error'       num2str       '       occurred       while       doing
PositionerSGammaParametersSet']);
    return;
end

[errorCode]=GroupMoveRelative(socketID,positionerx,-adjust);
if (errorCode~=0)
    disp(['Error' num2str ' occurred while doing GroupMoveRelative']);
    return;
```

```
end

[errorCode]=GroupMoveRelative(socketID,positionery,adjust);
if (errorCode~=0)
    disp(['Error' num2str ' occurred while doing GroupMoveRelative']);
    return;
end
end
```

C.3 Newport Stage LabView

A graphical user interface was created to control scaffold fabrication using LabView (Credit: Clark Teeple). This interface gives the user options to control the fast and slow speed and acceleration, which are used during the scaffold fabrication process (Figure 3.18). Different scaffold properties can also be altered by simply changing the values in the dialog boxes for pore size, grid number, leg length, and # of layers. These values are outlined in Figure 3.19. A fiber frame option is also included, which writes a coiled fiber segment around the edge of the scaffold, which was mainly utilized during cell culture applications. The interface also displays the current layer number, fiber stack number, stage position, and elapsed program time. A simple button press begins the fabrication of the scaffold based on the settings programmed in the 'Grid Settings' window. The speed of the fiber jet can be altered in real time during the fabrication of the scaffold by simply changing the values of fast and slow speed and acceleration in the 'Speed Settings' window. This provides complete control over the stage , and requires no programming knowledge on the part of the user. Stopping the stage movement immediately (Abort Program), at the end of the row (Stop Stack), and at the end of that layer (Stop Grid), can be accomplished by the press of a button or keyboard hotkey. LabView provides complete control over the collection stage that MATLAB or the other stage were able to achieve.

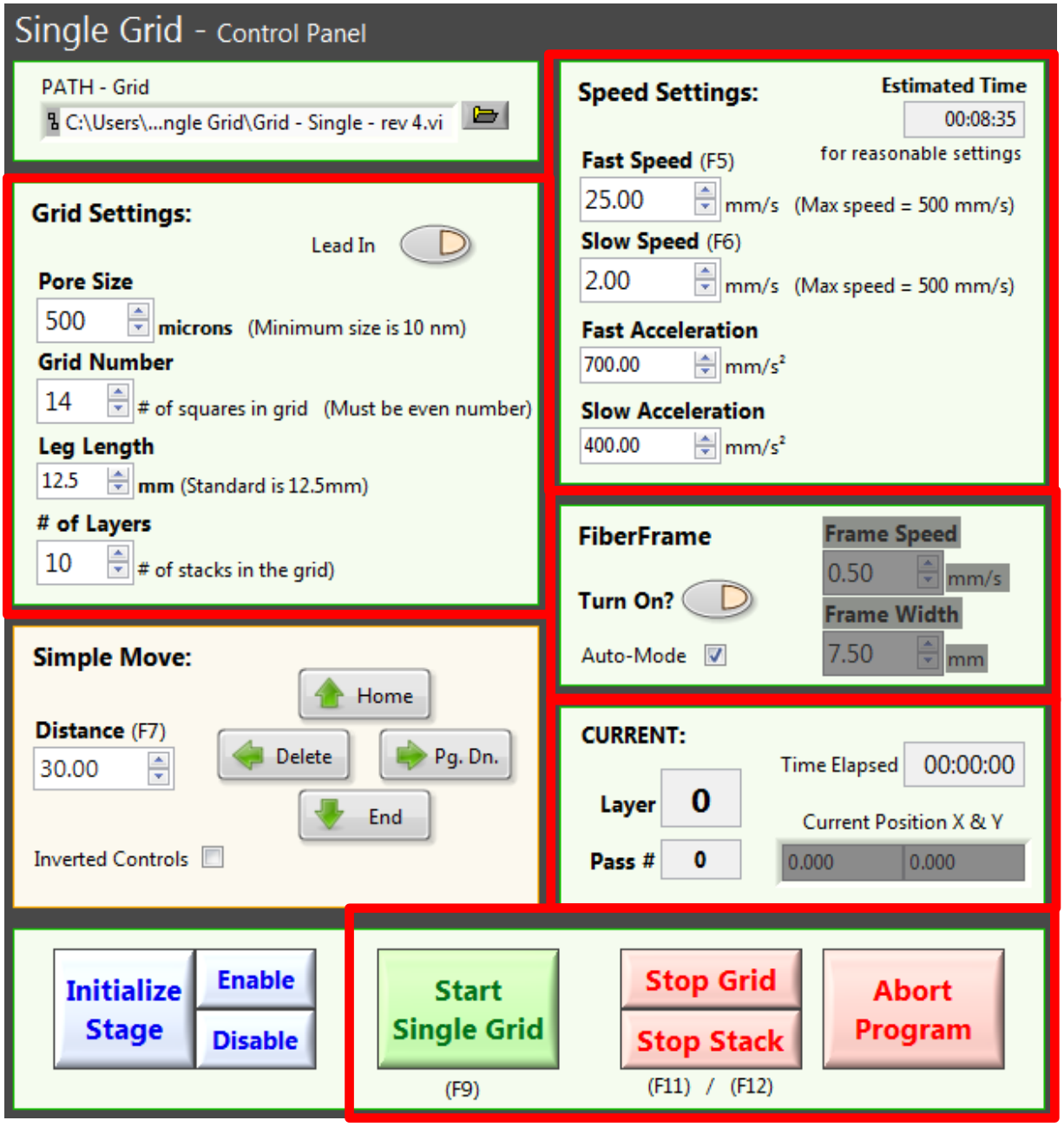

Figure C.1. LabView graphical user interface for scaffold fabrication. The portions of the graphical user interface enclosed in the red rectangles depict the stage controls which are used during scaffold fabrication. In the "Speed Settings" window, the 'Fast Speed' and 'Fast Acceleration' boxes dictate the speed and acceleration of the stage during the writing of the straight segments of the scaffolds, while 'Slow Speed' and 'Slow Acceleration' control the speed when changing directions. In the 'Grid Settings' window, the pore size, grid number, lead in length, and number of layers of the scaffold are able to be controlled. A coiled fiber fram can be enabled in the 'FiberFrame' window. The 'Current' window displays the current layer, stack number, and elapsed time of the current scaffold. Scaffold fabrication is started by pressing the 'Start Single Grid' button or pressing F9. Stopping the stage movement immediately (Abort Program), at the end of a row (Stop Stack), or at the end of a layer (Stop Grid) are each accomplished at the press of a button or hotkey (F11/F12)

Appendix D

MATLAB Code to Create Curvilinear Structures

D.1 MATLAB Code to Produce Polar Rose COSMOS Stage Movement

COSMOS stage movement code was produced via MATLAB to create polar rose structures. The parameters in the MATLAB code were altered to create the different polar rose structures, varying from six to nine petal roses and circles. Adjustable parameters include velocity of the stage (V), the number of line segments (lines), and the parameters n and d which are used to define what polar rose structures will be produced (Figure D.1). The code used to produce these polar rose structures is included below.

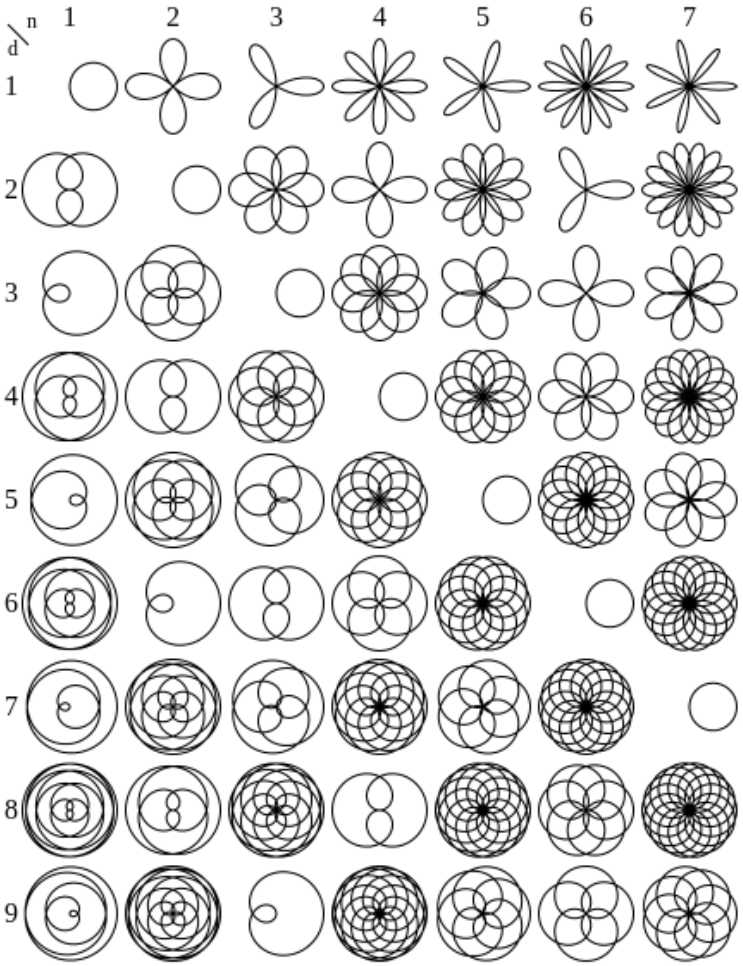

Figure D.1. Effect of n and d parameters on polar rose structure. Chart depicting the variety of polar rose structures, and how parameters n and d effect the architecture. Source: Wikipedia - Rose (Mathematics)

```
clear all
clc
y(1)=0;
V=1000;
lines=100
a=100;
x(1)=a;
n=9;
d=7;
t=lines/d/3.1415;
k=n/d;
time(1)=0;
Vx(1)=00;
Vy(1)=700;
dx(1)=0;
dy(1)=0;
totV(1)=700;
dt(1)=0
for i=1:lines
    r=a*cos(k*i/t);
    x(i+1)=r*cos(i/t);
    y(i+1)=r*sin(i/t);
    dx(i+1)=x(i+1)-x(i);
    dy(i+1)=y(i+1)-y(i);
    dt(i+1)=sqrt(dx(i+1)^2+dy(i+1)^2)/V
    Vx(i+1)=abs(dx(i+1)/dt(i+1));
    Vy(i+1)=abs(dy(i+1)/dt(i+1));
    A=[Vx;dx];
    B=[Vy;dy];
    totV(i+1)=sqrt(Vx(i+1)^2+Vy(i+1)^2);
    time(i+1)=i/t;

end
    formatSpec =('S1M%1.0f,I1M%1.0f,\n');
    fprintf(formatSpec,A);
    disp('motor 3')
    formatSpec=('S1M%1.0f,I1M%1.0f,\n');
    fprintf(formatSpec,B);
    plot(x,y)
    totT(1)=0
for j=1:lines
    totT(j+1)=totT(j)+dt(j+1)
end
```

D.2. MATLAB Code to Produce Pacman Structure

Similar to polar rose structures created in section D1, Pacman structures were fabricated using controlled stage movements which were generated using a MATLAB code. The code for the Pacman structure is given below.

```
clear all
clc
r=100;
x(1)=r*sqrt(2)/2;
y(1)=r*sqrt(2)/2;
V=1500;
lines=20;
t=lines/2/3.1415;
for i=1:(3*lines/4)

    x(i+1)=r*cos(i/t+3.1415/4);
    y(i+1)=r*sin(i/t+3.1415/4);
end
x(3*lines/4+2)=x(3*lines/4+1)-sqrt((r^2)/2);
y(3*lines/4+2)=y(3*lines/4+1)+sqrt((r^2)/2);
x(3*lines/4+3)=x(3*lines/4+2)+sqrt((r^2)/2);
y(3*lines/4+3)=y(3*lines/4+2)+sqrt((r^2)/2);
x(3*lines/4+4)=x(3*lines/4+3)+150;
y(3*lines/4+4)=y(3*lines/4+3)
lines2=3*lines/4+4+lines/2
ay=y(3*lines/4+4)
ax=x(3*lines/4+4)+r
for j=19:lines2-1
    nx(j+1)=-r*cos(-(j-18)/t);
    ny(j+1)=r*sin((j-18)/t);
    x(j+1)=nx(j+1)+ax;
    y(j+1)=ny(j+1)+ay;
end
x(lines2+1)=x(lines2);
y(lines2+1)=y(lines2)-1.7*r;
lines3=lines2+1+20;
by=y(lines2+1);
bx=x(lines2+1);
for k=30:50
    x(k+1)=x(k)-1.9*r/20;
    y(k+1)=y(k)+30*sin(k/.7955);
end
y(52)=y(51)+1.69*r;
x(52)=x(51);
y(53)=y(52);
x(53)=x(52)-151;
for g=1:52
    dx(g+1)=x(g+1)-x(g);
    dy(g+1)=y(g+1)-y(g);
    dt(g+1)=sqrt(dx(g+1)^2+dy(g+1)^2)/V
    Vx(g+1)=abs(dx(g+1)/dt(g+1));
    Vy(g+1)=abs(dy(g+1)/dt(g+1));
    A=[Vx;dx];
    B=[Vy;dy];
end
    formatSpec =('S1M%1.0f,I1M%1.0f,\n');
    fprintf(formatSpec,A)
    disp('motor 3')
    formatSpec=('S1M%1.0f,I1M%1.0f,\n');
    fprintf(formatSpec,B)
    plot(x,y)
```

D.3 MATLAB Code to Produce Lahann Structure

Similar to polar rose structures created in section D1, the Lahann structures were fabricated using controlled stage movements which were generated using a MATLAB code. The code for the Lahann structure is given below. The strategy used to create the letters was to code small segments of each letter at a time. Each segment is depicted in the comments of the code. This strategy can be used to create code to create any fiber structures of arbitrary complexity.

```
clear all
clc
r=70;
x(1)=-3*r;
y(1)=-0.6*r;
V=700;
lines=10;
t=lines/2/3.1415;
pi=3.1415

%L top curve 1
for a=1:(lines/2)
    x(a+1)=r*cos(a/t+3.1415);
    y(a+1)=r*sin(a/t+3.1415);
end

%L top curve 2
for b=lines/2+1:(lines)
    x(b+1)=-r/2*cos(b/t)+x(lines/2+1)-r/2;
    y(b+1)=-r/2*sin(b/t)+y(lines/2+1);
end

%L line down
x(lines+2)=x(lines+1);
y(lines+2)=y(lines+1)-3*r;

%L bottom circle
for c=lines+2:lines+7
    x(c+1)=-r/2*cos((c-lines/2+1)/t)+x(lines+2);
    y(c+1)=r/2*sin((c-lines/2+1)/t)+y(lines+2)+r/4;
end

%L end
for d=lines+8:lines+17
    x(d+1)=x(lines+8)+r/7*(d-lines-8);
    y(d+1)=y(lines+8)+-r/2*cos((d-lines+8)/t)-4*r/10;
end

%a circle
for e=lines+18:lines+31
    x(e+1)=r/2*sin((e-lines+19)/t+pi/2)+x(lines+18)+r/4;
```

```
    y(e+1)=r/2*cos((e-lines+19)/t+pi/2)+y(lines+18)-r/2;
end

%a stem
for f=lines+32:lines+35
    x(f+1)=x(lines+32)+-r/2*sin((f-lines+32)/t)+r/2;
    y(f+1)=y(lines+32)+r/2*cos((f-lines+32)/t);
end

%h upward
x(lines+37)=4.5*r;
y(lines+37)=0;

%h top curve
for g=lines+37:lines+41
    x(g+1)=x(lines+37)+r/2*sin((g-lines+37)/t)-r/2;
    y(g+1)=y(lines+37)+-r/2*cos((g-lines+37)/t);
end

%h down stroke
y(lines+43)=-3.15*r;
x(lines+43)=x(lines+42);

%h hump
for h=lines+43:lines+46
    x(h+1)=x(lines+43)+r/2*cos(-(h-lines+43)/t)+r;
    y(h+1)=y(lines+43)+r*-sin((h-lines+43)/t);
end

%h end
for i=lines+47:lines+52
    x(i+1)=x(lines+47)+r/5*(i-lines-46);
    y(i+1)=y(lines+47)-0.6*r*sin((i-lines-46)/t);
end

%a circle
for j=lines+53:lines+66
    x(j+1)=r/2*sin((j-lines+53)/t+pi/1.5)+x(lines+53)+r/4;
    y(j+1)=r/2*cos((j-lines+53)/t+pi/1.5)+y(lines+53)-r/2;
end

%a stem
for k=lines+67:lines+75
    x(k+1)=x(lines+67)+r/5*(k-lines-66);
    y(k+1)=y(lines+67)-r/2*sin((k-lines-66)/t);
end

%n beginnning

x(lines+77)=x(lines+76);
y(lines+77)=-3.2*r;
x(lines+78)=x(lines+77);
y(lines+78)=-2.7*r;

%n curve
```

```
for l=lines+78:lines+82
    x(l+1)=x(lines+78)+r/2*-cos(-(l-lines-77)/t)+r/2;
    y(l+1)=y(lines+78)+r/2*sin((l-lines-77)/t);
end

%n end
for m=lines+83:lines+92
    x(m+1)=x(lines+83)+r/5*(m-lines-82);
    y(m+1)=y(lines+83)-r/2*sin((m-lines-82)/t);
end

%n beginning
x(lines+94)=x(lines+93);
y(lines+94)=-3.2*r;
x(lines+95)=x(lines+93);
y(lines+95)=-2.7*r;

%n hump
for n=lines+95:lines+100
    x(n+1)=x(lines+95)+r/2*-cos(-(n-lines-95)/t)+r/2;
    y(n+1)=y(lines+95)+r/2*sin((n-lines-95)/t);
end

%n end
for n=lines+101:lines+106
    x(n+1)=x(lines+101)+r/5*(n-lines-100);
    y(n+1)=y(lines+101)-r/2*sin((n-lines-100)/t);
end
x(lines+108)=x(lines+107);
y(lines+108)=y(lines+107)+3.2*r;
x(lines+109)=x(lines+108)-17*r;
y(lines+109)=y(lines+108);
x(lines+110)=x(1);
y(lines+110)=y(1);
%comiple into code
for o=1:lines+109
    dx(o+1)=x(o+1)-x(o);
    dy(o+1)=y(o+1)-y(o);
    dt(o+1)=sqrt(dx(o+1)^2+dy(o+1)^2)/V
    Vx(o+1)=abs(dx(o+1)/dt(o+1));
    Vy(o+1)=abs(dy(o+1)/dt(o+1));
    A=[Vx;dx];
    B=[Vy;dy];
    totV(o+1)=sqrt(Vx(o+1)^2+Vy(o+1)^2);
    time(o+1)=o/t;
end
    formatSpec =('S1M%1.0f,I1M%1.0f,\n');
    fprintf(formatSpec,A);
    disp('motor 3')
    formatSpec=('S1M%1.0f,I1M%1.0f,\n');
    fprintf(formatSpec,B);
    plot(x,y)
```

References

1. Li, D. & Xia, Y.N. Electrospinning of nanofibers: Reinventing the wheel? *Adv Mater* **16**, 1151-1170 (2004).
2. Barrero, A., Ganan-Calvo, A.M., Davila, J., Palacio, A. & Gomez-Gonzalez, E. Low and high Reynolds number flows inside Taylor cones. *Phys Rev E* **58**, 7309-7314 (1998).
3. Hohman, M.M., Shin, M., Rutledge, G. & Brenner, M.P. Electrospinning and electrically forced jets. I. Stability theory. *Phys Fluids* **13**, 2201-2220 (2001).
4. Rutledge, G.C. & Fridrikh, S.V. Formation of fibers by electrospinning. *Adv Drug Deliver Rev* **59**, 1384-1391 (2007).
5. Shtern, V. & Barrero, A. Striking Features of Fluid-Flows in Taylor Cones Related to Electrosprays. *J Aerosol Sci* **25**, 1049-1063 (1994).
6. Taylor, G. Disintegration of Water Drops in Electric Field. *Proc R Soc Lon Ser-A* **280**, 383-+ (1964).
7. Zeleny, J. Instability of electrified liquid surfaces. (s.n., S.l.; 1917).
8. Cloupeau, M. & Prunetfoch, B. Electrohydrodynamic Spraying Functioning Modes - a Critical-Review. *J Aerosol Sci* **25**, 1021-1036 (1994).
9. Gañan-Calvo, A.M., Pantano, C. & Barrero, A. The equilibrium shapes of liquid menisci emitting liquid and charges in steady cone-jet mode. *J Aerosol Sci* **27**, S187-S188 (1996).
10. Hartman, R.P.A., Brunner, D.J., Camelot, D.M.A., Marijnissen, J.C.M. & Scarlett, B. Jet break-up in electrohydrodynamic atomization in the cone-jet mode. *J Aerosol Sci* **31**, 65-95 (2000).
11. Pantano, C., Gañán-Calvo, A.M. & Barrero, A. Zeroth-order, electrohydrostatic solution for electrospraying in cone-jet mode. *J Aerosol Sci* **25**, 1065-1077 (1994).
12. Verdoold, S., Agostinho, L.L.F., Yurteri, C.U. & Marijnissen, J.C.M. A generic electrospray classification. *J Aerosol Sci* **67**, 87-103 (2014).
13. Ganan-Calvo, A.M., Rebollo-Munoz, N. & Montanero, J.M. The minimum or natural rate of flow and droplet size ejected by Taylor cone-jets: physical symmetries and scaling laws. *New J Phys* **15** (2013).
14. de la Mora, J.F. The fluid dynamics of Taylor cones. *Annu Rev Fluid Mech* **39**, 217-243 (2007).
15. Hayati, I., Bailey, A. & Tadros, T.F. Investigations into the Mechanism of Electrohydrodynamic Spraying of Liquids .2. Mechanism of Stable Jet Formation and Electrical Forces Acting on a Liquid Cone. *J Colloid Interf Sci* **117**, 222-230 (1987).
16. Hayati, I., Bailey, A.I. & Tadros, T.F. Mechanism of Stable Jet Formation in Electrohydrodynamic Atomization. *Nature* **319**, 41-43 (1986).
17. Shtern, V. & Barrero, A. Instability Nature of the Swirl Appearance in Liquid Cones. *Phys Rev E* **52**, 627-635 (1995).

18. Huang, Z.M., Zhang, Y.Z., Kotaki, M. & Ramakrishna, S. A review on polymer nanofibers by electrospinning and their applications in nanocomposites. *Compos Sci Technol* **63**, 2223-2253 (2003).
19. Lee, A., Jin, H., Dang, H.W., Choi, K.H. & Ahn, K.H. Optimization of Experimental Parameters To Determine the Jetting Regimes in Electrohydrodynamic Printing. *Langmuir* **29**, 13630-13639 (2013).
20. Cherney, L.T. Structure of Taylor cone-jets: limit of low flow rates. *J Fluid Mech* **378**, 167-196 (1999).
21. Roselllllompart, J. & Delamora, J.F. Generation of Monodisperse Droplets 0.3 to 4 Mu-M in Diameter from Electrified Cone-Jets of Highly Conducting and Viscous-Liquids. *J Aerosol Sci* **25**, 1093-1119 (1994).
22. Ku, B.K. & Kim, S.S. Electrospray characteristics of highly viscous liquids. *J Aerosol Sci* **33**, 1361-1378 (2002).
23. Roh, K.H., Martin, D.C. & Lahann, J. Biphasic Janus particles with nanoscale anisotropy. *Nat Mater* **4**, 759-763 (2005).
24. Bhaskar, S., Hitt, J., Chang, S.W.L. & Lahann, J. Multicompartmental Microcylinders. *Angew Chem Int Edit* **48**, 4589-4593 (2009).
25. Bhaskar, S. & Lahann, J. Microstructured Materials Based on Multicompartmental Fibers. *J Am Chem Soc* **131**, 6650-+ (2009).
26. Mandal, S., Bhaskar, S. & Lahann, J. Micropatterned Fiber Scaffolds for Spatially Controlled Cell Adhesion. *Macromol Rapid Comm* **30**, 1638-1644 (2009).
27. Bhaskar, S., Roh, K.H., Jiang, X.W., Baker, G.L. & Lahann, J. Spatioselective Modification of Bicompartmental Polymer Particles and Fibers via Huisgen 1, 3-Dipolar Cycloaddition (vol 29, pg 1655, 2008). *Macromol Rapid Comm* **29**, 1973-1973 (2008).
28. Rahmani, S. et al. Chemically Orthogonal Three-Patch Microparticles. *Angew Chem Int Edit* **53**, 2332-2338 (2014).
29. Lee, K.J. et al. Spontaneous shape reconfigurations in multicompartmental microcylinders. *P Natl Acad Sci USA* **109**, 16057-16062 (2012).
30. Rahmani, S., Park, T.H., Dishman, A.F. & Lahann, J. Multimodal delivery of irinotecan from microparticles with two distinct compartments. *J Control Release* **172**, 239-245 (2013).
31. K.J. Lee, J.Y., S. Rahmani, S. Hwang, S. Bhaskar, S. Mitragotri, J. Lahann Spontaneous shape reconfigurations in multicompartmental microcylinders. *Proc. Natl. Acad. Sci.* **109**, 16057 - 16062 (2012).
32. Rahmani, S. et al. Dual Release Carriers for Cochlear Delivery. *Adv Healthc Mater* **5**, 94-+ (2016).
33. Yoon, J., Eyster, T.W., Misra, A.C. & Lahann, J. Cardiomyocyte-Driven Actuation in Biohybrid Microcylinders. *Adv Mater* **27**, 4509-4515 (2015).
34. S. Saha, D.C., S. Bhaskar, N. Clay, A. Donini, A.J. Hart, J. Lahann Chemically Controlled Bending of Compositionally Anisotropic Microcylinders. *Angewandte Chemie International Edition* **51**, 660 - 665 (2012).
35. Sitt, A. et al. Microscale Rockets and Picoliter Containers Engineered from Electrospun Polymeric Microtubes. *Small* **12**, 1432-1439 (2016).
36. Lv, W.P. et al. Anisotropic Janus Catalysts for Spatially Controlled Chemical Reactions. *Small* **8**, 3116-3122 (2012).

37. Kwon, I.K., Kidoaki, S. & Matsuda, T. Electrospun nano- to microfiber fabrics made of biodegradable copolyesters: structural characteristics, mechanical properties and cell adhesion potential. *Biomaterials* **26**, 3929-3939 (2005).
38. Reneker, D.H. & Chun, I. Nanometre diameter fibres of polymer, produced by electrospinning. *Nanotechnology* **7**, 216-223 (1996).
39. Greiner, A. & Wendorff, J.H. Electrospinning: A fascinating method for the preparation of ultrathin fibres. *Angew Chem Int Edit* **46**, 5670-5703 (2007).
40. Xie, J.W., Lim, L.K., Phua, Y.Y., Hua, J.S. & Wang, C.H. Electrohydrodynamic atomization for biodegradable polymeric particle production. *J Colloid Interf Sci* **302**, 103-112 (2006).
41. Reneker, D.H., Yarin, A.L., Fong, H. & Koombhongse, S. Bending instability of electrically charged liquid jets of polymer solutions in electrospinning. *J Appl Phys* **87**, 4531-4547 (2000).
42. Kwon, M.S. et al. Multi-luminescent switching of metal-free organic phosphors for luminometric detection of organic solvents. *Chem Sci* **7**, 2359-2363 (2016).
43. Wang, X.Y. et al. Electrospun nanofibrous membranes for highly sensitive optical sensors. *Nano Lett* **2**, 1273-1275 (2002).
44. Gibson, P., Schreuder-Gibson, H. & Rivin, D. Transport properties of porous membranes based on electrospun nanofibers. *Colloid Surface A* **187**, 469-481 (2001).
45. Li, W.J., Laurencin, C.T., Caterson, E.J., Tuan, R.S. & Ko, F.K. Electrospun nanofibrous structure: A novel scaffold for tissue engineering. *J Biomed Mater Res* **60**, 613-621 (2002).
46. Sill, T.J. & von Recum, H.A. Electro spinning: Applications in drug delivery and tissue engineering. *Biomaterials* **29**, 1989-2006 (2008).
47. Yoshimoto, H., Shin, Y.M., Terai, H. & Vacanti, J.P. A biodegradable nanofiber scaffold by electrospinning and its potential for bone tissue engineering. *Biomaterials* **24**, 2077-2082 (2003).
48. Chakraborty, S., Liao, I.C., Adler, A. & Leong, K.W. Electrohydrodynamics: A facile technique to fabricate drug delivery systems. *Adv Drug Deliver Rev* **61**, 1043-1054 (2009).
49. Loscertales, I.G. et al. Micro/nano encapsutation via electrified coaxial liquid jets. *Science* **295**, 1695-1698 (2002).
50. Rahmani, S. et al. Long-circulating Janus nanoparticles made by electrohydrodynamic co-jetting for systemic drug delivery applications. *J Drug Target* **23**, 750-758 (2015).
51. Sokolovskaya, E., Rahmani, S., Misra, A.C., Brase, S. & Lahann, J. Dual-Stimuli-Responsive Microparticles. *Acs Appl Mater Inter* **7**, 9744-9751 (2015).
52. Lee, J., Park, T.H., Lee, K.J. & Lahann, J. Snail-like Particles from Compartmentalized Microfibers. *Macromol Rapid Comm* **37**, 73-78 (2016).
53. Saha, S. et al. Chemically Controlled Bending of Compositionally Anisotropic Microcylinders. *Angew Chem Int Edit* **51**, 660-665 (2012).
54. Yarin, A.L. & Zussman, E. Upward needleless electrospinning of multiple nanofibers. *Polymer* **45**, 2977-2980 (2004).
55. Lu, B.A. et al. Superhigh-Throughput Needleless Electrospinning Using a Rotary Cone as Spinneret. *Small* **6**, 1612-1616 (2010).
56. Thoppey, N.M., Bochinski, J.R., Clarke, L.I. & Gorga, R.E. Unconfined fluid electrospun into high quality nanofibers from a plate edge. *Polymer* **51**, 4928-4936 (2010).

57. Wang, X., Niu, H.T., Lin, T. & Wang, X.G. Needleless Electrospinning of Nanofibers With a Conical Wire Coil. *Polym Eng Sci* **49**, 1582-1586 (2009).
58. Forward, K.M. & Rutledge, G.C. Free surface electrospinning from a wire electrode. *Chem Eng J* **183**, 492-503 (2012).
59. Hotaling, N.A., Bharti, K., Kriel, H. & Simon, C.G. DiameterJ: A validated open source nanofiber diameter measurement tool. *Biomaterials* **61**, 327-338 (2015).
60. Bhaskar, S., Pollock, K.M., Yoshida, M. & Lahann, J. Towards Designer Microparticles: Simultaneous Control of Anisotropy, Shape, and Size. *Small* **6**, 404-411 (2010).
61. Yoshida, M. et al. Structurally Controlled Bio-hybrid Materials Based on Unidirectional Association of Anisotropic Microparticles with Human Endothelial Cells. *Adv Mater* **21**, 4920-+ (2009).
62. Bock, N., Woodruff, M.A., Hutmacher, D.W. & Dargaville, T.R. Electrospraying, a Reproducible Method for Production of Polymeric Microspheres for Biomedical Applications. *Polymers-Basel* **3**, 131-149 (2011).
63. Lee, K.J., Park, T.H., Hwang, S., Yoon, J. & Lahann, J. Janus-Core and Shell Microfibers. *Langmuir* **29**, 6181-6186 (2013).
64. Roh, K.H., Martin, D.C. & Lahann, J. Triphasic nanocolloids. *J Am Chem Soc* **128**, 6796-6797 (2006).
65. Viswanadam, G. & Chase, G.G. Modified electric fields to control the direction of electrospinning jets. *Polymer* **54**, 1397-1404 (2013).
66. Collins, G., Federici, J., Imura, Y. & Catalani, L.H. Charge generation, charge transport, and residual charge in the electrospinning of polymers: A review of issues and complications. *J Appl Phys* **111** (2012).
67. Vaquette, C. & Cooper-White, J. The use of an electrostatic lens to enhance the efficiency of the electrospinning process. *Cell Tissue Res* **347**, 815-826 (2012).
68. Lee, J., Lee, S.Y., Jang, J., Jeong, Y.H. & Cho, D.W. Fabrication of Patterned Nanofibrous; Mats Using Direct-Write Electrospinning. *Langmuir* **28**, 7267-7275 (2012).
69. Deitzel, J.M., Kleinmeyer, J.D., Hirvonen, J.K. & Tan, N.C.B. Controlled deposition of electrospun poly(ethylene oxide) fibers. *Polymer* **42**, 8163-8170 (2001).
70. Bellan, L.M. & Craighead, H.G. Control of an electrospinning jet using electric focusing and jet-steering fields. *J Vac Sci Technol B* **24**, 3179-3183 (2006).
71. Pham, Q.P., Sharma, U. & Mikos, A.G. Electrospinning of polymeric nanofibers for tissue engineering applications: A review. *Tissue Eng* **12**, 1197-1211 (2006).
72. Carnell, L.S. et al. Aligned mats from electrospun single fibers. *Macromolecules* **41**, 5345-5349 (2008).
73. Sun, Z.C., Deitzel, J.M., Knopf, J., Chen, X. & Gillespie, J.W. The effect of solvent dielectric properties on the collection of oriented electrospun fibers. *J Appl Polym Sci* **125**, 2585-2594 (2012).
74. Katta, P., Alessandro, M., Ramsier, R.D. & Chase, G.G. Continuous electrospinning of aligned polymer nanofibers onto a wire drum collector. *Nano Lett* **4**, 2215-2218 (2004).
75. Teo, W.E. & Ramakrishna, S. A review on electrospinning design and nanofibre assemblies. *Nanotechnology* **17**, R89-R106 (2006).
76. Pan, H., Li, L.M., Hu, L. & Cui, X.J. Continuous aligned polymer fibers produced by a modified electrospinning method. *Polymer* **47**, 4901-4904 (2006).

77. Xu, C.Y., Inai, R., Kotaki, M. & Ramakrishna, S. Aligned biodegradable nanofibrous structure: a potential scaffold for blood vessel engineering. *Biomaterials* **25**, 877-886 (2004).
78. Fennessey, S.F. & Farris, R.J. Fabrication of aligned and molecularly oriented electrospun polyacrylonitrile nanofibers and the mechanical behavior of their twisted yams. *Polymer* **45**, 4217-4225 (2004).
79. Theron, A., Zussman, E. & Yarin, A.L. Electrostatic field-assisted alignment of electrospun nanofibres. *Nanotechnology* **12**, 384-390 (2001).
80. Sundaray, B. et al. Electrospinning of continuous aligned polymer fibers. *Appl Phys Lett* **84**, 1222-1224 (2004).
81. Wu, Y.Q., Carnell, L.A. & Clark, R.L. Control of electrospun mat width through the use of parallel auxiliary electrodes. *Polymer* **48**, 5653-5661 (2007).
82. Carnell, L.S., Siochi, E.J., Wincheski, R.A., Holloway, N.M. & Clark, R.L. Electric field effects on fiber alignment using an auxiliary electrode during electrospinning. *Scripta Mater* **60**, 359-361 (2009).
83. Teo, W.E., Kotaki, M., Mo, X.M. & Ramakrishna, S. Porous tubular structures with controlled fibre orientation using a modified electrospinning method. *Nanotechnology* **16**, 918-924 (2005).
84. Wittmer, C.R., Hebraud, A., Nedjari, S. & Schlatter, G. Well-organized 3D nanofibrous composite constructs using cooperative, effects between electrospinning and electrospraying. *Polymer* **55**, 5781-5787 (2014).
85. Zhang, D.M. & Chang, J. Patterning of electrospun fibers using electroconductive templates. *Adv Mater* **19**, 3664-+ (2007).
86. Li, D., Ouyang, G., McCann, J.T. & Xia, Y. Collecting electrospun nanofibers with patterned electrodes. *Nano Lett* **5**, 4 (2005).
87. Li, D., Wang, Y.L. & Xia, Y.N. Electrospinning nanofibers as uniaxially aligned arrays and layer-by-layer stacked films. *Adv Mater* **16**, 361-366 (2004).
88. Lee, M. & Kim, H.Y. Toward Nanoscale Three-Dimensional Printing: Nanowalls Built of Electrospun Nanofibers. *Langmuir* **30**, 1210-1214 (2014).
89. Teo, W.E. & Ramakrishna, S. Electrospun fibre bundle made of aligned nanofibres over two fixed points. *Nanotechnology* **16**, 1878-1884 (2005).
90. Kakade, M.V. et al. Electric field induced orientation of polymer chains in macroscopically aligned electrospun polymer nanofibers. *J Am Chem Soc* **129**, 2777-2782 (2007).
91. Li, D., Wang, Y.L. & Xia, Y.N. Electrospinning of polymeric and ceramic nanofibers as uniaxially aligned arrays. *Nano Lett* **3**, 1167-1171 (2003).
92. Sun, D.H., Chang, C., Li, S. & Lin, L.W. Near-field electrospinning. *Nano Lett* **6**, 839-842 (2006).
93. Chang, C., Limkrailassiri, K. & Lin, L.W. Continuous near-field electrospinning for large area deposition of orderly nanofiber patterns. *Appl Phys Lett* **93** (2008).
94. Bisht, G.S. et al. Controlled Continuous Patterning of Polymeric Nanofibers on Three-Dimensional Substrates Using Low-Voltage Near-Field Electrospinning. *Nano Lett* **11**, 1831-1837 (2011).
95. Zheng, G.F. et al. Precision deposition of a nanofibre by near-field electrospinning. *J Phys D Appl Phys* **43** (2010).

96. Cai, Y.L. et al. Collagen grafted 3D polycaprolactone scaffolds for enhanced cartilage regeneration. *J Mater Chem B* **1**, 5971-5976 (2013).
97. Brown, T.D., Dalton, P.D. & Hutmacher, D.W. Direct Writing By Way of Melt Electrospinning. *Adv Mater* **23**, 5651 - 5657 (2011).
98. Hutmacher, D.W. & Dalton, P.D. Melt Electrospinning. *Chem-Asian J* **6**, 44-56 (2011).
99. Hatchett, D.W., Kodippili, G., Kinyanjui, J.M., Benincasa, F. & Sapochak, L. FTIR analysis of thermally processed PU foam. *Polym Degrad Stabil* **87**, 555-561 (2005).
100. Signori, F., Coltelli, M.B. & Bronco, S. Thermal degradation of poly(lactic acid) (PLA) and poly(butylene adipate-co-terephthalate) (PBAT) and their blends upon melt processing. *Polym Degrad Stabil* **94**, 74-82 (2009).
101. Zhou, H.J., Green, T.B. & Joo, Y.L. The thermal effects on electrospinning of polylactic acid melts. *Polymer* **47**, 7497-7505 (2006).
102. Frokjaer, S. & Otzen, D.E. Protein drug stability: A formulation challenge. *Nat Rev Drug Discov* **4**, 298-306 (2005).
103. Kim, G.H. Electrospun PCL nanofibers with anisotropic mechanical properties as a biomedical scaffold. *Biomed Mater* **3** (2008).
104. Gladman, A.S., Matsumoto, E.A., Nuzzo, R.G., Mahadevan, L. & Lewis, J.A. Biomimetic 4D printing. *Nat Mater* **15**, 413-+ (2016).
105. Dawson, J., Vincent, J.F.V. & Rocca, A.M. How pine cones open. *Nature* **390**, 668-668 (1997).
106. Noblin, X. et al. The Fern Sporangium: A Unique Catapult. *Science* **335**, 1322-1322 (2012).
107. Burgert, I. & Fratzl, P. Actuation systems in plants as prototypes for bioinspired devices. *Philos T R Soc A* **367**, 1541-1557 (2009).
108. Yamato, M., Kwon, O.H., Hirose, M., Kikuchi, A. & Okano, T. Novel patterned cell coculture utilizing thermally responsive grafted polymer surfaces. *J Biomed Mater Res* **55**, 137-140 (2001).
109. Yu, Y.L., Nakano, M. & Ikeda, T. Directed bending of a polymer film by light - Miniaturizing a simple photomechanical system could expand its range of applications. *Nature* **425**, 145-145 (2003).
110. Shim, T.S., Kim, S.H., Heo, C.J., Jeon, H.C. & Yang, S.M. Controlled Origami Folding of Hydrogel Bilayers with Sustained Reversibility for Robust Microcarriers. *Angew Chem Int Edit* **51**, 1420-1423 (2012).
111. Lipomi, D.J. et al. Skin-like pressure and strain sensors based on transparent elastic films of carbon nanotubes. *Nat Nanotechnol* **6**, 788-792 (2011).
112. Chang, C.E., Tran, V.H., Wang, J.B., Fuh, Y.K. & Lin, L.W. Direct-Write Piezoelectric Polymeric Nanogenerator with High Energy Conversion Efficiency. *Nano Lett* **10**, 726-731 (2010).
113. Lee, S., Limkrailassiri, K., Gao, Y., Chang, C. & Lin, L.W. Chip-to-chip fluidic connectors via near-field electrospinning. *Proc Ieee Micr Elect*, 252-255 (2007).
114. Liu, H.Q., Edel, J.B., Bellan, L.M. & Craighead, H.G. Electrospun polymer nanofibers as subwavelength optical waveguides incorporating quantum dots. *Small* **2**, 495-499 (2006).
115. Bitzer, T. Honeycomb technology : materials, design, manufacturing, applications and testing, Edn. 1st. (Chapman & Hall, London ; New York; 1997).
116. Knippers, J. & Speck, T. Design and construction principles in nature and architecture. *Bioinspiration & biomimetics* **7**, 015002 (2012).

117. Lakes, R. Materials with structural hierarchy. *Nature* **361**, 4 (1993).
118. Ritchie, R.O. The conflicts between strength and toughness. *Nat Mater* **10**, 817-822 (2011).
119. Altering bacteriological plastic petri dishes for tissue culture use. *Public health reports* **81**, 843-844 (1966).
120. Amstein, C.F. & Hartman, P.A. Adaptation of plastic surfaces for tissue culture by glow discharge. *Journal of clinical microbiology* **2**, 46-54 (1975).
121. Maroudas, N.G. Adhesion and Spreading of Cells on Charged Surfaces. *J Theor Biol* **49**, 417-424 (1975).
122. Maroudas, N.G. Sulphonated polystyrene as an optimal substratum for the adhesion and spreading of mesenchymal cells in monovalent and divalent saline solutions. *Journal of cellular physiology* **90**, 511-519 (1977).
123. Ott, H.C. et al. Perfusion-decellularized matrix: using nature's platform to engineer a bioartificial heart. *Nat Med* **14**, 213-221 (2008).
124. Grayson, W.L. et al. Engineering anatomically shaped human bone grafts. *P Natl Acad Sci USA* **107**, 3299-3304 (2010).
125. Dvir, T., Timko, B.P., Kohane, D.S. & Langer, R. Nanotechnological strategies for engineering complex tissues. *Nat Nanotechnol* **6**, 13-22 (2011).
126. Lutolf, M.P. & Hubbell, J.A. Synthetic biomaterials as instructive extracellular microenvironments for morphogenesis in tissue engineering. *Nat Biotechnol* **23**, 47-55 (2005).
127. Lee, J., Cuddihy, M.J. & Kotov, N.A. Three-dimensional cell culture matrices: State of the art. *Tissue Eng Pt B-Rev* **14**, 61-86 (2008).
128. Billiet, T., Vandenhaute, M., Schelfhout, J., Van Vlierberghe, S. & Dubruel, P. A review of trends and limitations in hydrogel-rapid prototyping for tissue engineering. *Biomaterials* **33**, 6020-6041 (2012).
129. Bissell, M.J., Radisky, D.C., Rizki, A., Weaver, V.M. & Petersen, O.W. The organizing principle: microenvironmental influences in the normal and malignant breast. *Differentiation* **70**, 537-546 (2002).
130. Tibbitt, M.W. & Anseth, K.S. Hydrogels as Extracellular Matrix Mimics for 3D Cell Culture. *Biotechnol Bioeng* **103**, 655-663 (2009).
131. Griffith, L.G. & Swartz, M.A. Capturing complex 3D tissue physiology in vitro. *Nat Rev Mol Cell Bio* **7**, 211-224 (2006).
132. Stevens, M.M. & George, J.H. Exploring and engineering the cell surface interface. *Science* **310**, 1135-1138 (2005).
133. Kunz-Schughart, L.A., Freyer, J.P., Hofstaedter, F. & Ebner, R. The use of 3-D cultures for high-throughput screening: The multicellular spheroid model. *J Biomol Screen* **9**, 273-285 (2004).
134. Miyahara, Y. et al. Monolayered mesenchymal stem cells repair scarred myocardium after myocardial infarction. *Nat Med* **12**, 459-465 (2006).
135. Nishida, K. et al. Corneal reconstruction with tissue-engineered cell sheets composed of autologous oral mucosal epithelium. *New Engl J Med* **351**, 1187-1196 (2004).
136. Mehta, G., Hsiao, A.Y., Ingram, M., Luker, G.D. & Takayama, S. Opportunities and challenges for use of tumor spheroids as models to test drug delivery and efficacy. *J Control Release* **164**, 192-204 (2012).

137. Hirose, M., Kwon, O.H., Yamato, M., Kikuchi, A. & Okano, T. Creation of designed shape cell sheets that are noninvasively harvested and moved onto another surface. *Biomacromolecules* **1**, 377-381 (2000).
138. Wang, A.J. & McDowell, D.L. In-plane stiffness and yield strength of periodic metal honeycombs. *J Eng Mater-T Asme* **126**, 137-156 (2004).
139. Bleicher, M.N. & Toth, L.F. Two-Dimensional Honeycombs. *The American Mathematical Monthly* **72**, 969-973 (1965).
140. Rim, N.G., Shin, C.S. & Shin, H. Current approaches to electrospun nanofibers for tissue engineering. *Biomed Mater* **8** (2013).
141. Langer, R. & Vacanti, J.P. Tissue Engineering. *Science* **260**, 920-926 (1993).
142. Lee, K.Y. & Mooney, D.J. Hydrogels for tissue engineering. *Chem Rev* **101**, 1869-1879 (2001).
143. Murphy, S.V. & Atala, A. 3D bioprinting of tissues and organs. *Nat Biotechnol* **32**, 773-785 (2014).
144. Bhatia, S.N., Yarmush, M.L. & Toner, M. Controlling cell interactions by micropatterning in co-cultures: Hepatocytes and 3T3 fibroblasts. *J Biomed Mater Res* **34**, 189-199 (1997).
145. Lowery, J.L., Datta, N. & Rutledge, G.C. Effect of fiber diameter, pore size and seeding method on growth of human dermal fibroblasts in electrospun poly(epsilon-caprolactone) fibrous mats. *Biomaterials* **31**, 491-504 (2010).
146. Chen, Q.Z. Foaming technology of tissue engineering scaffolds - a review. *Bubble Science, Engineering and Technology* **3**, 34 - 47 (2011).
147. T. Billiet, M.V., J. Schelfhout, S. Van Vlierberghe, P. Dubruel A review of trends and limitations in hydrogel-rapid prototyping for tissue engineering. *Biomaterials* **33**, 6020 - 6041 (2012).
148. G.H. Kim, S.H.A., H.J. Lee, S. Lee, Y. Cho, W. Chun A new hybrid scaffold using rapid prototyping and electrohydrodynamic direct writing for bone tissue. *J. Mater. Chem* **21**, 19138 - 19143 (2011).
149. G.H. Kim, S.H.A., H. Yoon, Y.Y. Kim, W. Chun A cryogenic direct-plotting system for fabrication of 3D collagen scaffolds for tissue engineering. *J. Mater. Chem* **19**, 8817 - 8823 (2009).
150. C.J. Hansen, R.S., D.B. Kolesky, J.J. Vericella, S.J. Kranz, G.P. Muldowney, K.T. Christensen, J.A. Lewis Inkjet Printing: High-Throughput Printing via Microvascular Multinozzle Arrays. *Adv Mater* **25**, 96 - 102 (2013).
151. C. Vaquette, J.C.-W. The use of an electrostatic lens to enhance the efficiency of the electrospinning process. *Cell Tissue Res.* **347**, 815 - 826 (2011).
152. N.G. Rim, C.S.S., H. Shin Current approaches to electrospun nanofibers for tissue engineering. *Biomed. Mater.* **8**, 014102 (2013).
153. Q.P. Pham, U.S., A.G. Mikos Electrospinning of Polymeric Nanofibers for Tissue Engineering Applications: A Review. *Tissue Eng* **12**, 1197 - 1211 (2006).
154. W.E. Teo, W.H., S. Ramakrishna Electrospun scaffold tailored for tissue-specific extracellular matrix. *Biotechnol. J.* **1**, 918 - 929 (2006).
155. Pham, Q.P., Sharma, U. & Mikos, A.G. Electrospun poly(epsilon-caprolactone) microfiber and multilayer nanofiber/microfiber scaffolds: Characterization of scaffolds and measurement of cellular infiltration. *Biomacromolecules* **7**, 2796-2805 (2006).

156. S. Mandal, S.B., J. Lahann Micropatterned Fiber Scaffolds for Spatially Controlled Cell Adhesion. *Macromol. Rapid Commun.* **30**, 1638 - 1644 (2009).
157. Mueller-Klieser, W. Tumor biology and experimental therapeutics. *Crit Rev Oncol Hemat* **36**, 123-139 (2000).
158. Tung, Y.C. et al. High-throughput 3D spheroid culture and drug testing using a 384 hanging drop array. *Analyst* **136**, 473-478 (2011).
159. Grimes, D.R., Kelly, C., Bloch, K. & Partridge, M. A method for estimating the oxygen consumption rate in multicellular tumour spheroids. *J R Soc Interface* **11** (2014).
160. Yang, J. et al. Reconstruction of functional tissues with cell sheet engineering. *Biomaterials* **28**, 5033-5043 (2007).
161. Haraguchi, Y. et al. Fabrication of functional three-dimensional tissues by stacking cell sheets in vitro. *Nat Protoc* **7**, 850-858 (2012).
162. Solorio, L.D., Vieregge, E.L., Dhami, C.D., Dang, P.N. & Alsberg, E. Engineered cartilage via self-assembled hMSC sheets with incorporated biodegradable gelatin microspheres releasing transforming growth factor-beta 1. *J Control Release* **158**, 224-232 (2012).
163. Reubinoff, B.E., Pera, M.F., Fong, C.Y., Trounson, A. & Bongso, A. Embryonic stem cell lines from human blastocysts: somatic differentiation in vitro. *Nat Biotechnol* **18**, 399-404 (2000).
164. Höpfl, G., Gassmann, M. & Desbaillets, I. in Germ Cell Protocols: Volume 2: Molecular Embryo Analysis, Live Imaging, Transgenesis, and Cloning. (ed. H. Schatten) 79-98 (Humana Press, Totowa, NJ; 2004).
165. Bratt-Leal, A.M., Carpenedo, R.L. & McDevitt, T.C. Engineering the Embryoid Body Microenvironment to Direct Embryonic Stem Cell Differentiation. *Biotechnol Progr* **25**, 43-51 (2009).
166. Thomson, J.A. et al. Embryonic stem cell lines derived from human blastocysts. *Science* **282**, 1145-1147 (1998).
167. Adams, G.B. & Scadden, D.T. The hematopoietic stem cell in its place. *Nat Immunol* **7**, 333-337 (2006).
168. Doetsch, F. A niche for adult neural stem cells. *Curr Opin Genet Dev* **13**, 543-550 (2003).
169. Blanpain, C. & Fuchs, E. Epidermal stem cells of the skin. *Annu Rev Cell Dev Biol* **22**, 339-373 (2006).
170. Chen, Z. et al. Characterization of putative stem cell phenotype in human limbal epithelia. *Stem Cells* **22**, 355-366 (2004).
171. Fujimoto, K., Beauchamp, R.D. & Whitehead, R.H. Identification and isolation of candidate human colonic clonogenic cells based on cell surface integrin expression. *Gastroenterology* **123**, 1941-1948 (2002).
172. Jones, P.H. & Watt, F.M. Separation of human epidermal stem cells from transit amplifying cells on the basis of differences in integrin function and expression. *Cell* **73**, 713-724 (1993).
173. Suzuki, A. et al. Flow-cytometric separation and enrichment of hepatic progenitor cells in the developing mouse liver. *Hepatology* **32**, 1230-1239 (2000).
174. Shinohara, T., Avarbock, M.R. & Brinster, R.L. beta1- and alpha6-integrin are surface markers on mouse spermatogonial stem cells. *Proc Natl Acad Sci U S A* **96**, 5504-5509 (1999).

175. Lathia, J.D. et al. Patterns of laminins and integrins in the embryonic ventricular zone of the CNS. *J Comp Neurol* **505**, 630-643 (2007).
176. Lathia, J.D. et al. Integrin alpha 6 regulates glioblastoma stem cells. *Cell stem cell* **6**, 421-432 (2010).
177. Xu, C.H. et al. Feeder-free growth of undifferentiated human embryonic stem cells. *Nat Biotechnol* **19**, 971-974 (2001).
178. Xu, C. et al. Feeder-free growth of undifferentiated human embryonic stem cells. *Nat Biotechnol* **19**, 971-974 (2001).
179. Miyazaki, T. et al. Recombinant human laminin isoforms can support the undifferentiated growth of human embryonic stem cells. *Biochem Biophys Res Commun* **375**, 27-32 (2008).
180. Braam, S.R. et al. Recombinant vitronectin is a functionally defined substrate that supports human embryonic stem cell self-renewal via αVβ5 integrin. *Stem Cells* **26**, 2257-2265 (2008).
181. Lu, J., Hou, R., Booth, C.J., Yang, S.H. & Snyder, M. Defined culture conditions of human embryonic stem cells. *Proc Natl Acad Sci U S A* **103**, 5688-5693 (2006).
182. Laperle, A. et al. Alpha-5 Laminin Synthesized by Human Pluripotent Stem Cells Promotes Self-Renewal. *Stem Cell Reports* **5**, 195-206.
183. Martin, G.R. & Evans, M.J. Differentiation of Clonal Lines of Teratocarcinoma Cells - Formation of Embryoid Bodies Invitro. *Proc Natl Acad Sci U S A* **72**, 1441-1445 (1975).
184. Evans, M.J. & Kaufman, M.H. Establishment in Culture of Pluripotential Cells from Mouse Embryos. *Nature* **292**, 154-156 (1981).
185. Martin, G.R. Isolation of a Pluripotent Cell-Line from Early Mouse Embryos Cultured in Medium Conditioned by Teratocarcinoma Stem-Cells. *P Natl Acad Sci-Biol* **78**, 7634-7638 (1981).
186. Bongso, A., Fong, C.Y., Ng, S.C. & Ratnam, S. Isolation and Culture of Inner Cell Mass Cells from Human Blastocysts. *Hum Reprod* **9**, 2110-2117 (1994).
187. Amit, M. et al. Clonally derived human embryonic stem cell lines maintain pluripotency and proliferative potential for prolonged periods of culture. *Dev Biol* **227**, 271-278 (2000).
188. Takahashi, K. et al. Induction of pluripotent stem cells from adult human fibroblasts by defined factors. *Cell* **131**, 861-872 (2007).
189. Copelan, E.A. Medical progress: Hematopoietic stem-cell transplantation. *New Engl J Med* **354**, 1813-1826 (2006).
190. Majumdar, M.K., Thiede, M.A., Haynesworth, S.E., Bruder, S.P. & Gerson, S.L. Human marrow-derived mesenchymal stem cells (MSCs) express hematopoietic cytokines and support long-term hematopoiesis when differentiated toward stromal and osteogenic lineages. *Journal of hematotherapy & stem cell research* **9**, 841-848 (2000).
191. Flores-Guzman, P., Fernandez-Sanchez, V. & Mayani, H. Concise review: ex vivo expansion of cord blood-derived hematopoietic stem and progenitor cells: basic principles, experimental approaches, and impact in regenerative medicine. *Stem cells translational medicine* **2**, 830-838 (2013).
192. Xu, M.J. et al. Stimulation of mouse and human primitive hematopoiesis by murine embryonic aorta-gonad-mesonephros-derived stromal cell lines. *Blood* **92**, 2032-2040 (1998).

193. Wilson, A. & Trumpp, A. Bone-marrow haematopoietic-stem-cell niches. *Nature reviews. Immunology* **6**, 93-106 (2006).
194. Nagasawa, T., Omatsu, Y. & Sugiyama, T. Control of hematopoietic stem cells by the bone marrow stromal niche: the role of reticular cells. *Trends in immunology* **32**, 315-320 (2011).
195. Taichman, R.S. & Emerson, S.G. Human Osteoblasts Support Hematopoiesis through the Production of Granulocyte-Colony-Stimulating Factor. *J Exp Med* **179**, 1677-1682 (1994).
196. McNiece, I., Harrington, J., Turney, J., Kellner, J. & Shpall, E.J. Ex vivo expansion of cord blood mononuclear cells on mesenchymal stem cells. *Cytotherapy* **6**, 311-317 (2004).
197. Kadereit, S. et al. Expansion of LTC-ICs and maintenance of p21 and BCL-2 expression in cord blood CD34(+)/CD38(-) early progenitors cultured over human MSCs as a feeder layer. *Stem Cells* **20**, 573-582 (2002).
198. Zhang, Y. et al. Human placenta-derived mesenchymal progenitor cells support culture expansion of long-term culture-initiating cells from cord blood CD34(+) cells. *Exp Hematol* **32**, 657-664 (2004).
199. Rosler, E., Brandt, J., Chute, J. & Hoffman, R. Cocultivation of umbilical cord blood cells with endothelial cells leads to extensive amplification of competent CD34(+)CD38(-) cells. *Exp Hematol* **28**, 841-852 (2000).
200. Nolta, J.A. et al. The AFT024 stromal cell line supports long-term ex vivo maintenance of engrafting multipotent human hematopoietic progenitors. *Leukemia* **16**, 352-361 (2002).
201. Xu, M.J. et al. Stimulation of mouse and human primitive hematopoiesis by murine embryonic aorta-gonad-mesonephros-derived stromal cell lines. *Blood* **92**, 2032-2040 (1998).
202. de Lima, M. et al. Cord-Blood Engraftment with Ex Vivo Mesenchymal-Cell Coculture. *New Engl J Med* **367**, 2305-2315 (2012).
203. Richards, M., Fong, C.Y., Chan, W.K., Wong, P.C. & Bongso, A. Human feeders support prolonged undifferentiated growth of human inner cell masses and embryonic stem cells. *Nat Biotechnol* **20**, 933-936 (2002).
204. Hovatta, O. et al. A culture system using human foreskin fibroblasts as feeder cells allows production of human embryonic stem cells. *Hum Reprod* **18**, 1404-1409 (2003).
205. Ludwig, T.E. et al. Derivation of human embryonic stem cells in defined conditions. *Nat Biotechnol* **24**, 185-187 (2006).
206. Amit, M., Shariki, C., Margulets, V. & Itskovitz-Eldor, J. Feeder layer- and serum-free culture of human embryonic stem cells. *Biology of reproduction* **70**, 837-845 (2004).
207. Rodin, S. et al. Long-term self-renewal of human pluripotent stem cells on human recombinant laminin-511. *Nat Biotech* **28**, 611-615 (2010).
208. Rodin, S. et al. Clonal culturing of human embryonic stem cells on laminin-521/E-cadherin matrix in defined and xeno-free environment. *Nature communications* **5**, 3195 (2014).
209. Braam, S.R. et al. Recombinant vitronectin is a functionally defined substrate that supports human embryonic stem cell self-renewal via alpha V beta 5 integrin. *Stem Cells* **26**, 2257-2265 (2008).

210. Saha, K. et al. Surface-engineered substrates for improved human pluripotent stem cell culture under fully defined conditions. *Proc Natl Acad Sci U S A* **108**, 18714-18719 (2011).
211. Hakala, H. et al. Comparison of biomaterials and extracellular matrices as a culture platform for multiple, independently derived human embryonic stem cell lines. *Tissue engineering. Part A* **15**, 1775-1785 (2009).
212. Michael, K.E. et al. Adsorption-induced conformational changes in fibronectin due to interactions with well-defined surface chemistries. *Langmuir* **19**, 8033-8040 (2003).
213. Katz, B.Z. et al. Physical state of the extracellular matrix regulates the structure and molecular composition of cell-matrix adhesions. *Mol Biol Cell* **11**, 1047-1060 (2000).
214. Garcia, A.J., Vega, M.D. & Boettiger, D. Modulation of cell proliferation and differentiation through substrate-dependent changes in fibronectin conformation. *Mol Biol Cell* **10**, 785-798 (1999).
215. Hernandez, J.C.R., Sanchez, M.S., Soria, J.M., Ribelles, J.L.G. & Pradas, M.M. Substrate chemistry-dependent conformations of single laminin molecules on polymer surfaces are revealed by the phase signal of atomic force microscopy. *Biophys J* **93**, 202-207 (2007).
216. Kohen, N.T., Little, L.E. & Healy, K.E. Characterization of Matrigel interfaces during defined human embryonic stem cell culture. *Biointerphases* **4**, 69-79 (2009).
217. Nilsson, S.K. et al. Osteopontin, a key component of the hematopoietic stem cell niche and regulator of primitive hematopoietic progenitor cells. *Blood* **106**, 1232-1239 (2005).
218. Rowland, T.J. et al. Roles of Integrins in Human Induced Pluripotent Stem Cell Growth on Matrigel and Vitronectin. *Stem Cells Dev* **19**, 1231-1240 (2010).
219. Lambshead, J.W., Meagher, L., O'Brien, C. & Laslett, A.L. Defining synthetic surfaces for human pluripotent stem cell culture. *Cell Regen (Lond)* **2**, 7 (2013).
220. Villa-Diaz, L.G., Kim, J.K., Laperle, A., Palecek, S.P. & Krebsbach, P.H. Inhibition of Focal Adhesion Kinase Signaling by Integrin alpha6beta1 Supports Human Pluripotent Stem Cell Self-Renewal. *Stem Cells* **34**, 1753-1764 (2016).
221. Notta, F. et al. Isolation of single human hematopoietic stem cells capable of long-term multilineage engraftment. *Science* **333**, 218-221 (2011).
222. Pollard, S.M. et al. Glioma stem cell lines expanded in adherent culture have tumor-specific phenotypes and are suitable for chemical and genetic screens. *Cell stem cell* **4**, 568-580 (2009).
223. Chang, C. et al. A laminin 511 matrix is regulated by TAZ and functions as the ligand for the alpha6Bbeta1 integrin to sustain breast cancer stem cells. *Genes & development* **29**, 1-6 (2015).
224. Ben-Porath, I. et al. An embryonic stem cell-like gene expression signature in poorly differentiated aggressive human tumors. *Nature genetics* **40**, 499-507 (2008).
225. Pierschbacher, M.D. & Ruoslahti, E. Cell Attachment Activity of Fibronectin Can Be Duplicated by Small Synthetic Fragments of the Molecule. *Nature* **309**, 30-33 (1984).
226. Ruoslahti, E. RGD and other recognition sequences for integrins. *Annu Rev Cell Dev Bi* **12**, 697-715 (1996).
227. Pfaff, M. et al. Selective recognition of cyclic RGD peptides of NMR defined conformation by alpha IIb beta 3, alpha V beta 3, and alpha 5 beta 1 integrins. *The Journal of biological chemistry* **269**, 20233-20238 (1994).
228. Kolhar, P., Kotamraju, V.R., Hikita, S.T., Clegg, D.O. & Ruoslahti, E. Synthetic surfaces for human embryonic stem cell culture. *J Biotechnol* **146**, 143-146 (2010).

229. Hern, D.L. & Hubbell, J.A. Incorporation of adhesion peptides into nonadhesive hydrogels useful for tissue resurfacing. *J Biomed Mater Res* **39**, 266-276 (1998).
230. Melkoumian, Z. et al. Synthetic peptide-acrylate surfaces for long-term self-renewal and cardiomyocyte differentiation of human embryonic stem cells. *Nat Biotechnol* **28**, 606-U695 (2010).
231. Klim, J.R., Li, L.Y., Wrighton, P.J., Piekarczyk, M.S. & Kiessling, L.L. A defined glycosaminoglycan-binding substratum for human pluripotent stem cells. *Nat Methods* **7**, 989-U972 (2010).
232. Yang, X., Sarvestani, S.K., Moeinzadeh, S., He, X. & Jabbari, E. Effect of CD44 binding peptide conjugated to an engineered inert matrix on maintenance of breast cancer stem cells and tumorsphere formation. *PloS one* **8**, e59147 (2013).
233. Raic, A., Rodling, L., Kalbacher, H. & Lee-Thedieck, C. Biomimetic macroporous PEG hydrogels as 3D scaffolds for the multiplication of human hematopoietic stem and progenitor cells. *Biomaterials* **35**, 929-940 (2014).
234. Schweller, R.M. & West, J.L. Encoding Hydrogel Mechanics via Network Cross-Linking Structure. *ACS biomaterials science & engineering* **1**, 335-344 (2015).
235. Qian, X., Villa-Diaz, L.G. & Krebsbach, P.H. Advances in Culture and Manipulation of Human Pluripotent Stem Cells. *J Dent Res* **92**, 956-962 (2013).
236. Villa-Diaz, L.G., Ross, A.M., Lahann, J. & Krebsbach, P.H. Concise Review: The Evolution of human pluripotent stem cell culture: From feeder cells to synthetic coatings. *Stem Cells* **31**, 1-7 (2013).
237. Villa-Diaz, L.G. et al. Synthetic polymer coatings for long-term growth of human embryonic stem cells. *Nat Biotechnol* **28**, 581-583 (2010).
238. Villa-Diaz, L.G. et al. Derivation of mesenchymal stem cells from human induced pluripotent stem cells cultured on synthetic substrates. *Stem Cells* **30**, 1174-1181 (2012).
239. Villa-Diaz, L. et al. Culture and passage of human embryonic stem cells on an artificial synthetic matrix composed of polykedsah hydrogel. *Biology of reproduction*, 186-186 (2007).
240. Villa-Diaz, L.G., Kim, J.K., Lahann, I. & Krebsbach, P.H. Derivation and Long-Term Culture of Transgene-Free Human Induced Pluripotent Stem Cells on Synthetic Substrates. *Stem cells translational medicine* **3**, 1410-1417 (2014).
241. Qian, X., Villa-Diaz, L.G., Kumar, R., Lahann, J. & Krebsbach, P.H. Enhancement of the propagation of human embryonic stem cells by modifications in the gel architecture of PMEDSAH polymer coatings. *Biomaterials* **35**, 9581-9590 (2014).
242. Irwin, E.E., Gupta, R., Dashti, D.C. & Healy, K.E. Engineered polymer-media interfaces for the long-term self-renewal of human embryonic stem cells. *Biomaterials* **32**, 6912-6919 (2011).
243. Brafman, D.A. et al. Long-term human pluripotent stem cell self-renewal on synthetic polymer surfaces. *Biomaterials* **31**, 9135-9144 (2010).
244. Pittenger, M.F. et al. Multilineage potential of adult human mesenchymal stem cells. *Science* **284**, 143-147 (1999).
245. Huang, W., Yang, S.Y., Shao, J.Z. & Li, Y.P. Signaling and transcriptional regulation in osteoblast commitment and differentiation. *Front Biosci* **12**, 3068-3092 (2007).
246. Milona, M., Gough, J.E. & Edgar, A.J. Expression of alternatively spliced isoforms of human Sp7 in osteoblast-like cells. *Bmc Genomics* **4** (2003).

247. Kirkham, G.R. & Cartmell, S.H. in Genes and Proteins Involved in the Regulation of Osteogenesis, Vol. 3 22 (Expertissues, 2007).
248. Jaiswal, N., Haynesworth, S.E., Caplan, A.I. & Bruder, S.P. Osteogenic differentiation of purified, culture-expanded human mesenchymal stem cells in vitro. *J Cell Biochem* **64**, 295-312 (1997).
249. Gjelstrup, L. & Stelzer, T. Expansion and differentiation of human mesenchymal stromal cells. *VWR bioMarke* **28**, 20-22 (2012).
250. Bonewald, L.F. et al. Von Kossa staining alone is not sufficient to confirm that mineralization in vitro represents bone formation. *Calcified Tissue Int* **72**, 537-547 (2003).
251. Rungby, J., Kassem, M., Eriksen, E.F. & Danscher, G. The Vonkossa Reaction for Calcium Deposits - Silver Lactate Staining Increases Sensitivity and Reduces Background. *Histochem J* **25**, 446-451 (1993).
252. Gregory, C.A., Gunn, W.G., Peister, A. & Prockop, D.J. An Alizarin red-based assay of mineralization by adherent cells in culture: comparison with cetylpyridinium chloride extraction. *Anal Biochem* **329**, 77-84 (2004).
253. Sun, H.L. et al. Osteogenic differentiation of human amniotic fluid-derived stem cells induced by bone morphogenetic protein-7 and enhanced by nanofibrous scaffolds. *Biomaterials* **31**, 1133-1139 (2010).
254. Ogawa, R. et al. Osteogenic and chondrogenic differentiation by adipose-derived stem cells harvested from GFP transgenic mice. *Biochem Bioph Res Co* **313**, 871-877 (2004).
255. Shao, Y., Sang, J.M. & Fu, J.P. On human pluripotent stem cell control: The rise of 3D bioengineering and mechanobiology. *Biomaterials* **52**, 26-43 (2015).
256. Gerecht, S. et al. Hyaluronic acid hydrogen for controlled self-renewal and differentiation of human embryonic stem cells. *P Natl Acad Sci USA* **104**, 11298-11303 (2007).
257. Li, Z.S., Leung, M., Hopper, R., Ellenbogen, R. & Zhang, M.Q. Feeder-free self-renewal of human embryonic stem cells in 3D porous natural polymer scaffolds. *Biomaterials* **31**, 404-412 (2010).
258. Siti-Ismail, N., Bishop, A.E., Polak, J.M. & Mantalaris, A. The benefit of human embryonic stem cell encapsulation for prolonged feeder-free maintenance. *Biomaterials* **29**, 3946-3952 (2008).
259. Levenberg, S. et al. Differentiation of human embryonic stem cells on three-dimensional polymer scaffolds. *P Natl Acad Sci USA* **100**, 12741-12746 (2003).
260. Park, I.H. et al. Disease-specific induced pluripotent stem cells. *Cell* **134**, 877-886 (2008).
261. Yu, J.Y. et al. Induced pluripotent stem cell lines derived from human somatic cells. *Science* **318**, 1917-1920 (2007).
262. Cukierman, E., Pankov, R., Stevens, D.R. & Yamada, K.M. Taking cell-matrix adhesions to the third dimension. *Science* **294**, 1708-1712 (2001).
263. Discher, D.E., Janmey, P. & Wang, Y.L. Tissue cells feel and respond to the stiffness of their substrate. *Science* **310**, 1139-1143 (2005).
264. Ungrin, M.D., Joshi, C., Nica, A., Bauwens, C. & Zandstra, P.W. Reproducible, Ultra High-Throughput Formation of Multicellular Organization from Single Cell Suspension-Derived Human Embryonic Stem Cell Aggregates. *PloS one* **3** (2008).

265. Lei, Y.G. & Schaffer, D.V. A fully defined and scalable 3D culture system for human pluripotent stem cell expansion and differentiation. *P Natl Acad Sci USA* **110**, E5039-E5048 (2013).
266. Lee, J.B. et al. Highly Porous Electrospun Nanofibers Enhanced by Ultrasonication for Improved Cellular Infiltration. *Tissue Eng Pt A* **17**, 2695-2702 (2011).
267. Rahman, C.V. et al. Controlled release of BMP-2 from a sintered polymer scaffold enhances bone repair in a mouse calvarial defect model. *J Tissue Eng Regen M* **8**, 59-66 (2014).
268. Moshaverinia, A. et al. Co-encapsulation of anti-BMP2 monoclonal antibody and mesenchymal stem cells in alginate microspheres for bone tissue engineering. *Biomaterials* **34**, 6572-6579 (2013).
269. Li, L. et al. Controlled dual delivery of BMP-2 and dexamethasone by nanoparticle-embedded electrospun nanofibers for the efficient repair of critical-sized rat calvarial defect. *Biomaterials* **37**, 218-229 (2015).
270. Quinlan, E. et al. Development of collagen-hydroxyapatite scaffolds incorporating PLGA and alginate microparticles for the controlled delivery of rhBMP-2 for bone tissue engineering. *J Control Release* **198**, 71-79 (2015).
271. Liao, Y.H. et al. Osteogenic differentiation of adipose-derived stem cells and calvarial defect repair using baculovirus-mediated co-expression of BMP-2 and miR-148b. *Biomaterials* **35**, 4901-4910 (2014).
272. V, L., Meinel, L., Merkle, H.P. & Gander, B. Localized delivery of growth factors for bone repair. *Eur J Pharm Biopharm* **58**, 197-208 (2004).
273. Zong, C. et al. Reconstruction of Rat Calvarial Defects with Human Mesenchymal Stem Cells and Osteoblast-Like Cells in Poly-Lactic-Co-Glycolic Acid Scaffolds. *Eur Cells Mater* **20**, 109-120 (2010).
274. Ma, J.L. et al. Concise Review: Cell-Based Strategies in Bone Tissue Engineering and Regenerative Medicine. *Stem cells translational medicine* **3**, 98-107 (2014).
275. Cowan, C.M. et al. Adipose-derived adult stromal cells heal critical-size mouse calvarial defects. *Nat Biotechnol* **22**, 560-567 (2004).
276. Yoon, E., Dhar, S., Chun, D.E., Gharibjanian, N.A. & Evans, G.R.D. In vivo osteogenic potential of human adipose-derived stem cells/poly lactide-co-glycolic acid constructs for bone regeneration in a rat critical-sized calvarial defect model. *Tissue Eng* **13**, 619-627 (2007).
277. Levi, B. et al. Human Adipose Derived Stromal Cells Heal Critical Size Mouse Calvarial Defects. *PloS one* **5** (2010).
278. Rai, B. et al. Differences between in vitro viability and differentiation and in vivo bone-forming efficacy of human mesenchymal stem cells cultured on PCL-TCP scaffolds. *Biomaterials* **31**, 7960-7970 (2010).
279. Zhou, J. et al. The repair of large segmental bone defects in the rabbit with vascularized tissue engineered bone. *Biomaterials* **31**, 1171-1179 (2010).
280. Kaigler, D. et al. Transplanted endothelial cells enhance orthotopic bone regeneration. *J Dent Res* **85**, 633-637 (2006).
281. Ducic, J. Titanium mesh and hydroxyapatite cement cranioplasty: A report of 20 cases. *J Oral Maxil Surg* **60**, 272-276 (2002).
282. Pierdomenico, L. et al. Multipotent mesenchymal stem cells with immunosuppressive activity can be easily isolated from dental pulp. *Transplantation* **80**, 836-842 (2005).

283. Bianco, P., Robey, P.G. & Simmons, P.J. Mesenchymal stem cells: Revisiting history, concepts, and assays. *Cell stem cell* **2**, 313-319 (2008).
284. Akahane, M. et al. Osteogenic matrix sheet-cell transplantation using osteobtastic cell sheet resulted in bone formation without scaffold at an ectopic site. *J Tissue Eng Regen M* **2**, 196-201 (2008).
285. Pirraco, R.P. et al. Development of Osteogenic Cell Sheets for Bone Tissue Engineering Applications. *Tissue Eng Pt A* **17**, 1507-1515 (2011).
286. Kim, J.Y. et al. Evaluation of Solid Free-Form Fabrication-Based Scaffolds Seeded with Osteoblasts and Human Umbilical Vein Endothelial Cells for Use In Vivo Osteogenesis. *Tissue Eng Pt A* **16**, 2229-2236 (2010).
287. Costa-Pinto, A.R. et al. Chitosan-poly(butylene succinate) scaffolds and human bone marrow stromal cells induce bone repair in a mouse calvaria model. *J Tissue Eng Regen M* **6**, 21-28 (2012).
288. Siegel, R.L., Miller, K.D. & Jemal, A. Cancer Statistics, 2016. *Ca-Cancer J Clin* **66**, 7-30 (2016).
289. Coleman, R.E. Metastatic bone disease: clinical features, pathophysiology and treatment strategies. *Cancer Treat Rev* **27**, 165-176 (2001).
290. Weilbaecher, K.N., Guise, T.A. & McCauley, L.K. Cancer to bone: a fatal attraction. *Nat Rev Cancer* **11**, 411-425 (2011).
291. Mundy, G.R. Metastasis to bone: Causes, consequences and therapeutic opportunities. *Nat Rev Cancer* **2**, 584-593 (2002).
292. Weigelt, B., Peterse, J.L. & van't Veer, L.J. Breast cancer metastasis: Markers and models. *Nat Rev Cancer* **5**, 591-602 (2005).
293. Mishra, A., Shiozawa, Y., Pienta, K.J. & Taichman, R.S. Homing of Cancer Cells to the Bone. *Cancer Microenvironment* **4**, 221-235 (2011).
294. Sloan, E.K. et al. Tumor-specific expression of alpha v beta 3 integrin promotes spontaneous metastasis of breast cancer to bone. *Breast Cancer Res* **8** (2006).
295. Sharp, J.A., Waltham, M., Williams, E.D., Henderson, M.A. & Thompson, E.W. Transfection of MDA-MB-231 human breast carcinoma cells with bone sialoprotein (BSP) stimulates migration and invasion in vitro and growth of primary and secondary tumors in nude mice. *Clin Exp Metastas* **21**, 19-29 (2004).
296. Thibaudeau, L. et al. A tissue-engineered humanized xenograft model of human breast cancer metastasis to bone. *Dis Model Mech* **7**, 299-309 (2014).
297. Kuperwasser, C. et al. A mouse mode of human breast cancer metastasis to human bone. *Cancer Res* **65**, 6130-6138 (2005).
298. Schuster, J., Zhang, J. & Longo, M. A novel human osteoblast-derived severe combined immunodeficiency mouse model of bone metastasis. *J Neurosurg-Spine* **4**, 388-391 (2006).
299. Suzuki, C. et al. Radiologic measurements of tumor response to treatment: Practical approaches and limitations. *Radiographics* **28**, 329-344 (2008).
300. Schoenfeld, A. et al. The detection of micrometastases in the peripheral blood and bone marrow of patients with breast cancer using immunohistochemistry and reverse transcriptase polymerase chain reaction for keratin 19. *Eur J Cancer* **33**, 854-861 (1997).
301. Moreau, J.E. et al. Tissue-engineered bone serves as a target for metastasis of human breast cancer in a mouse model. *Cancer Res* **67**, 10304-10308 (2007).

302. Stacer, A.C. et al. Imaging Reporters for Proteasome Activity Identify Tumor- and Metastasis-Initiating Cells. *Mol Imaging* **14**, 414-432 (2015).
303. Cavnar, S.P. et al. Modeling Selective Elimination of Quiescent Cancer Cells from Bone Marrow. *Neoplasia* **17**, 625-633 (2015).
304. Smith, M.C.P. et al. CXCR4 regulates growth of both primary and metastatic breast cancer. *Cancer Res* **64**, 8604-8612 (2004).
305. Sun, H.L., Jung, Y.H., Shiozawa, Y., Taichman, R.S. & Krebsbach, P.H. Erythropoietin Modulates the Structure of Bone Morphogenetic Protein 2-Engineered Cranial Bone. *Tissue Eng Pt A* **18**, 2095-2105 (2012).
306. Park, T.H. et al. Photoswitchable Particles for On-Demand Degradation and Triggered Release. *Small* **9**, 3051-3057 (2013).
307. Lu, P.F., Weaver, V.M. & Werb, Z. The extracellular matrix: A dynamic niche in cancer progression. *J Cell Biol* **196**, 395-406 (2012).
308. Fidler, I.J. Timeline - The pathogenesis of cancer metastasis: the 'seed and soil' hypothesis revisited. *Nat Rev Cancer* **3**, 453-458 (2003).
309. O'Brien, C.A., Pollett, A., Gallinger, S. & Dick, J.E. A human colon cancer cell capable of initiating tumour growth in immunodeficient mice. *Nature* **445**, 106-110 (2007).
310. Qian, X.M. et al. In vivo tumor targeting and spectroscopic detection with surface-enhanced Raman nanoparticle tags. *Nat Biotechnol* **26**, 83-90 (2008).
311. Whittle, J.R., Lewis, M.T., Lindeman, G.J. & Visvader, J.E. Patient-derived xenograft models of breast cancer and their predictive power. *Breast Cancer Res* **17** (2015).
312. Zhang, X.M. et al. A Renewable Tissue Resource of Phenotypically Stable, Biologically and Ethnically Diverse, Patient-Derived Human Breast Cancer Xenograft Models. *Cancer Res* **73**, 4885-4897 (2013).